Preferred Orientation Modelling in High-Pressure Powder Diffraction Applied To Structural Studies Of Semiconductors.

Thesis submitted by

Nicholas George Wright

For the Degree of

Doctor of Philosophy

Department of Physics and Astronomy

The University of Edinburgh

1994

ACKNOWLEDGEMENTS

Firstly, I would like to thank my supervisor, Richard Nelmes, for all his help and encouragement over the entire period of this thesis. I am also very grateful to all the staff of the Physics department of Edinburgh University for the kindness and friendship they have shown to me over many years. In particular, I would like to thank Malcolm McMahon, Dave Allan, John Loveday, and Rory Wilson for their help and companionship during the many late nights that are the lot of an experimental physicist.

I am also very grateful for the assistance and friendship of the staff at SRS Daresbury. I would like to express my thanks particularly to Graham Bushnell-Wye and the other members of the Daresbury Diffraction Project for their expert assistance, without which most of the experiments described in this thesis could not have been performed.

Lastly, and perhaps most importantly, I would like to thank all my family and friends.

Abstract

One of the main problems encountered in structure refinement from powder-diffraction data collected under high-pressure is severe preferred orientation in the sample, which results in inaccurate relative intensities of the diffraction peaks. Correlation between the effects of structure and preferred orientation on the reflection intensities may result in serious errors in refined structural parameters from least-squares (Rietveld) refinement. Therefore, in high-pressure studies, it is particularly crucial to determine any sample texture independently from the crystal structure. Collecting data with the sample (i.e. the high-pressure cell) in different orientations relative to the incident beam allows the influence of texture on the reflection intensities to be directly determined.

This thesis presents a new technique which makes use of the ability of area detectors, such as image-plates, to record simultaneously data from crystallites in many different orientations to model texture from samples under pressure. Experimental methods have been developed to allow data to be collected of sufficient quality to allow preferred orientation of the sample to be accurately modelled. A new preferred orientation model is presented that describes the effect of preferred orientation on the whole 2-D powder pattern and is suitable for the transmission geometry used in high-pressure angle-dispersive diffraction. Techniques are developed which make use of the new model and the 2-D character of the effect of preferred orientation on the powder pattern to de-correlate the effects of texture and structure on the powder pattern. The model and these techniques are tested against diffraction data collected from a wide range of sample orientations from a sample of known texture.

The techniques are applied to a study of the crystal structures of three high-pressure phases of the II-VI semiconductor HgTe. A detailed study of the crystal structure of the cinnabar phase of HgTe is presented, which shows the structure to be different from the prototype HgS cinnabar, with coordination much closer to 4-fold. Results on the pressure dependence of the structure are presented and discussed in relation to the transformation upon further pressure increase to the NaCl structure. A structural study of the previously unsolved HgTe phase IV is presented. This phase, which forms with particularly severe preferred orientation, is found to be an orthorhombic distortion of the NaCl structure. Also presented is a short study of HgTe phase V, which is observed to occur above 29 GPa and to have a disordered b.c.c. structure.

The new techniques can also be used to extract from the microstructure of the sample valuable information on the transition mechanisms between phases. The precise mechanisms by which many phase transitions under pressure occur remain unknown, and this is one of the most significant unsolved problems in condensed matter science. The preferred orientation techniques developed in this thesis are used to extract information on the phase transition sequence seen in Si under pressure. Results are presented on changes in texture observed at the β-tin→Imma and the Imma→simple hexagonal transitions of Si and are discussed in the light of a simple transition mechanism between these phases.

CONTENTS

CHAPTER ONE

1.1 Introduction To The Thesis

Of the two thermodynamic variables, temperature and pressure, the latter is the most neglected as a probe of the solid-state. Application of high-pressure to a solid can dramatically alter its crystal lattice, atomic structure and electronic properties in a very different manner to temperature variation. Placing a solid under pressure causes (in general) a contraction of the lattice but without the change in thermal energy of the atoms that is caused by changing the lattice by a temperature variation. In addition, the increased overlap of electronic wavefunctions from lattice contraction can cause large changes in electronic properties, i.e. many insulators become metals under pressure. Perhaps one of the most dramatic examples of pressure-induced electronic transitions is found in Caesium, which undergoes a series of transitions as the pressure increases (Hall *et al*, (1964), Takemura and Shimomura, (1982)). At ambient pressure Caesium has the b.c.c. structure. Under pressure it transforms to the f.c.c. structure, which is a close-packed arrangement of the atoms in the lattice. Upon further pressure increase it transforms to another f.c.c. structure (a rare example of an isomorphic transition) and then to a tetragonal structure. This tetragonal structure is not close-packed and therefore the arrangement of the atoms in the structure becomes more open as the lattice contracts. This structural transition sequence is thought to be induced by a series of electronic transitions (the electrons change between different electron shells with pressure). During the transitions to the f.c.c. structures the 6s electrons are driven towards the nucleus, so that they are accommodated into the 5d shell, and the size of the atom itself decreases. This causes a very rapid decrease in the lattice parameter with pressure and as a result the compressibility is very large (see figure 1.1). However after the transition to the tetragonal phase, all the electrons have moved into the 5d shell and compression of the structure becomes much more difficult. Further pressure increase causes only a contraction of the distance between the atoms. Thus, initially, the compressibility of Caesium is very high but reduces rapidly once all the electrons have transferred to the 5d shell.

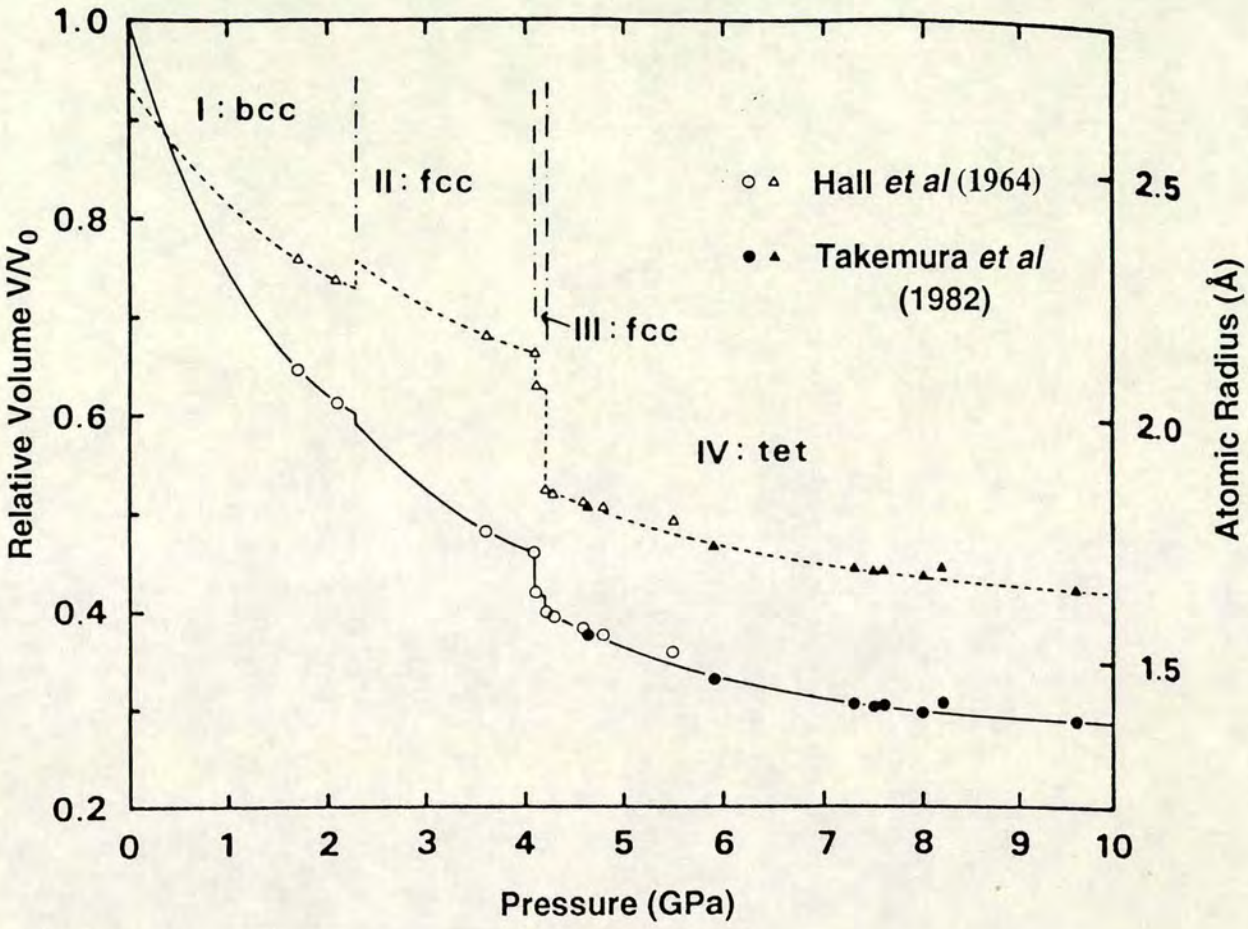

Figure 1.1 Variation of relative volume (circles) and atomic radius (triangles) of Cs with pressure. Closed symbols are those of Hall *et al* (1964) and open symbols those of Takemura *et al.* (1982) (from Takemura *et al*, (1982))

Semiconductors have long been considered to be one of the most interesting class of materials under pressure. The group IV elements Si and Ge and a great many III-V and II-VI compounds are semiconducting at ambient or very low pressure. As the pressure is increased semiconductors undergo structural phase transitions, which are linked to changes in electronic properties. For example, Si transforms from the ambient pressure semiconducting cubic structure to a metallic tetragonal phase, which has the same crystal structure as the β-phase of Sn. Early high-pressure studies of semiconductors were performed by pressurising the sample in a piston-cylinder device. Volume collapses of the lattice at a phase transition were determined from direct measurement of the piston translation. This method, and later studies of resistivity under pressure, were responsible for the discovery of many phase transitions. In order to identify the structural changes accompanying these transitions, it was necessary to design and develop more specialised equipment so that x-ray diffraction studies could be performed on samples held under high-pressure.

The large volume collapse that occurs at semiconductor phase transitions results in the pulverisation of single crystal samples. This has ensured that powder diffraction techniques have been widely adopted for the study of semiconductors under pressure. Early high-pressure cells were based on hydraulically driven piston-cylinder or multi-anvil designs. Although these early devices were only capable of reaching pressures of about 10 GPa, the structures of many high-pressure semiconductor phases were nevertheless identified. These studies were mainly conducted using monochromatic x-ray radiation in conjunction with photographic film to detect the angle-dispersive diffraction (ADX) pattern. One of the principal problems with powder-diffraction techniques for high-pressure work is preferred orientation, or texture, which causes the reflection intensities to be unreliable. The compression of the sample frequently causes the crystallites, that make up the powder, to orientate along one particular direction. If such a preferred orientation exists, the intensity of each reflection will no longer depend on just the crystal structure and reflection multiplicities but will also depend on the number of crystallites in the diffraction condition. At this early stage texture problems limited high-pressure work to determining only very simple structures and more complex cases eluded solution.

The development of the diamond anvil cell, in which pressure is applied to the gasketed sample through single-crystal diamond anvils, allowed much higher pressures to be reached. However attaining pressures as high as 400 GPa requires extremely small sample volumes, which results in a weak signal compared to the unavoidable and relatively high background from the diamonds and other illuminated pressure cell components. Energy-dispersive diffraction (EDX) techniques overcome this limitation by utilising the full power of a polychromatic x-ray beam, often from a synchrotron source. However the high degree of collimation necessary in EDX studies ensures that the diffraction pattern is arising from scattering by very few crystallites. The powder averaging is therefore fairly poor and any preferred orientation in the sample will affect the reflection intensities greatly. These problems and the general difficulties of white beam work (e.g. complex energy dependencies in the detector sensitivity) meant that EDX studies under pressure have been largely limited to determining to only very simple structures.

Although the general systematics of semiconductor phase transitions was determined to very high pressures, the understanding of the underlying atomic structure under pressure did not advance significantly until angle-dispersive techniques became

feasible. With photographic film or 1-D electronic detectors, the intensity measured using monochromatic techniques is much too weak from the small sample volumes in DACs. However the development of extremely sensitive 2-D (or area) detectors, which were capable of recording simultaneously a significant fraction of the whole powder pattern, has meant that the ADX technique has become feasible for diffraction work at high pressures. If the intensity of a reflection is averaged around the powder ring, a large increase in the signal-to-noise ratio can be achieved. In addition, the intensities resulting from angle-dispersive techniques do not suffer from the poor powder averaging and energy-dependent corrections of EDX work and it is now possible to perform reliable structural studies under pressure. Research groups in Japan and the UK have developed image-plate techniques considerably in the last five years and detailed studies of crystal structures have been reported up to ~50 GPa. However, the compression of the sample to such high pressures has made the problem of preferred orientation even more severe.

The effect of preferred orientation on the relative intensities of the diffraction peaks can be modelled during analysis of the powder diffraction data. However such a texture model will depend critically on the experimental geometry. Since the geometry used in high-pressure studies is generally different from that used in ambient crystallography, modelling of sample texture under pressure requires a quite different texture model to those commonly applied in conventional studies. However, even when the correct model for sample preferred orientation is known it is nevertheless difficult to determine from a single powder pattern whether individual reflections are (say) observed to be weak due to structural reasons or due to texture. During structure solution from data obtained from powder samples, it is vital that the effects of preferred orientation on the relative intensities of the diffraction peaks are separated from possible structural causes. As a powder held at high-pressure can have severe sample texture, the effects of preferred orientation on the diffraction pattern can be a serious source of error. De-correlating the influences of crystal structure and sample texture on the diffraction pattern can be performed by obtaining data from the same sample in different orientations (the crystal structure will be identical but the effect of the sample texture on the diffraction pattern should change systematically with sample orientation). In ambient pressure crystallography such texture studies are common but, until the recent development of area detectors, studies of preferred orientation from samples under pressure were impractical, due principally to the low diffracted intensity from the small sample volumes used in diamond-anvil pressure cells.

This thesis presents the work undertaken by the author as a member of The University of Edinburgh image-plate group based at the UK synchrotron source at Daresbury, Cheshire. In the last three years the Edinburgh group have developed image-plate techniques for high-pressure powder-diffraction studies considerably and have produced a significant amount of work on the crystal structures of semiconductors and related materials under pressure (see for example Nelmes *et al*, (1993)). As part of that work it has become apparent that modelling of microstructural effects, such as preferred orientation, is crucial for structure solution and refinement of high-pressure powder-diffraction data. This thesis presents the author's contribution to the understanding of the effects of sample preferred orientation on high-pressure angle-dispersive powder-diffraction data. Experimental techniques for obtaining data on preferred orientation under pressure are presented and discussed. A technique to model the effect of preferred orientation on the full 2-D powder pattern recorded by an image-plate has been developed and applied in various high-pressure structural studies of semiconductors.

1.2 Thesis Layout

Chapter 2 serves as an introduction to the main experimental techniques used in high-pressure powder-diffraction studies and the experimental methods developed for use with the University of Edinburgh image-plate set-up at SRS Daresbury. The computer software used in this thesis for the processing of the image-plate data and the specialist experimental techniques developed for the study of preferred orientation are presented. It is felt necessary to present this information at this stage of the thesis, as knowledge of the experimental geometry and restrictions is important for the understanding of subsequent chapters.

Chapter 3 contains a short introduction to preferred orientation and a review of previous work on the subject. A phenomenological approach, developed by the author, to facilitate the understanding of texture effects on the full 2-D powder pattern (in the diffraction geometry used in high-pressure studies) is presented and discussed. The effects of preferred orientation on the diffraction pattern with different orientations of the sample is also discussed.

Chapter 4 presents a new mathematical model to describe the effects of preferred orientation on the full 2-D diffraction pattern, which is suitable for the transmission

geometry of a high-pressure cell. The model is tested against diffraction data from a sample of known texture and its use in determining the correct relative intensities of reflections in the data without reference to a structural model is discussed. Preliminary work from this section has been published (Wright *et al*, (1993a)).

Chapter 5 focuses on the experimental and modelling techniques developed for performing texture studies on materials under pressure and details results from such studies in a variety of materials. The first section presents the results of a detailed study on the strong preferred orientation in the high-pressure β-tin phase of silicon. As the structure of this phase is known, it presents an ideal opportunity to investigate the experimental and modelling difficulties associated with the study of preferred orientation in the necessarily small sample volumes used in high-pressure work. A study of the extreme preferred orientation found in the previously unsolved high-pressure orthorhombic phases of the II-VI semiconductors HgTe, CdTe and ZnTe is presented in the second section. Due to the degree of texture in these materials, the careful modelling of the preferred orientation was crucial to the structure solution of these phases. A third section details the results from a briefer investigation of the preferred orientation found in the III-VI semiconductor InSb, performed in support of a series of structural studies on the core group IV, III-V and II-VI semiconductor materials by the Edinburgh group.

Chapter 6 presents the application of the information gained from the texture studies of chapter 5 to a study of the crystal structures of three high-pressure phases of the II-VI semiconductor HgTe. Isomorphous phases of CdTe and ZnTe show preferred orientation effects similar to those observed in HgTe phase IV. The texture effects seen in all three compounds are compared. This chapter represents the principal work on crystal structure solution and refinement in the thesis and has produced two published papers (Wright *et al*, (1993b)) and Nelmes *et al*, (1993)). Results are also presented from a study of the sample texture in three adjacent high-pressure phases of Si and discussed in the context of using sample texture to extract information on possible transition mechanisms between phases.

Chapter 7 draws conclusions from the work in this thesis and discusses possible future work and experimental developments.

CHAPTER TWO

Experimental Methods

2.1 Introduction

This chapter serves as an introduction to both the physics of powder diffraction and the specialised experimental techniques that are required for powder diffraction at high-pressure. The experimental methods and high-pressure equipment, that have been used in or developed for this thesis, are described in detail. Alternative high-pressure techniques and possible future developments are presented and discussed. All of the experimental work performed by the author has utilised the image-plate system, which has been developed for high-pressure structural studies by a group from The University of Edinburgh based at the SRS Daresbury Laboratory. The high sensitivity of the image-plate has enabled the principal problem of high-pressure angle-dispersive techniques, namely low signal intensity, to be overcome and has allowed for the first time full structural studies to be performed under pressure using x-ray powder-diffraction. Work on the image-plate system, whose development has required specialist beamline techniques and data processing software, began in 1991 and has continued through out the author's PhD studies. The author was not involved in the initial set-up of the basic image-plate system at SRS Daresbury but has played an integral part in the subsequent development of experimental technique, that has produced a significant improvement in data quality.

2.2 Why powder methods are used

Under pressure, a great many simple compounds and all group IV, II-VI, and III-V semiconductors undergo first-order phase transitions, often with a large change in unit cell volume. For example, Silicon transforms at ~8 GPa from the ambient pressure cubic diamond structure to the tetragonal β-tin structure with a ~20% change in unit-cell volume. It is not possible to take a single-crystal sample through such a transition without the crystal becoming pulverised by the magnitude of the volume

change. Because of this, powder diffraction techniques have become the dominant method for studying semiconductors and many other compounds under pressure.

2.3 Basic physics of powder crystallography

Consider a powder sample consisting of a large number of small crystallites and allow an incident x-ray beam to strike the sample as shown in figure 2.1. The incident radiation enters the powder and, provided a correctly oriented crystallite is present, is diffracted at some angle θ. The diffraction angle (θ) is determined by the Bragg diffraction condition

$$n\lambda = 2 d_{hkl} \sin(\theta) \tag{2.1}$$

where λ is the wavelength of the incident radiation, d_{hkl} is the spacing between the (hkl) planes that are in the diffraction condition and n is the order of reflection. By standard crystallographic convention, the need to explicitly state the reflection order disappears if families of lattice planes (nh, nk, nl) are defined as parallel to the (hkl) lattice plane with spacing d_{hkl}/n.

Figure 2.2 shows Bragg's Law in terms of the reciprocal lattice. The condition for a diffraction peak to occur is now expressed in terms of vectors as

$$\frac{\mathbf{s} - \mathbf{s}_0}{\lambda} = \mathbf{K}_{hkl} \tag{2.2}$$

where **s** is the diffracted beam, $\mathbf{s}_0$ the incident beam* and $\mathbf{K}_{hkl}$ is the reciprocal lattice vector (or scattering vector) for the (hkl) set of lattice planes. The intensity (I) of a given reflection from a small parallelopipedon crystallite can be shown to be given within kinematical diffraction theory (Warren, (1969)) by

$$I \propto P\, I_0 \lambda\, L\, F^2 \prod_{i=1}^{i=3} \frac{\sin^2(\pi/\lambda)(\mathbf{s}-\mathbf{s}_0).N_i\mathbf{a}_i}{\sin^2(\pi/\lambda)(\mathbf{s}-\mathbf{s}_0).\mathbf{a}_i} \tag{2.3}$$

where P is a factor which describes the effect of the polarisation of the incident beam, I_0 is the intensity in the incident beam, λ is the wavelength of the incident x-rays, L is a factor which describes the geometry of the data collection (the Lorentz factor) and F is the so-called structure factor for that (hkl) reflection. The intensity from N small

* Note: **s** and $\mathbf{s}_0$ are both unit vectors.

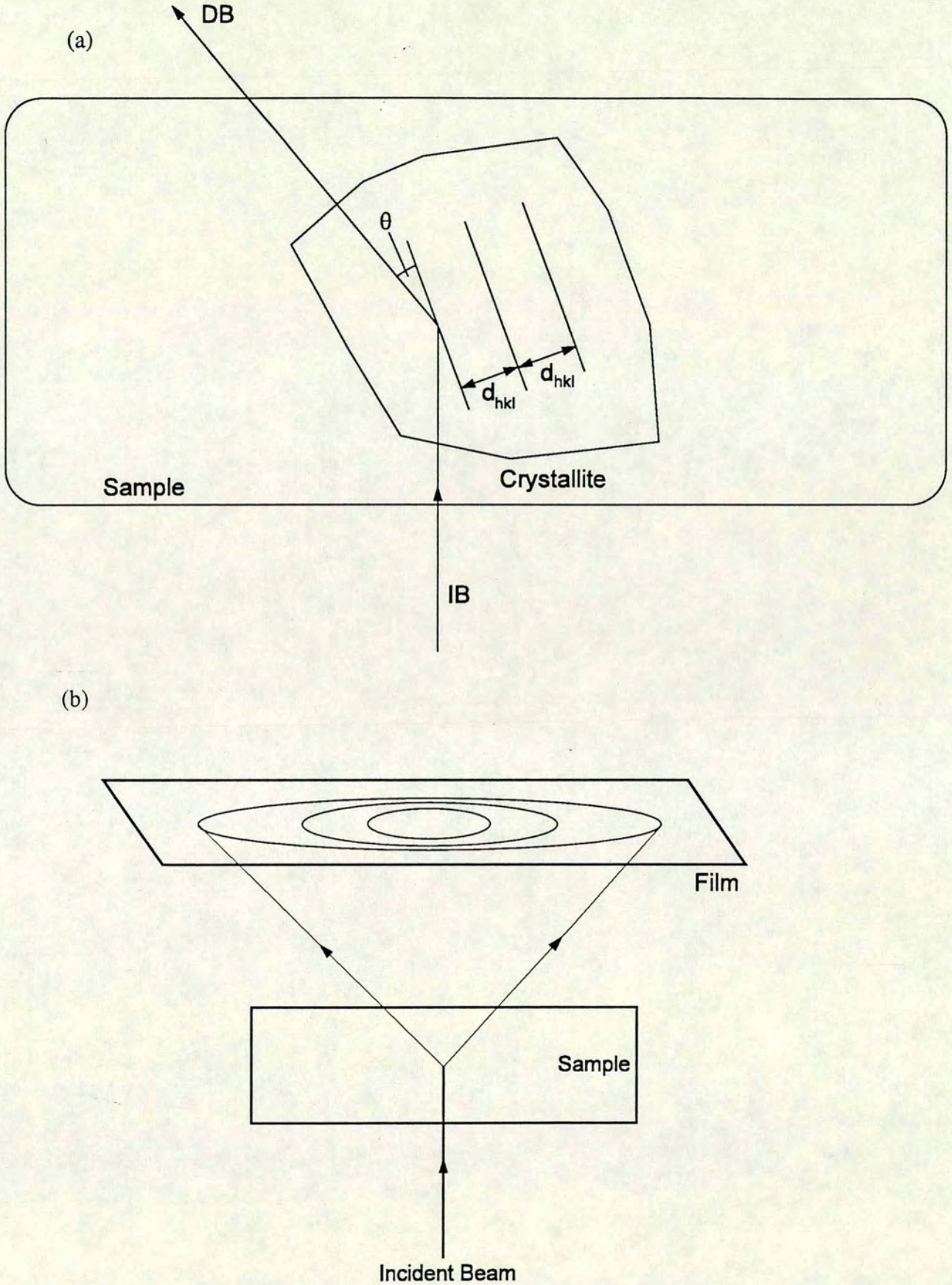

Figure 2.1 (a)The basic details of powder diffraction. Diffraction occurs from an individual crystallite if the set of lattice planes with spacing d_{hkl} are orientated at the correct θ angle with respect to the incident beam. (b) The full diffraction pattern is a series of concentric circles about the incident beam.

crystallites (as in powder diffraction) is given by N times the intensity from a single crystallite.

The polarisation factor (P) will depend on the characteristics of the incident radiation. If the incident beam is unpolarised then the effect of the polarisation factor is constant around the powder ring. Synchrotron radiation is almost 100% polarised in the horizontal plane. Therefore the effect of the polarisation of the synchrotron beam is not constant around a given powder ring but depends on the angle from the plane of polarisation of the radiation. The polarisation factor is given by (Kahn *et al*, (1982), Papiz and Helliwell (1985))

$$P = \frac{1+\cos^2(2\theta)}{2} - \frac{\tau}{2}\sin(2\gamma)\sin^2(2\theta) \qquad (2.4)$$

where θ is the diffraction angle, γ is the angle around the powder ring (γ=0° is the vertical) and τ is a factor which describes the degree of polarisation of the incident beam. For station 9.1 of the SRS, τ=0.96 (Cernik, (1994)).

The product in equation 2.3 is over the number (N_i) of unit-cells along a specific direction ($\mathbf{a_i}$) in the lattice. Thus this product describes the influence of the crystallite shape on the reflection intensity. For crystallites with a large number of unit-cells, each term in the product tends towards a delta function and the diffraction peak will be sharp in all directions. If in one or more lattice directions there are (for example) significantly fewer unit-cells, then the reflection will be broader in that direction. If the crystal lattice contains faulting then equation 2.3 will no longer be valid but must be modified to describe the (hkl)-dependent effect of the lattice faulting on the intensity. The microstructure of the crystallites (crystallite shape, faulting etc.) effects the shape of the diffraction peak but not in general the total intensity of the reflections. In addition, even in an ideal case the intensity diffracted from the crystallite is not concentrated in a single perfectly sharp peak but is spread out due to factors such as divergence of the incident beam etc. A more sensible measure is the integrated intensity, which represents the total intensity in the reflection. The integrated intensity can be shown (Warren, (1969)) to be proportional to

$$I \propto I_0 V \lambda^3 P L F^2 \qquad (2.5)$$

where V is the volume of the crystallites that make up the sample.

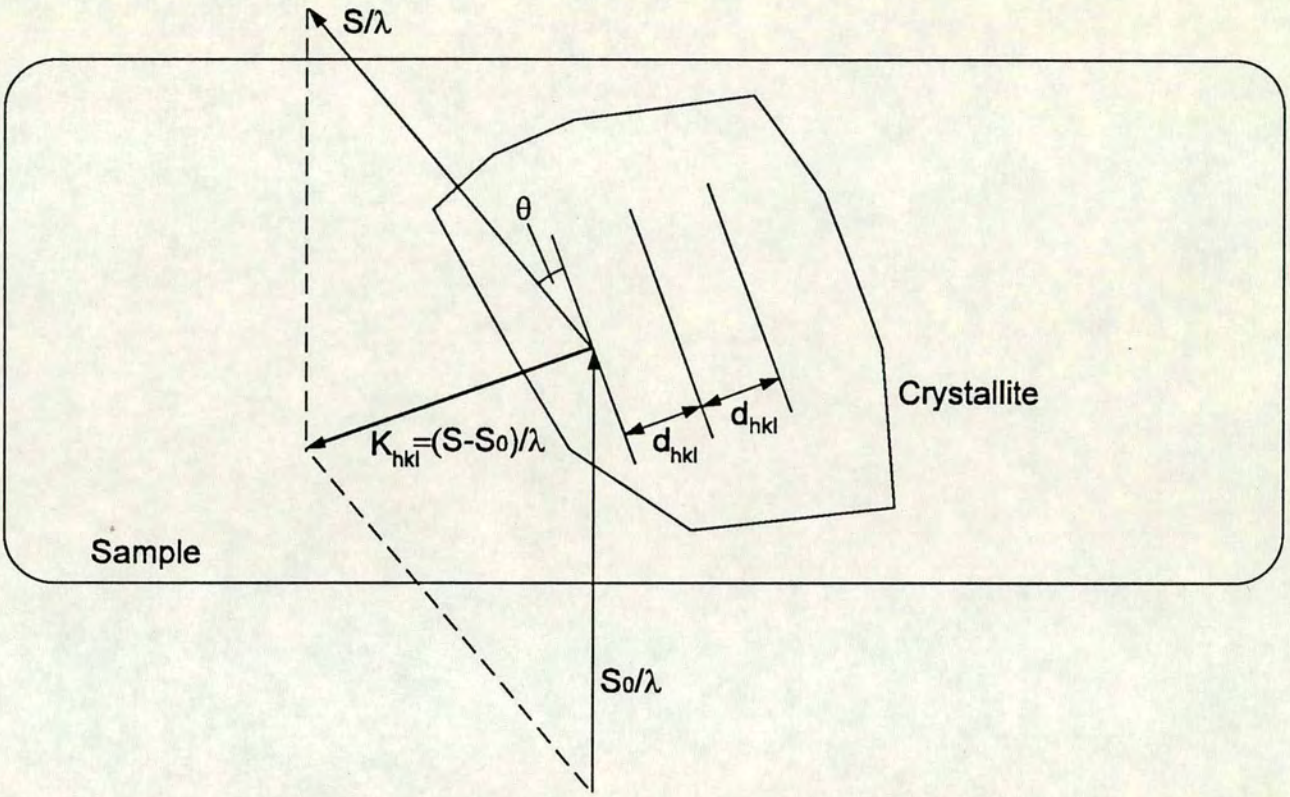

Figure 2.2 The vector representation of Bragg's Law. Diffraction occurs if the reciprocal lattice vector $\mathbf{K_{hkl}}=(\mathbf{S}-\mathbf{S_0})/\lambda$ where $\mathbf{S_0}$ is the vector representing the incident beam, $\mathbf{S}$ represents the diffracted beam and λ is the wavelength of the incident radiation.

In powder diffraction, there will also be crystallites with other orientations around the incident beam and so the diffraction pattern consists of a series of concentric cones of radiation. If the sample consists of randomly oriented crystallites then the intensity of each reflection will be constant around the cone (neglecting effects such as the polarisation of the x-ray beam which affect the full 2-D powder pattern). In such an ideal sample, the proportion of crystallites contributing to the intensity of each reflection will be constant (ignoring the effect of multiplicity, see below) and the relative intensities of the reflections will not depend on the number of crystallites. However, in many samples, the crystallites are not randomly arranged but show a preference to orientate in a specific manner. This preferred orientation of the crystallites will affect the relative intensities of the reflections as the number of crystallites contributing to each reflection will be different.

As the crystallites bathed by the incident beam are of finite size and of limited number, it is possible that the diffraction pattern will be uneven even if the sample crystallites are randomly oriented. This can be understood by considering a sample consisting of only a few large randomly oriented crystallites (the dimension of the crystallites is relative to the size of the incident beam). In such a case the diffraction pattern will consist of a series of small spots. Because the number of crystallites in the diffraction condition is so low, the reflections are not a proper measure of the average intensities expected from the crystal structure. Such a data set is said to suffer from 'poor powder averaging'. Problems of poor powder averaging can be overcome by oscillating the sample slightly whilst the diffraction pattern is measured. This will ensure that a larger fraction of crystallites will be correctly oriented for diffraction and the average intensities will be more accurate.

The characteristics of powder diffraction data are largely determined by whether monochromatic or polychromatic ('white') radiation is used. If the incident radiation is monochromatic then diffraction will occur only at those selected θ angles where the crystal structure has a corresponding d-spacing that satisfies the Bragg condition. With monochromatic radiation different reflections are separated in angle and so this type of powder diffraction is known as angle-dispersive diffraction (ADX). The simplest method for detection of an ADX diffraction pattern is through the use of photographic film (as shown in figure 2.1b). The data recorded are then a series of concentric circles (powder rings) of radius d. The radius of the powder rings is given by

$$d = D \tan(2\theta) \qquad (2.6)$$

where D is the sample-to-detector distance and θ is the Bragg diffraction angle. Conventional powder diffractometers rather than use film generally use an electronic scanning detector which measures in a narrow strip across the diffraction pattern. Therefore, it records only a thin section through the diffraction pattern and a considerable fraction of the pattern is not detected. This obviously means that a great deal of diffracted intensity is discarded as well as any information that is missing from the recorded section due to a non-ideal sample.

If the incident radiation is polychromatic then a given set of lattice planes will diffract over a range of angles and the overall diffraction pattern will consist of a complex overlapping of diffraction patterns from each wavelength in the incident beam. In such a case it is not necessary to scan a detector over the whole pattern in order to record information from all the d-spacings in the lattice. Provided a sufficiently wide range of wavelengths is present, the total diffracted intensity at any θ angle will contain a diffraction peak from all the sets of lattice planes in the crystal. Therefore it is necessary merely to place a detector at some suitable fixed θ angle in order to collect the entire diffraction pattern. However, the detector must be capable of distinguishing between the contributions to the total intensity recorded by the detector from each set of lattice planes. Since the diffraction is occurring at a fixed θ angle from different d-spacings, Bragg's law requires that each reflection, that enters the fixed detector, is from a different wavelength of radiation. Because the energy of the radiation is related to the wavelength (for x-rays $E=2\pi h/\lambda$), the discrimination between the contributions from different sets of lattice planes can be performed by using detectors with energy sensitivity. This type of diffraction, where the energy of the diffraction peaks is used to separate the contributions from sets of lattice planes with different d-spacings, is called energy-dispersive diffraction (EDX). In order to achieve good energy resolution it is necessary to restrict the opening angle of the detector as much as possible. In such a case, the measured intensity is originating from very few crystallites and thus EDX studies often suffer from poor powder averaging.

2.3.1 Multiplicity

Depending on the lattice type, it is possible for there to be more than one set of lattice planes with the same d-spacing. For example in a tetragonal lattice (a=b≠c) any (hkl) set of lattice planes must have the same d-spacing as the sets of planes (-hkl), (h-kl),

(-h-kl), (khl), (-khl), (-k-hl) and (k-hl). Such a set of lattice planes forms a family known as 'hkl-type' reflections and the number of different sets of planes in a family is referred to as the multiplicity. For example the (110) type lattice planes in a cubic system have a multiplicity of 12. As all the sets of planes in a family have identical d-spacings they will all diffract radiation at the same θ angle. Thus a detector will record the contribution from all the members of a given reflection family simultaneously and can not distinguish between them.

2.3.2 Accidental overlap of reflections

It is possible in many lattice systems for two general reflections to have the same d-spacing, although this may only occur if the lattice parameters have particular values. For example, in a tetragonal system if the lattice constants are a=b=1Å and c=2Å then the (308) lattice planes have the same d-spacing as the (406) planes, thus both reflections will occur at the same θ angle. Therefore the diffracted intensity from these sets of planes will overlap with each other and cannot be separated by the detector. Such an overlapping of reflections is known as 'accidental ' because it results from a particular combination of (hkl) indices and lattice constants and, unlike multiplicity, is not generally true for all sets of planes in the lattice. Note that if the lattice parameters change (perhaps due to temperature or pressure variation) then the d-spacings of the overlapping reflections may not necessarily remain the same and the diffraction angles will therefore become different.

2.4 Different Diffraction geometries

Although the basic physics involved is identical, it is possible to use many different experimental arrangements to collect the diffraction pattern from a powder sample. Perhaps the most common is flat-plate or Bragg-Brentano geometry, as shown in figure 2.3. Monochromatic radiation is incident on a compressed briquette sample (usually cylindrical with radius ≈5mm and thickness ≈1mm) and the diffraction pattern is collected by a detector placed at an angle symmetric to the sample face and the incident beam. The angle is varied by driving the sample and detector simultaneously as shown. As the diffraction is occurring from the sample planes close to the surface, this geometry is reminiscent of simple reflection of light from a mirror and is therefore sometimes referred to as a reflection geometry.

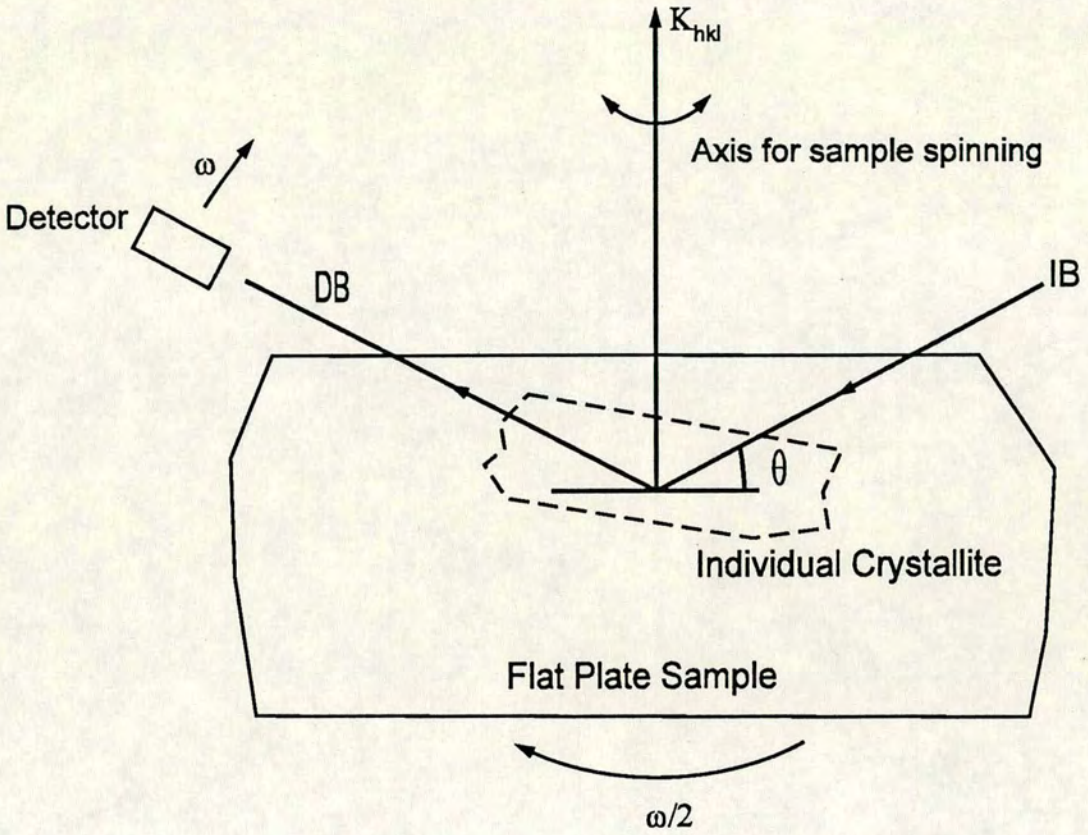

Figure 2.3 Bragg-Brentano diffraction geometry. The sample and detector are rotated at angular speeds ω/2 and ω respectively and the sample is spun about the normal to the flat-plate. DB=diffracted beam, IB=incident beam, and $\mathbf{K_{hkl}}$ is the reciprocal lattice vector.

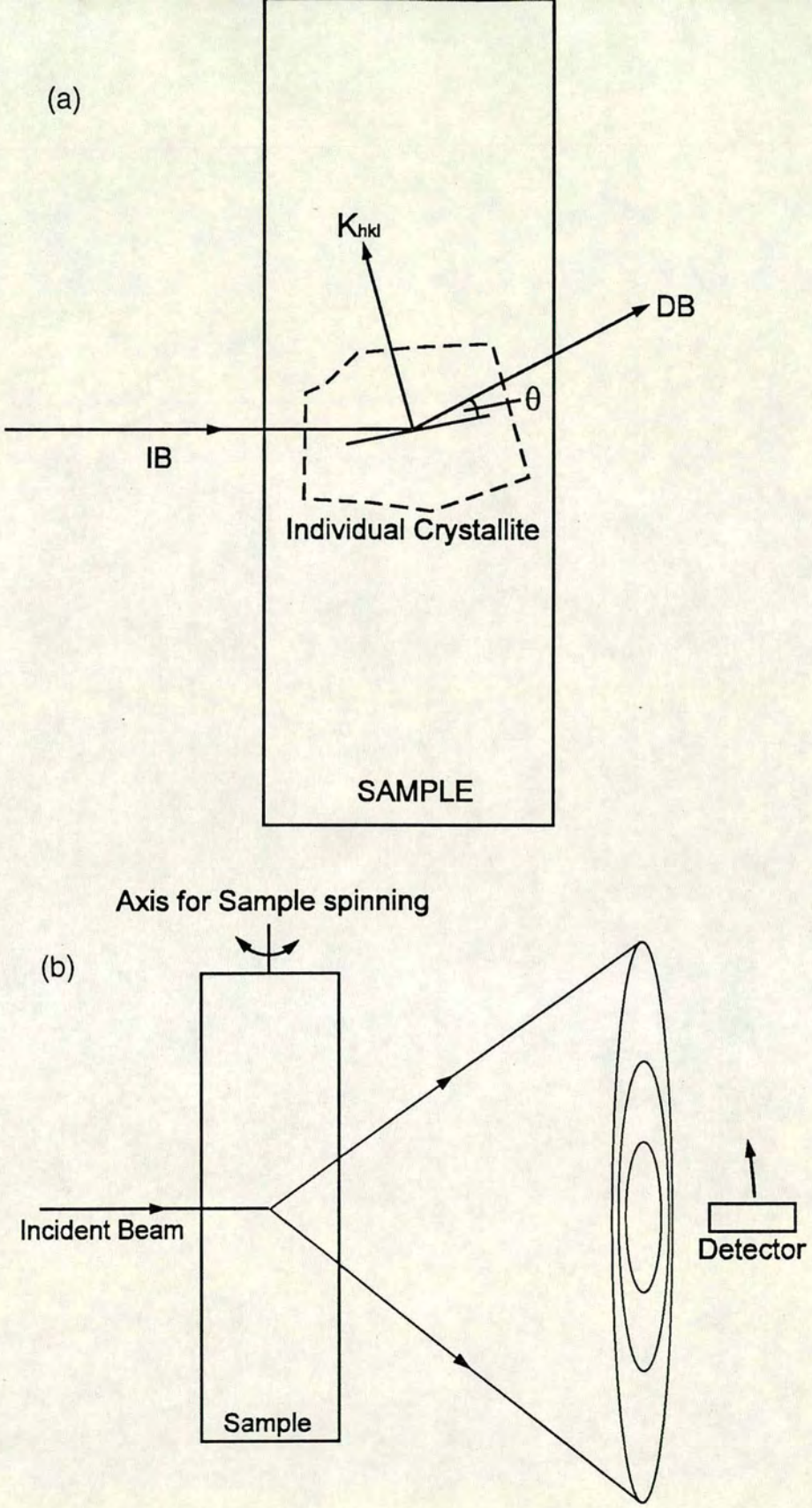

Figure 2.4 Debye-Scherrer diffraction geometry. (a) The arrangement of the incident beam (IB), diffracted beam (DB) and scattering vector ($\mathbf{K_{hkl}}$) for diffraction into a point on the diffraction pattern. (b) The full 2-D diffraction pattern. The detector is scanned across the diffraction pattern, normally at constant distance from the sample.

Another common geometry is shown in figure 2.4. The sample is held in a thin capillary (usually a glass or quartz tube with internal diameter ≈0.5mm) upon which the incident beam strikes from the side. This type of arrangement is referred to as capillary or Debye-Scherrer geometry. Note that in this case the diffracted beam is collected in transmission, with the axis of the sample perpendicular to the incident beam. If, on the other hand, the axis of the sample is parallel to the incident beam then it is known as simple transmission geometry. This kind of arrangement is commonly employed in high pressure diffraction studies where the axis of the sample (i.e. the pressure cell axis) is aligned along the incident beam. Note that in all these experimental arrangements the sample is commonly oscillated or rotated about a suitable axis to improve powder averaging and reduce the effects of preferred orientation.

2.5 Criterion for accurate powder diffraction

Any subsequent analysis of the powder pattern relies on accurate measurement of the diffraction peaks and so it is important to establish criteria to ascertain the quality of the experimental procedure. The following four criteria are probably the most important:

(a) the sample is a randomly oriented powder whose particle size is sufficiently small to give sharp Bragg peaks.
(b) the background radiation is low in intensity compared to the diffraction peaks from the sample, and varies smoothly with angle (or energy).
(c) there are no contaminant diffraction peaks from the radiation striking equipment etc.
(d) the diffraction pattern can be corrected for the effect of sample and equipment absorption and for polarisation of the x-ray beam.

2.6 Detectors

The simplest form of x-ray detector has a single x-ray sensitive element, that is step-scanned through the powder pattern. The method of x-ray detection can vary: the three most popular methods being a solid-state detector (usually a high-quality ultra-pure Ge crystal), a NaI scintillation detector or a gas ionisation detector. The solid-state detector functions by analysing the pulse of current induced into the crystal by the incident photons. In the NaI scintillation detector, fluorescent light is produced

in the slightly Tl doped NaI single crystal by the incident x-rays. The fluorescence is detected by a photomultiplier, whose spectral sensitivity is matched to the wavelength of the fluorescence. Both of these types of detectors can be made to have energy discrimination by analysing the height of the current pulse and this makes them particularly popular for EDX work. The gas ionisation detector works by detecting the ionisation current induced into the gas by the x-ray photon.

Any detector made of a single element, must be scanned through the powder pattern, a highly inefficient process. In order to collect more of the pattern simultaneously, it is possible to construct a number of these elements to form a line detector, which is either read out sequentially or in parallel. A simple line detector can be constructed from a single gas ionisation chamber using a number of anode or cathode elements to allow the detection and location of x-ray photons entering the chamber. This type of device, known as a position sensitive detector (PSD) can be placed radially across the powder pattern and can therefore collect a larger portion of the diffraction simultaneously. This dramatically reduces the required counting period, which is particularly important for high-pressure work where the signal is very weak. It is prohibitively expensive to have counting electronics on each element of the PSD and so the read-out is generally by a delay-line method, which can limit the maximum count rate before the detector becomes saturated. Such detectors have been proved to be very useful for high-pressure work (Takemura *et al*, (1979), Fujii *et al* (1980)), although problems such as asymmetric line profiles (unless the PSD is curved) and non-homogeneity of the individual elements limit their usefulness for structural refinement.

An area detector is a 2-D detector capable of recording a significant portion of the 2-D diffraction pattern from the sample. There are two main types of area detector in operation:

(1) Image-plates: These consist of aluminium plates, onto which is bonded an x-ray sensitive storage phosphor (usually BaFBr doped with Eu). The absorbed incident x-ray photons cause trapped excited electronic states (colour centres) in the phosphor. When the plate is scanned by a laser, these colour centres are stimulated to photoluminesce - each giving off approximately 1-3 visible light photons for each incident x-ray photon. The photoluminescent light is guided by fibre-optics to a photomultiplier detector, which measures the light level. The intensity data obtained from the image-plate is recorded as a grid of pixel points. These detectors were

originally developed for medical imaging and complete image-plate systems (a reader to measure the intensity held in the phosphor plus image-plates) can be obtained from several manufacturers. The image-plate system used by the author for all experimental work in this thesis was a Molecular Dynamics 400APhosphorImager with Kodak image-plates. The scanner has two different modes: a high-resolution mode (pixel size 88 μm) and a low resolution 'fast scan' mode (pixel size 176 μm). For the thesis work, data were read from the plates using the 88 μm mode with a photomultiplier voltage of 965V exclusively.

The process of scanning the image-plate introduces various spatial and intensity distortions into the data, depending on the characteristics of the reader. With a Molecular Dynamics reader, the image-plate is read by mechanically tracking the plate over a laser, which raster scans perpendicular to the mechanical motion. The mechanical tracking is performed by pulling the cartridge, which holds the image-plate, using a steel wire attached via a pulley to a stepper motor. The distance that the cartridge must be advanced (and the length of steel wire that is wrapped taut on to the steeper motor wheel) is approximately 25 cm. The wrapping of the wire is not completely even and the motion of the image-plate is therefore not constant. Thus a spatial distortion is introduced into the data in the direction of mechanical motion. If this distortion was completely predictable, then it would be a simple matter to eliminate its effect in a spatial calibration. Unfortunately, the wire wraps unevenly and slightly unpredictably on the stepper motor wheel and so accurate calibration for this effect is difficult. This could be greatly improved by redesigning the motor wheel to enable the wire to be wound in a much more controlled manner (Hammersly (1993)). A second spatial distortion is caused by the laser itself. The laser is at an optical distance from the plate of a few metres, which means that the size and position of the laser spot varies across the plate. However, due to mechanical stability, the scan is highly reproducible and this effect is readily characterised.

The spatial calibration for both distortions is generally performed by placing onto an image-plate a metal foil grid (with holes of accurately known position and size) (Stanton *et al* (1992)). A parallel beam of x-rays (with an area greater than that of the plate) is allowed to expose the plate through the foil. Provided that the energy of the incident x-rays is not too high, the image on the plate has an even background superimposed with a grid of spots, whose relative position is known. The plate is then read in the usual manner and the location in pixels of the spots determined, usually by fitting a function to each spot. Since the correct pixel position of each spot can be

calculated (from the known dimensions of the grid and the pixels), it is possible to calculate the spatial distortion at the position of each spot. The spatial distortion at pixel positions between the spots can then be determined by interpolation.

In addition to the spatial distortions, the process of reading the image-plate also introduces intensity distortions into the data. The two main intensity distortions are: the sensitivity of the optical system (which detects the photoluminescent light) is not uniform across the plate and the recorded intensity does not vary linearly with the incident intensity. In order to correct for the non-uniformity of the sensitivity, an image-plate is exposed to a uniform beam of radiation and the plate read in the normal manner. The measured intensity from this calibration plate will reflect the variation in sensitivity of the optical system and thus subsequent data can be corrected by normalising the measured data using the intensity variation from the calibration exposure. The non-linearity of the response of the system is corrected for by exposing different sections of an image-plate to varying, but known, amounts of radiation. This allows the response of the system to different intensities of radiation to be calculated and subsequent data to be corrected. Both these intensity calibrations are performed by the manufacturer at regular intervals.

The principal advantage of image-plates for high-pressure studies is their high-sensitivity (about 60 times that of photographic film). The spatial resolution of an image-plate (which, in practice, is measured by the width of the diffraction peaks) is moderate compared to other detectors. In general, the width of a measured reflection is a convolution of the width of the diffraction peak from the sample and the effect of the measuring instrument (e.g. image-plate, reader etc.). In the case of an image-plate system, the influence of the instrument is usually greater than that of the sample and so the resolution obtained is mostly determined by the effect of the instrument, which is determined by several factors (most of which are fixed). The only aspect of the instrument contribution to the observed reflection width that is in the control of the experimenter is the angular size (in terms of 2θ) of the pixels. Increasing the distance between the sample and the image-plate decreases the angular size of the pixels and thus improves the resolution of the data.

The influence on the resolution of the image-plate reader and image-plates themselves is determined by the manufacturer. It has been shown (Bourgeois *et al*, (1993)) that the point spread function (PSF) of the plate (and hence the spatial resolution) is determined by the amount of light-scattering inside the plate. Bourgeois notes that the

PSF of the plate can be improved by using a thin phosphor layer and a relatively fine grain size, thereby inhibiting light-scattering. However, since the sensitivity increases with grain size in storage phosphors (McKeever, (1985)), a compromise between spatial resolution and sensitivity must be sought. The influence of the image-plate scanner on the PSF is determined by factors such as the laser spot size and the acceptance angles of the fibre optic guides and there is little apparent difference between manufacturers (Bourgeois *et al*, (1993)). It has been shown (Shaw *et al*, (1992)) that there is significant fading of the image during the first 5 hours after exposure. The degree of fading during the reading process can be determined from the intensity variation around the powder rings from a standard sample (different sections of the powder rings are scanned at different times after the exposure has finished). Tests with standard powders have shown that the intensities can be determined to be constant around the ring to the order of 1% - indicating that the image does not fade significantly over the time scale of reading (about 10 minutes for a commercial image plate scanner).

(2) X-Ray TV Cameras: These generally consist of an x-ray image intensifier device coupled optically to a cooled CCD camera. The intensifier is a large vacuum vessel with a thin x-ray transparent window. A scintillating layer on the window converts the x-ray image into light which, in turn, is converted into an electron image by a photodiode. The electron image is focussed (and magnified if required) by electrodes onto a high resolution phosphor screen. This gives off a visible light image which is detected by the CCD camera. X-ray TV cameras have the significant advantage of providing a fast read-out time (1-3s) whilst maintaining a similar sensitivity to image-plates (Nadayet *et al*, (1987), Arndt *et al*, (1988)). These devices have excellent potential as detectors of synchrotron radiation, particularly for kinetics studies (Moy *et al*, (1993)). However, they suffer from severe spatial distortion, mostly induced by the focusing electrodes, and are very sensitive to electromagnetic noise. Therefore, the problems of spatial and intensity distortion restrict their present use to mostly qualitative work.

2.7 The Image-Plate set-up at SRS Daresbury

The volume of sample contained in a diamond-anvil pressure cell is generally of the order of 1000 times less than that used in conventional powder diffraction. Therefore the signal obtained from a sample contained within a DAC is extremely weak. At low pressures the problem of low signal can be overcome by using a relatively large gasket

hole, which allows more sample to be held in the pressure cell. However this greatly restricts the pressure that can be attained and, until recently, high-pressure work using ADX techniques was therefore limited to the low pressure region. This situation has been revolutionised by the development of sensitive area detectors, which collect a significant portion of the powder pattern and can therefore be used with smaller sample volumes. Pioneering studies with image-plates at the Photon Factory in Japan (Fujii *et al*, (1989)) have proved that the high sensitivity and moderate resolution of such devices makes them extremely suitable for high-pressure work. Further development at SRS Daresbury has shown (Nelmes *et al*, (1992)) that, if the angle-dispersive pattern is azimuthally integrated around the powder rings, the subsequent improvement in signal-to-noise ratio makes structure refinement feasible.

2.7.1 Station 9.1

All experiments described in this thesis have taken place at SRS Daresbury on station 9.1. The station is situated 15m from the three-pole wiggler, which is configured to give appreciable flux between 1.5Å to 0.4Å wavelength radiation. Figure 2.5 shows the intensity measured by a scintillation counter receiving the scatter from a piece of kapton foil as a function of the wavelength of incident x-ray radiation (Busnell-Wye, (1993)). Although the recorded intensity contains dependencies on effects such as the detector sensitivity and the wavelength dependence of the scattering power of the foil (see equation 2.5), the broad features of the figure give an indication of the flux available on the station as a function of wavelength. The peak intensity is at $\lambda \approx 0.6$Å and below $\lambda \approx 0.3$Å the intensity is negligible.

The white beam is monochromatised by a standard monolithic double-bounce channel-cut silicon (111) monochromator. Because the structure factor for the silicon (333) reflection is not negligible, there is significant $\lambda/3$ contamination of the monochromatic beam. The ratio of the intensities of the λ:$\lambda/3$ components is determined by the spectrum of the wiggler and the structure factor of the λ and $\lambda/3$ reflections from the monochromator. At $\lambda \approx 0.45$Å (close to the wavelengths generally used by the The University of Edinburgh group for high-pressure work), the ratio of the intensities of the λ:$\lambda/3$ components is about 99:1.

The station can be configured into a conventional powder diffractometer for both flat-plate and capillary work. For most of the experiments in this thesis, the wavelength was determined at the start of the experiment by recording the diffraction

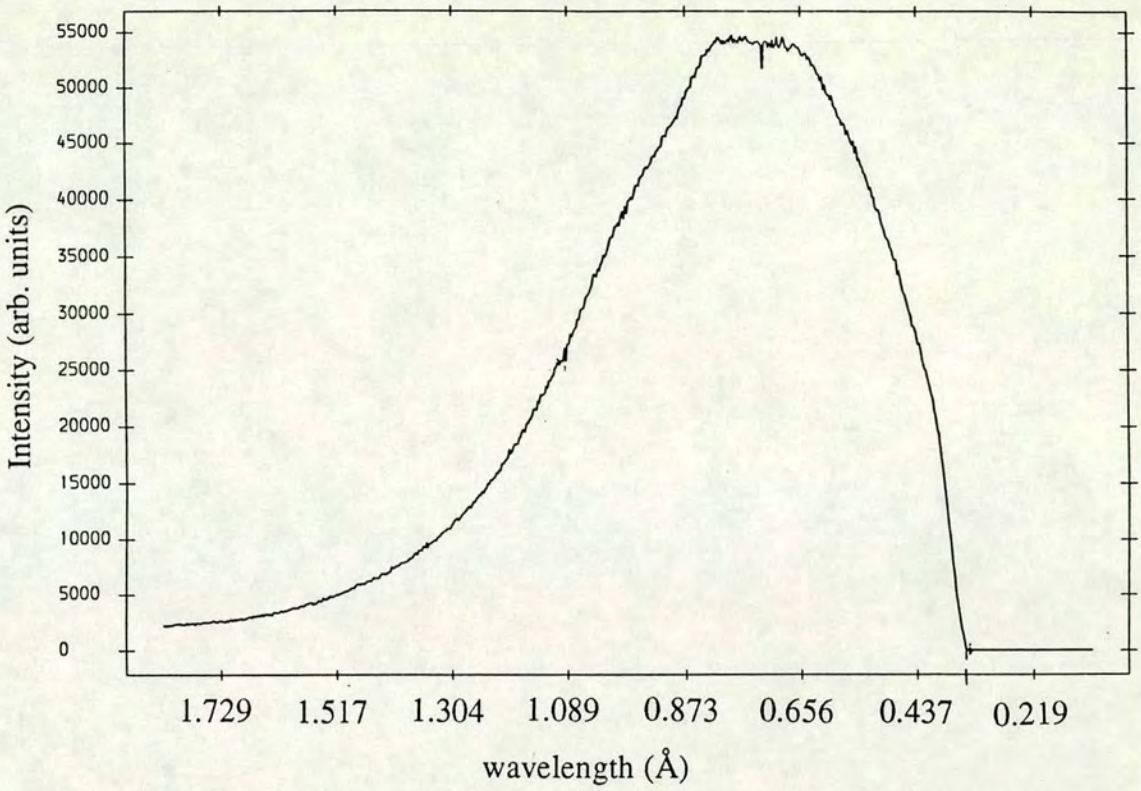

Figure 2.5 An approximate indication of the intensity of radiation available at station 9.1 at SRS Daresbury vs wavelength of the radiation. The measured intensity was obtained by detecting the scatter from a Kapton foil and thus the data contains contributions from both the variation in scattered intensity and detector sensitivity with wavelength. (G. Bushnell-Wye, (1993)).

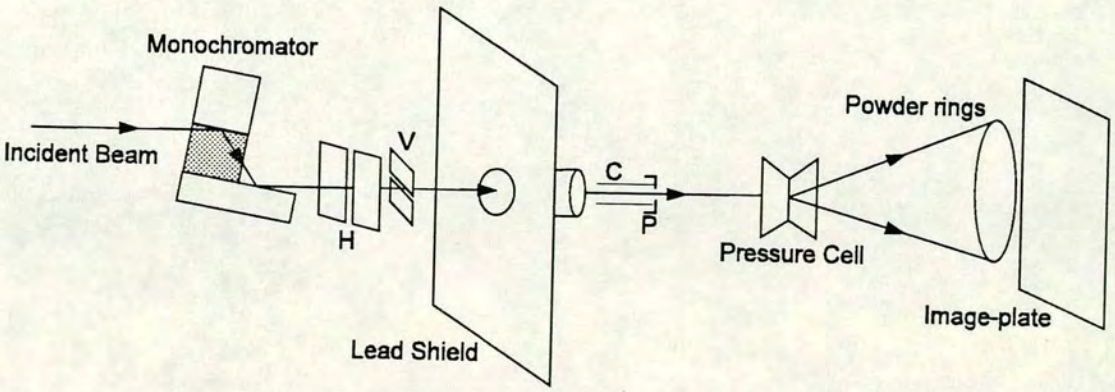

Figure 2.6 The beam line equipment in use with the University of Edinburgh image-plate set-up on station 9.1 of the SRS. H and V are horizontal and vertical slits respectively. C= collimator, P=pin-hole (usually Pt).

pattern from a standard silicon sample held in a glass capillary using the high resolution mode of the scanning detector. This is standard procedure for many experimenters using the station and is performed in collaboration with the station scientist, Dr. G. Bushnell-Wye. In some cases, when the wavelength was changed during the experiment to selected absorption edges (in order to take advantage of resonant effects), the wavelength was determined from the measured absorption edges. Further details of this technique are given in the related sections of the thesis.

2.7.2 Image-Plate optics and shielding

During image-plate operation the scanning detector is withdrawn from the beam and plays no subsequent part in the experiment. The beamline set-up (see figure 2.6) and experimental procedures are based on those used at the Photon Factory (Shimomura *et al*, (1992)) but have been developed considerably at SRS Daresbury over the last three years. The whole image-plate set-up is supported by a horizontal optical bench, which lies ~265mm below the monochromatised beam. After the monochromator the beam is reduced to ≈0.5mm square by a pair of crossed tungsten carbide slits. It then passes down a 2mm diameter tungsten carbide tube on the end of which is mounted a platinum pinhole. This reduces the beam to its final dimensions (generally a circular cross-section with a diameter of ≈75μm).

The beam striking the pinhole is a square of size 0.5mm x 0.5mm consisting of λ and $\lambda/3$ components. The pinhole material is normally Platinum, which is chosen for its ability to preferentially absorb the $\lambda/3$ component of the beam. Figure 2.7 shows a graph of the absorption of Platinum against the wavelength of the incident radiation. If the experimental wavelength is set at $\lambda \approx 0.45$Å then there is high absorption of both the λ and $\lambda/3$ components. Therefore, the beam cross-section is cut down to the pinhole size (75μm diameter) and consists of a ratio of 99:1 $\lambda:\lambda/3$ (as determined by the spectrum of the wiggler and the effect of the monchromator). The small amount of $\lambda/3$ presents no problem as it only strikes the sample and is of such low intensity that it is not detected.

If the wavelength is set at $\lambda \approx 0.48$Å, then the $\lambda/3$ component lies just above the Platinum absorption edge and will suffer little attenuation from the Platinum. The pinhole will not attenuate the $\lambda/3$ component significantly and the whole 0.5mm x 0.5mm square $\lambda/3$ component passes through the pinhole material. The λ component is absorbed by the material so will be cut down to the 75μm hole size. Therefore, the

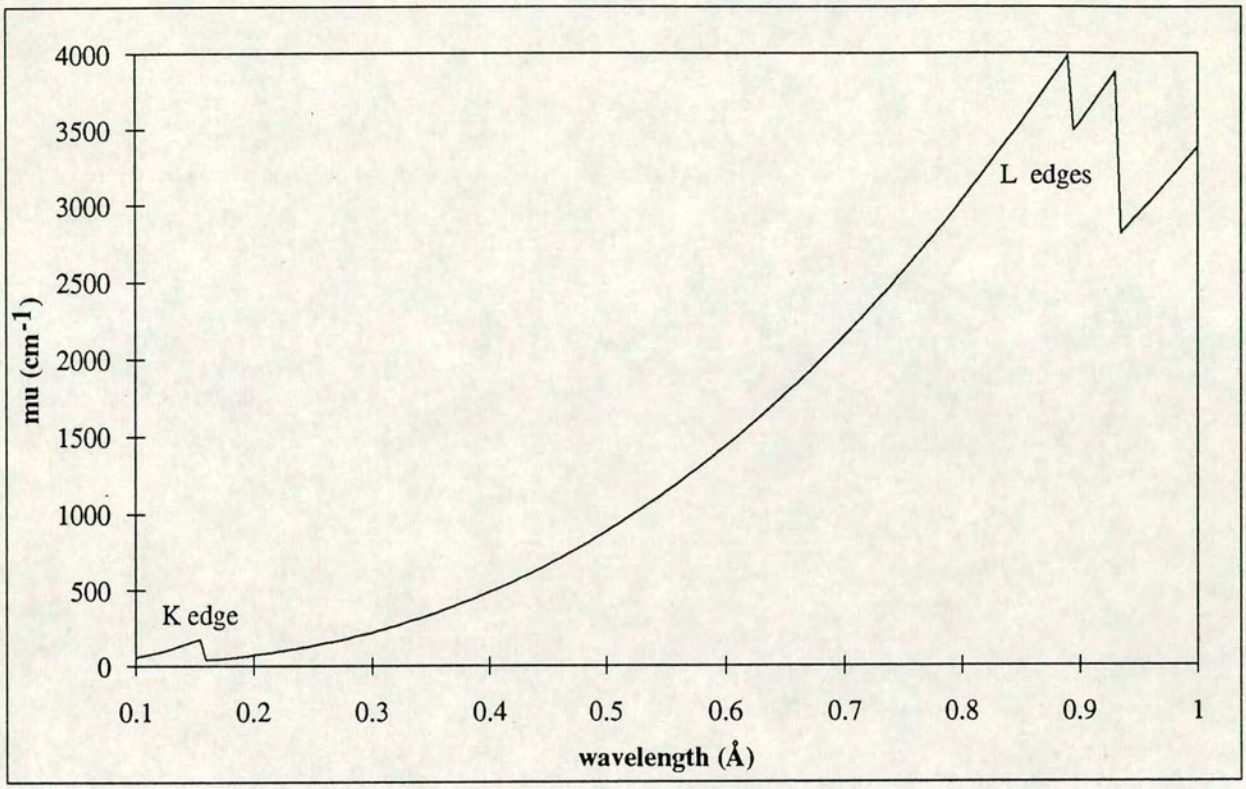

Figure 2.7 The absorption co-efficient of Pt vs wavelength of incident radiation.

beam after the pinhole will consist of a 75μm λ and λ/3 beam plus a λ/3 halo of 0.5mm x 0.5mm square. This λ/3 halo will strike the Tungsten gasket in the pressure cell. Because Tungsten is such a strong scatterer and the volume of gasket material illuminated by the λ/3 halo is relatively large, there will be significant contamination of the diffraction pattern by the λ/3 Tungsten pattern. If the experimental wavelength is kept below λ=0.47448Å (= 3 x 0.15816Å, the Platinum K-edge) then both the λ and λ/3 components are cut down to 75μm and the pattern will have negligible λ/3 contamination.

The whole tube and pinhole assembly can be driven vertically and horizontally (perpendicular to the beam). At the beginning of the experiment and after each refill of the synchrotron, the position of the pinhole is optimised for maximum intensity by scanning it through the beam and detecting the collimated beam with an ion chamber, which is placed in front of the image-plate holder. After the position of the pinhole has been set, the ion chamber is removed from the beamline. The sample is mounted on an x-y-z stage about 2cm from the pinhole. The distance between the sample and the image-plate is generally in the range 250mm to 350mm, giving a reasonable compromise between the number of the diffraction lines recorded and resolution. All of the equipment described above is shielded by a large lead rubber enclosure which limits background radiation reaching the image-plate. Additional shielding, in the form of a lead plate, is placed before the pin-hole assembly to screen the image plate from the background originating from the monochromator vessel.

2.8 Data processing

The image-plate reader produces data files, which contain the intensity (in a compressed scale) at each pixel position. In the data file the information is stored sequentially, starting at the top left corner of the image-plate. The file also contains a header section, which details the size of the scan and other relevant information. The x-y co-ordinate of a given data point on the image-plate can be inferred from that data point's position in the file and the scan size parameters. These data files are transferred by local ethernet link from the PC, which controls the reader, to a DEC5200 workstation, where the main data processing takes place.

2.8.1 The Platypus suite of programs

The main processing software, which was specially written for the image-plate project, is the 'windows' based program 'PLATYPUS' (Piltz *et al*, (1992)). This allows display of the raw data and graphical display of the output files. A typical image consists of about 2800 x 2000 pixels, which produces a data file of about 11 Mbytes long. Due to the sheer amount of data recorded by the image-plate, it is not yet possible to perform full structural refinement of the 2-D image. To overcome this problem, the data is azimuthally averaged (i.e. the intensity around the powder rings is averaged over the pixels which contribute to the intensity at a given radius from the beam centre). This algorithm effectively converts the 2-D data into a conventional 1-D powder pattern, which contains the average intensities around the powder rings. The averaging process helps to overcome the main problems associated with high-pressure powder crystallography: low signal to noise ratio and poor powder averaging (Nelmes *et al*, (1992)). The correct allocation of intensity into radial bins requires that several geometrical parameters must be accurately known, e.g. the tilt of the plate relative to the incident beam, any spatial distortion or intensity errors introduced during the reading process, etc. It was found that measurement of the plate tilt to sufficient accuracy was difficult (especially as it could not be ensured that each plate would return to exactly the position of the previous plate) and so a numerical data processing procedure was developed to correct for any tilt of the plate (Piltz *et al* (1992)). This tilt correction technique and correction for the spatial distortion introduced by the scanner (using the method of Staunton *et al* detailed above) is incorporated into PLATYPUS.

After the program has corrected for the spatial distortion, each data point is assigned to one of sixty sectors (depending on the position of that data point around the powder ring). The location within the sector that a given pixel intensity is placed is determined by its radial distance from the beam centre. Thus each sector is, in itself, a conventional 1-D powder profile averaged over the pixels that contribute to that sector. At this stage, no correction for the plate tilt has been applied and so the sectored intensity is not yet accurate. However since the effect of the plate tilt is small within a single sector, the sectored data is of sufficient accuracy for the next stage of data processing.

The tilt correction is calculated by defining a 'sharpness' criteria and refining the tilt values until maximal sharpness is achieved. This process corresponds to moving the

relative radial position of the data points until all the sectors come into register (i.e. until all peaks lie exactly on top of each other). The raw data file is then read in again and the intensity at each pixel assigned (taking into account the correct tilt values and any spatial distortion) into radial bins. This is then averaged over the number of data points contributing to a given data bin and, after correction for polarisation of the incident x-ray beam, the output is written to a file as a conventional 1-D powder pattern.

Rietveld refinement of data processed with this method gives good agreement with known structural values (Piltz *et al* (1992), Nelmes *et al* (1992)), indicating that the tilt correction method works well. The principal sources of error in the PLATYPUS program are residual problems with the spatial correction, particularly if the spatial calibration has not been performed in a period sufficiently close to the data collection. This problem affects mainly the position of diffraction peaks at the edge of the image-plate (the effect of the spatial distortion is greater there) and can be a serious problem during Rietveld refinement, when it essential that errors in peak positions are kept to an absolute minimum.

2.8.2 Other programs

For analysis of the preferred orientation of the sample, it is important to know not just the average intensity around the powder rings as given by the PLATYPUS program but also the intensity variation around the powder rings. A specially written program, which follows the PLATYPUS algorithm closely, was produced for this purpose. This program performs essentially the same functions as the PLATYPUS package up to the point of producing the sixty 1-D sectored profiles. At this stage each sectored profile is corrected for the Lorentz and polarisation factors directly (see equation 2.3) and the profiles written out to separate output files. Extraction of the integrated intensities of the diffraction peaks around the powder ring is performed by analysis of each 1-D sector in turn. To obtain accurate information on the intensity variation around the powder rings it is necessary first to convert the data into an intensity vs 2θ form (see section 2.9, below) and then to fit using a least-squares method an analytic peak shape to the diffraction profile.

2.9 Data Analysis

The first stage of the analysis of the data from the image-plate is to convert the data from an intensity vs pixel radius form to intensity vs scattering angle (2θ), which requires that the distance between the sample and image-plate be accurately known. This is performed by simple geometry and the use of equation 2.6. For each pressure cell, the sample to image-plate distance (D, in equation 2.6) is obtained by collecting a diffraction pattern from a sample of known lattice parameter at ambient pressure. As the wavelength and ambient lattice parameters are known, the observed 2θ angles can be used to calculate the distance between the image-plate and the sample. This distance can then be used to convert all subsequent data collected with that pressure cell into an intensity vs 2θ form.

Determining the lattice type and lattice parameters, is usually performed by extracting the positions of the diffraction peaks from the data and using a specialist indexing or unit cell computer program. In this thesis, the author has made use of the indexing program TREOR (Werner *et al*, (1985)) and the unit cell refinement program REFCEL (provided as part of the Daresbury crystallographic program suite), both of which are widely used in the crystallographic community.

Because it is not generally possible to extract the phases of the reflections from the powder pattern, the crystal structure (i.e. the atomic co-ordinates of the atoms) cannot be determined directly. One of the principal problems in structural solution from powder diffraction data is that in a powder pattern each reflection generally consists of many equivalent reflections. Also, there is often considerable overlapping of non-equivalent reflections, especially at high scattering angle. This makes structural solution from powder data more difficult than those cases where single-crystal data are available.

For simple structures it is often possible to infer from the observed intensities an approximate crystal structure, which can be used as input to structural refinement packages. For more complicated structures or situations where a simple analysis yields no solution, various techniques have been developed for obtaining a trial structure. The most commonly employed method for structure solution is the 'Direct Methods' (Schenk, (1980)) technique, which looks for correlations in the relative intensities of different reflections. This allows limits on the atomic co-ordinates to be calculated and thus provides starting values for refinement packages. Other techniques

developed in recent years for structure solution include simulated annealing techniques (Newsam *et al*, (1992)).

In order to determine the exact positions of the atoms in the structure, it is necessary to compare the observed peak integrated intensities with those calculated from a model structure. This is generally performed by a structural refinement package, which optimises the parameters of this trial structure until the difference between the observed and calculated intensity is at a minimum. Early methods of structural refinement from powder diffraction data (Pawley, (1980)) extracted the relative integrated intensities of the different reflections from the powder pattern and used this information in single-crystal structure refinement programs. Because of the difficulty in assigning intensity to individual reflections in a clump of overlapping peaks, this type of method has limited accuracy. The development of the Rietveld method (Rietveld, (1969)), which fits a calculated powder profile directly to the observed pattern by least-squares refinement, has revolutionised powder techniques. The calculated profile is computed from starting values of the lattice parameters and atomic co-ordinates plus parameters to describe corrections for effects such as peak width variation, preferred orientation of the sample, polarisation of the incident beam, etc. The parameters of the calculated profile are varied until the match between the observed and calculated profiles is optimised. This method has proved to be of excellent accuracy and is now widely used. The principle disadvantage of the Rietveld method is that the starting structural parameters must be reasonably close to the correct values for the least-squares algorithm to function. Thus the Rietveld method is a method of structure refinement and not of structure solution.

2.10 Pressure cells and techniques

2.10.1 Pressure cells

Since the pioneering high-pressure work of Bridgman in the 1940's (Bridgman, (1940)), there have been several types of high-pressure cell used for x-ray diffraction studies. Early high-pressure cells were based on hydraulically driven piston-cylinder or multi-anvil designs. This type of equipment was large and cumbersome, which generally meant that high-pressure studies were restricted to specialist laboratories.

The most significant advance was the development of the diamond anvil cell (DAC) (Weir *et al*, (1965), Merrill and Bassett, (1974)), whose basic details have remained essentially unchanged. In these small and compact cells the sample is contained within a sheet of gasket material and force applied using simple bolts to two opposed diamond anvils, between which the sample is held (see figure 2.8). The sample volume is flooded with a pressure transmitting fluid, which ideally should remain liquid up to the highest pressure used. The use of diamonds, with their high-strength allows anvil tips of very small size. With small anvil tips high pressures can be reached for relatively small forces on the cell, although the relatively small sample size results in weak diffracted intensity. In order to maximise the stability of the pressure cell, the diameter of the gasket hole is generally about 1/3 of the tip diameter. The choice of gasket material can vary, although the most popular are inconel, a moderately hard nickel alloy (Ni:Cr:Fe=72:16:8) and various steels.

The anvils are mounted on high strength backing discs, which must have a low x-ray absorption (as the diffraction x-rays must exit through them). Perhaps the material with the best combination of high strength and low x-ray absorption is Be, although this it has the disadvantage of being difficult to machine and toxic when oxidised. The backing plates are supported by the cell body, which is generally composed of two halves. In simple designs the two halves of the cell body are identical. In more advanced designs though, a more stable geometry is created by shaping the two halves, perhaps as a matched piston-cylinder pair. Pressure is generated by driving the two halves of the cell body together, either by a system of bolts or, in more recent piston-cylinder designs, by a gas membrane device. In general DAC's are used in a transmission geometry, i.e. the incident beam enters through one diamond and the diffracted beams (and the fraction of the incident beam which is undiffracted) leave the cell through the other diamond. However, transverse geometry cells have been developed (Ahsbahs (1984), Malinowski (1987)). In this cell design, the diffracted beams leave through the same diamond that the incident beam entered.

Because pressure cells designed for EDX work require only small beam entry and exit holes, the anvils can be highly supported. This allows the strength of the cell to be optimised and higher pressures reached. Angle-dispersive cells however, must allow a wide angle of the diffraction cone to leave the cell. This requires that at least one diamond must be mounted on a material of low x-ray absorption or that an exit hole with a substantial opening angle be provided. Designs for ADX work can be strengthened by allowing only a part of the diffraction cone to leave the cell, i.e. have

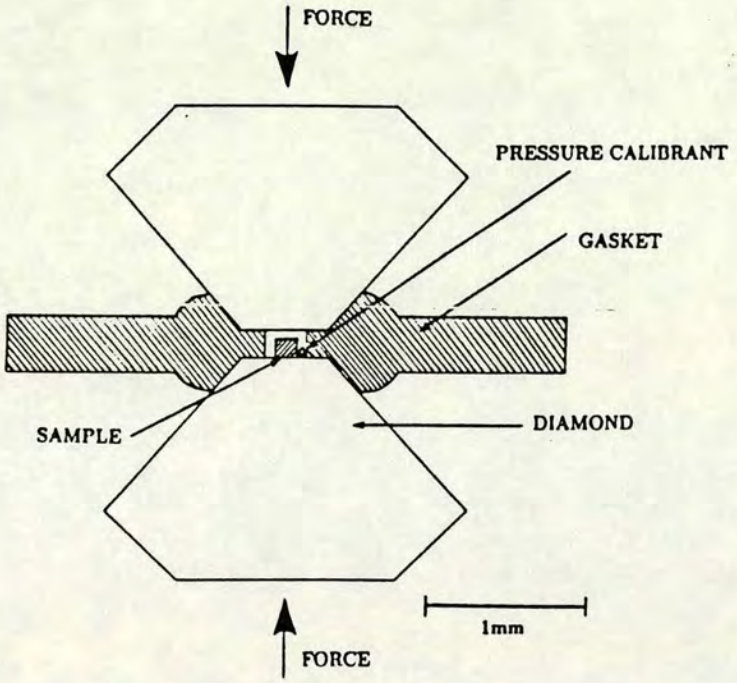

Figure 2.8 The basic design of a diamond anvil pressure cell (DAC).

a slot rather than conical exit aperture. Using a slot increases the supporting strength of the anvils and allows higher pressures to be reached, although obviously only part of the diffraction pattern can now be observed. To benefit from the ability of area detectors to collect the full diffraction pattern, pressure cells with conical apertures must be used.

It would be a great advantage, both for ADX and EDX studies, to construct pressure cells capable of reaching high pressures with a large sample volume. This would help to increase the strength of the signal and alleviate the problem of poor powder averaging (particularly for the EDX method). Increasing the sample volume significantly in DAC's would require diamonds of very large size, which would be prohibitively expensive. So called 'large volume cells' make use of other anvil materials, such as tungsten carbide, to overcome this problem. These anvils are polycrystalline materials and so, if illuminated by the incident beam, an ADX diffraction pattern will be heavily contaminated by diffraction peaks from the anvil materials. This contamination is difficult to avoid in ADX work and so this type of pressure cell is not commonly used for ADX studies. In EDX studies with large volume cells, careful collimation of the diffracted beam can prevent this contamination

reaching the detector, and so these type of pressure cells are popular for EDX work. Generating high pressure with a large sample volume requires a very large force, which is usually supplied by a hydraulic ram (Besson *et al*, (1992), Kikegawa (1992)). Large volume EDX cells are currently restricted to low relatively pressures (~20 GPa), although recent improvements in cell design and materials suggest that in near future higher pressures will be attained.

In the experimental sections of this thesis, the author has made use of two types of full conical aperture diamond anvil cell, Merrill-Bassett pressure cells (Merrill and Bassett, (1974)) and DXR-4 and DXR-5 pressure cells (Adams, (1992)). The Merrill-Bassett cell is shown in figure 2.9 and can be seen to have a very simple design. The diamond anvils (usually with culet size 600 μm) are mounted on Be backing plates, which sit directly on the steel cell body. These plates, which are relatively transparent to x-rays, have a tapered centre hole. The hole allows the direct beam to enter and exit the cell without striking the Be, which reduces the background scatter and prevents Be powder lines contaminating the diffraction pattern from the sample. The relative alignment of the diamonds can be adjusted by translating one of the Be discs, using small grub screws. However, there is no provision for the adjustment of the diamond tilts in this cell. Force is applied to the cell by evenly tightening the three main pressureing bolts. The lack of tilt adjustment and the relatively weak construction of the steel cell body limit the stable pressure obtainable with these cells to ~18 GPa. The principal advantages of the Merrill-Bassett design is its lightness, cheapness and relatively large angular access (about 40°).

The DXR-4 cell and the slightly more advanced DXR-5 cell are piston-cylinder designs, precision machined from high-quality steel (see figure 2.10). Both diamond anvils are mounted onto Be backing discs, one of which is held by the piston and the other on the cell body. In the DXR-4 cell the diamond on the piston is fixed but the translation and tilt of the bottom diamond (on the cell body) can be adjusted with grub screws. Force is applied by tightening two screws, which are oppositely threaded for better control and more even force application. The much stronger cell body and the higher quality diamond alignment allow this cell to reach greater pressures than the Merrill-Bassett cell. With 600 μm diamond culets, pressures up to ~20 GPa are possible while with 300 μm culets pressures up to ~40 GPa are feasible. The DXR-5 design (a revised version of the DXR-4) has the translation and tilt adjustment on different diamonds, allowing the cell to be aligned with more ease and much more

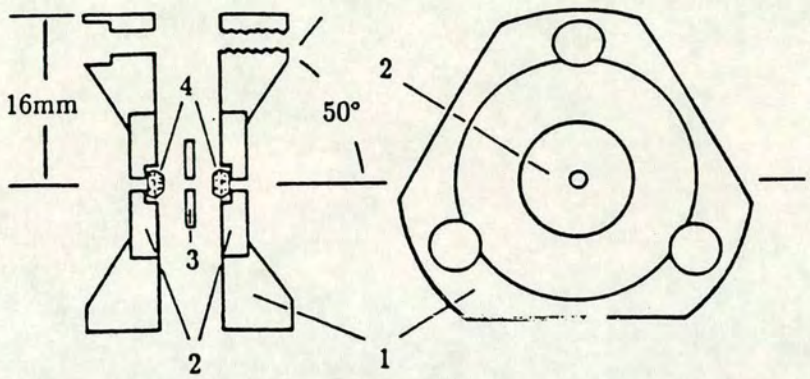

Figure 2.9 A Merrill-Bassett DAC. 1=steel cell body, 2=Be backing disc, 3=gasket, 4=diamond anvils.

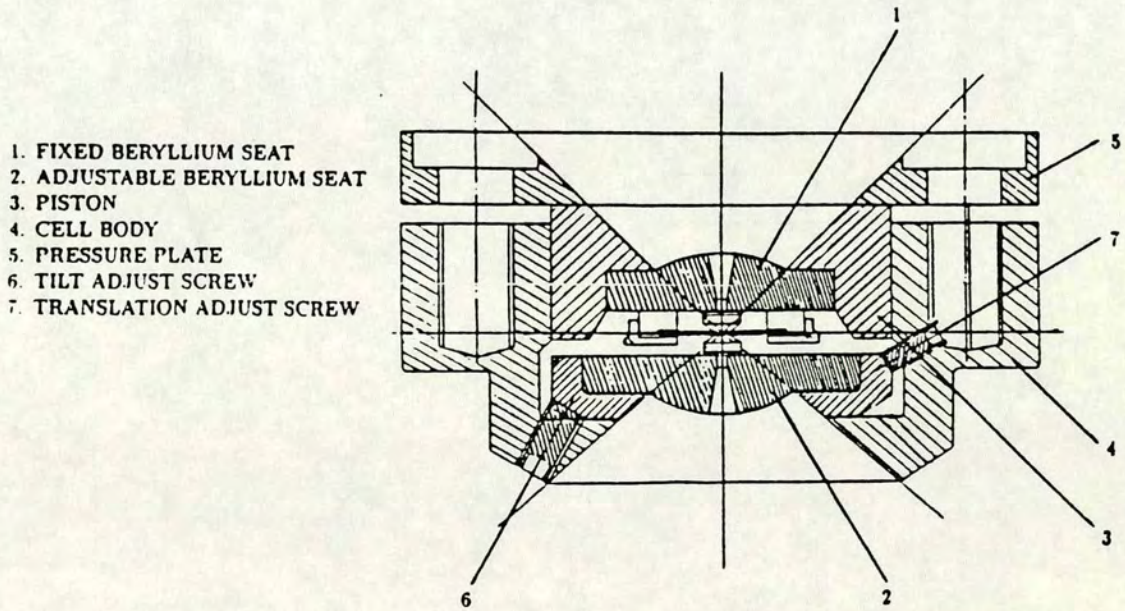

Figure 2.10 A DXR-4 Diacell DAC.

accuracy. This increases the maximum pressure considerably and pressures up to ~60 GPa have been reached with this cell.

2.10.3 Correction for pressure cell absorption

The diamond anvil and the Be backing discs, on the side of the diffraction cone, will attenuate the diffraction signal from the sample. The amount of absorption will depend on both the path length through the diamond and the Be plate and the energy of the diffracted photon. As figure 2.11 shows, the path length of a photon through the various pressure-cell materials depends on the diffraction angle of the photon. As the diffraction angle increases from zero (position 1 in figure 2.11), the absorption of the beam increases with the path length through the diamond. At $2\theta \approx 10°$ the beam starts to pass through the Be backing disc as well as the diamond and the absorption of the beam increases markedly (position 2 in figure 2.11). By about $2\theta \approx 12°$ the beam passes completely through the Be plate (position 3 in figure 2.11). As the diffraction angle is increased further, the absorption increases slowly as the path length through the cell increases with angle. Therefore, in angle-dispersive work the effect of the cell absorption will vary across the diffraction pattern as the path length changes. However, the change in absorption with diffraction angle is reproducible and can be measured quite accurately. In contrast, although the path taken by the diffracted photons is constant in energy-dispersive diffraction, the attenuation has a complex energy dependence, which makes modelling or measurement of the cell absorption highly problematic for high-pressure energy-dispersive work.

It is possible to correct an angle-dispersive diffraction pattern for cell absorption by either calculating the absorption from the known geometry, although this is difficult to do accurately, or by measuring the absorption directly. Figure 2.12 shows the measured intensity of a 75 μm beam through a Merrill-Bassett pressure cell (with a tungsten gasket of hole size 150 μm) as the pressure cell was rotated. The intensity of the transmitted beam was measured with an ion chamber situated on the optical bench just in front of the image-plate holder. As expected, the most striking feature of the absorption profile is the step region as the effect of the Be becomes apparent. Because it is common for the first diffraction lines to lie slightly below the step in absorption at ~10°, this feature is of great importance. These peaks will be attenuated less (by up to 15%) than those reflections which lie at higher diffraction angles. In this thesis, the absorption correction of all the presented data was been performed by correcting the

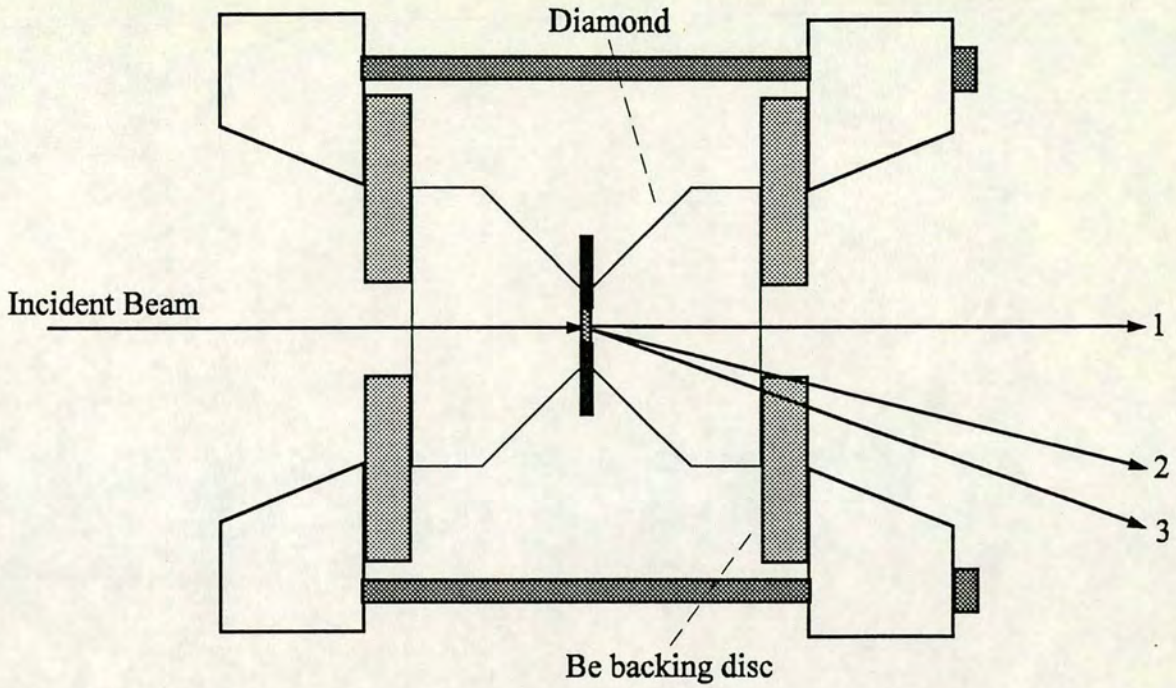

Figure 2.11 The absorption of the diffracted beam depends on its path through the pressure cell. Beam 1=straight-through beam, attenuated by the diamond anvils only, Beam 2=attenuated by the diamonds and the edge of the Be backing disc, Beam 3=attenuated by the diamonds and the Be backing disc.

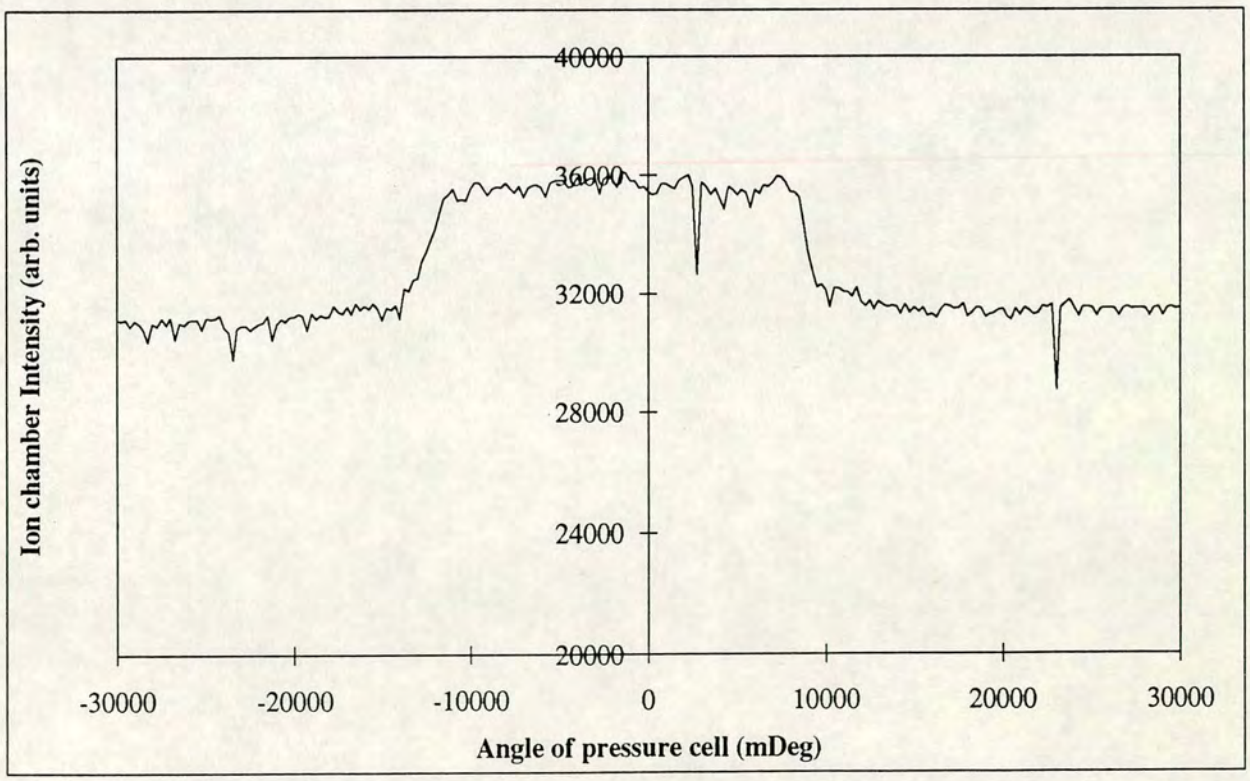

Figure 2.12 The transmission of a 75μm beam through a Merrill-Bassett DAC with a 150μm gasket hole. The step in transmission at ≈10° corresponds to Beam 2 in figure 2.11. The sharp dips in transmission (for example at ≈24°) are due to Bragg diffraction by the diamond crystals.

diffraction profile using a measured absorption profile (similar to that shown in figure 2.12) for the particular pressure cell in which data were collected.

2.10.4 Cell loading techniques

This section details the pressure cell loading techniques used by the author and the University of Edinburgh group. These techniques are similar to those used by most high-pressure groups, although this section does not present any detailed comparison with sample preparation techniques used by other workers. The first stage of loading a sample into the pressure cell is the preparation of the gasket. The choice of gasket material is dependent on the sample being studied. Although extreme care is taken to ensure that contamination of the diffraction pattern with gasket reflections is kept to a minimum, it is sensible to select a gasket material that has diffraction peaks well away from those of the sample. In this thesis, tungsten and steel have been used as gasket materials. The gasket is placed on the bottom diamond anvil and lightly held in position with plasticine. The cell is closed and pressure applied to the gasket. This pre-indents the gasket to the shape of the diamond tip and work hardens the metal. Once indented to a reasonable pressure, which is usually judged by the force required to turn the screws, the cell is opened and the gasket gently lifted off the anvil. A small hole, typically 100-200 μm in diameter, is spark-eroded into the centre of the pre-indentation. The gasket is then replaced on the anvil and the cell closed again. A small amount of pressure is applied to the cell, in order to ensure that the gasket is firmly secured to the bottom diamond face. The cell is then opened and the sample loaded into the hole with the aid of a fine needle.

The sample is prepared by grinding it with a mortar and pestle until it is a suitably fine powder. In order to have sufficient a number of crystallites to ensure that the powder rings are smooth and even, it is desirable that the particle size is in the order of 1-2 μ m, although generally the sample material will contain particles of various size. If the sample is wetted with a small quantity of methanol, capillary action will draw the smallest particles up the side of the mortar as the methanol evaporates. The pressure cell is then loaded with material taken from high up the sides of the mortar. Once the gasket hole is filled with sample material the cell is closed so that the opposing anvil gently presses into the preindentation on the gasket. This has the effect of pressing the sample firmly into the hole and cleaning up any residual sample from around the hole. The cell is opened and the top diamond face cleaned with methanol. This face is then covered with a thin film of vaseline and a small chip of single-crystal ruby (~30 μm

diameter) is placed on the top diamond face, at the position that will correspond to the centre of the gasket hole once the cell is closed. The ruby chip (which is held in position by the vaseline) is included for measurement of the pressure (see following section). The gasket hole is then filled with a pressure transmitting fluid (for the work in this thesis, a 4:1 mixture of methanol:ethanol was used to transmit the pressure) and the cell closed. Pressure can now be applied to the sample as required.

2.10.5 Pressure measurement

A determination of pressure from first principles would require a measurement of force/area acting on the sample. This is not possible for most pressure cell designs and so a calibration technique is required. The two most popular methods are to include in the sample chamber a reference material, whose equation of state is known, or the ruby fluorescent method.

In the first method a diffraction pattern is collected from a mixture of the sample and the reference material. From the position of the diffraction peaks of the reference material and the known equation of state, the pressure can be determined. For x-ray diamond anvil work NaCl is often chosen as a suitable reference material. Its equation of state has been theoretically determined up to 29 GPa (Decker, (1972)) and it gives a number of sharp strong diffraction lines at reasonably low 2θ angles. NaCl cannot be used as a reference material beyond ~29 GPa as it undergoes a phase transformation to the CsCl structure.

Other common choices of equation-of-state pressure standards include gold, silver and platinum. These have the advantage of being stronger x-ray scatterers than NaCl and can be used to higher pressures (they do not undergo phase transitions until much higher pressures) but their equations of state are less accurately known. One of their main uses is in experiments where the NaCl diffraction peaks would overlap the sample's peaks, making analysis of the sample diffraction pattern very difficult. The use of a reference material ensures that, inevitably, the data will be contaminated with the reference's diffraction peaks, thus reducing the accuracy of subsequent analysis- particularly Rietveld refinement. It is possible to avoid this problem by performing two experiments, one with a reference and one without, and use the first to calibrate the pressure in the second more accurate run. However this is time consuming and inconvienent.

Pressure measurement using the ruby fluorescence technique does not suffer from the contamination problem. This method makes use of the fluorescence from Cr doped ruby illuminated by strong incident visible light. The wavelength of the fluorescence line (at 6942 Å) has been shown (Piermarini *et al*, (1975)) to vary linearly (within experimental error) with pressure up to at least 29 GPa. At very high pressures (~100GPa) a slight non-linearity has been observed (Mao *et al*, (1978)). The wavelength shift of the ruby line is also temperature dependent and so care must be taken to ensure that corrections are applied for the temperature and that the temperature of the sample remains constant during both pressure measurement and data collection. Although it should be noted that the ruby scale is calibrated against the NaCl scale and so is a secondary calibration. The ruby technique must therefore necessarily not only suffer from measuring errors but also from inaccuracies from the NaCl scale itself. In diamond anvil cell work this method is utilised by enclosing a small ruby chip (<20 μm diameter) with the sample. The ruby is stimulated by directing a laser through the diamond anvils. The fluorescent spectrum can be detected either in transmission or reflection, depending on the opacity of the sample. The wavelength of the fluorescence line is measured by a spectrometer and the pressure determined from:

$$P = A(\Delta\lambda) \qquad (2.7)$$

where $\Delta\lambda$ is the change in wavelength of the 6942Å fluorescence line from ambient pressure and A is a constant (A= 2.735 kbar/Å from Piermarini *et al*, (1975))

The ruby fluorescence method produces little, if any, contamination of the diffraction pattern but has the disadvantage that, unless the laser and detector equipment can be situated on the beamline, the pressure is not measured at the same time as the sample diffraction pattern is recorded. This can lead to errors in the pressure determination, especially if the beamline area is at different temperature to the sample preparation laboratory or more seriously if the pressure cell has not been allowed to settle to a steady pressure. These errors can be minimised by measuring the pressure immediately before and immediately after recording the diffraction pattern. If the two measurements are significantly different, then the diffaction pattern can be re-collected if desired.

The pressure measurement apparatus used at Daresbury, and for all work in this thesis, is shown schematically in figure 2.13. As many high-pressure powder samples

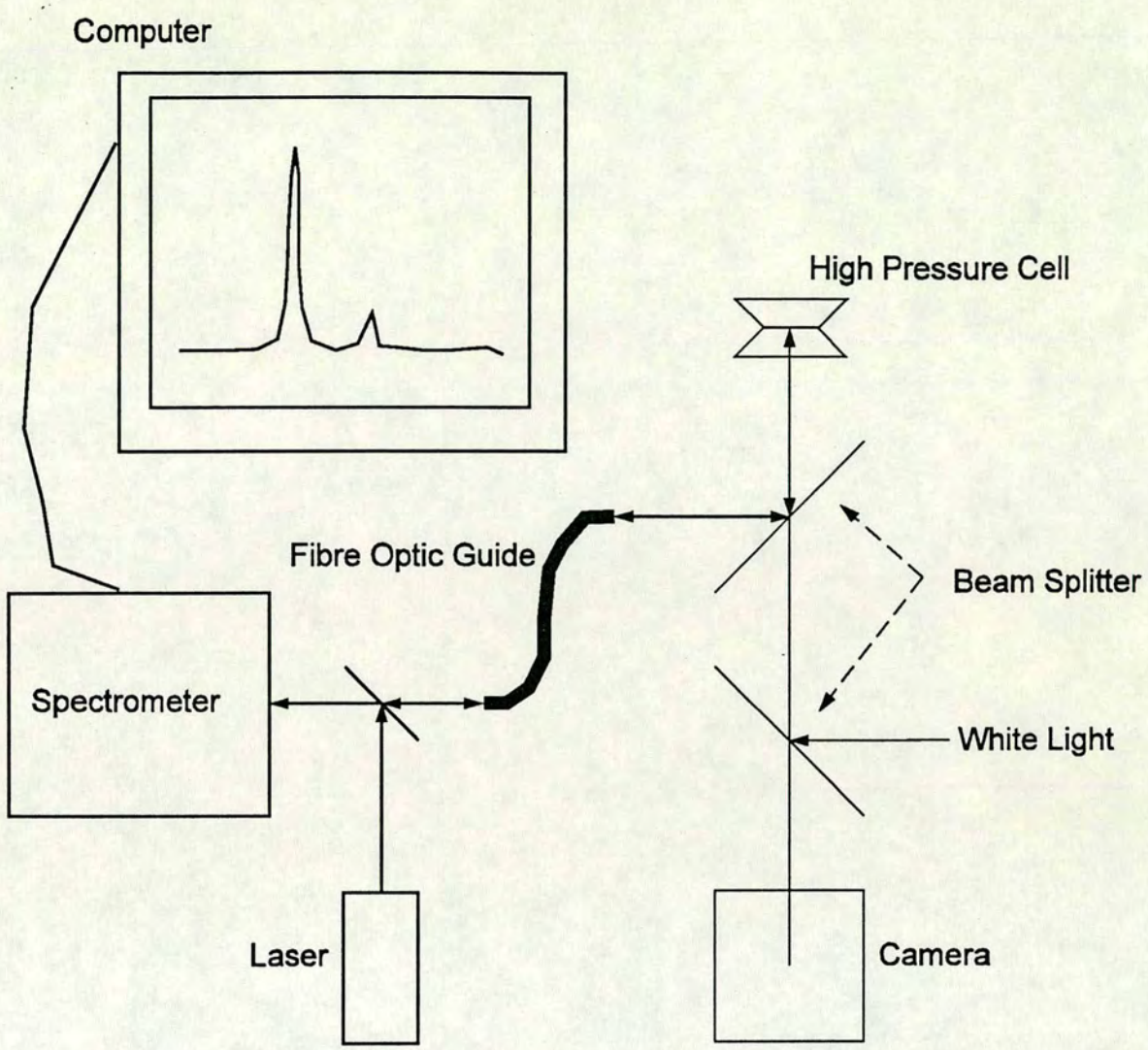

Figure 2.13 The ruby pressure measurement equipment at SRS Daresbury. The laser spot is positioned on the ruby chip by visual observation of the laser spot position using the camera. The fluorescence signal is carried by fibre optic to the spectrometer and the spectrum displayed on the computer.

are opaque, the system is configured to measure the ruby fluorescence in a reflection geometry. The system, manufactured by Dilor, uses a 1.5 W green helium/neon laser to stimulate ruby fluorescence. The laser light is guided to the sample area by a fibre optic cable, which is also used to guide the fluorescence spectrum to the spectrometer. This uses a 1600 g/mm line diffraction grating and 1024 diode array to analyse the diffracted light. The spectrum received by the fibre optic cable consists of several fluorescence lines of different wavelengths and general background signal. This is angle dispersed by the diffraction grating such that the position (from straight-on) of any light on the diode array is a function of the wavelength. Thus to determine the wavelength of the fluorescent line, the diode position of the line is recorded. This is converted into a pressure reading by using a calibration of the spectrometer against a known emission line spectrum, usually a neon vapour lamp. Ideally the position of the fluorescent line would be determined by fitting an analytic peak-shape to the spectrum but at present this is not possible. The recorded spectrum is displayed onto a P.C. and the centre of the peak measured by placing a cursor at the peak centre by inspection.

The precision in pressure measurement using the ruby fluorescent technique is quite good (~ 0.1 GPA at 10 GPa) but a conservative estimate of the accuracy would be 0.3 GPa at 10 GPa and lower still as the pressure is raised (Piermarini *et al*, (1975)).

2.10.6 Alignment

A typical gasket hole for general high-pressure work using Diacell and Merrill-Bassett pressure cells is of the order of 150 μm in diameter. Since the incident x-ray beam is between 75-100 μm in diameter, precise alignment of the pressure cell relative to the beam is required if contamination of the diffraction pattern with gasket peaks is to be avoided. The method of alignment used by the Edinburgh group at SRS Daresbury is an optical method based on that employed at the Photon Factory (Shimomura *et al*, (1992)), although it has been developed considerably at SRS Daresbury during the last few years.

The basic technique is as follows: The pressure cell is placed at approximately the correct position on the sample mount and a high-magnification telescope focused on the gasket hole. The pressure cell is then removed from the mount and replaced with a metal frame, whose position along the beam direction can be accurately adjusted. Mounted on the frame is a piece of x-ray sensitive paper. The telescope focus is left

untouched and the position of the paper along the beam is adjusted until it is in focus. This places the paper and the sample at the same optical distance from the telescope. The paper and sample position do not coincide in real space due to the fact that the sample is viewed through the diamond, which has a high refractive index. The paper is exposed to the x-ray beam, which leaves a small mark, that is approximately equal in size to the pinhole. The paper is developed by exposing it to strong light and the telescope translated perpendicular to the beam until the telescope cross-hair is on the centre of the mark. The paper and metal frame are now removed and the sample replaced on the mount. The position of the sample stage is now adjusted, until the gasket hole is centred on the telescope cross-hair.

It has been shown (Allan (1993)) that the principal sources of error in such a procedure are related to the high refractive index of the diamond anvils. If the telescope axis is not exactly parallel to the incident beam and the diamond face closest to the telescope is not exactly perpendicular to the beam, then the image of the gasket hole is shifted significantly. The maximum tolerable misalignment of either the telescope axis or the diamond relative to the beam is 0.57° (for a typical diamond thickness of 2 mm with a gasket hole diameter of 150μm and a beam of 75μm diameter cross-section) (Allan, (1993)). The procedure developed in the last two years to achieve such a high-quality of alignment makes use of a laser, which is mounted at the end of the optical bench and whose beam is aligned to coincide with the incident beam. The laser beam is aligned by placing two pieces of x-ray sensitive paper on the optical bench, the first piece close to the laser and the second at the far end, next to the tungsten carbide tube. Both pieces of paper are exposed to the beam and a small hole made at the position of the beam on the piece of paper nearest to the laser. The translation and tilt of the laser is then adjusted until the beam is directed through the hole in the first piece of paper onto the mark on the second. Since the distance between the pieces of paper is ~1m and the position of the laser spot can be determined to an accuracy of about 1mm, the accuracy of this method is estimated to be of the order of 0.06°. The laser acts as a reference for the subsequent stages of the alignment procedure.

The second stage of the alignment procedure is to align the telescope such that the optic axis of the telescope lies along the x-ray beam, now accurately defined by the laser. The telescope is essentially constructed from a metal tube, which holds the objective and eyepiece lens. The lenses are removed from the telescope and a flat mirror placed at the objective end with the mirror's reflective surface facing the laser.

The tilt of the telescope tube is then adjusted until the reflected image of the laser spot coincides with the exit aperture of the laser. At this point the telescope axis is parallel to the laser beam, although not necessarily coincident with it. The mirror is then removed from the telescope tube and the lenses carefully replaced.

The third stage of the procedure is to align the back face of the diamond (through which the sample is viewed) to be perpendicular to the laser beam. This is achieved by placing the pressure cell on its mount and adjusting the tilt of the mount until the laser spot reflection from the diamond face is coincident with the laser exit aperture. If each pressure cell has its own customised mount, this process can be performed once for each cell at the beginning of the experiment. Although this whole procedure for aligning the laser, telescope and pressure cells does require the use of up to 1 hour of synchrotron time, the subsequent improvement in data quality is significant. If performed accurately, contamination of the diffraction pattern with gasket peaks is very rare. Once the telescope and pressure cells have been so aligned relative to the laser, alignment of the sample relative to the beam can then be performed using the simple Photon Factory procedure detailed above. The alignment time for each exposure is then approximately 6-10 minutes.

2.10.7 Precision alignment for rotation work

In order to model preferred orientation effects, it is desirable to perform experiments with the incident beam entering the pressure cell at an angle to the cell axis. It is not possible to use the simple alignment procedure described above when the pressure cell axis is not parallel to the beam as the diamond face will then no longer be perpendicular to the incident beam and the image of the sample in the telescope will be shifted significantly. In addition, the effective size of the gasket hole is reduced if the beam enters the cell at an angle and consequently alignment must be to an even higher standard of accuracy.

The method developed by the author was to first align the sample onto the axis of a specially constructed rotation stage (designed by the author). The stage consists of a precision machined axis, onto which the pressure cell is mounted using a standard crystallographic goniometer head (see figure 2.14). The axis can be freely turned by hand and then clamped to the angle required. When the sample is accurately on the rotation axis (to a tolerance of 10 μm), the sample is aligned relative to the beam using the standard method (with the diamond face perpendicular to the beam). To

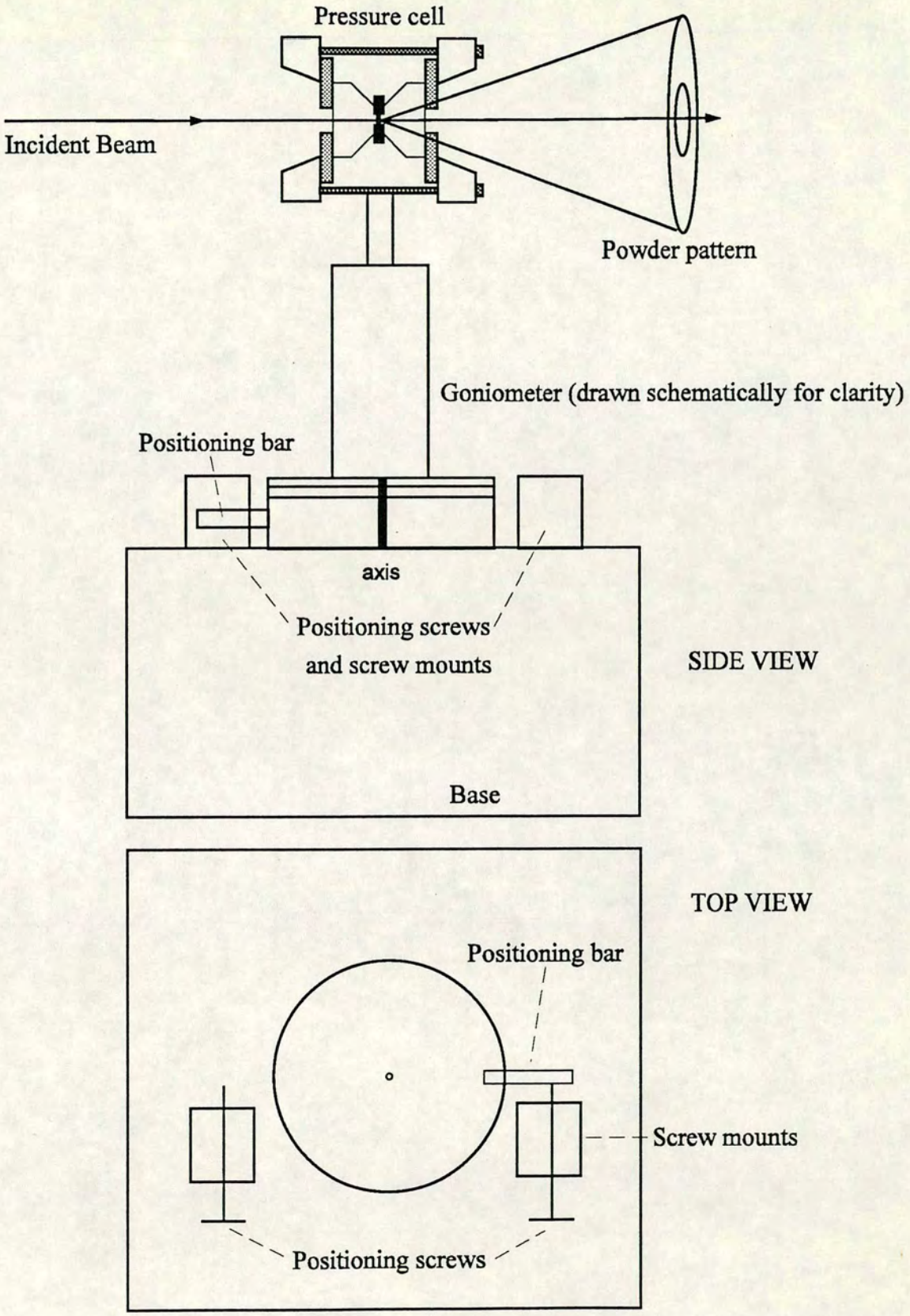

Figure 2.14 The purpose built rotation mount for preferred orientation studies. The pressure cell is mounted on a standard goniometer, which screws onto the rotation axis. The positioning screws and bar allow the pressure cell to be rotated rapidly between positions with the diamond faces perpendicular to the beam.

move the sample relative to the beam the whole rotation stage is moved by manually translating the x-y stage, on which the rotation stage is mounted. Once aligned in this way, the sample can be rotated to the required angle and, if the alignment onto the rotation axis is of sufficient standard, the beam should pass cleanly through the sample without striking the gasket.

The precision alignment of the sample, which is not necessarily at the centre of the pressure cell, onto the rotation axis is performed optically. The critical point of this procedure is that the alignment is only possible if the sample is viewed with the telescope axis perpendicular to the diamond face. If this is not the case, then, due to the high refractive index of the diamond, the image will be shifted significantly and misalignment will occur. The optical procedure requires that the sample is rotated repeatedly by 180° (the sample must be viewed through each diamond) and so it was necessary to design the rotation stage such that the cell could be repositioned accurately and quickly with either diamond face perpendicular to the beam.

The rapid repositioning of the pressure cell was achieved by attaching onto the rotation axis a small positioning bar. On the base of the axis two adjustable fine threaded screws are placed. These screws are positioned such, that by moving the screws slightly, the angle of the rotation stage can be set at the points where the diamond face is perpendicular to the beam (see figure 2.16). At the beginning of the alignment procedure, the vertical tilt of the pressure cell is adjusted on the goniometer head until the reflected laser spot is in the same horizontal plane as the laser beam. The positioning screws are then adjusted until at each 180° position the reflected laser spot coincides with the incident laser beam. In a number of pressure cells, the faces of the two diamonds are not quite parallel and so, as the cell is rotated, the reflected laser spot is translated vertically. This will shift the optical image vertically, but, since this is parallel to the rotation axis, it does not affect alignment onto the axis itself. However when aligning the sample relative to the beam, the non-parallelness of the diamonds is significant. This problem was resolved by ensuring that the diamond face through which the sample is viewed (when aligning relative to the beam) is adjusted to be accurately perpendicular to the beam.

The basic method of alignment onto the rotation axis is to move the sample onto the telescope cross-hairs, by viewing the sample through one diamond. Then, the cell is reversed by rotating the axis through 180° and the resulting position of the sample relative to the telescope cross-hair is observed. Any misalignment of the sample

perpendicular to the beam can be corrected for by translating the sample using the goniometer translations to the midpoint of the two observed positions. The position of the sample in the along beam direction is corrected by using the telescope focus. Assuming the thicknesses of the diamonds are equal, then the sample will be in focus from both viewing directions only if it is exactly on the rotation axis. If there is any misalignment along the beam, the sample will appear blurred when viewed from one direction. Alignment along the beam is performed by noting the telescope focus position for one direction and rotating the cell so as to look through the other diamond. The focus position from this side is noted and the telescope is translated along the beam direction until it is midway between the two focus points. The sample is then moved along the beam using the goniometer translation until it is in focus. During alignment with this technique, it is generally necessary to repeat the adjustments several times, which requires that the sample be rotated repeatedly through 180°. If limited synchrotron time is not to be wasted, then it is necessary to be able to rotate the pressure cell quickly and accurately. This was the principal reason for designing a purpose built rotation stage. It is possible to purchase motorised rotation stages designed for other purposes, but they take many minutes to rotate by 180°.

Once the sample has been positioned accurately onto the rotation axis, it is necessary to align the axis relative to the incident beam. To acheive this, the pressure cell and goniometer are removed from the rotation stage. A goniometer with a paper holder frame is placed on the stage and the position of the beam found using the same method as in the standard procedure. The telescope cross-hair is now translated onto the beam mark and the paper holder and its goniometer removed. The sample is then replaced on the stage and the stage translated until the centre of the sample is on the cross-hair. At this point, it is possible to check that the sample position relative to the rotation axis is correct. This must be performed without moving the telescope (as it now defines the beam position). The pressure cell is now rotated to its desired angle and the exposure taken. Obviously, once aligned on the axis, exposures at many angles can be performed by simply rotating the pressure cell and it is not necessary to re-align the sample. Although the alignment procedure contains several steps, it can be performed in approximately 20 minutes. If several exposures at different angles are required, this procedure compares well in efficiency with the standard method as there is no need to realign the sample between exposures.

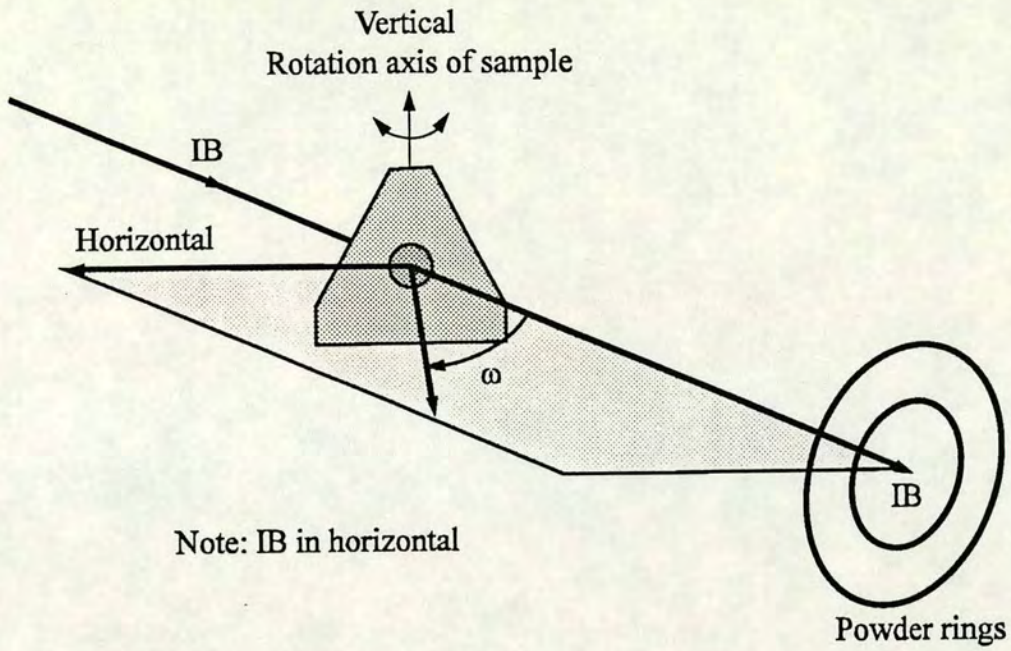

Figure 2.15 With the pressure cell mounted on the purpose built rotation stage, both the incident beam (IB) and pressure cell axis lie in the same horizontal plane. The orientation of the pressure cell is defined by the acute angle (ω) between the pressure-cell axis and the incident beam.

With the pressure cell aligned on the rotation stage, the axis of the pressure cell will lie in the same horizontal plane as the incident beam (this plane is shown shaded in figure 2.15). In order to describe the orientation of the sample at different angles to the incident beam, define ω to be the acute angle between the presssure-cell axis and the incident beam (see figure 2.15). Note that ω=0 is defined as the pressure-cell axis coincident with the incident beam. The rotation stage can also be used to explore the preferred orientation in ambient pressure flat-plate samples and ,in such cases, ω is defined as the acute angle between the flat-plate normal and the incident beam.

CHAPTER THREE

Preferred Orientation

3.1 Introduction

An ideal polycrystalline material consists of crystallites that are randomly distributed, i.e. there are equal numbers of crystallites in all possible orientations. In practice most powders have more crystallites in some orientations than others and the sample is then said to exhibit preferred orientation or texture. There seems to be little agreement in convention over the use of the two terms, although perhaps a broad distinction is that texture is used to describe gross non-uniformity of the sample and the term preferred orientation reserved for cases where the sample texture is relatively mild and smoothly varying.

The particular nature of the texture in a polycrystalline material is determined mainly by the crystallite shape and the mechanical and thermal history of the sample. Preferred orientations in metals have received a great deal of study, because of the influence of texture on the mechanical properties. A metal with strong texture, induced perhaps by cold-rolling or extrusion, may have anisotropic properties, the desirability of which depends on the intended use of the metal. For example, the metal used for transformer cores is manufactured deliberately to be textured with the easily magnetised [100] reciprocal lattice directions oriented in the rolling direction (Barrett and Massalski, (1992)). Studies of compressed metals, perhaps the most analogous work to high-pressure studies, have shown that orientation under compression can be very strong and varies significantly both in degree and nature between different metals (Barrett and Massalski, (1992)).

In powder diffraction, the relative intensities of reflections from a sample with preferred orientation will reflect differences in not just structure factors and multiplicity but in the number of crystallites contributing intensity to each reflection.

The effect of sample texture on the diffraction pattern can be very strong, particularly in high-pressure studies. However, if the proportion of crystallites contributing to each reflection is known, then the reflection intensities can be corrected. The fraction of crystallites with different orientations can be measured by recording diffraction patterns with various orientations of the sample. If a sufficient variety of sample orientations can be measured, then a map (a pole-figure) can be built-up of the density of the normal (pole) to a set of particular lattice planes at different sample positions (Peiser *et al*, (1955). It is possible to fit an analytic model to this information and extract from this model the true intensity of the reflection, a process which is known as pole-figure inversion (Matthies *et al* (1988), Dahms and Bunge (1989)). To perform pole-figure inversion accurately requires a considerable amount of data for each reflection, which is often difficult or too time consuming to obtain in many powder diffraction experiments. Alternatively, if the orientation of all the crystallites in the powder is not available, a model that describes the preferred orientation can be refined along with the structure model during Rietveld refinement. These preferred orientation models are generally constructed by modelling the pole-figure of a single reflection from which the pole-figure of other reflections is calculated (Valvoda, (1992). Provided there are sufficient data to permit the effects on the diffraction pattern of the structure and texture to bedecorrelated this procedure has been shown to work well (Dollase, (1986)).

There are two aspects to constructing any preferred orientation model: choosing a suitable function to describe the distribution of the crystallite orientations, and modelling how this distribution interacts with the diffraction geometry in use to produce the observed diffracted intensity. The relative intensities of the diffraction peaks from an oriented sample depend strongly on the diffraction geometry used. Figure 3.1 shows 1-D powder diffraction profiles obtained from the same alumina sample in Bragg-Brentano and DAC transmission geometry along with the calculated profile from a non-textured sample of this material. There are obvious differences in relative peak intensity between the two observed profiles and between each of the observed profiles and the calculated pattern. The interaction with the diffraction geometry can also produce a diffraction pattern with definite 2-D character (in the sense that reflections are not constant in intensity around the powder rings). This is illustrated in figure 3.2 which shows a 2-D image obtained from HgTe at 13.1 GPa in DAC transmission geometry. The image has been computer enhanced to emphasis the strong variation in intensity around the powder rings. The degree of intensity variation

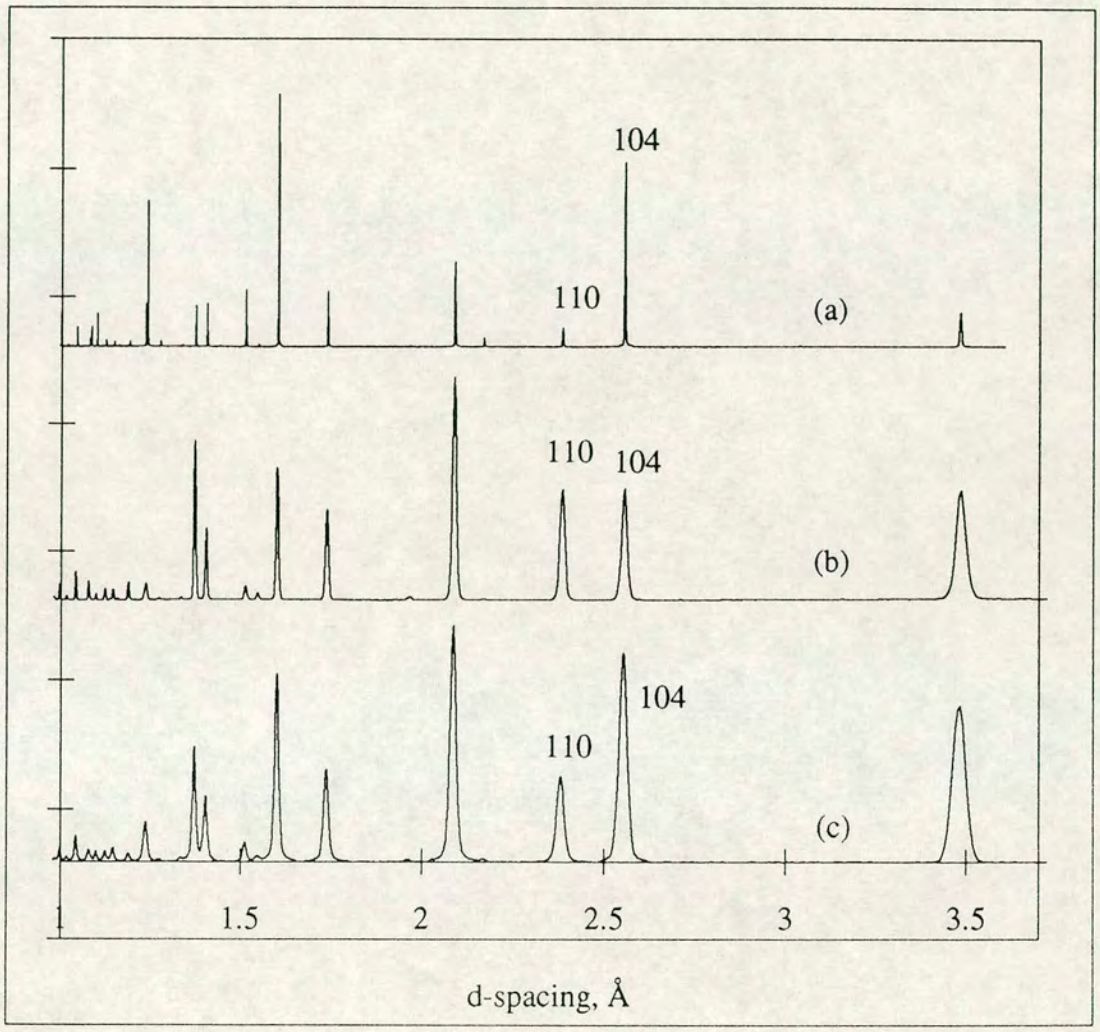

Figure 3.1 Powder-diffraction spectra obtained from the same strongly textured alumina sample in: (a) Bragg-Brentano geometry, (b) DAC transmission geometry (c) simulated spectra with no preferred orientation

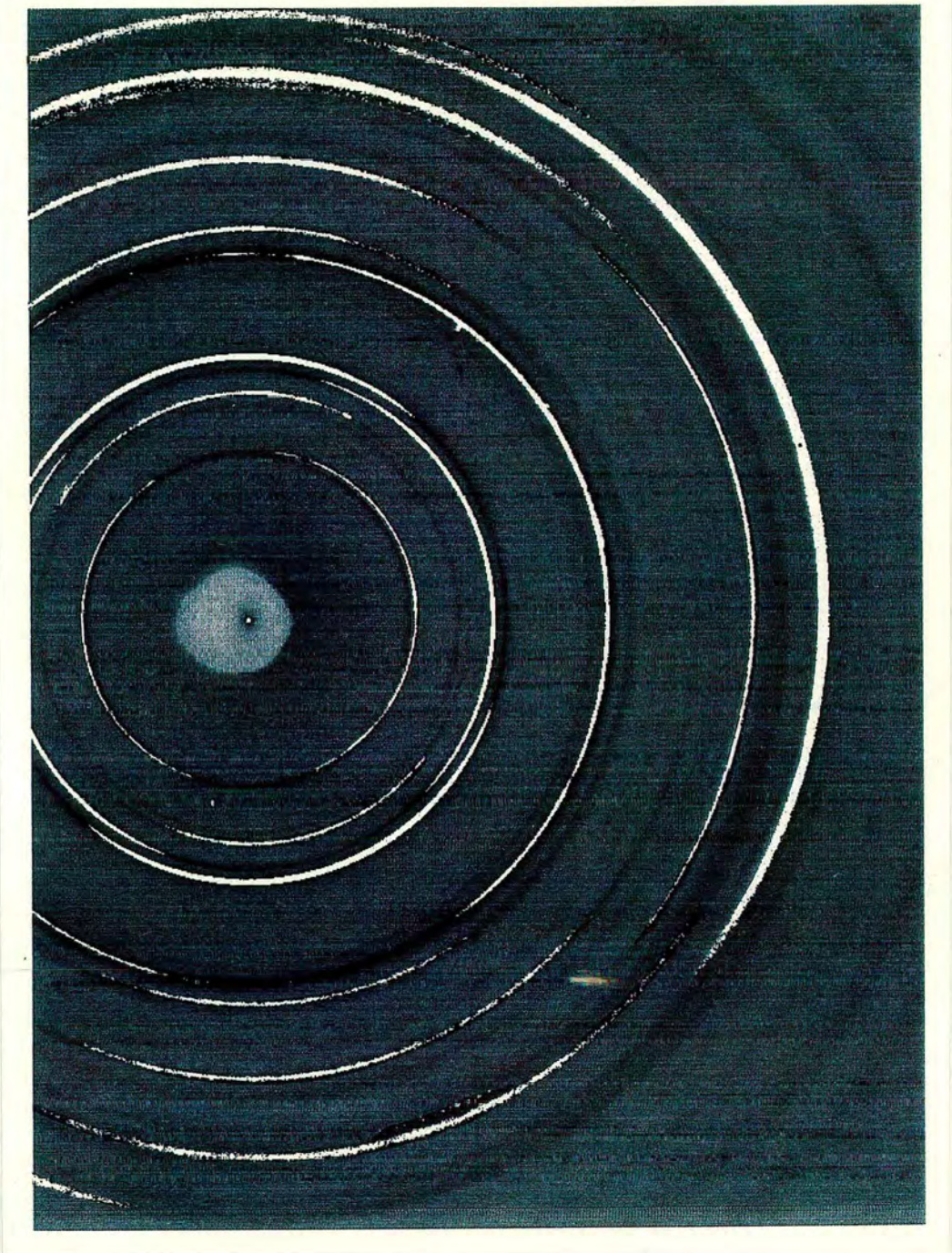

Figure 3.2 A 2-D image from HgTe at 13.1 GPa. The image has been computer enhanced with a non-linear intensity scale to emphasis the strong intensity variation around the powder rings.

around the powder rings can be very severe (as much as a factor of ten in extremely oriented samples). Since the maxima and minima of different reflections do not necessarily occur at the same positions around the powder rings (as seen in figure 3.2), great care must be taken in interpreting the relative intensities observed from an incomplete diffraction pattern. Thus a preferred orientation model must be 2-D in nature and describe correctly the interaction between the crystallite distribution and the diffraction geometry.

This chapter presents a review of existing preferred orientation models and their use in describing the effect of sample texture on the powder pattern. The interaction between the sample texture and the diffraction geometry is discussed in the context of the development of a suitable 2-D preferred orientation model for the transmission geometry used in high-pressure work. The recent development of area detectors, such as image-plates, offers for the first time the possibility of preferred orientation modelling of samples under pressure and the phenomenology of the effect of texture on the full 2-D powder pattern is discussed in detail.

3.2 The Crystallite Distribution

There is no reason why the crystallites that make up a powder sample should be in random orientations. Take for example a powder sample, which is shaped like a small box. If the constituent crystallites are shaped like flakes then it is possible that the crystallites may align along a particular axis in the sample in the manner shown in figure 3.3a. The preferred orientation axis (or POA) is defined to be the single axis in the sample, about which the crystallites tend to align. Assuming that the distribution of crystallites is symmetric around the preferred orientation axis (POA) and the morphology of all the crystallites is identical, the orientation of a particular crystallite can be defined by the angle (α) between the normal to the flake surface and the POA (in figure 3.3a this angle is shown for one of the crystallites). The distribution of crystallite orientations may be modelled by a simple distribution function $P(\alpha)$ and figure 3.3b shows the form of such a distribution for the crystallite orientation distribution drawn in figure 3.3a. If the morphology of the flakes is such that the crystallites form with, say, their (001) reciprocal lattice vectors (K_{001}) parallel to the flake normal, then $P(\alpha)$ describes the distribution of the K_{001} vectors about the POA. The $P(\alpha)$ distribution can also be represented as contours on a unit sphere, whose axis is the POA (see figure 3.4). For comparison, the angle α (between the POA and

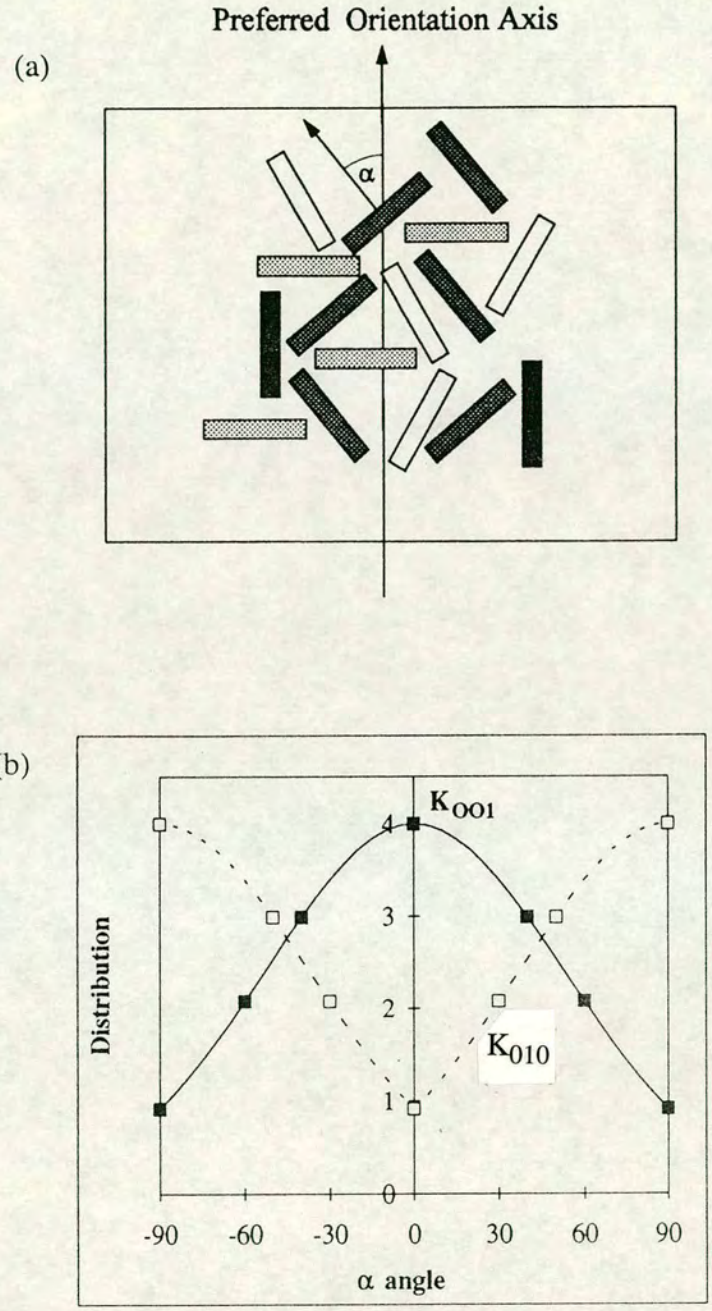

Figure 3.3 (a) An example population of oriented 'flake-like' crystallites. The crystallites show a strong tendency to align with the normals to the flakes parallel with an axis in the sample (the preferred orientation axis or POA). The angle (α) between the flake normal and the POA can be used to define the orientation of a crystallite. (b) The distribution of the K_{001} and K_{010} vectors versus α for the sample of figure 3.3a (assuming that the morphology of the crystallites is such that the (001) reciprocal lattice vector, K_{001}, is coincident with the flake normal).

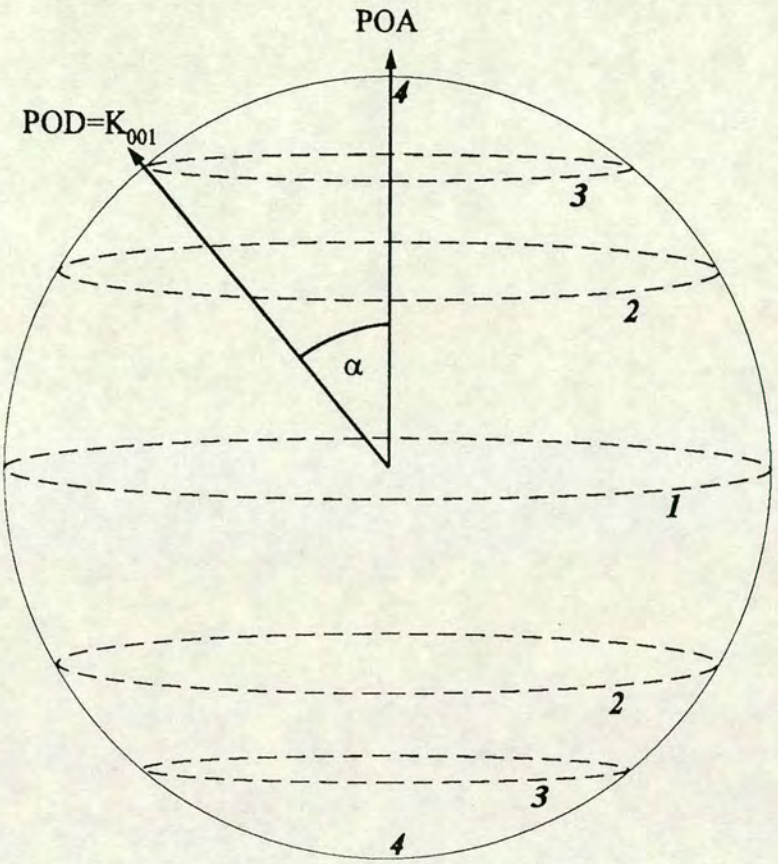

Figure 3.4 The distribution of the crystallites can be represented by contours on a sphere. The italic figures give the number of crystallites with their POD vector at that angle α to the POA. The figure shows the contour distribution of the K_{001} vectors (defined to be the preferred orientation direction or POD) of the crystallite population of figure 3.3a. The angle α is shown for the same crystallite as in figure 3.3a.

K_{001}), is also drawn in figure 3.4 for the same crystallite orientation as in figure 3.3a.). The value of the contour (and hence the number of crystallites with a particular orientation) is determined by the angle (α) between the K_{001} vector and the position of the POA vector.

Similar distribution functions can be defined to describe the orientations of other reciprocal lattice vectors relative to the POA. Figure 3.3b shows the form of the distribution of the (010) reciprocal lattice vectors in the crystallites in figure 3.3a (the lattice is assumed to be cubic). However, the forms of all such distributions are not

independent of each other, but are related by the symmetry of the lattice. Hence, if the angle between the reciprocal lattice vectors is known (i.e. the lattice parameters are available), then it is necessary to specify only the distribution for one reciprocal lattice vector: the number of crystallites with a particular orientation of any other reciprocal lattice vector can be obtained from the angle of that vector relative to the reference vector and its $P(\alpha)$ distribution. For example, suppose, that in order to satisfy the Bragg condition for the (010) reflection from the sample of figure 3.3, the (010) reciprocal lattice vector must lie at 60° to the POA. If the K_{010} vector is at 60° to the POA, then, by the (assumed) cubic symmetry of the lattice, the angle between the POA and the K_{001} vector is 30°, i.e. $\alpha=30°$. Therefore the number of crystallites with K_{010} at 60° to the POA is obtained from the K_{001} distribution in figure 3.3b at $\alpha=30°$.

Thus, if the lattice parameters are known, a preferred orientation model can be constructed by defining one reciprocal lattice vector to be the reference preferred orientation direction, or POD. Strictly speaking, the choice of which reciprocal lattice vector is the POD is arbitrary. However the form of distribution necessary to describe the orientation of reciprocal lattice vectors which tend to lie neither parallel nor perpendicular to the POA is more complex (in the example of figure 3.3 a distribution to model the orientation of the K_{111} vector would peak at $\alpha=\pm45°$). Therefore, we define the reciprocal lattice direction that has either the highest or lowest probability of aligning coincident with the POA to be the preferred orientation direction (or POD) e.g. K_{001} or K_{010} in this example. Of course it is also possible that there may be more than one morphology of crystallites and there may be other populations of crystallites which align with different reciprocal lattice vectors along the preferred direction. However, as this consideration can be simply added to the model at a later stage, it will not be considered further in this section.

In most experimental set-ups, the sample has a readily identifiable axis (defined as the sample axis or SA). For example, in Bragg-Brentano geometry the SA is defined to be the normal to the flat-plate sample, in Debye-Scherrer capillary geometry the SA is defined to be the capillary axis and in diamond-anvil cell transmission geometry the SA is defined to be the pressure-cell axis. The preparation of the sample often forces the POA to be coincident with the SA. Thus it is often assumed that in a flat-plate sample for Bragg-Brentano work the POA is coincident with the SA (the flat-plate normal). However, it should be emphasised that the POA is not always identifiable in such a simple manner. For example, it is common for the POA in a diamond-anvil cell

to lie at angle to the pressure-cell axis, perhaps because of the diamond anvils not being perfectly aligned.

3.3 Modelling Functions

In order to perform quantitative analysis of the effect of preferred orientation on the diffraction pattern, it is necessary to model the crystallite distribution mathematically. In a strongly oriented sample or in a powder sample made up of clumps of crystallites, the distribution will contain discontinuities, which will be difficult to model accurately. Such cases lie outside the scope of standard preferred orientation modelling and will not be considered here: the distribution of crystallites will be assumed to be sufficiently smooth to be modelled by using an analytic function, with a small number of refinable parameters. A suitable function to describe the distribution must be itself smoothly varying, provide an accurate description of the distribution and be easy to compute (especially if the correction is to be implemented into crystallographic refinement packages where the calculation will be repeated many times each refinement cycle). It is also highly advantageous if the function chosen to model the crystallite distribution is normalised. Then the value of the function at any point on the sphere is simply the probability of finding a crystallite in that orientation, and any refinement of the distribution during analysis is independent of changes in scale factor. These simple requirements can be satisfied by many simple functions and there is a variety of modelling functions commonly used to describe the distribution of crystallites in the powder.

3.3a Spherical Harmonics

A possible choice for an accurate modelling function is a linear combination of spherical harmonics, or, more precisely, a suitably chosen subset of harmonics (Jarvinen *et al*, (1970)). The distribution $P(\alpha)$ is written in terms of spherical harmonics as:

$$P(\alpha) = \sum_{i,j} C_{ij} K_{ij}(\alpha) \qquad (3.1)$$

where C_{ij} are constants and K_{ij} are the relevant spherical harmonics.

It has been shown (Jarvinen *et al*, (1970), Pesonen, (1979), Matthies *et al*, (1988), Dahms and Bunge, (1989)) that spherical harmonics can describe the distribution in most lattice types and the corrected intensities match the predicted values for known structures well. In some simple cases it is possible to obtain sufficient accuracy with only two orders of harmonics. If the distribution is complex a prohibitively large number of spherical harmonics are needed, which can be very slow computationally and give ill-conditioned refinements. For pole-figure inversion of data from a sample of known structure, a linear combination of spherical harmonics is the most frequently used choice of modelling function and several different numerical techniques have been developed to fit the texture model to the observed diffraction data. Perhaps the most accurate of these methods is the iterative series-expansion method (Dahms and Bunge, (1989), Bunge *et al,* (1989)), which calculates the even and odd terms of the harmonic expansion separately. The calculation of the distribution is then repeated until a sufficiently good match between the predicted intensity and the observed data is obtained. Recently, spherical harmonic methods have been incorporated into Rietveld refinement packages (Ahtee *et al*, (1989), Jarvinen *et al*, (1993)). However, due to the large number of extra parameters that this introduces into structure refinement, the use of spherical harmonics for this purpose is not wide-spread.

3.3b Simple Analytic Functions

If sufficient information is not available for spherical harmonics to be used or if computational time is at a premium (perhaps during Rietveld refinement), it can be desirable to use a simple function to describe $P(\alpha)$. Early developments in this area centred on using gaussian functions to model the crystallite distribution (Uda (1967), Rietveld (1969)) and then later modified gaussian functions (Capkova and Valdova (1974), Parrish and Huang (1983)). A significant breakthrough occurred with the widespread adoption in Rietveld packages of the March-Dollase model (Dollase (1986)), which is based on a physical model of crystallite rotation under stress (March (1932)). The March-Dollase model is a modified trigonometric function and has the form

$$P(\alpha) = [R^{-1} \sin^2 \alpha + R^2 \cos^2 \alpha]^{-1.5} \qquad (3.2)$$

where α is an angle defined by the reflection under consideration (see phenomenological discussion above), R is the refinable parameter, and $P(\alpha)$ is the

relative probability of there being a crystallite whose POD is at angle α to the POA. Note that for a random powder,

$$R=1 \tag{3.3}$$

The March-Dollase function is used with considerable success in many Rietveld refinement packages (e.g. GSAS, (Larson and Von Dreele, 1985)). In most cases it describes $P(\alpha)$ more accurately than gaussian functions (Dollase (1986)) and has the distinct advantage over many other possible functions of being normalised (i.e. adjusting $P(\alpha)$ does not require the scale factor to be altered).

It would be possible to use any of the modelling functions (including harmonic expansions) discussed to describe the crystallite distribution. However it was considered that, since this was the first attempt to perform texture modelling from samples under pressure, it would be advantageous to keep the number of parameters introduced by the model as low as possible. Because of the limited information that can be obtained from a sample in a pressure cell (compared to ambient-pressure texture studies), harmonic expansions were not considered suitable due to the large number of parameters in such models. Of the simple analytic functions commonly used for texture studies the March-Dollase function is the most suitable. As discussed above, it has been shown to describe the crystallite distributions commonly encountered in ambient-pressure work well and is simple to use, which makes physical interpretation of results straight-forward. Thus in this thesis, the March-Dollase function will be used for all quantitative texture studies. The limitations of this function and possible future developments to improve the accuracy of this technique are discussed at a later stage.

3.4 The Interaction Between The Crystallite Distribution and the Diffraction Geometry.

As seen in figure 3.1, the relative intensities of the diffraction peaks from an oriented sample are determined by both the crystallite distribution and the diffraction geometry in use. Only the small subset of crystallites that satisfy the Bragg condition can diffract, and thus there is a limited range of possible orientations of these crystallites with respect to the incident beam. The function of the preferred orientation model is to establish the orientations of this subset of crystallites with respect to the crystallite

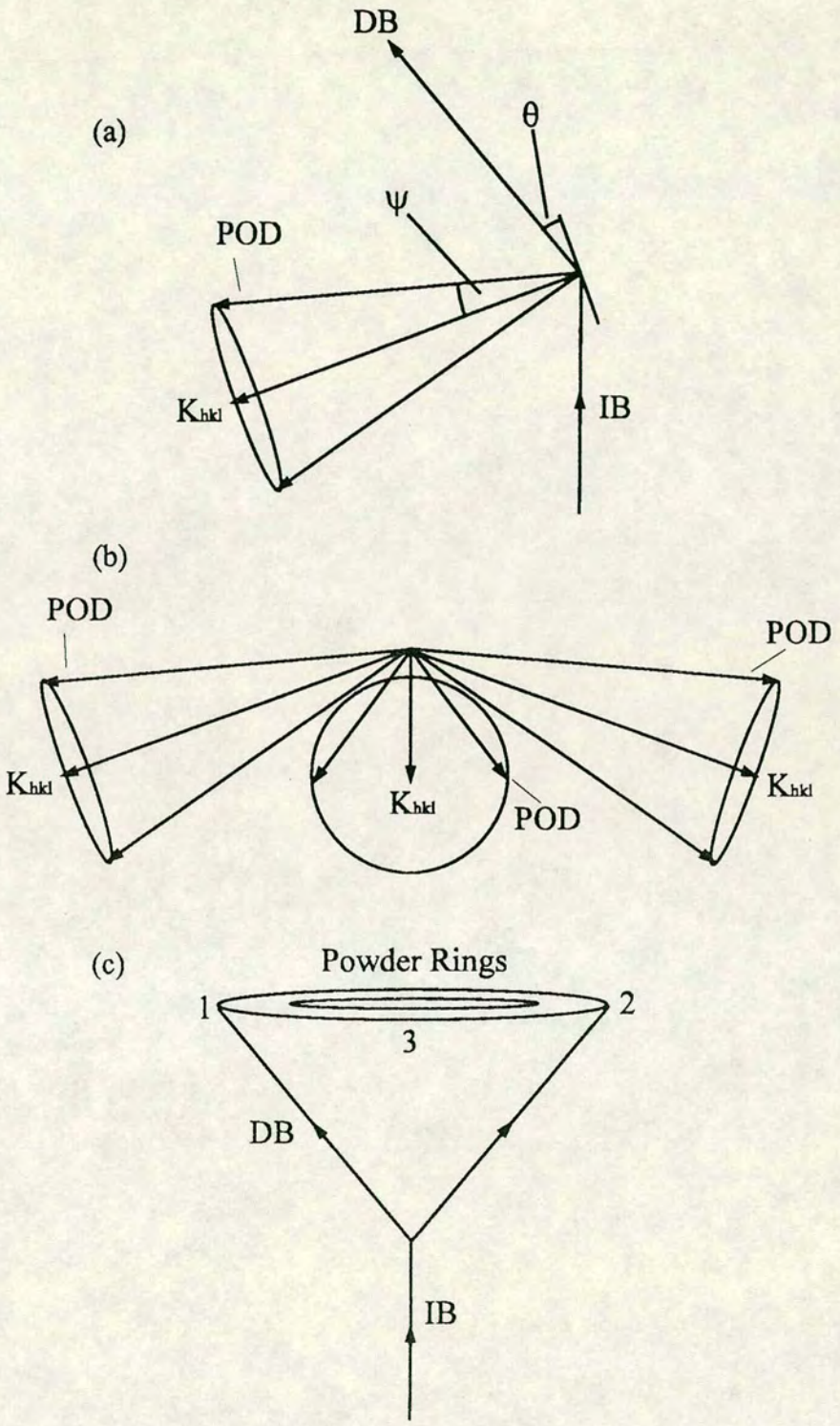

Figure 3.5 (a) The orientation of the scattering vector, K_{hkl}, with respect to the incident beam, IB for diffraction at one point on a powder ring. DB=diffracted beam, θ=Bragg scattering angle. The POD must lie somewhere on a cone (the POD cone) of half-angle ψ about K_{hkl}. (b) The POD cones for diffraction to three selected points on a powder ring. (c) The three selected points on the powder ring of figure 3.5b.

distribution and hence determine the relative fraction of crystallites in those orientations. As the orientation of a crystallite is specified by the orientation of its POD vector, the model must determine the orientation of the POD vector of the diffracting crystallites. Figure 3.5a shows the orientation of the scattering vector (K_{hkl}) of the diffracting crystallites for diffraction at the point labelled '1' on a powder ring. The possible orientations of the crystallites that can contribute to this diffracted beam are obtained by rotation about K_{hkl}. Since the reciprocal lattice vector defined to be the POD is at some fixed angle ψ to K_{hkl}, the POD's of the diffracting crystallites must lie somewhere on the surface of a cone (the POD cone) of half-angle ψ about K_{hkl}. Note that the observed intensity at this point will be due to all the reflections that make up the multiplicity set, which will not necessarily have the same ψ angle between their scattering vectors and the POD. Thus, in calculating the effect of preferred orientation, each reflection in the multiplicity set must be considered in turn.

The following discussion concerns the effect of preferred orientation on the whole 2-D diffraction pattern and so it is necessary to represent the orientation of the POD cone in relation to the crystallite distribution at several positions around the powder rings. Figure 3.5b shows the POD cones for diffraction at three selected points, 1,2 and 3, on the powder ring of figure 3.5c. (For clarity the incident beam, diffracted beams and diffracting planes have been omitted from figure 3.5b.) These three points on the powder ring, and their corresponding POD cones, will be used in the following discussion to illustrate the effect of preferred orientation on the 2-D diffraction pattern. First, a phenomenological description is given of the effect of preferred orientation on the full 2-D diffraction pattern for a general orientation of the uniaxial distribution discussed in section 3.2. Special cases corresponding to specific diffraction geometries in common use (namely Bragg-Brentano, Debye-Scherrer, and DAC transmission geometries), are then considered.

3.4a The General Case

Consider what happens when the incident beam strikes the crystallite distribution of figure 3.4 at an angle β to the POA, as shown in figure 3.6. The probability of finding a crystallite correctly oriented for diffraction into point 1 of that powder ring in the diffraction pattern of figure 3.6 is given by the average probability of the POD vectors on the corresponding cone. In general, the probability of different points on a given

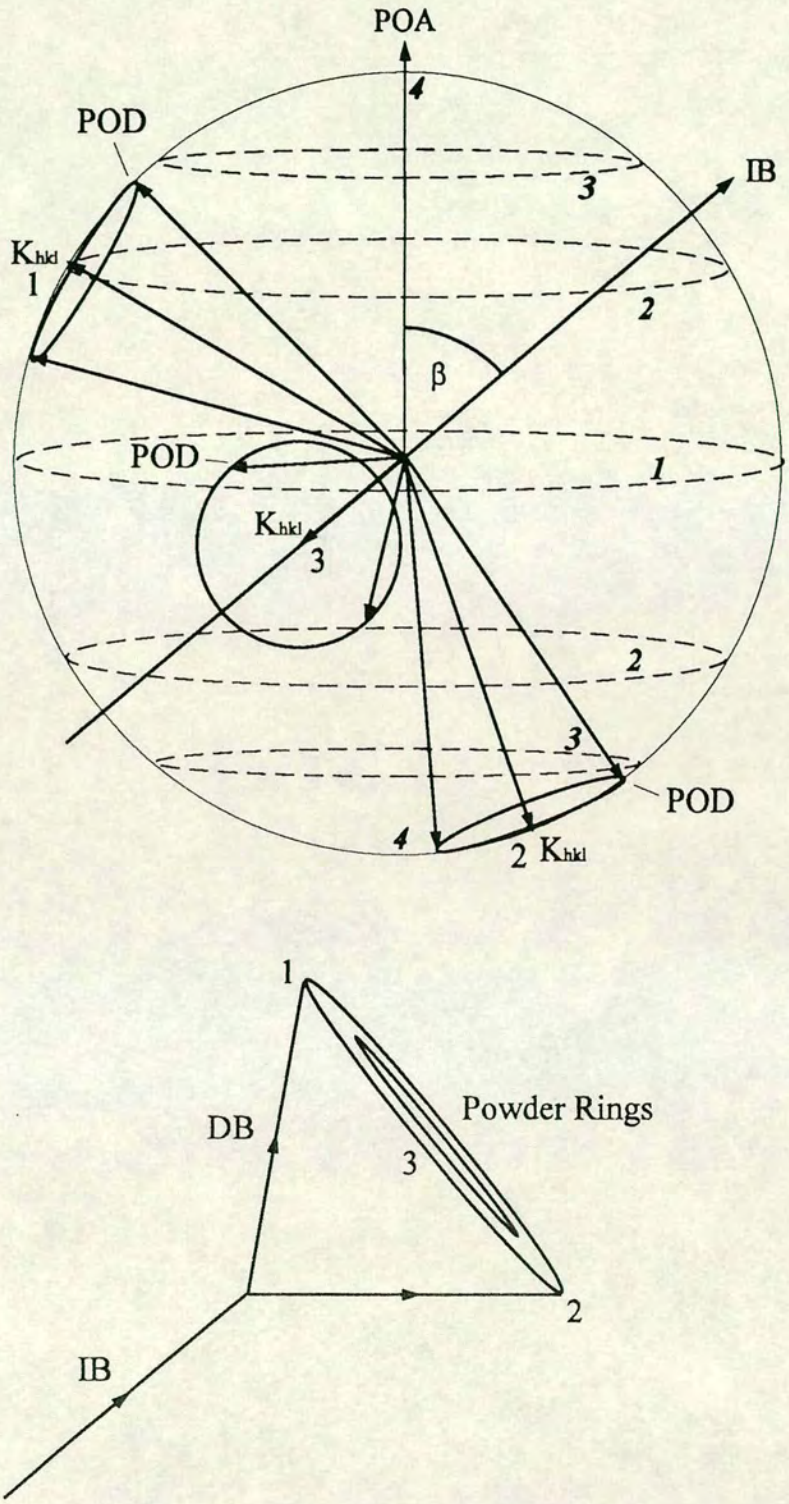

Figure 3.6 The orientation of the POD cones for diffraction into three selected points on a powder ring (shown in the lower figure) for the incident beam striking the crystallite distribution of figure 3.4 at a general angle. The contours intersected by the POD cones have different values at all three points on the powder ring and consequently the intensity around the powder ring is not constant.

POD cone is not uniform (in figure 3.6, the POD vectors do not lie on the same contour) and so it is necessary to calculate an average over the cone ($<P(\alpha)>$). The angle α, which specifies the orientation of the POD relative to the POA, will vary in quite a complex manner for different positions of the POD on the cone. The preferred orientation model must calculate angle α at each position of the POD on the cone and then determine $<P(\alpha)>$ using equation 3.2.

The same applies to all other points on the powder ring and to the powder rings from all other reflections and the intensity observed at any point on the powder ring of any (hkl) reflection is thus given by:

$$I_{observed}(hkl) = I_{true}(hkl) \sum_{M(hkl)} \frac{< P(\alpha) >_{hkl}}{M(hkl)} \qquad (3.4)$$

where $I_{observed}(hkl)$ is the observed intensity of the powder ring from (hkl) reflection, $I_{true}(hkl)$ is the intensity of the (hkl) powder ring from an ideal randomly oriented sample of that volume, M(hkl) is the multiplicity of the (hkl) reflection and $<P(\alpha)>_{hkl}$ is the average value of the normalised distribution for that point on the powder ring. The sum in equation 3.4 is over all members of the multiplicity set.

The contours intersected by the POD cones for the three points in the diffraction pattern of figure 3.6 can be seen to represent different probabilities. Thus the average probability around the three cones is different and from equation 3.4, the intensity at these three points on the same powder ring will not be the same. The POD cones at points 1 and 2 intersect contours of higher value than those at point 3 and so point 3 will be an intensity minimum. It is this effect that creates the pattern of intensity variation around the powder rings seen in figure 3.2. It is evident that the contours for the POD cone at point 2 are of higher value than those at point 1 with the result that the maxima at points 1 and 2 do not have the same intensity. This asymmetry arises because the POD cone axis (K_{hkl}) is not perpendicular to the incident beam, but is rotated down in the figure through the diffraction angle θ. Thus the asymmetry between the two maxima will increase with diffraction angle (for a given β angle between the incident beam and the POA).

The POD cones drawn in figure 3.6 are for a reflection whose scattering vector lies at a small angle (ψ) to the POD. Now consider a reflection with a substantially different ψ angle between its scattering vector and the POD. As the half-angle of the POD

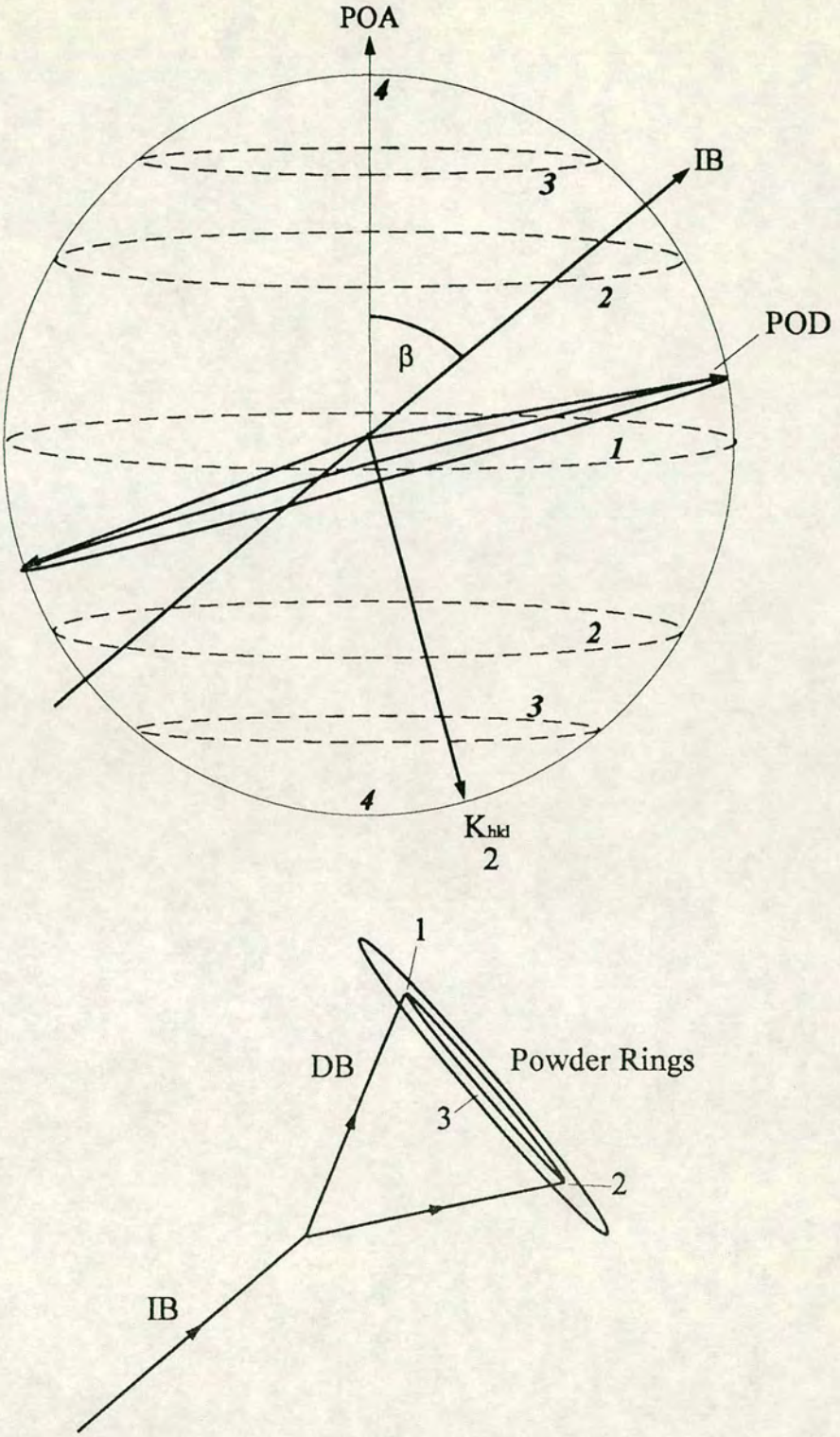

Figure 3.7 The orientation of the POD cone for diffraction into point 2 on a different powder ring to that of figure 3.6 (as shown in the lower figure) for the incident beam striking the crystallite distribution at the same general angle as figure 3.6. The contours intersected by the POD cone of this reflection are markedly different to the reflection shown in figure 3.6.

cone is different to that drawn in figure 3.6, the POD cone of this reflection will intersect different contours and will be more or less preferred accordingly. Figure 3.7 shows the POD cone of a reflection whose scattering vector lies almost perpendicular to the POD (i.e. $\psi \approx \pi/2$) for diffraction at point 2 in the diffraction pattern of figure 3.6 (the vectors for points 1 and 3 are omitted for clarity). On average over the POD cone, the contours intersected by the POD are of low value and thus this reflection will have a minimum at this point in the diffraction pattern. By similar arguments, points 1 and 3 will be a minimum and maximum respectively. Thus the positions around the powder ring, at which the maxima/minima of intensity occur, are determined by the angle ψ between the scattering vector and the POD.

In general, changing the wavelength of the incident radiation alters the orientation of the scattering vector (K_{hkl}) with respect to the incident beam, and consequently the contours experienced by the POD cone of a reflection will change. Thus the effect of preferred orientation on the relative intensities of the diffraction peaks is wavelength dependent.

3.4b Debye-Scherrer geometry

In this geometry, the incident beam enters the crystallite distribution perpendicular to the sample axis (SA). If the SA and the POA axis coincide, then the interaction of the diffraction geometry and the crystallite distribution is as shown in figure 3.7. The POD cones at points 1 and 2 in the diffraction pattern are at higher probability than point 3 and so point 3 is a minimum (as in the general case). The contours experienced by the POD cones at points 1 and 2 are identical and thus the maxima at points 1 and 2 are of equal intensity. It is common during data collection in this geometry to rotate the capillary about its own axis. This enforces the symmetry about the POA (which is otherwise only assumed). However the variation in intensity around the powder ring is unaffected.

In this geometry, reflections whose scattering vectors are at low ψ angles to the POD, will have strong maxima at points 1 and 2 in the diffraction pattern. This will ensure that the average intensity around the powder ring is stronger than would be expected from a sample with no preferred orientation. Reflections with a large ψ angle between the scattering vector and the POD, will intersect much lower valued contours at points 1 and 2 and thus these points in the diffraction pattern will be minima and point

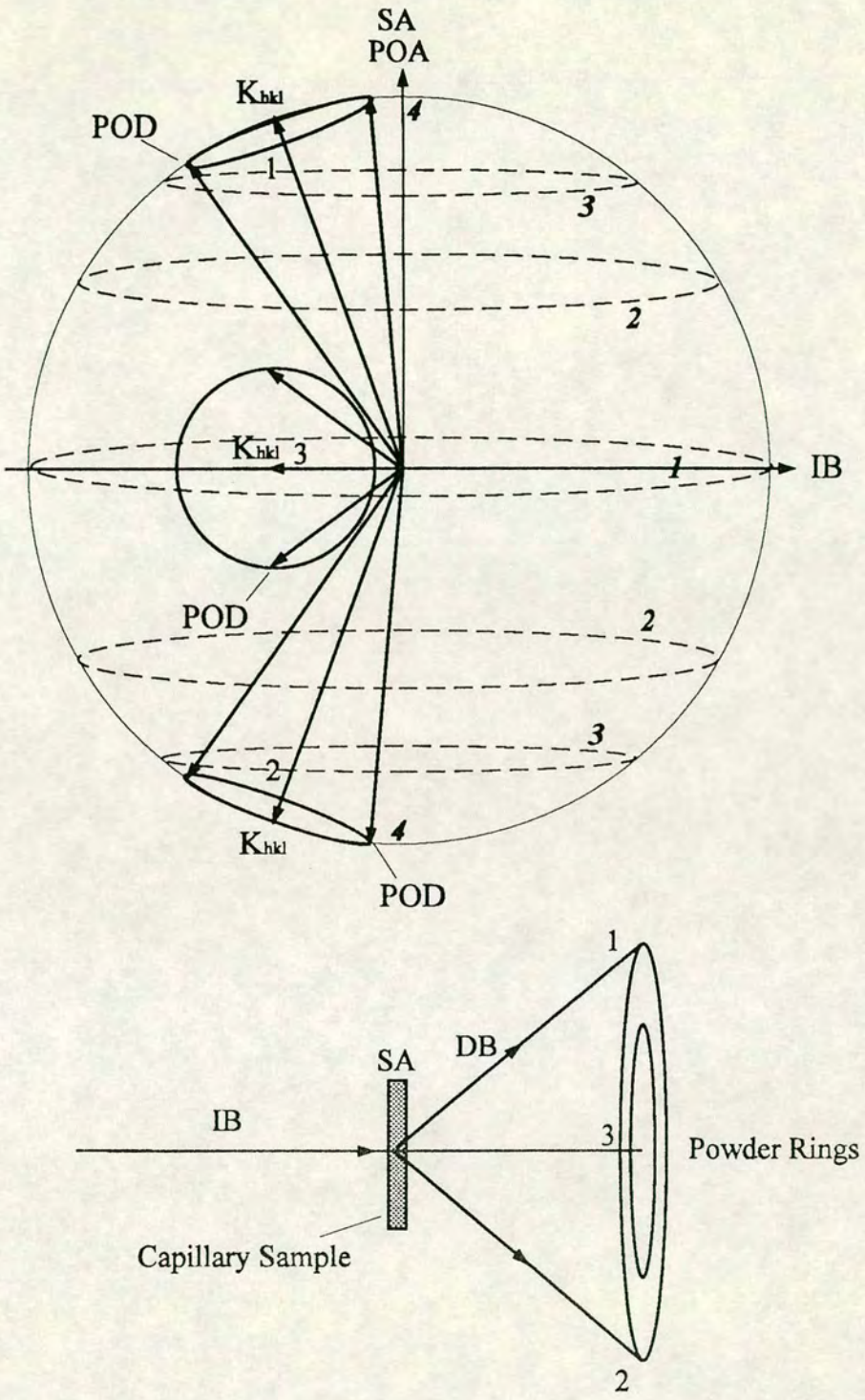

Figure 3.8 Debye-Scherrer geometry. The orientation of the POD cones for diffraction into three selected points on a powder ring (shown in the lower figure) for the incident beam (IB) striking the crystallite distribution of figure 3.4 perpendicular to the sample axis (SA). The SA is assumed to be coincident with the POA. By comparing the values of the contours intersected by the POD cones at the three selected points, it can be seen that points 1 and 2 are relative maxima and point 3 is a minimum.

3 will be a relative maximum. On average around the powder ring, those reflections with $\psi \approx \pi/2$ will have a lower intensity than that expected from a randomly oriented powder.

This geometry is commonly used with a high-resolution scanning detector, which records a thin strip of the diffraction pattern in the plane perpendicular to the POA/SA. No information on intensity variation around the powder rings is recorded, and hence the presence of preferred orientation cannot be determined unless a structural model is available. The degree of preferred orientation could be assessed by placing an area detector, such as an image-plate, so as to record a substantial fraction of the powder rings. Averaging of the intensity around the powder rings will produce intensities closer to those expected from a ideal sample than those obtained by the scanning detector, although for optimum accuracy the intensity variation around the powder rings should be modelled and the correct intensities obtained accordingly.

3.4c Bragg-Brentano geometry

In this geometry, the orientation of the sample relative to the incident beam is adjusted for each reflection such that the scattering vector coincides with the SA (the flat-plate normal) for the crystallites contributing to the measured intensity. This is shown in figure 3.9, with the detector taken to be at point 1 on the powder ring, and the POA assumed to coincide with the SA (see figure 3.9). For low ψ, points 1 and 2 are maxima in the diffraction pattern (as in the Debye-Scherrer case) and point 3 is a minimum. This geometry is normally used with a small conventional detector, which records the intensity only at point 1 on the powder ring; the intensity variation around the powder rings is thus not observed. This geometry represents a special case, in which measurements are made with all positions on the POD cone lying on the same contour ($\alpha=\psi$), and thus the value of $P(\alpha)$ is the same for all contributing crystallites. The crucial difference between Bragg-Brentano and other geometries is that the sample orientation relative to the incident beam is altered during data collection to ensure that (at point 1 in the diffraction pattern) the scattering vector for each reflection is coincident with the POA. Thus the POD cone, for the recorded section of the powder ring from all reflections, will lie on constant contours.

As in the Debye-Scherrer case, reflections with $\psi \approx 0$ will be stronger at point 1 in the diffraction pattern than expected from an ideal sample. A reflection with a large ψ

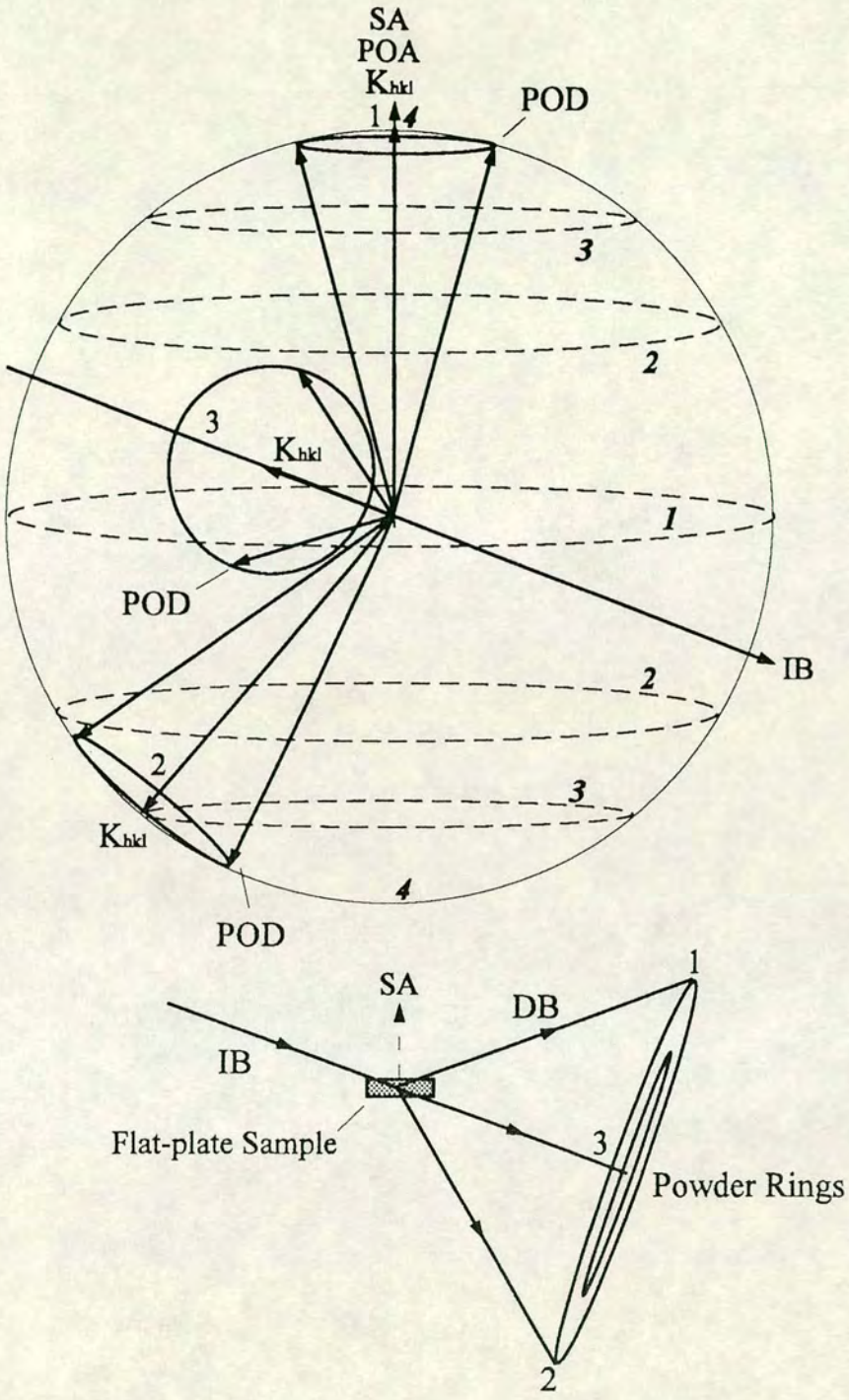

Figure 3.9 Bragg-Brentano geometry. The orientation of the POD cones for diffraction into three selected points on a powder ring (shown in the lower figure) for the incident beam (IB) striking the crystallite distribution of figure 3.4 such that, at point 1, the scattering vector K_{hkl} is coincindent with the sample axis (SA). The SA is assumed to be coincident with the POA. By comparing the values of the contours intersected by the POD cones at the three selected points, it can be seen that points 1 and 2 are relative maxima and point 3 is a minimum. At point 1, the contours intersected by the POD cone are of constant value.

angle will intersect lower valued contours at point 1 than the reflection shown in figure 3.9, and will therefore, be weaker with respect to the intensities expected from an ideal sample. Thus in the example of figure 3.1 (in which sample the K_{001} vector is the POD), the intensity of the (104) reflection ($\psi \approx 39°$) is (in the diffraction profile collected in this geometry) stronger than expected from a ideal sample and the (110) reflection ($\psi = \pi/2$) is weaker.

Placing an image-plate so as to record the whole 2-D pattern allows the presence and degree of preferred orientation to be assessed. If the sample contains preferred orientation, intensity variation around the powder rings will be observed and can be used to model the crystallite distribution separately from the data obtained from the standard detector.

Note that, in the Bragg-Brentano case, changing the wavelength has no effect on the effect of preferred orientation on any reflection at point 1 in the diffraction pattern. This is because at all wavelengths the scattering vector, K_{hkl}, is arranged to lie along the POA and consequently the angle α between the POD and the POA is fixed (at $\alpha = \psi$) for each reflection at all incident beam wavelengths.

3.4d DAC transmission geometry

The normal orientation of the pressure cell during data collection is with the pressure-cell axis (the SA) coincident with the incident beam. The POA is often not coincident with the SA, but it is helpful first to discuss the case where they are coincident. The POA is then coincident with the incident beam. Figure 3.10 shows the cones described by the POD for the three selected points in the diffraction pattern. The contours intersected by the POD cones are identical in all three positions and consequently the intensity is the same at these three points on the powder ring. Since a similar argument applies to any point on the powder ring, the influence of preferred orientation on the intensity will be identical at all points on a given powder ring; i.e. the intensity around any powder ring is uniform (ignoring other possible effects, such as polarisation of the incident beam). So in this case, the effect of preferred orientation on the pattern is seen only in changes to the relative intensities between reflections compared to those obtained from an ideal non-textured sample. This means that the presence of preferred orientation is not readily apparent and can only be detected if a structural model is available.

In this geometry, the POD cones for reflections with $\psi \approx 0$ intersect low-valued contours and so these reflections will be recorded as weaker than expected from an ideal sample. A reflection with a large ψ angle will intersect higher valued contours than the reflection shown in figure 3.10 and will be more intense compared to the intensities obtained from an ideal sample (see figure 3.1). Thus in the example of figure 3.1 (in which sample, the K_{001} vector is the POD), the intensity of the (104) reflection ($\psi \approx 39°$) is less intense in the diffraction profile collected in this geometry than expected from a ideal sample and the (110) reflection ($\psi = \pi/2$) is more intense.

As said, it is quite common for the POA not to be coincident with the SA, perhaps due to the misalignment of the diamond anvils. This case is exactly the same as the general case shown in figure 3.6. As already shown, the influence of any sample texture will then not be the same at different points on a powder ring and the intensity around the powder ring is no longer uniform. Thus with the POA not along the incident beam, the effect of texture is seen in variation of intensity around the powder rings as well as in the change to the relative intensities between reflections. It should also be noted that the average intensity around the powder ring is different from the simple case of the POA being coincident with the beam.

Even if the POA is coincident with the SA, rotating the sample such that the POA is no longer coincident with the incident beam is a powerful technique for determining sample preferred orientation. Therefore it is worth summarising the effects on the whole 2-D powder pattern of rotating an oriented sample away from the straight-on transmission position (defined to be the orientation of the pressure-cell with the SA coincident with the incident beam): with the POA coincident with the incident beam, there is no intensity variation around the powder rings and the effect of texture is observed only in changes to the relative intensities of reflections compared to those expected from an ideal sample. As the POA is rotated away from the incident beam, intensity variation around the powder rings will occur and increase with the angle β between the POA and the incident beam. The maxima and minima of the reflections occur at points around the powder ring determined by the magnitude of the angle ψ between the POD and the scattering vector. The degree of variation in intensity around the powder ring is determined by the amount of texture, the (hkl) indices of the reflection (which determine the angle ψ) and the angle (β) between the POA and the incident beam.

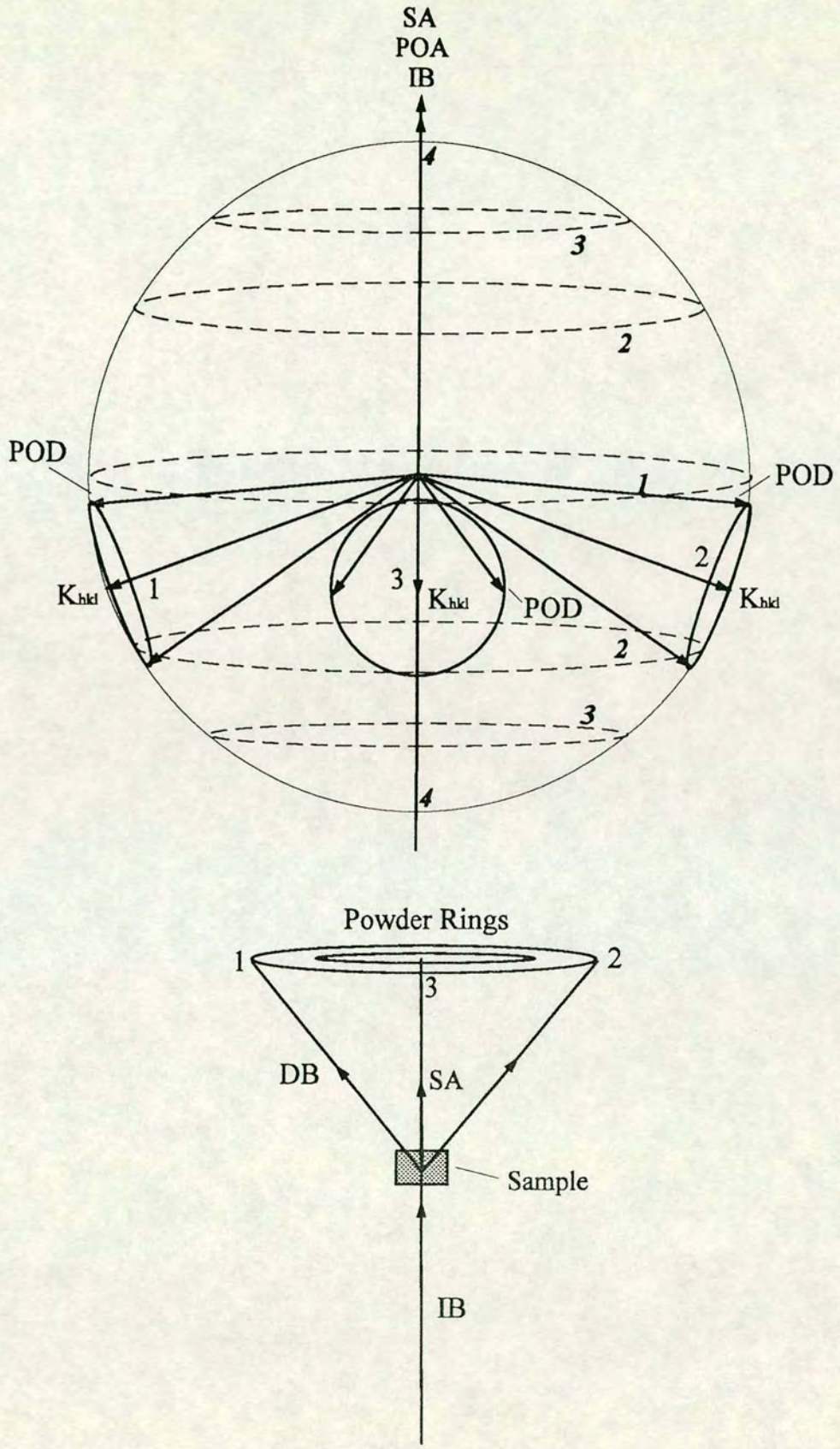

Figure 3.10 DAC transmission geometry. The orientation of the POD cones for diffraction into three selected points on a powder ring (shown in the lower figure) for the incident beam (IB) striking the crystallite distribution of figure 3.4 such that the incident beam is coincident with the sample axis (SA). The SA is assumed to be coincident with the POA. Since the contours intersected by the POD cones at the three selected points are identical, it can be seen that all three points will have equal intensity.

3.5 Conclusions

This section has presented an introduction to the concepts required for understanding the effects of preferred orientation on the 2-D diffraction pattern. The discussion has shown that it is both the crystallite distribution and the diffraction geometry which determine the relative intensities of the reflections from an oriented sample. In general, the effect on the diffraction pattern can be expected to show definite 2-D character. The following chapters will show how this 2-D character, and the changes in the average intensities around the powder rings as the sample orientation is altered, can be used to determine the preferred orientation separately from the structure.

CHAPTER FOUR

A 2-D Preferred Orientation Model For Transmission Geometry

4.1 Introduction

As seen in the previous chapter, the influence of the experimental diffraction geometry on the observed intensities from an oriented powder is not trivial. There are marked systematic differences in the relative intensities of diffraction peaks between a spectrum collected in say diamond-anvil cell transmission geometry to one obtained in the more conventional Bragg-Brentano geometry. This means that existing preferred orientation models, which have been developed for Bragg-Brentano geometry and Debye-Scherrer geometry (Dollase, (1986)), may not describe accurately the effect of sample texture on the relative intensities of the diffraction peaks. Therefore, attempts to perform Rietveld refinement on data collected in DAC transmission geometry using such models will have limited validity. In addition the effects of preferred orientation can show definite 2-D character (in the sense of not being constant around the powder ring). This means that any texture model should also be fully two-dimensional, an aspect that has hitherto been ignored.

In transmission geometry, with the preferred orientation axis (the POA) parallel to the incident beam, the intensity around all powder rings is constant (assuming symmetry of the crystallite distribution around the POA and neglecting effects such as polarisation of the incident beam etc.). If the sample is rotated such that the POA is no longer along the incident beam, the intensity around the powder rings will vary, as discussed in the previous chapter. Clearly the crystal structure of the sample remains unchanged if the sample is rotated and any differences between data collected with the POA at different angles to the incident beam must result from the preferred orientation. Thus a technique, which collects data from crystallites at different orientations with respect to the incident beam, can be used to de-correlate the

influence of texture and crystal structure on the diffraction pattern. With a conventional detector, collecting sufficient data to model preferred orientation is very time-consuming, even from a sample of appreciable volume. Prior to the recent development of area detectors, obtaining enough data with a standard detector from a sample in a pressure cell to allow for texture modelling was impractical. The ability of an area detector to collect diffracted intensity from crystallites in many different orientations simultaneously makes texture modelling much quicker, which is important considering the limited signal intensity from a sample in a high-pressure cell. The high sensitivity of an image-plate allows good quality powder patterns from a typical sample to be obtained in times as short as 30 minutes. Using an area detector thus presents a practical opportunity to exploit the 2-D character of the effect of texture on the powder pattern to model the preferred orientation effects separately from a structural model (unlike in conventional Rietveld techniques). This can be very useful in structure solution and, since the model is dependant on the lattice type and (hkl) indices of the reflections, any such analysis acts as a powerful check on *ab initio* indexing.

This chapter presents a new 2-D preferred orientation model (suitable for the transmission geometry of a diamond-anvil pressure cell) which has been developed by the author for use with an Image Plate area detector. The model enables the effect of preferred orientation on the intensity at any point on any powder ring to be calculated. The effect on the whole powder ring is obtained by calculating (in turn) the effect at each point on the ring. In order to show that this model describes correctly the observed relative intensities, the model is compared to data obtained from a sample of known texture in different orientations with respect to the incident beam. The use of the model to calculate the distribution of crystallites and to correct the intensities of the reflections separately from a structural model is also discussed

4.2 Transmission Geometry

Figure 4.1a shows a set of orthonormal cartesian axes, which will be used in this thesis to describe the experimental geometry. The z-axis is defined as coincident with the (assumed horizontal) incident x-ray beam, the y-axis is in the same horizontal plane as the z-axis and the x-axis is vertical. Let the vectors **a**,**b**,**c** be unit vectors coincident with the x, y, z-axes respectively (in the rest of this chapter vector quantities will be shown in bold type).

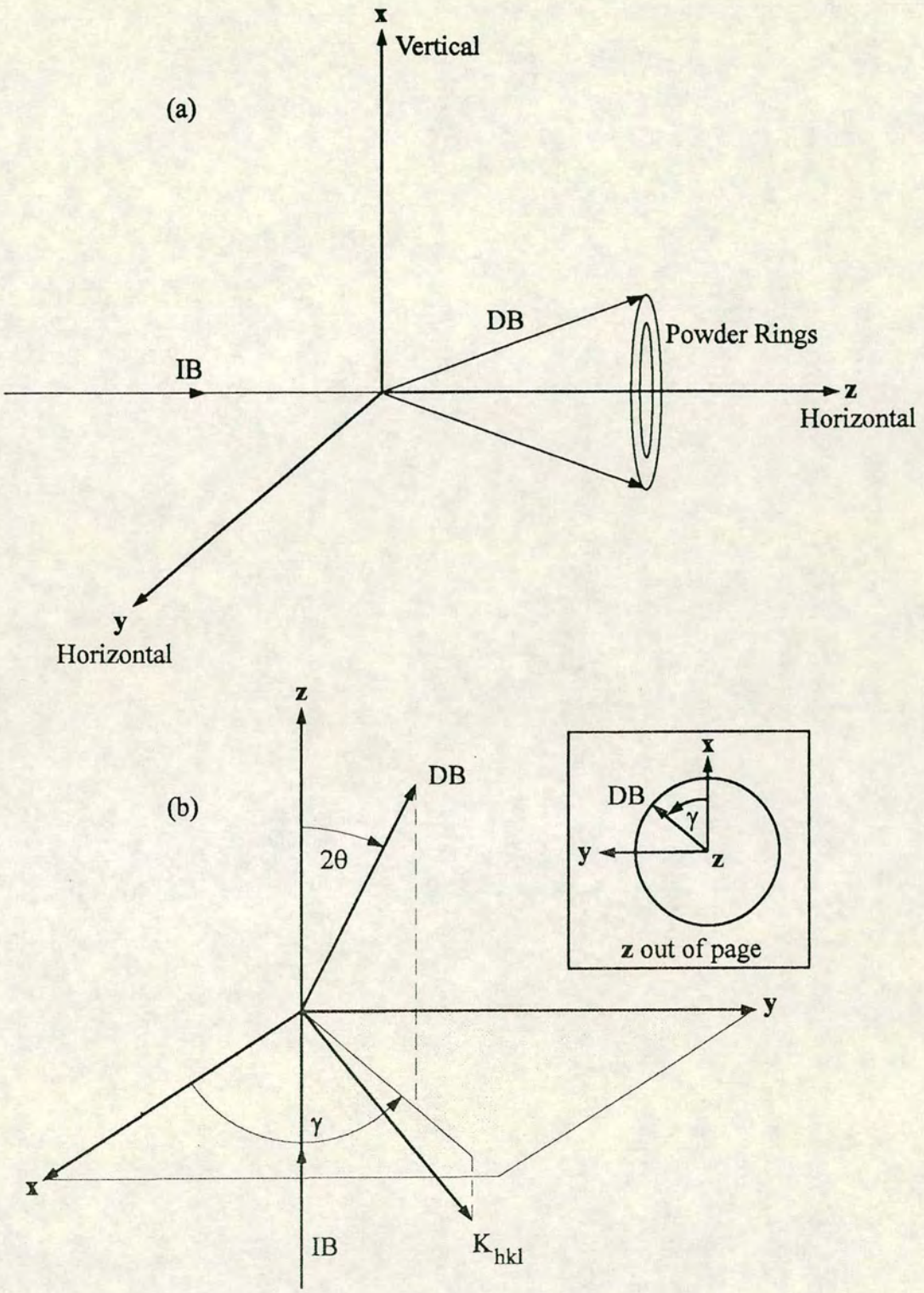

Figure 4.1 (a) The cartesian axes used to describe the experimental geometry. The z-axis is coincident with the incident beam (IB). (b) The diffraction geometry, from a different perspective to figure 4.1a.: **IB**=incident beam, **DB**=diffracted beam, $\mathbf{K_{hkl}}$ is the scattering vector of the (hkl) reflection. The boxed inset shows the view down the incident beam (z-axis). From the boxed inset, it can be seen that γ describes the angle of the diffracted beam around the powder ring.

Consider a general point on any powder ring. Figure 4.1b shows the orientation of the incident beam (**IB**), diffracted beam (**DB**) and scattering vector ($\mathbf{K_{hkl}}$) for diffraction at that point on the selected powder ring (the diagram is from a different perspective to that of figure 4.1a). Let θ be the scattering angle (as defined by Bragg's Law) and γ be the angle between the projection of the diffracted beam vector onto the x-y plane (shown shaded in figure 4.1b) and the x-axis. Since the diffracted beam, incident beam and scattering vector all lie in the same plane (from Bragg's Law), angle γ also describes the orientation of the scattering vector. The boxed inset in figure 4.1b shows the diffracted beam vector viewed down the z-axis. From this perspective it can be seen that the angle γ represents the angle around the powder ring (if γ=0, the diffracted beam and the scattering vector are in the x-z plane).

In terms of these coordinates, the diffracted beam (**DB**) and scattering vector (**K**) are given by

$$\mathbf{DB} = \mathbf{a}\sin(2\theta)\cos(\gamma) + \mathbf{b}\sin(2\theta)\sin(\gamma) + \mathbf{c}\cos(2\theta) \tag{4.1}$$

$$\mathbf{K} = \mathbf{a}\sin(90+\theta)\cos(\gamma) + \mathbf{b}\sin(90+\theta)\sin(\gamma) + \mathbf{c}\cos(90+\theta) \tag{4.2}$$

The last equation can be simplified to:

$$\mathbf{K} = \mathbf{a}\cos(\theta)\cos(\gamma) + \mathbf{b}\cos(\theta)\sin(\gamma) - \mathbf{c}\sin(\theta) \tag{4.3}$$

4.3 The Preferred Orientation Model

Most high-pressure experiments using DAC's are carried out with the pressure-cell axis aligned along the incident x-ray beam. However, the **POA** is not necessarily coincident with the pressure cell axis (perhaps because of misalignment of the diamond anvils) and so the **POA** may not be coincident with the incident beam. As it is the orientation of the **POA** relative to the incident beam that is important, the model is constructed in terms of the **POA** and not the pressure-cell axis. In addition, even if the **POA** is coincident with the pressure-cell axis, rotating the sample so that the incident beam strikes the crystallite distribution at an angle can be a powerful technique in helping to characterise any texture in the sample. Thus a general model, which allows any orientation of the **POA** with respect to the incident beam, is required.

The orientation of the **POA** with respect to the cartesian axes of figure 4.1a can be described by spherical polar coordinates (see figure 4.2a). Let β be the angle between the **POA** vector and the z-axis and let φ be the angle between the projection of the **POA** vector onto the x-y plane (shown shaded in figure 4.2a) and the x-axis. If φ=0, the **POA** vector is defined to lie in the x-z plane. In terms of these coordinates, the orientation of the **POA** can be expressed as :

$$\mathbf{POA} = \mathbf{a}\sin(\beta)\cos(\varphi) + \mathbf{b}\sin(\beta)\sin(\varphi) + \mathbf{c}\cos(\beta) \qquad (4.4)$$

where **a**,**b**,**c** are unit vectors along the x,y,z axes respectively.

As seen in chapter three, it is the orientation of the **POD** relative to the **POA** (defined by angle α in figure 4.2b) that determines the effect of the preferred orientation on the intensity at a given point on a powder ring. Now for a general (hkl) reflection, the scattering vector ($\mathbf{K_{hkl}}$) will be at angle ψ to the **POD**. As discussed in chapter three, the orientation of the scattering vector with respect to the incident beam is determined by Bragg's Law and so the **POD** must then lie somewhere on a cone (the **POD** cone) of half-angle ψ around $\mathbf{K_{hkl}}$. The angle α is different at each position on the **POD** cone, and so the average of the **POD** around the cone must be calculated. Giving the orientation of the **POD** relative to the axes of figure 4.1a is not trivial and so it is necessary to define a new set of axes, which are more naturally suited to describing the **POD**, and then transform between the two representations. A suitable choice (shown in figure 4.3a) can be obtained by defining: z' to be coincident with the scattering vector ($\mathbf{K_{hkl}}$), y' to lie at angle θ to the incident beam (and thus the z-axis) with the projection of y' onto the x-y plane lying at angle γ to the x-axis (i.e. y' lies in the same plane as the **IB**, **DB** and $\mathbf{K_{hkl}}$) and x' in the x-y plane at angle ($\pi/2$-γ) to the −x-axis. Also define a set of unit vectors **a'**, **b'**, **c'** which lie coincident with the x', y', z' -axes respectively. This implies

$$\mathbf{a'} = -\mathbf{a}\sin(\gamma) + \mathbf{b}\cos(\gamma) \qquad (4.5)$$

$$\mathbf{b'} = \mathbf{a}\sin(\theta)\cos(\gamma) + \mathbf{b}\sin(\theta)\sin(\gamma) + \mathbf{c}\cos(\theta) \qquad (4.6)$$

$$\mathbf{c'} = \mathbf{a}\cos(\theta)\cos(\gamma) + \mathbf{b}\cos(\theta)\sin(\gamma) - \mathbf{c}\sin(\theta) \qquad (4.7)$$

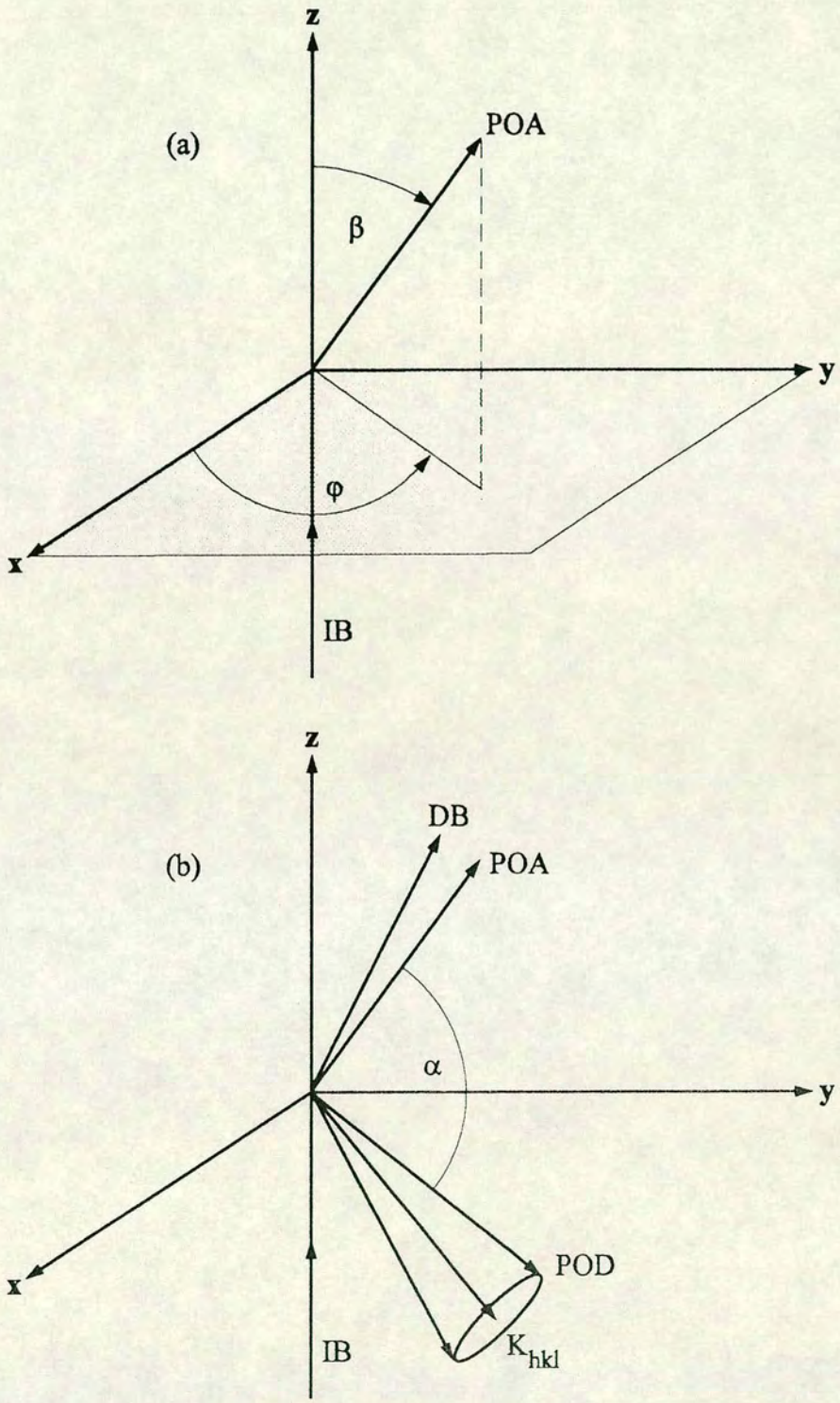

Figure 4.2 (a) The orientation of the **POA** vector with respect to the incident beam. β is the angle between the **POA** and the z-axis and φ the angle between the projection of the **POA** onto the shaded x-y plane and the x-axis. (b) The orientation of the **POD** cone with respect to the **POA**. Angle α is defined to be the angle between the **POA** and the **POD**.

The orientation of the **POD** with respect to these new axes (see figure 4.3b) can be described by defining spherical polar coordinates ψ and δ, where ψ is defined to be the angle between the **POD** and the z'-axis (and hence the angle between the **POD** and $\mathbf{K_{hkl}}$) and δ is the angle between the projection of the **POD** onto the x'-y' plane (shown shaded in figure 4.3b) and the x'-axis. If δ=0, the **POD** lies in the x'-z' plane. In terms of these coordinates the **POD** is given by

$$\mathbf{POD} = \mathbf{a'}\sin(\psi)\cos(\delta) + \mathbf{b'}\sin(\psi)\sin(\delta) + \mathbf{c'}\cos(\psi) \tag{4.8}$$

The transformation of the axes from x,y,z to x',y',z' can be written as

$$\begin{pmatrix} x' \\ y' \\ z' \end{pmatrix} = \begin{pmatrix} -\sin(\gamma) & \cos(\gamma) & 0 \\ \sin(\theta)\cos(\gamma) & \sin(\theta)\sin(\gamma) & \cos(\theta) \\ \cos(\theta)\cos(\gamma) & \cos(\theta)\sin(\gamma) & -\sin(\theta) \end{pmatrix} \begin{pmatrix} x \\ y \\ z \end{pmatrix} \tag{4.9}$$

or

$$\mathbf{x'} = \mathbf{L}\mathbf{x} \tag{4.10}$$

Since the components of a vector transform by the same transformation law as the axes the **POD** can be expressed in terms of the original x,y,z axes as

$$\mathbf{POD} = \mathbf{L}^{-1} \begin{pmatrix} \sin(\psi)\cos(\delta) \\ \sin(\psi)\sin(\delta) \\ \cos(\psi) \end{pmatrix} \tag{4.11}$$

which implies that

$$\begin{aligned} \mathbf{POD} = \mathbf{a}[&-\sin(\gamma)\sin(\psi)\cos(\delta) + \sin(\theta)\cos(\gamma)\sin(\psi)\sin(\delta) + \cos(\theta)\cos(\theta)\cos(\gamma)\cos(\psi)] + \\ &\mathbf{b}[\cos(\gamma)\sin(\psi)\cos(\delta) + \sin(\theta)\sin(\gamma)\sin(\delta) + \cos(\theta)\sin(\gamma)\cos(\psi)] \\ &+\mathbf{c}[\cos(\theta)\sin(\psi)\sin(\delta) - \sin(\theta)\cos(\psi)] \end{aligned} \tag{4.12}$$

Now from equation 4.4

$$\mathbf{POA} = \mathbf{a}\sin(\beta)\cos(\varphi) + \mathbf{b}\sin(\beta)\sin(\varphi) + \mathbf{c}\cos(\beta) \tag{4.13}$$

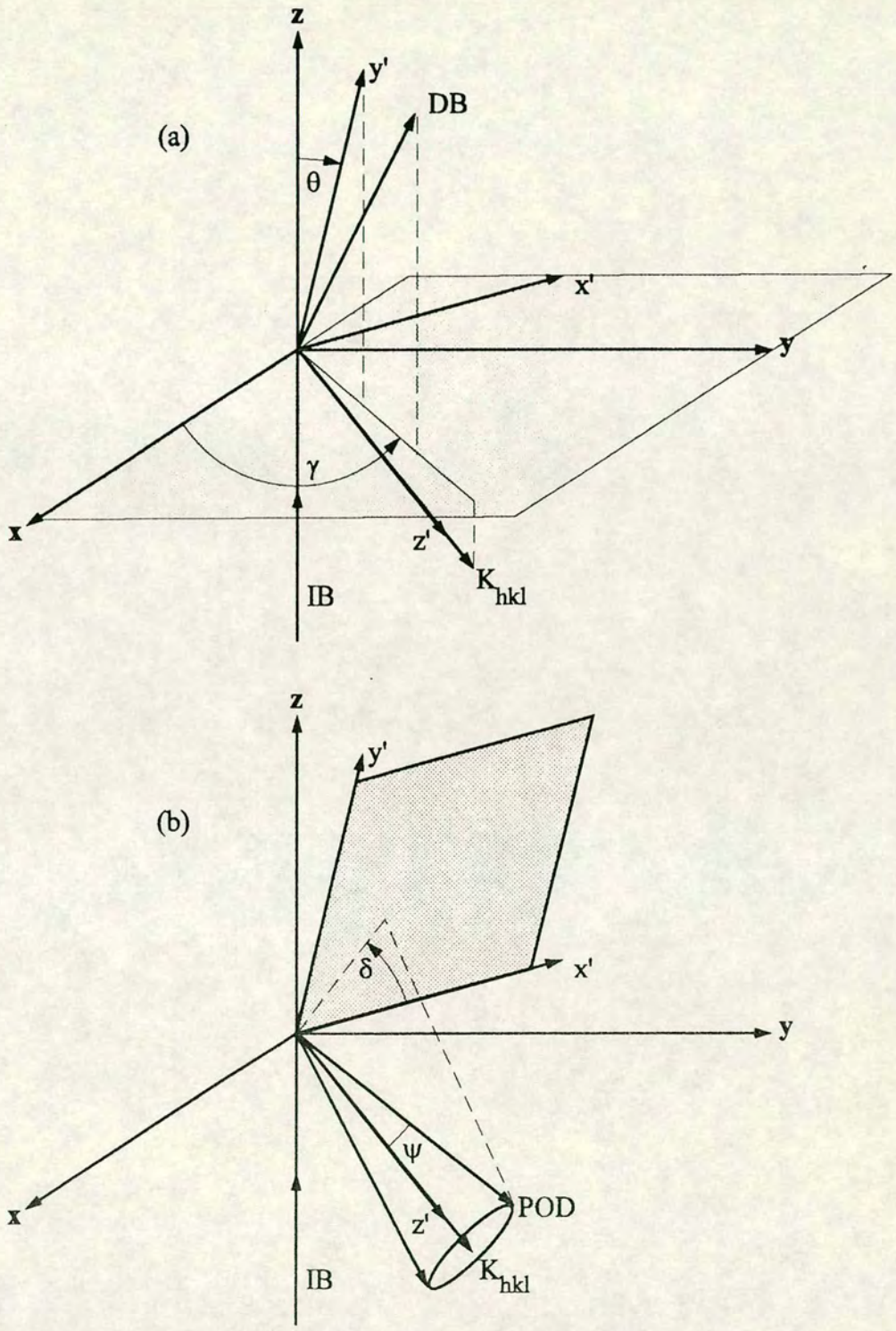

Figure 4.3 (a) The orientation of the new cartesian axes x',y',z' relative to the axes x,y,z. y' is chosen to lie at angle θ (the Bragg angle) to the z-axis and to lie in the same plane as the diffracted beam (**DB**) and the scattering vector $\mathbf{K_{hkl}}$ (i.e. the projection of y' onto the x-y plane lies at angle γ to the x-axis). z' is defined to be coincident with $\mathbf{K_{hkl}}$. x' is then chosen to make up an orthonormal set. (b) The **POD** relative to the new axes x',y',z'. ψ is the angle between the **POD** and the z'-axis and δ the angle between the projection of the **POD** onto the shaded x'-y' plane and the x'-axis.

A simple dot product of the **POD** and **POA** vectors gives (since both are unit vectors)

$$\cos(\alpha) = \begin{pmatrix} \sin(\beta)\cos(\varphi) \\ \sin(\beta)\sin(\varphi) \\ \cos(\beta) \end{pmatrix} \cdot \begin{pmatrix} -\sin(\gamma)\sin(\psi)\cos(\delta) + \sin(\theta)\cos(\gamma)\sin(\psi)\sin(\delta) + \cos(\theta)\cos(\gamma)\cos(\psi) \\ \cos(\gamma)\sin(\psi)\cos(\delta) + \sin(\theta)\sin(\gamma)\sin(\psi)\sin(\delta) + \cos(\theta)\sin(\gamma)\cos(\psi) \\ \cos(\theta)\sin(\psi)\sin(\delta) - \sin(\theta)\cos(\psi) \end{pmatrix}$$

-(4.14)

which implies

$$\begin{aligned} \cos(\alpha) = \sin(\beta)\cos(\varphi)[-\sin(\gamma)\sin(\psi)\cos(\delta) + \sin(\theta)\cos(\gamma)\sin(\psi)\sin(\delta) + \cos(\theta)\cos(\gamma)\cos(\psi)] + \\ \sin(\beta)\sin(\varphi)[\cos(\gamma)\sin(\psi)\cos(\delta) + \sin(\theta)\sin(\gamma)\sin(\psi)\sin(\delta) + \cos(\theta)\sin(\gamma)\cos(\psi)] \\ +\cos(\beta)[\cos(\theta)\sin(\psi)\sin(\delta) - \sin(\theta)\cos(\psi)] \end{aligned}$$

-(4.15)

This gives the values of $\cos(\alpha)$ at any point on the cone, which the **POD** describes. From this the average value of the probability around the cone, $\langle P(\alpha) \rangle$, can be calculated by integrating $P(\alpha)$ over the cone (usually numerically). If the function chosen to model the distribution of crystallites is the March-Dollase function (as in this thesis) then the integral is

$$< P(a) >= \frac{1}{t} \oint_{2\pi} [R^{-1}\sin^2(\alpha) + R^2\cos(\alpha)]^{-1.5} ds \qquad (4.16)$$

where R is the refinable parameter in the March-Dollase function, s is a parameter which describes the path around the cone and t is the total path length around the cone.

Now, t is given by

$$t = 2\pi\sin(\psi) \qquad (4.17)$$

and since

$$ds = \sin(\psi)d\delta \qquad (4.18)$$

the integral can be evaluated as

$$< P(\alpha) >= \frac{1}{2\pi} \int_0^{2\pi} [R^{-1} \sin^2(\alpha) + R^2 \cos(\alpha)]^{-1.5} d\delta \qquad (4.19)$$

Therefore, as seen in chapter three, the intensity observed at that point on the powder ring is given by:

$$I_{observed}(hkl) = I_{true}(hkl) \sum_{M(hkl)} \frac{< P(\alpha) >}{M(hkl)} \qquad (4.20)$$

where $I_{observed}(hkl)$ is the observed intensity of the powder ring from (hkl) reflection, $I_{true}(hkl)$ is the intensity of the (hkl) powder ring from an ideal randomly oriented sample of that volume, M(hkl) is the multiplicity of the (hkl) reflection and $<P(\alpha)>$ is the average value of the normalised distribution for that point on the powder ring. The sum in equation 4.20 is over all members of the multiplicity set. Unless the **POA** is one of the principal lattice vectors, $<P(\alpha)>$ will be different for each member of the multiplicity set and so it is vital to carry out the summation in equation 4.20.

Note that for a particular point on a given powder ring the following are fixed: the angles (β and φ), which describe the orientation of the **POA** with respect to the incident beam, the angle around the powder ring (γ), the angle between the scattering vector of that reflection, $\mathbf{K_{hkl}}$, and the **POD** (ψ), and the diffraction angle (θ). If the sample orientation is kept fixed, the correction for the same point on a different powder reflection involves the same β, φ and γ angles but different values of ψ and θ.

4.4 The simple case of the POA parallel to the Incident Beam

If the **POA** is parallel to the beam (β=0) then equation 4.15 simplifies greatly to

$$\cos(\alpha) = [\cos(\theta)\sin(\psi)\sin(\delta) - \sin(\theta)\cos(\psi)] \qquad (4.21)$$

It can be seen that, in contrast to Bragg-Brentano geometry, the observed intensity from a textured sample measured in transmission geometry will depend on the diffraction angle. As expected, the contribution of different positions of the **POD** to a given reflection is no longer constant (as is shown by the dependance on the δ angle) and so it is vital to carry out the integration over the **POD** cone as described above.

Notice that in this special case there is no dependence on the angle around the powder ring (γ). This means that, at any point on a given ring, the intensity will be constant and so the influence of the texture is seen only in the change to the relative intensity between powder rings compared to the relative intensities expected from an ideal sample. In collaboration with R. B. Von Dreele, this simplified model has been programmed into the Rietveld refinement program GSAS (Von Dreele and Larson, 1985).

In order to test this simplified model for use in Rietveld refinement, diffraction data were collected from a sample of known preferred orientation. The sample, kindly supplied by R. B. Von Dreele, was fine grained alumina (Al_2O_3) compressed into a cylindrical flat-plate of thickness 1.5mm. The strong compression during preparation induced strong orientation into the sample, which was known (Von Dreele, (1993)) to have the (001) scattering vector (the **POD**) preferentially aligned perpendicular to the flat-plate normal (the **POA** is coincident with the normal to the flat-plate). The sample was mounted on a lead frame to restrict the amount of fluorescence background from the Pt pinhole striking the image-plate. Data were collected with the **POA** coincident with the incident beam using the standard image-plate set-up on SRS station 9.1 as described in chapter two. In order to improve powder averaging and thus collect more reliable intensities the sample was oscillated ±4° throughout the exposure. The wavelength of the incident radiation was 0.4649A (determined from a standard silicon sample) and a 75μm Pt pinhole with a sample to plate distance of ~288mm was used. Figure 4.4 shows the average 1-D profile (processed using the PLATYPUS package) from this (alumina) sample collected in 20 minutes.

Al_2O_3 has a hexagonal crystal structure (space group R-3C) with six formula units in each unit cell. The structure is made up of oxygen atoms in layers (three atoms in each layer) arranged in an approximate equilateral triangle about the crystallographic c-axis. Between each layer of three oxygen atoms is a single Al atom. Each atom type has a single free fractional coordinate, the others being fixed by symmetry (Lewis, (1982)). The fit to the data from a full least-squares refinement of the structural parameters, scale factor, background and peak shape parameters is also shown in figure 4.4. The fit is obtained with the (001) scattering vector ($\mathbf{K_{001}}$) chosen as the **POD**. The refined texture parameter of R=0.608(1) indicates that there is a high probability (as expected) of finding an (001) scattering vector in a given crystallite along the incident beam. This means that reflections close to the (001) in reciprocal space will be measured as weak (compared to an ideal sample) and reflections such as

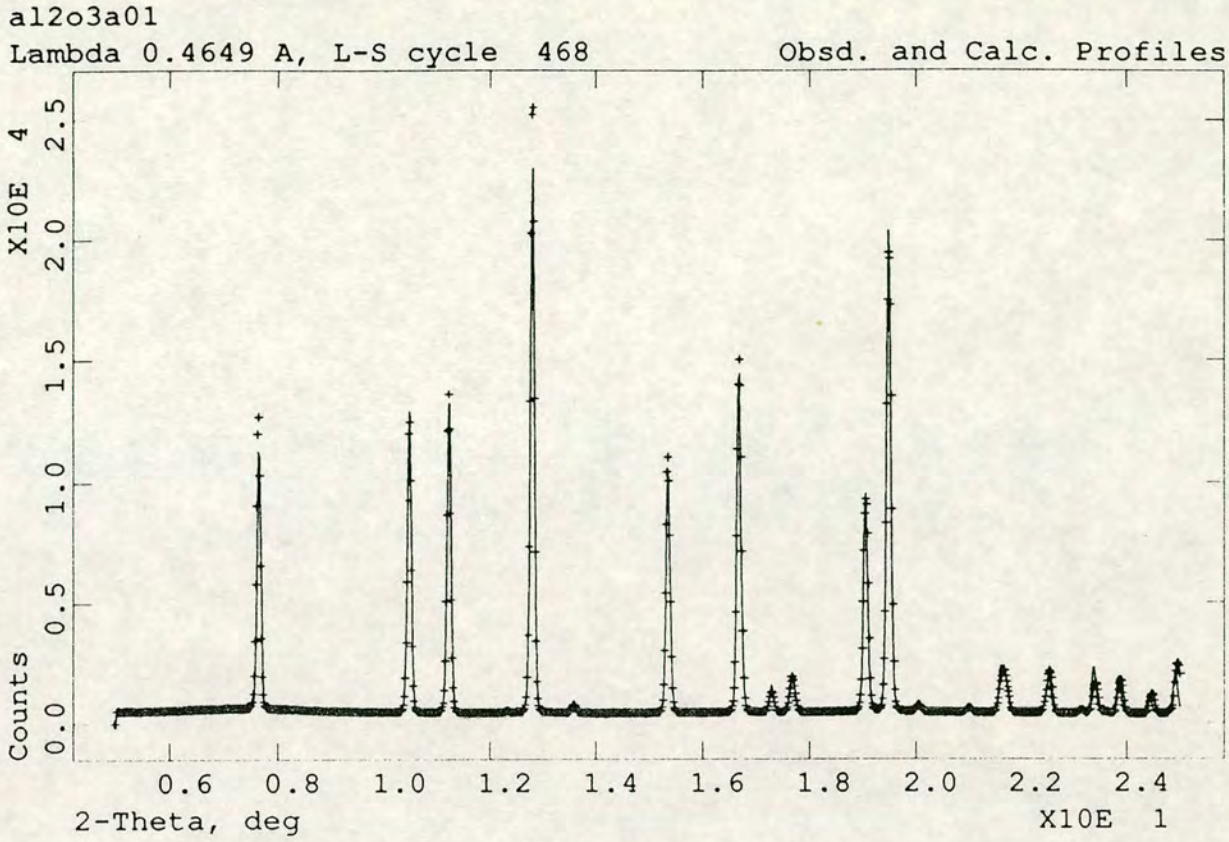

Figure 4.4 The Alumina data collected with the **POA** parallel to the incident beam. Also shown is the calculated intensity from Rietveld refinement of the crystal structure, lattice parameters, peak-shape parameters and preferred orientation model developed in this chapter.

the (110) which lie far from the (001) will be measured too strong. Despite the considerable texture of the sample (R=1 in an ideal non-textured sample), this model is able to fit the intensities reasonably correctly and gives refined fractional coordinates which compare well to the published single crystal values (see table 4.1). Thus, in the simple case of the **POA** being parallel to the incident beam (β=0°) the model developed here is able to describe accurately the intensity from the textured alumina sample. In addition the model gives a physically meaningful description, which matches the known texture in this material, of the crystallite distribution.

	This study	Single crystal values (Lewis, (1982))
Al at (0, 0, u)	u=0.352(2)	u=0.35200(7)
O at (v, 0, 1/4)	v=0.693(2)	v=0.69360(30)

Table 4.1 A comparison of the refined fractional coordinates for Alumina obtained from using this model with an orientated powder and published single crystal values.

4.5 The POA at an angle to the Incident Beam

In the general case ($\beta \neq 0°$), the angle α (and consequently the value of the preferred orientation correction) has a dependence upon the angle (γ), which describes the position of the diffracted beam around the powder ring. Thus, the intensity around the powder rings will not be constant if the **POA** is not coincident with the direct beam. In order to test accurately the texture model described in this chapter, experiments were performed using an alumina sample with the **POA** in a range of orientations with respect to the incident beam. The sample used in section 4.4 is a flat-plate sample, which is not suitable for this kind of experiment. If such a sample was rotated with respect to the incident beam, the sample thickness encountered by the incident beam would change with sample orientation, inducing effects such as peak broadening in the powder pattern.

Thus, two new samples were prepared by carefully cutting a small cylinder from the central section of other Alumina flat-plate samples. Each sample was then trimmed under a microscope until its shape was a small cylinder of diameter 1mm and height 5mm. The cutting of the cylinder was performed such that the **POA** (previously the flat-plate normal) was perpendicular to the axis of the cylinder. The **POA** of the flat-plate was carefully marked, so that the orientation of the **POA** in the cylindrical sample was accurately known. The sample used in a particular data collection was then mounted onto a standard goniometer with the cylinder axis perpendicular to the incident beam. The **POA** thus lay in the same horizontal plane as the incident beam, with which it could be easily arranged to be coincident (see figure 4.5). To check sample quality, data were collected from both samples using the rotation stage mount described in chapter 2 with the **POA** coincident with the incident beam (as in the previous section) and Rietveld refinement of the data performed. The refined

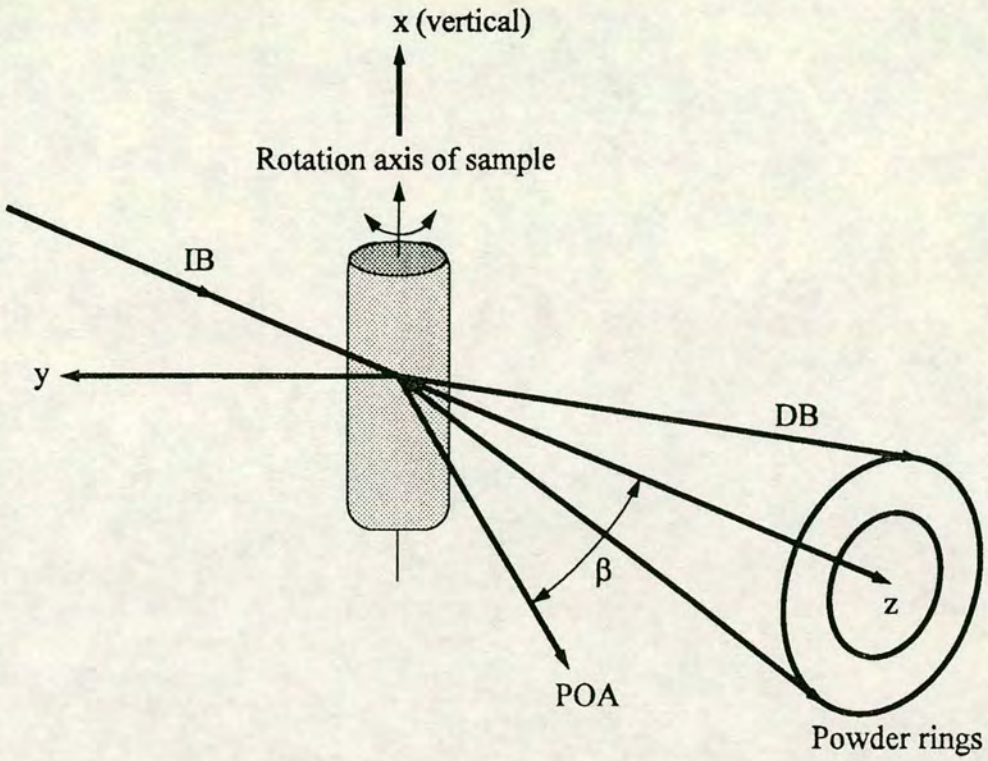

Figure 4.5 The arrangement of the sample in section 4.5. The incident beam and the **POA** both lie in the horizontal y-z plane. The rotation axis of the sample is vertical. Data were collected with various values of angle β between the **POA** and the incident beam. **IB**=incident beam, **DB**=diffracted beam.

structural parameters from both samples were within the estimated errors on the values given in section 4.4. The refined preferred orientation parameters using the model of section 4.4 were R=0.642 and R=0.603 for the first and second samples respectively.

The samples were then accurately aligned onto the rotation stage axis (as described in chapter 2). Because the orientation of the **POA** was known, data could be collected with various angles between the **POA** and incident beam in the range $\beta=0°$ and $\beta=90°$ by simply turning the rotation stage axis. With the **POA** in the horizontal plane, φ is fixed at $\varphi = \pm 90°$ (see figure 4.2). For both samples, the sample was oscillated (by mechanically driving the axis of the rotation stage) $\pm 4°$ throughout data collection to improve powder averaging and thus collect more reliable intensities. Figure 4.6 shows 2-D images of the data from one of the samples collected at $\beta=0°$ and $\beta=90°$, on

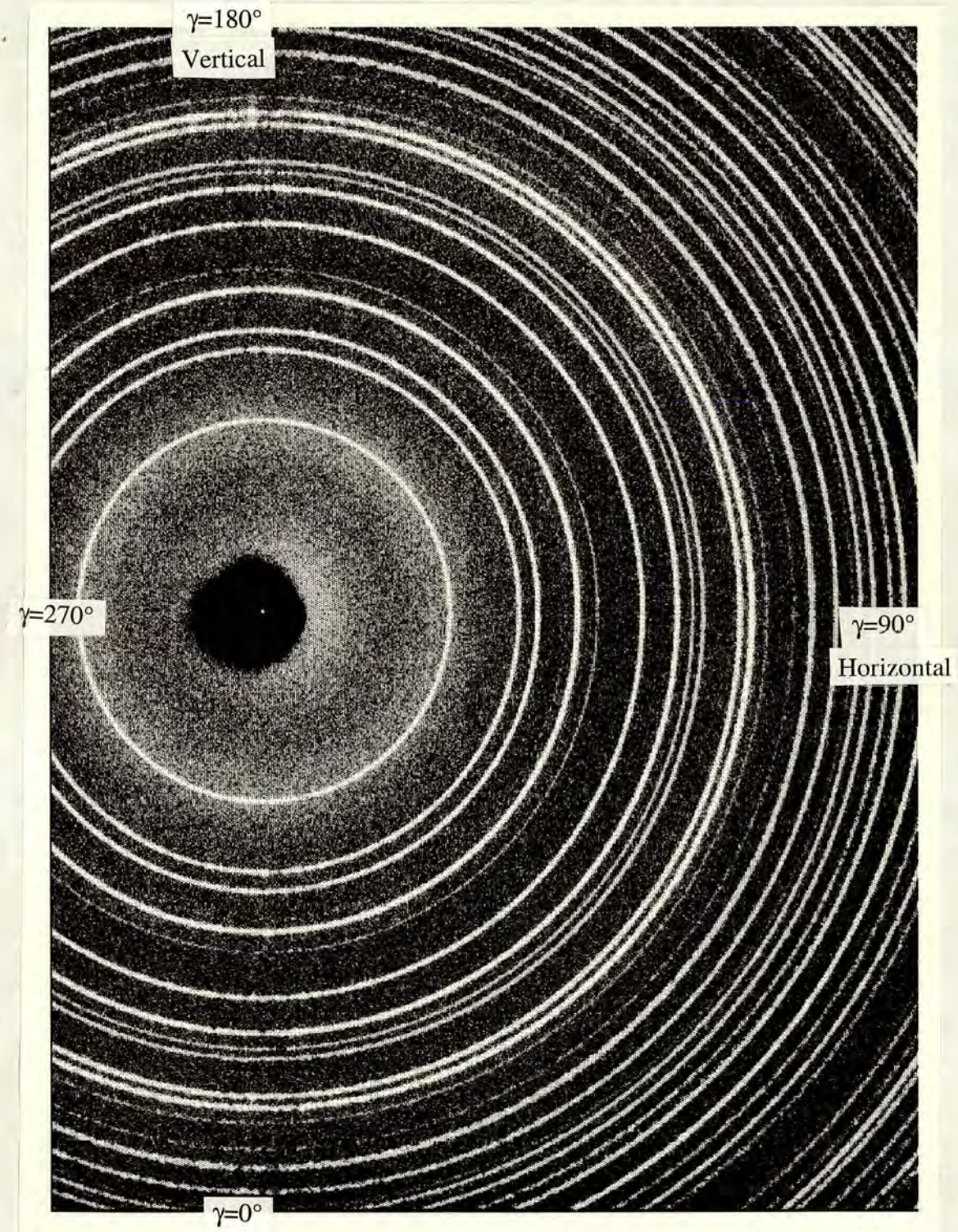

Figure 4.6 (a) 2-D image collected from the alumina sample with β=0° (the **POA** coincident with the incident beam. The values of the angle γ at **various** points on the powder ring are marked for ease of discussion.

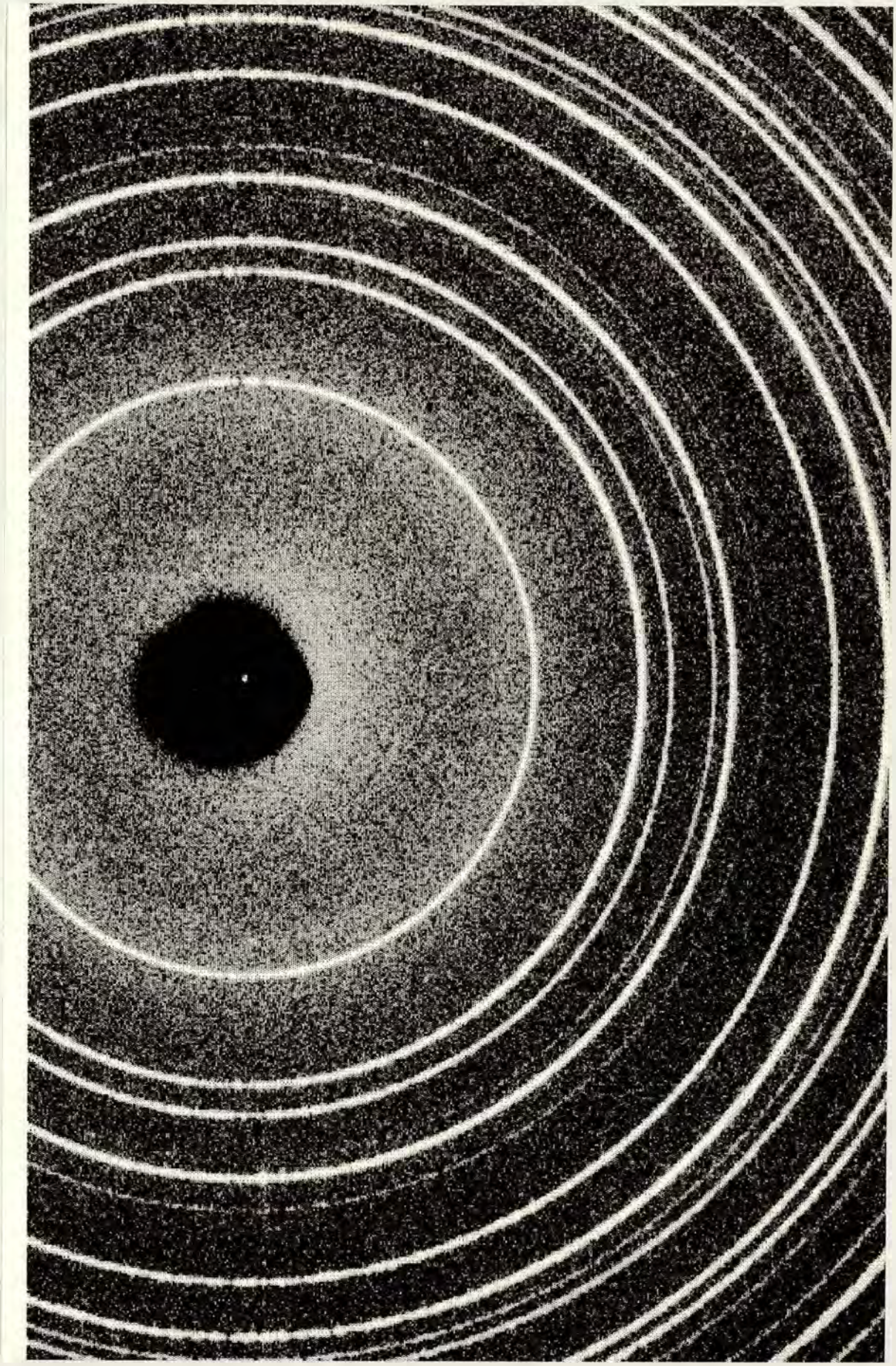

Figure 4.6 (b) 2-D image collected from the alumina sample with β=90° (the **POA** perpendicular to the incident beam

which are marked the gamma angles and the vertical and horizontal directions for ease of discussion. It is noticeable in both images that the data at γ=0° and γ=180° is slightly spotty. As the sample was oscillated about the vertical axis, the scattering vectors at the points on the powder rings that correspond to the vertical axis received little effective motion. Thus at γ=0° and γ=180° the powder averaging was poorer and the pattern is uneven. At the γ=90° and γ=270° positions, the sample received the maximum oscillation and more crystallites were able to contribute to the diffraction pattern. Hence the powder pattern is much smoother at these points. The image at β=90° shows the characteristic pattern of intensity variation around the powder ring expected from a textured sample with the **POA** at an angle to the incident beam.

The intensity around the powder ring was extracted by sectoring the data into 6° segments (in γ) and averaging over the data points in that sector to produce a profile of that sector. The integrated intensities were extracted by fitting an analytic peak-shape (a pseudo-voigt function) to the sectored profile (as described in chapter 2). Figure 4.7 shows the integrated intensities around the (104) and (110) powder rings for $\beta \approx 0°$, 30°, 50°, and 90° from the first sample. As expected the amplitude of intensity variation around the rings is almost zero for β=0° and increases with increasing β angle. Note that as expected from the phenomenological discussion of chapter 3, the intensity of the (104) reflection (whose scattering vector lies at a low ψ angle to the **POD**) grows in intensity with respect to the (110) reflection (whose scattering vector lies at a high ψ angle to the **POD**) as the angle between the **POA** and the incident beam increases. The results from the second sample showed similar changes in intensity as the orientation of the sample was altered.

Also shown on figure 4.7 is the calculated intensity for these reflections at the relevant angles. The calculated curves are obtained by assuming the single-crystal structural parameters (i.e. the ratio of the reflection intensities in an ideal randomly oriented sample) and a scale factor for each data set at a particular angle. It is necessary to assume a separate scale factor for each data set as it is difficult to correct the data accurately for changes in exposure time and synchrotron current. The value of the scale factor at each β angle has been chosen to optimise the match between the observed and calculated values. The calculated intensity is computed from the formula

$$I_{calculated}(hkl) = (\text{Scale factor}).I_{true}(hkl)\sum_{M(hkl)}\frac{<P(\alpha)>}{M(hkl)} \qquad (4.22)$$

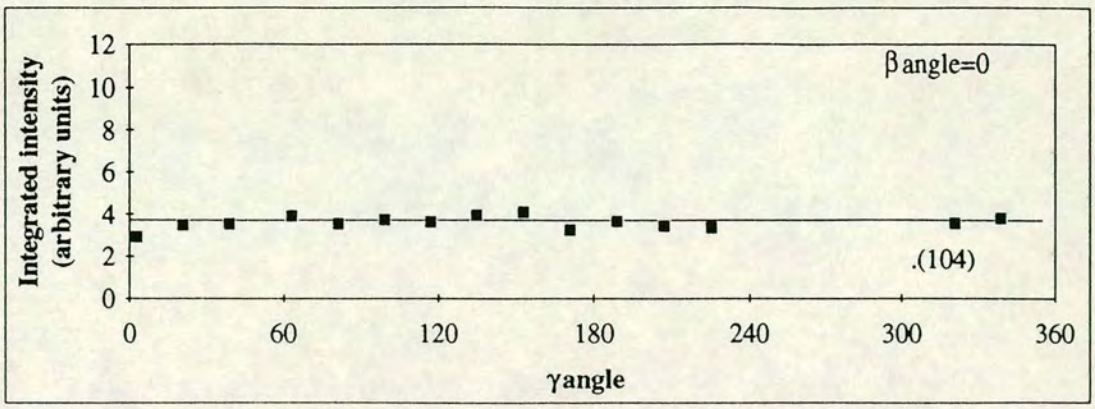

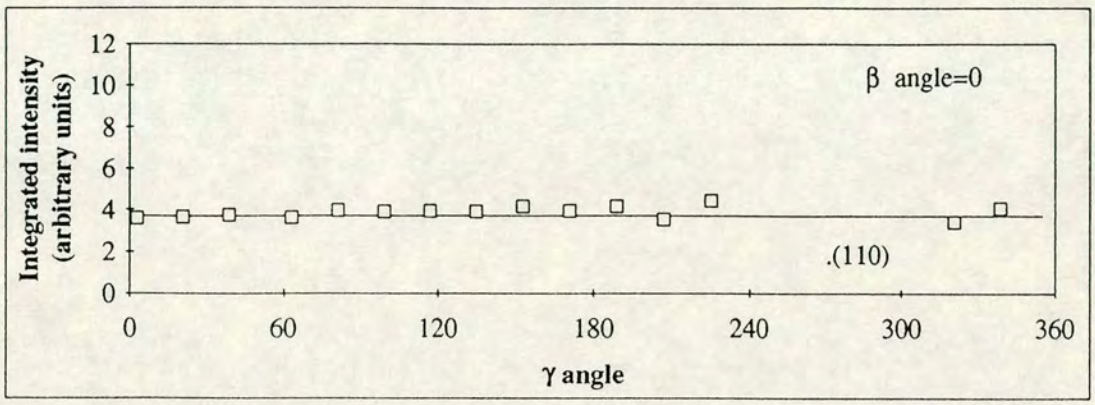

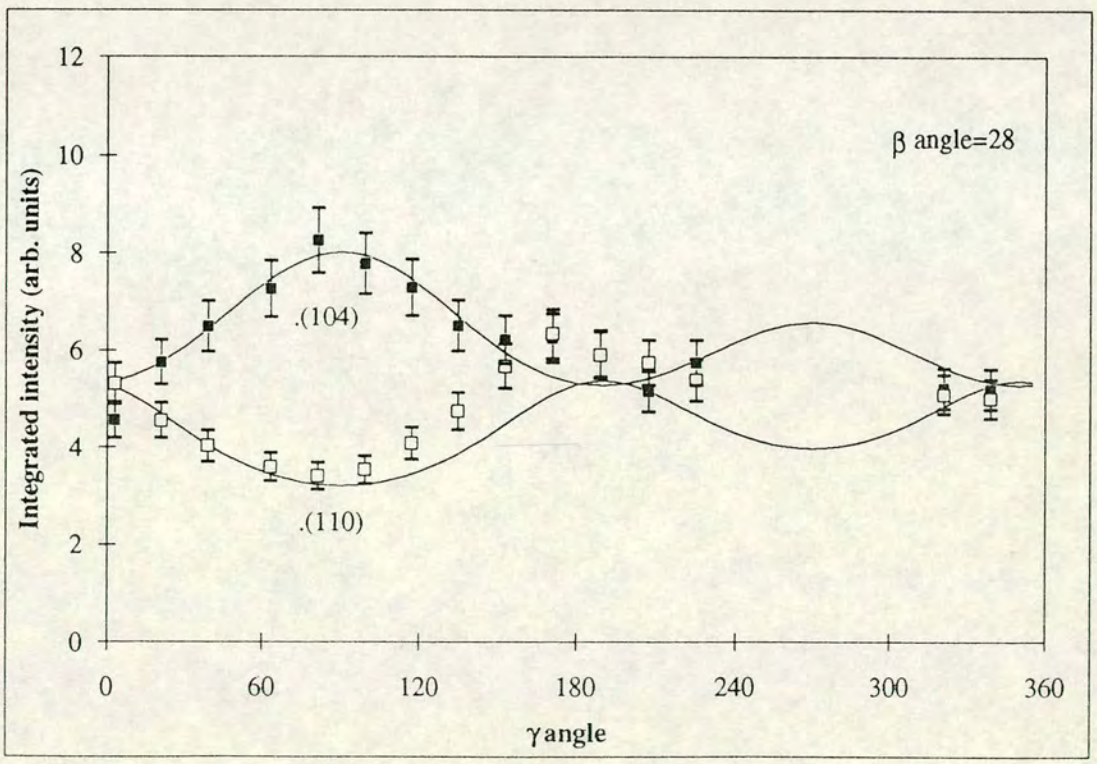

Figure 4.7 The observed and calculated intensities (shown as a solid line) of the (104) and (110) reflections from alumina at different β angles. The calculated lines are obtained by using the known structural parameters for alumina and a single scale factor for each data set. The data are drawn over similar y-ranges to enable comparison of the intensity variations around the powder rings.

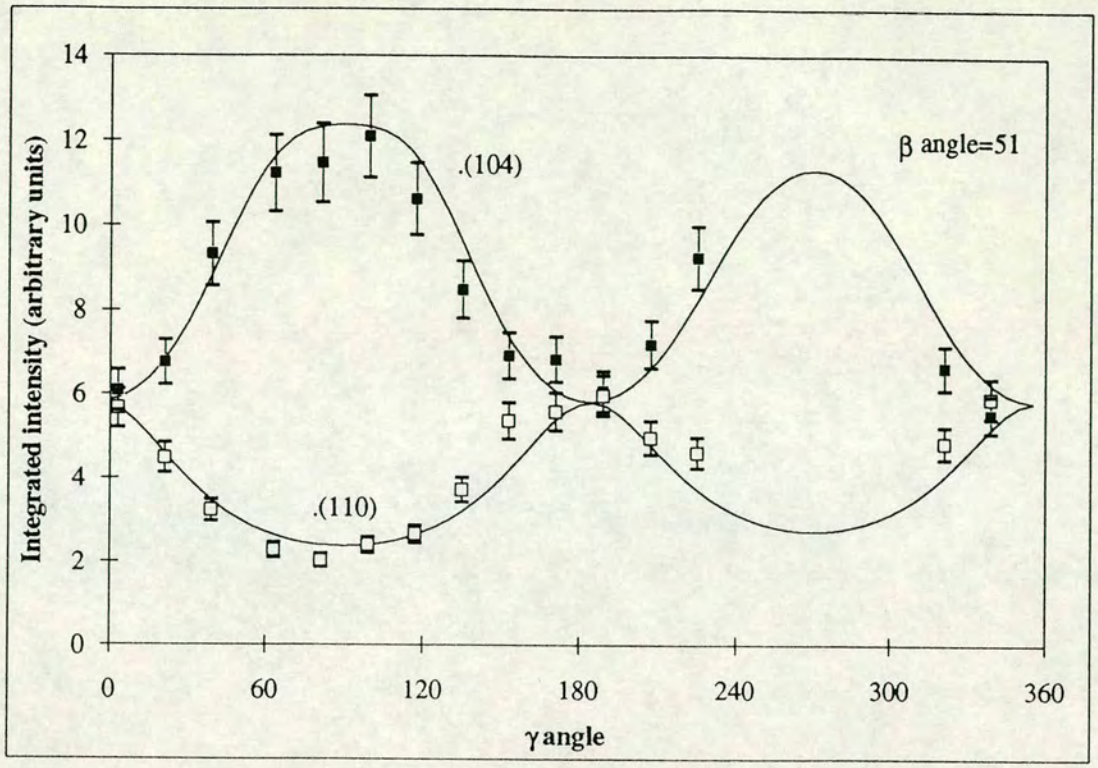

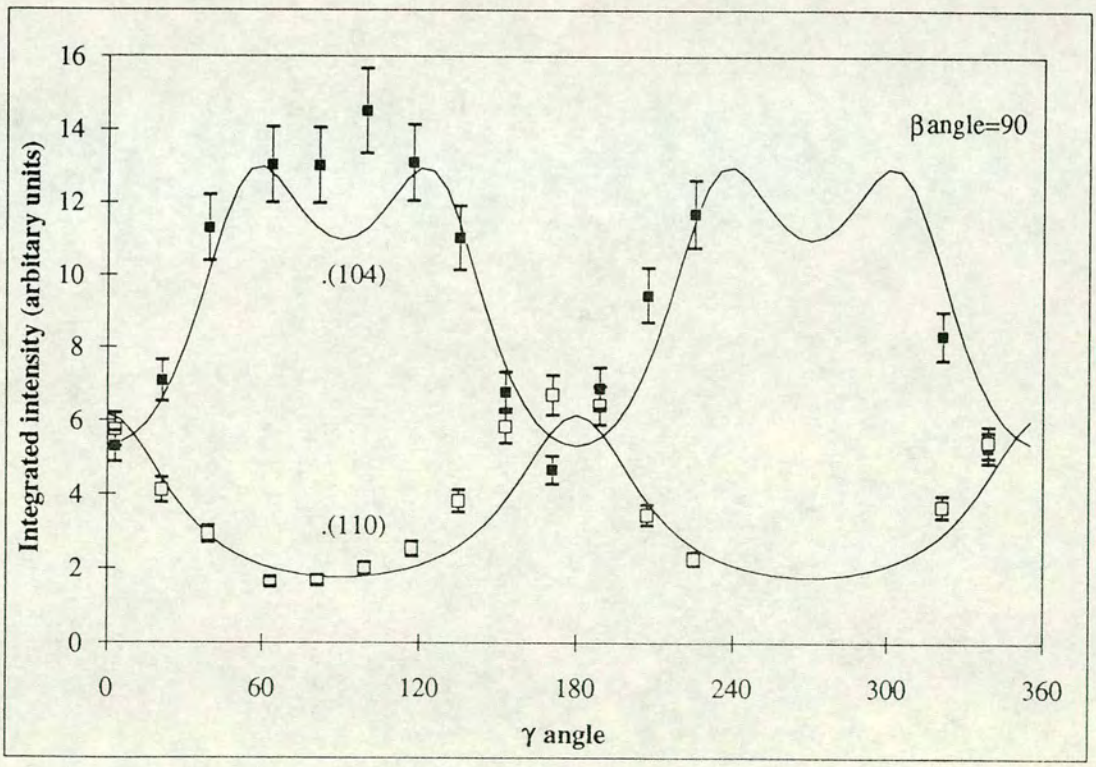

Figure 4.7 cont.

where $I_{calculated}(hkl)$ is the calculated intensity of the powder ring of the (hkl) reflection, $I_{true}(hkl)$ is the intensity of the (hkl) powder ring from an ideal randomly oriented sample of that volume (from the known structural parameters), M(hkl) is the multiplicity of the (hkl) reflection and $\langle P(\alpha) \rangle$ is the average value of the normalised distribution for that point on the powder ring. The sum in equation 4.20 is over all members of the multiplicity set. $\langle P(\alpha) \rangle$ is computed from the texture model described in this chapter using the relevant values of the angles β, θ, ψ and the value of R obtained from the Rietveld refinement of the data at $\beta=0°$.

The agreement between the observed and calculated intensities can be seen to be good, especially in the data at lower β angles. However it is difficult to assess the errors in the observed data. The number of data points contributing to a given point in a sector depends slightly on the position on the image-plate (there are more data points at larger distances from the centre of the diffraction pattern) and so the error due to counting statistics on the data points will be slightly different in each powder ring. Because the exact relationship between the intensity recorded by the image-plate as a function of incident photons is not known, it is not possible to calculate the counting statistics contribution to the error in the data. However, at the level of integrated intensity in these data, the error due to counting statistics is almost certainly within the size of the symbols and thus the intensity in each sector is well determined. A more serious source of error is local sample inhomogeniety, which is hard to estimate. A measure of the error due to sample inhomogeniety can be obtained by calculating the standard deviation in the observed intensity between different sectors at $\beta=0°$. If a data point lies more than twice the standard deviation from the average around the ring, it is likely that the sample contained a significant clump of powder at that point, which can be checked by close visual examination of the image. In such a case that data point is discarded from the analysis. The standard deviation in the data shown in figure 4.7 is of the order of 8% and this is used as the error in the observed values at $\beta\neq0°$.

At higher β angles the calculated intensity matches the observed values less well but the basic form of the variation is adequately modelled. In general, this model describes well the variation in intensity as the sample is rotated, even though at high β angles the variation in intensity around the powder ring can be as much as a factor of two. At $\beta=90°$ the **POA** is perpendicular to the incident beam, which is analogous to Debye-Scherrer geometry (as seen in chapter three). Scanning with a conventional detector through a strip of a powder pattern with this degree of variation around the

ring would produce relative intensities, which would depend strongly on exactly where in the pattern the detector scanned.

4.6 Using the intensity variation around the powder ring to characterise the preferred orientation of the sample.

In the previous section, the known value of the preferred orientation parameter, R, was used to calculate the intensity around the powder rings. Conversely, the variation in intensity around the powder rings from a sample with its **POA** at an angle to the incident beam can be used to determine the texture of the sample. In contrast to using a texture model during Rietveld refinement, where the structural model is obtained with the texture model, this method requires no prior knowledge of the crystal structure other than the lattice parameters and indexing of the reflections. A single orientation parameter which describes sample texture is used to describe the variation in intensity around the powder rings. The other parameters in this technique are values for the 'true' intensities of the diffraction peaks. These 'true' intensities are the values predicted by the model for the reflection intensities which would occur from an ideal non-textured sample.

The method fits (by least-squares refinement) the texture model of section 4.3 to the observed intensity around all the powder rings from data collected with the **POA** at an angle to the incident beam. The calculated intensity is obtained in a similar manner to the preceding section, i.e.

$$I_{calculated}(hkl) = I_{true}(hkl)\sum_{M(hkl)} \frac{<P(\alpha)>}{M(hkl)} \qquad (4.23)$$

where $I_{calculated}(hkl)$ is the calculated intensity of the powder ring of the (hkl) reflection, $I_{true}(hkl)$ is the predicted intensity of the (hkl) powder ring from an ideal randomly oriented sample of that volume, M(hkl) is the multiplicity of the (hkl) reflection and $<P(\alpha)>$ is the average value of the normalised distribution for that point on the powder ring. $<P(\alpha)>$ is computed from the texture model described in this chapter using the relevant values of the angles β, θ, ψ and the refined preferred orientation parameter R. In equation 4.23, the scale factor used in equations 4.20 and 4.22 has been absorbed into the $I_{true}(hkl)$ term. Thus, the true intensities predicted by the model must be considered as relative intensities from a sample of unknown volume.

The standard method of non-linear least-squares refinement (Hamilton, (1964)) is used to optimise the fit of the calculated intensity to the observed data. This fit is performed by minimisation of the function F(R) where

$$F(r) = \sum w.\left(I_{observed} - I_{calculated}\right)^2 \qquad (4.24)$$

The sum is over all the observed data points and w are the weights for each data point. The weights are calculated in line with common practice in least-squares refinements as the inverse of the estimated standard deviations of the data points. This technique requires initial estimates of the preferred orientation parameter, R, and the 'true' intensities of the reflections, although these estimates can be very crude and can be obtained by trial and error if necessary. The optimisation, which iteratively produces better estimates of the values of R and the 'true' intensities, can be stopped when the required level of accuracy is obtained. Refinement of the texture model requires initial assumptions of the value of the ψ angles for the different reflections and the choice of one reflection for the **POD**. In essence, the first of these assumptions is equivalent to assuming the angles between the various diffracting planes and the **POD**, i.e. assuming an indexing of the diffraction pattern and values for the lattice parameters. The choice of a reflection to be the **POD** is less straight-forward. This can be performed by a trial-and-error approach, although the possible choices can be narrowed down considerably. As seen in the phenomenological treatment of chapter 3 and in the preceding section, reflections close to the **POD** are observed as diminished when the **POA** is along the incident beam. The observed reflection which is closest to that direction in the lattice which tends to align coincident with the **POA** (i.e. the **POD**) will be that reflection which experiences the largest increase in intensity as the **POA** is rotated away from the incident beam.

A computer program called 'Texture-Fit' was written by the author to perform the least-squares fit of the texture model to the intensity variation around the powder rings. Figure 4.8 shows the results of such a fit produced by 'Texture-Fit' to a selection of the reflections from the first sample of the preceding section. The data was collected with an angle of ~50° between the **POA** and the incident beam and the fit to the observed values can be seen to be consistently good. In order to increase the accuracy of modelling, it is advantageous to maximise the intensity variation around

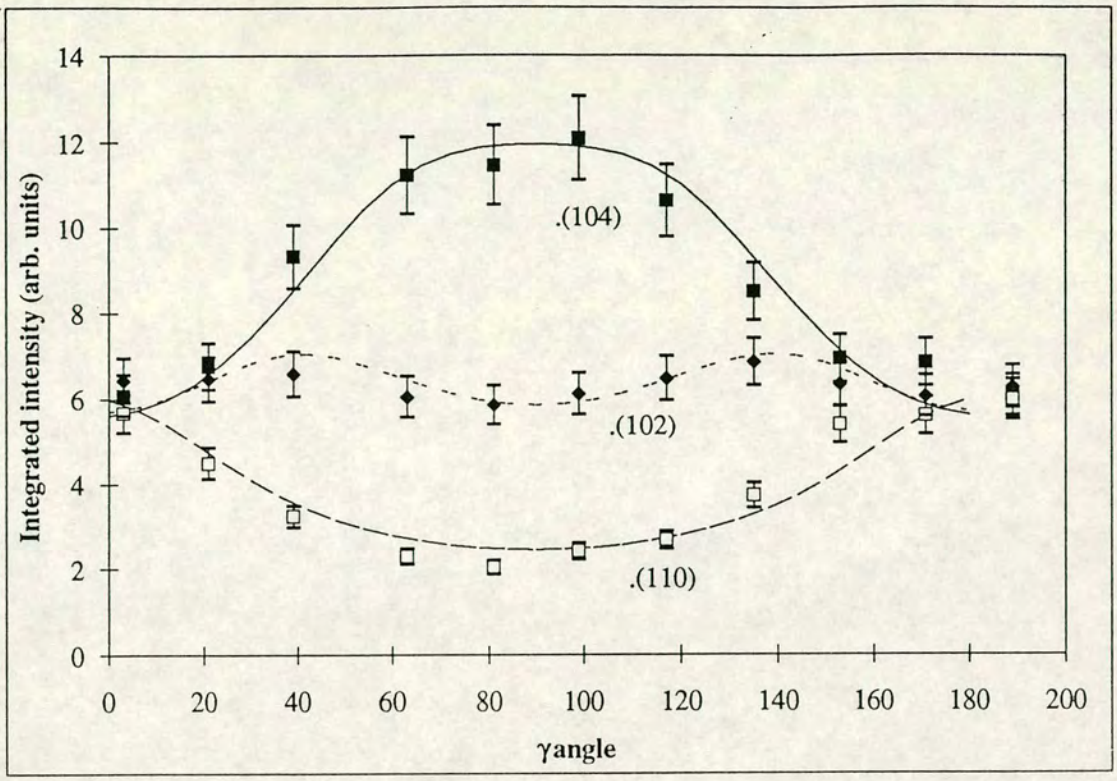

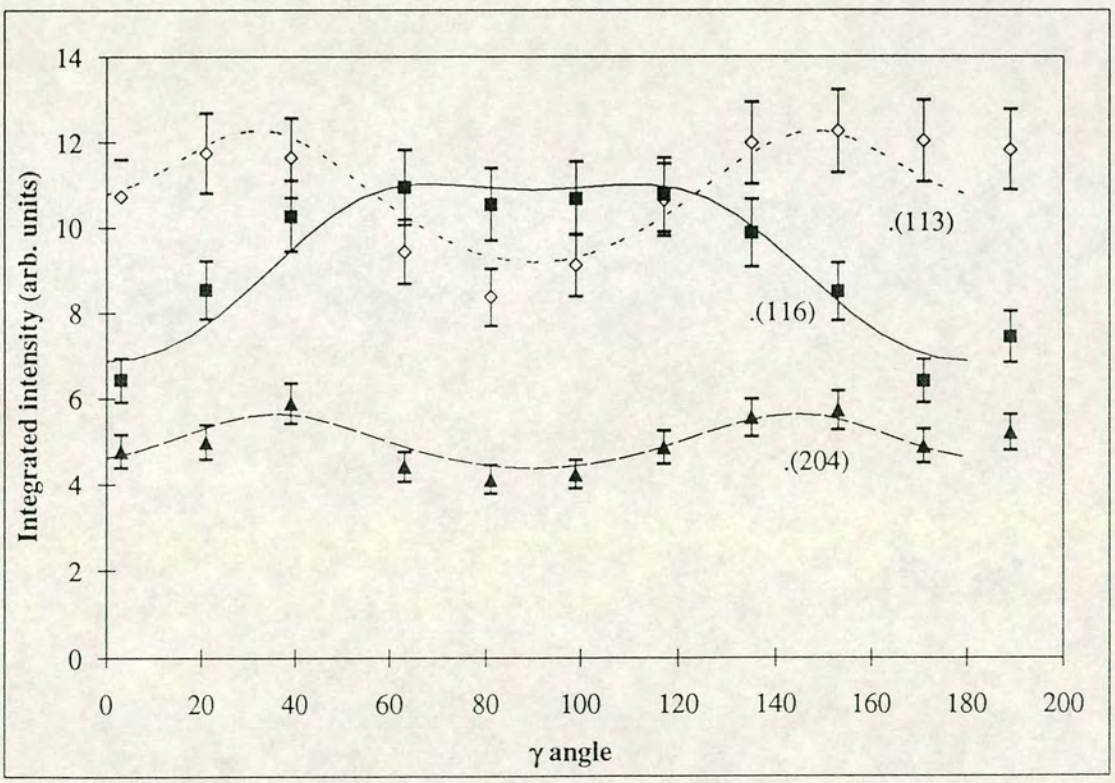

Figure 4.8 The observed and calculated integrated intensities of the reflections from the alumina sample versus angle γ (i.e. around the powder rings) for an angle of β=51° between the **POA** and the incident beam. The observed data is shown as points. The calculated line is obtained as described in the text.

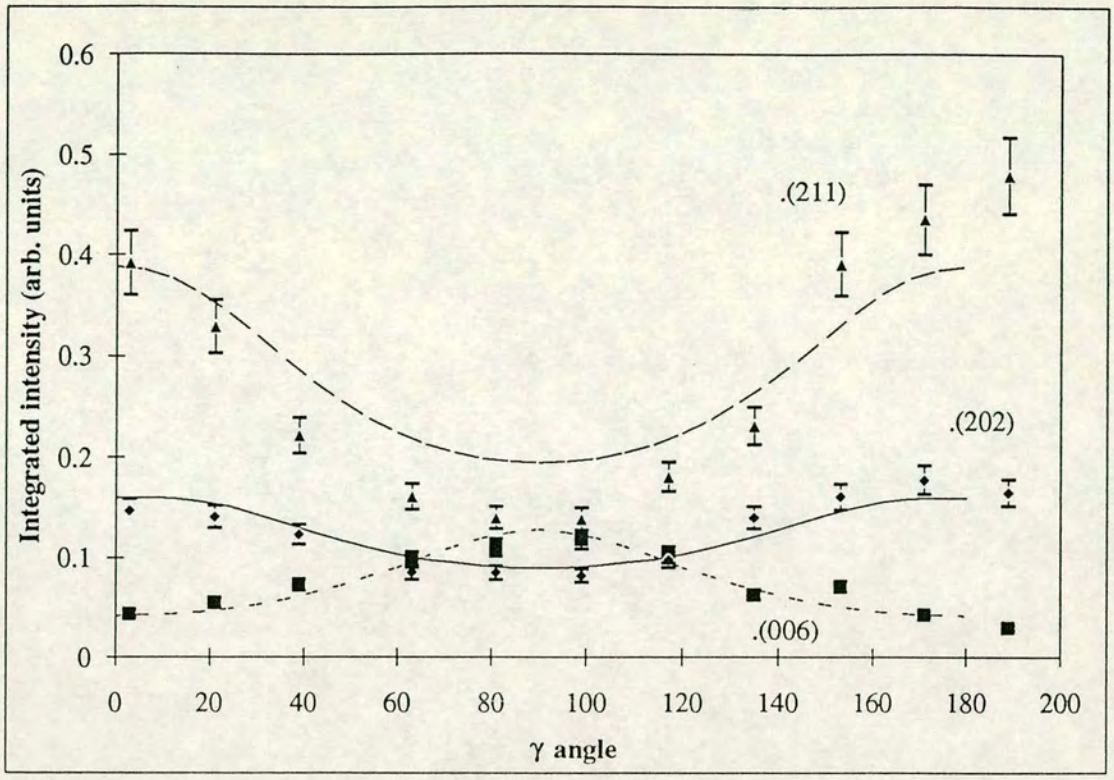

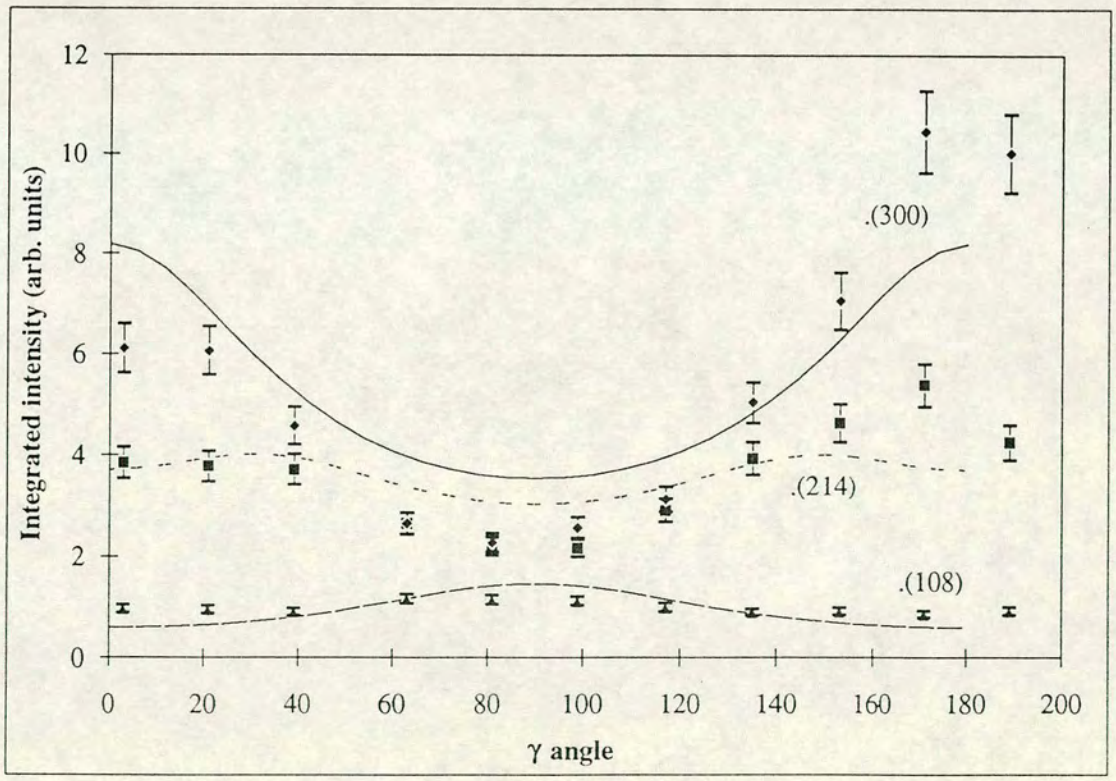

Figure 4.8 cont.

r=0.637	phi angle ψ	Intensity observed at $\beta=0°$	Intensity from ideal sample (I_{ideal})	Predicted Intensity from this model (I_{true})
102	57.62	4.62	7.5	5.70
104	38.29	4.73	9.0	7.81
110	90	5.02	4.0	3.65
006	0	<1	<1	0.07
113	61.23	10.0	10.0	10.0
202	71.96	0.13	0.2	0.12
204	57.62	4.44	4.5	4.57
116	47.8	6.65	8.0	8.32
211	78.66	0.38	0.4	0.26
212/108	68.13/11.11	0.81	1.4	1.05
214	64.40	4.50	3.0	3.25
300	90.0	9.14	5.0	4.96
R Factor	-	29 %	0 %	8.5 %

Table 4.1 The predicted 'true' intensities predicted by this model from a fit to data collected with an angle of $\beta=51°$ between the **POA** and the incident beam. Also shown for comparison are the intensities from an ideal sample of alumina and the observed intensities at $\beta=0°$ (i.e. the **POA** along the incident beam). A residual R factor ($R=\Sigma| I_{ideal}-I_{true}| /\Sigma I_{ideal}$) has been given in order to quantify the improvement offered by texture modelling.

the powder ring by increasing the angle β between the **POA** and the incident beam. Although data were collected up to $\beta=90°$, this set of data was selected for discussion as ~50° is approximately the maximum angle of access to a high-pressure cell. The true intensities are compared to the calculated intensities from an ideal sample in table 4.2. The values obtained match the ideal ones accurately for a range of reflections (over the full ψ range of 0 to $\pi/2$) and for reflections of widely differing intensity. The value of the refined texture parameter R=0.637 is in good agreement with that obtained from the Rietveld refinement of the data at $\beta=0°$.

It is noticeable from table 4.1, that the intensities observed at $\beta=0°$ show much less agreement with the ideal intensities than the values obtained after analysis with this model. The intensity variation around the powder rings can clearly be used to correct the reflection intensities. However, it should be noted that the use of the model in this manner can only correct those reflections actually observed, although the refined texture parameter can be used to predict the reflection intensities expected from test structures during structure solution. The true intensities from this texture model could be used to produce a corrected powder pattern for an initial Rietveld refinement of the crystal structure, once a trial structure has been hypothesised. Alternatively the intensities could be used directly in a single-crystal refinement package. The true intensities should be of sufficient accuracy to allow the structural parameters to be approximately determined and produce starting values for full Rietveld refinement (including a texture model) of the uncorrected powder pattern. Perhaps the ideal use of the information within the intensity variation around the powder rings would be to perform a full 2-D Rietveld refinement of the structure using the full 2-D texture model. Unfortunately the computing power neccessary to perform Rietveld refinement of the full 2-D powder pattern is not yet available. However the exponential increase in computing speeds in the last few decades suggests that such computational power will soon be available.

This method requires exposures of sufficient length to give good statistics (at least to the 5% level) on each point in the powder ring, which is quite feasible with a strongly scattering sample (i.e. high Z material) or with a large sample volume. Therefore in high-pressure work on relatively weakly scattering materials, a large gasket hole must be used. At present, this limits such a technique to the low pressure region, although the next generation of pressure cells with backing plates made of sintered diamond rather than Be should allow larger sample volumes to be taken to higher pressures.

4.7 The variation in average intensities around the powder ring with the angle between the POA and the incident beam.

In order to use the intensity variation around the powder rings for texture modelling, the data must be collected to good statistics on each sector of the powder ring. Since the sectors are calculated by averaging over only 6° segments of the powder rings, the signal-to-noise ratio of the data is considerably lower than the azimuthally integrated intensites produced by the Platypus package, which averages over the whole powder

ring. If counting statistics around the rings is a problem or a conventional Rietveld (1-D) refinement is required, the change in average intensities around the powder rings with β angle can be used to model the preferred orientation of the sample. This is performed by azimuthally integrated the data using the Platypus package to give the average intensities and using the preferred orientation model to calculate the corrections to these average intensities. The correction to the average intensities is obtained by calculating the correction to closely spaced points (in γ=0.1° steps) on the powder ring and averaging over the number of points.

The effect of preferred orientation on the average intensities will depend on the angle (β) between the **POA** and the incident beam. Figure 4.9 shows the ratio of the average intensities around the powder rings of the (110) and (104) reflections vs β from the data collected from the first sample of section 4.4. Also shown on the figure is the calculated intensity, which is obtained from the texture model described in this chapter. Note that this model can only give the ratio of the corrections to the average intensities and a value for the true ratio of the intensities of the (104) and (110) reflections ($I_{true}(104)/I_{true}(110)$) has been assumed. The assumed value of $I_{true}(104)/I_{true}(110)$=2.25 is the ratio of the intensities calculated from the structural parameters (from single-crystal diffraction studies) given in section 4.4. The values of the lattice parameters and preferred orientation parameter (R=0.642) have been assumed at those obtained in the Rietveld refinement of section 4.4. The calculated ratio is given by:

$$\left(\frac{I_{calc}\,(104)}{I_{calc}\,(110)}\right) = \left(\frac{I_{true}\,(104)}{I_{true}\,(110)}\right) \sum_{M(hkl)} \frac{<P_{104}\,(\alpha)>\,M(110)}{<P_{110}\,(\alpha)>\,M(104)} \qquad (4.25)$$

where $<P_{104}(\alpha)>$ is the correction to the (104) reflection and $<P_{110}(\alpha)>$ is the correction to the (110) reflection. The correction for each reflection is calculated from the formula given in section 4.3 and the relevant values of β, ψ, θ and γ.

The match between the calculated and observed ratios of the (104) and (110) reflections as the sample is rotated from β=0° to β=90° is reasonably good. The preferred orientation parameter has been assumed at R=0.642 from Rietveld refinement, which includes all the reflections in the powder pattern not just the two used here. Some of the discrepancy between the calculated and observed ratios can be attributed to the preferred orientation parameter being optimised by the Rietveld package to give the best fit over all reflections between the observed and calculated

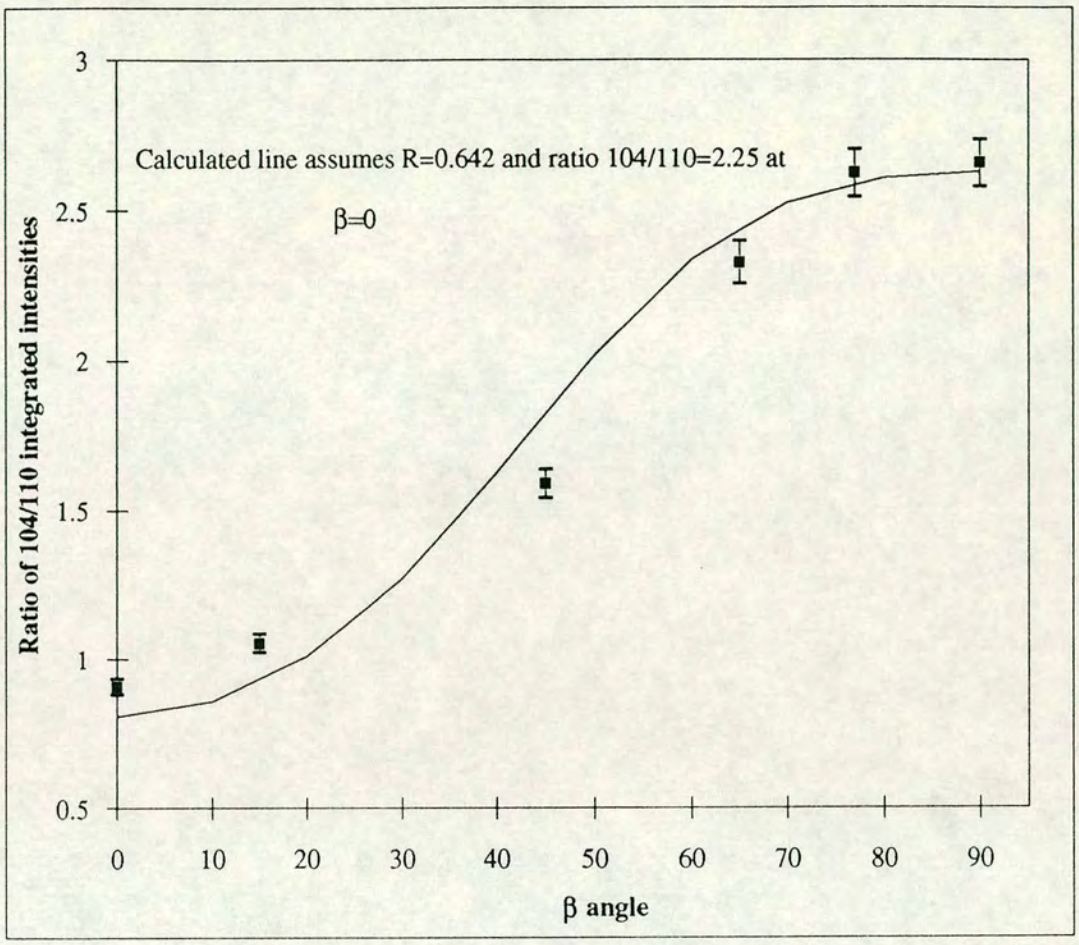

Figure 4.9 The ratio of the average integrated intensities of the (104) and (110) reflections vs the angle (β) between the **POA** and the incident beam. The observed data is shown as ■ and the solid line is the calculated ratio assuming a 'true' ratio of 2.25 (from the known structural parameters) and a value of the preferred orientation parameter of R=0.642.

spectra. Because the data has been azimuthally integrated and the integrated intensities extracted by fitting a pseudo-voigt peak-shape to the profiles, it is hard to assess the errors in the observed data of figure 4.9. Due to the averaging process, the error in the observed values will be below that obtained by assuming counting statistics. Rietveld refinement of data collected to similar statistics from standard samples using the image-plate technique has shown that the averaging process results in errors of the order of 2-3%. Error bars at this level have been dawn on figure 4.9. The success of the model in describing the average intensities with changing sample orientation illustrates that this model could be incorporated into a Rietveld refinement program, such as GSAS or MPROF, and used to refine structural parameters from data collected at any known angle to the incident beam.

Just as in section 4.6, where the intensity variation around the powder rings was used to correct the reflection intensites, the variation in average intensities with angle (β) between the **POA** and the incident beam can be used to calculate the values for the reflection intensities. This is performed by least-squares fitting of the model to a set of observed data, which is made up of the average intensities of reflections at different β angles. It would be possible to refine the intensities directly (i.e. not in a ratio form). However, this would require the additional assumption of a scale factor for each data point (it is difficult to correct for varying exposure times and synchrotron current variation). Using ratios avoids this complication as these factors are the same for all peaks collected in a single exposure at a given β angle. Because of the need to avoid introducing additional parameters into the calculation and the fact that it is relative intensities which are important from a crystallographic point of view, refinement of the relative intensities is more appropriate. Thus if the observed data consists of the measured intensities of say 10 reflections at various β angles, one reflection is chosen arbitarily and the ratio of the other intensities relative to the chosen reflection are refined by a similar least-squares technique to that described in section 4.6. It should be emphasied that this procedure does not regard the chosen reflection as having a fixed intensity but refines the correction to the other intensities relative to the refined correction of the 'standard' reflection. The parameters, which are refined in this calculation, are a single preferred orientation parameter (which describes the orientation of all the crystallites) and the 'true' intensity of each reflection relative to that reflection chosen as the standard. Thus this process offers a way to obtain corrected relative intensities without assuming any arrangement of the atoms within the unit cell.

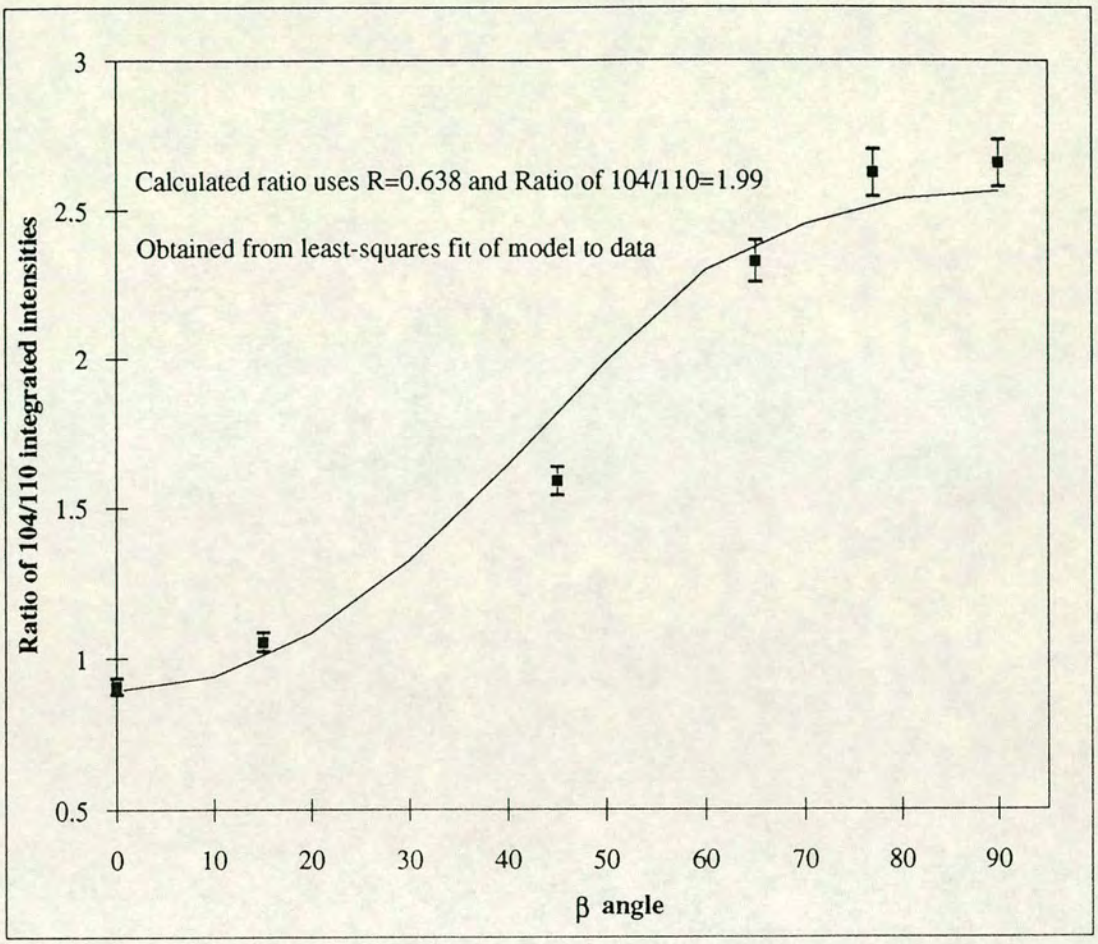

Figure 4.10 The ratio of the average integrated intensities of the (104) and (110) reflections vs the angle (β) between the **POA** and the incident beam. The observed data is shown as ■ and the solid line is the calculated ratio, which is calculated with a 'true' ratio of 1.99 and a preferred orientation parameter of R=0.638 both obtained from the least-squares fit of the texture model to the observed data.

This technique is demonstrated in figure 4.10, which shows the fit to the observed ratio of the (104) and (110) integrated intensities (the same data as in figure 4.9) obtained by such a least-squares refinement. The value for the preferred orientation parameter of R=0.638 is in reasonable agreement with the value (R=0.642) obtained from Rietveld refinement in the earlier sections of this chapter. The corrected ratio of intensities is I_{104}/I_{110}=1.99, which is in much closer agreement with the expected value of I_{104}/I_{110}=2.3 than the observed value of $I_{104}/I_{110}\approx$0.9 at β=0°. Thus this technique, which can provide a considerable improvement in the relative intensities of the diffraction peaks, offers a method to correct reflection intensities when the intensity around the powder ring is too weak to be reliably measured. It should be noted that the average intensities around the powder ring contain less information about the sample texture than the variation in intensity around the powder ring (in the sense that fine features of the variation around the powder ring are lost in the averaging process) and so this technique might be expected to be less accurate. However in many cases, high-pressure phases often nucleate to form uneven or 'spotty' powders and the intensity around the powder ring may reflect more the poor quality of the sample than any sample texture. In such cases the average intensity around the powder rings is often more accurate and so the technique described in this section can be very useful.

4.8 The variation in reflection intensities with the wavelength of the incident beam.

As seen in section 4.4 the general formula for angle α (equation 4.15), which determines the influence of the sample texture on a given reflection, contains a dependence on the scattering angle θ. This dependence on angle θ means that in transmission geometry the effect of preferred orientation on the reflection intensities is wavelength dependant (through Bragg's law). Collecting data at different wavelengths thus offers a way to determine the sample texture separately from the structure (in much the same manner as collecting data at different angles between the **POA** and the incident beam). However the scale of the changes in intensities due to variation in wavelength are quite small. In high-pressure diffraction studies using diamond anvil pressure cells, the maximum wavelength that can be used in practice is determined by the absorption of the diamonds. At wavelengths above ~1Å the diamond absorption of the incident and diffracted beams is very high. At very low wavelengths the wiggler stations on second generation synchrotrons (such as SRS Daresbury) can supply little intensity, although the insertion devices on the new generation of synchrotrons such

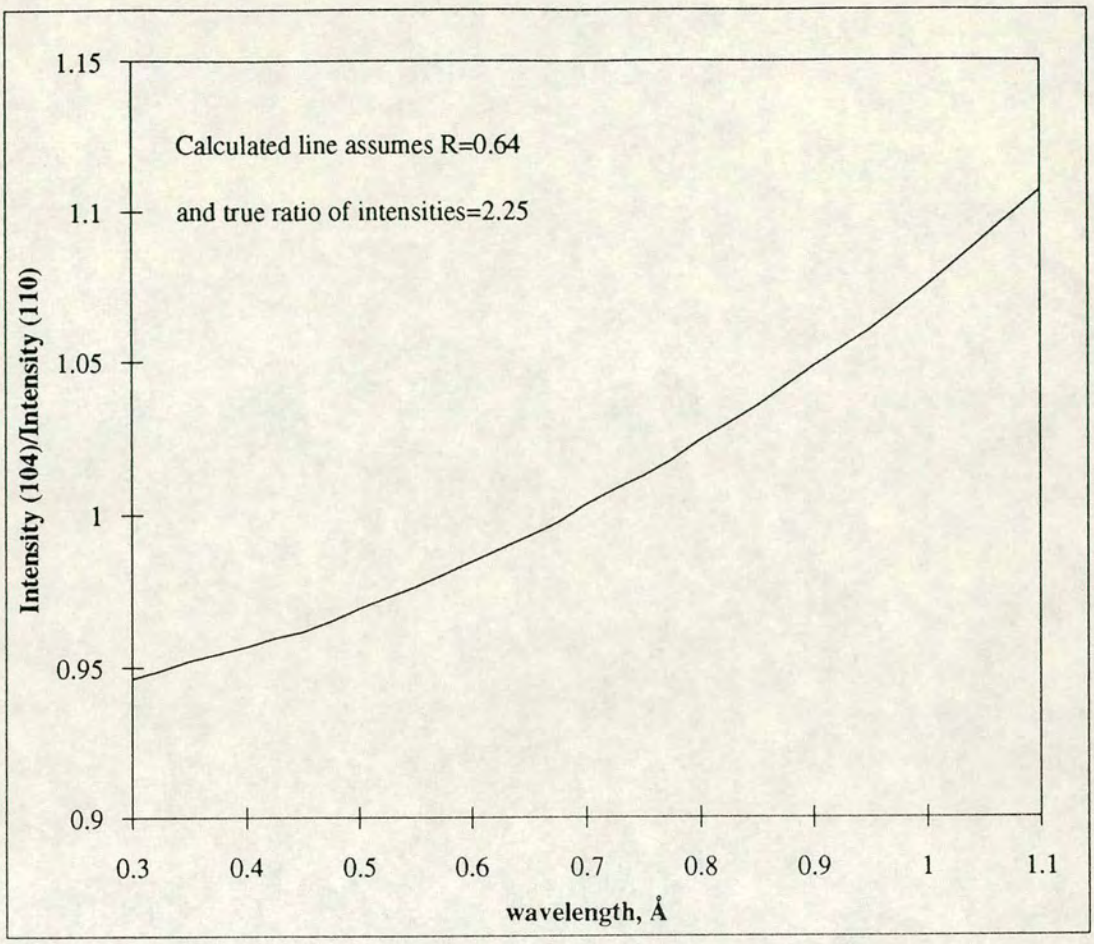

Figure 4.11 The calculated ratio of the average intensities of the (104) and (110) reflections vs wavelength of incident radiation. Note that the predicted variation in intensity is within the error bars of the data (in figures 4.7-4.10).

as the ESRF can have more flux at low wavelengths. These two considerations limit the viable range of wavelengths for high-pressure work at present to between 0.3-1Å. In this wavelength range the change in scattering angle is small and hence little effect on relative intensities can be expected. Figure 4.11 shows the predicted change in relative intensities of the (104) and (110) reflections from the alumina sample used in section 4.4. Clearly the change in relative intensities is less than the errors on the intensity measurements and, at present, this technique is of little use in high-pressure work for determining the sample texture.

4.9 Conclusions

This chapter has introduced and developed a new 2-D model for the effect of sample texture on the reflection intensities suitable for powder diffraction with a general orientation of the **POA** relative to the incident beam. As illustrated by the data from a sample of known texture, the model can calculate the changes to the reflection intensities expected from the range of sample orientations encountered in DAC transmission geometry.

By exploiting the variation in intensity around the powder ring (or changes to the average intensity around the powder rings) from data collected with the **POA** not parallel to the incident beam, the texture in the sample can be directly determined. The methods developed in this chapter allow the preferred orientation of the sample to be accurately modelled without any assumptions about the crystal structure other than the lattice parameters and indexing of the reflections., which can be of great benefit in structure solution. The use of these techniques in high-pressure diffraction studies will be discussed in the following chapters of this thesis.

CHAPTER FIVE

Preferred Orientation Studies On Samples Under Pressure

Introduction

The previous two chapters of this thesis have developed a new model for sample texture suitable for use in high-pressure studies with an image-plate area detector. This chapter presents experimental studies of the preferred orientation found in high-pressure samples and the results from modelling of these crystallite distributions. Results from two main studies are presented in consecutive sections: a study of the preferred orientation in the high-pressure Si β-tin phase (about which there has been active debate since the early 1960's) and the strong preferred orientation found in an unsolved phase of HgTe and other II-VI materials. A third section details results from a shorter study of the preferred orientation observed during a study of the structure of the III-V semiconductor InSb. The discussion in this chapter focuses on understanding the distributions themselves and the techniques used in studying texture of samples held under pressure. The use of the information obtained from modelling the preferred orientation of the sample in structure solution and refinement is presented in the following chapter.

Section 1: A Study of The Preferred Orientation in the β-tin phase of Silicon

5.1.1 Introduction

The alumina standard sample, which was used in the previous chapter to investigate the effect of texture on the full 2-D diffraction pattern, is much larger in volume than a typical sample that can be used in a DAC pressure cell. Since the diffracted intensity from any sample is proportional to the sample volume, the spectra recorded from samples in the pressure cell are much lower in intensity (and hence collected to poorer statistics), an important distinction if not just the azimuthally integrated intensity but the intensity at different points on the powder rings is to be modelled. In addition, the

steel pressure-cell body restricts the maximum angle between the pressure-cell axis and the incident beam to ~40°. If the preferred orientation axis (POA) is coincident with the cell axis, which, although not always true, greatly simplifies subsequent analysis, then the possible range of angle between the POA and the incident beam is also greatly reduced. Therefore, the information, which is obtainable on sample texture from a sample held in a pressure cell, is likely to have a smaller range (in angle) and a lower signal-to-noise ratio (unless counting times are prohibitively long) than that presented in the previous chapter. In order to investigate the importance of these restrictions, this section presents a study of the long-observed preferred orientation of the high-pressure Si β-tin phase.

The Si β-tin phase, which occurs in the pressure range ~10 GPa to 13.2 GPa, was one of the first high-pressure phases observed in a semiconductor (Jamieson, (1963)). In this pressure interval, Si has the white-tin or β-tin structure, which has a tetragonal lattice (for Si, a=4.686Å c=2.585Å at ~13 GPa, as given by Jamieson (1963)) with space-group I $4_1/a$ m d. The atoms are on 4-fold special positions with all atoms coordinates fixed by symmetry (as shown in figure 5.1.1). As it is known to form as a highly oriented powder (Jamieson, (1963)), this well-known structure is an ideal test case for the preferred orientation modelling techniques presented in this thesis. The structure is well-determined and the atoms are fixed on special positions within the unit cell. Thus, the relative intensities of the diffraction peaks are known and should not change with pressure within the β-tin phase. Thus any deviations of the relative peak intensities from the values expected of an ideal powder sample, are expected to be due to microstructural effects, principally preferred orientation, and not pressure induced structural changes. In light of the need to test the modelling techniques developed in this thesis against data collected from a sample held under pressure and the long-standing historical interest in the texture of the β-tin phase, a detailed study of preferred orientation in this phase was made.

5.1.2 Sample preparation prior to texture studies.

A sample of high purity Si (purity >99.999%) was fine ground and loaded into the steel gasket (hole size ~150μm) of a Diacell DAC. It is much easier to model the effects on the relative intensities of the diffraction peaks of rotating the pressure cell axis with respect to the incident beam, if the preferred orientation axis (POA) is parallel to the pressure-cell axis. In order to try and guarantee that the POA was along the pressure-cell axis, particular care was taken to align the diamonds in the cell as

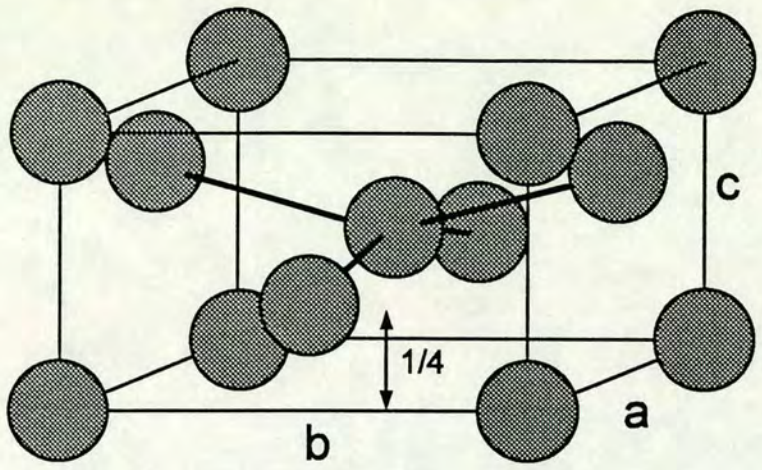

Figure 5.1.1 The crystal structure of the β-tin phase of Silicon. Note that since the symmetry of the lattice is tetragonal, a=b.

accurately as possible. Careful preparation of the pressure cell should ensure that any resultant force on the crystallites (and hence the POA) is parallel to the cell axis.

The choice of gasket material was dictated by the position of any gasket diffraction lines (should the incident beam have accidentally struck the gasket). Previous studies of silicon under pressure had shown that Tungsten has its first strong peak very close to the first β-tin doublet. Thus if the diffraction pattern became contaminated with peaks from a Tungsten gasket (as is possible whilst collecting data with the pressure cell axis at an angle to the incident beam), it would be hard to determine accurately the intensities of the β-tin reflections. In order to avoid any uncertainty, steel gaskets were used (simulations of the diffraction patterns expected from Fe, the principal component of steel, had shown that the diffraction peaks from a steel gasket could be expected to lie well clear of the sample peaks).

The diffraction pattern from the sample at ambient pressure was then recorded using the standard image-plate set-up (as described in chapter 2). This diffraction spectra acted as the sample to image-plate calibration pattern and all data collected on the

standard mount were converted into an intensity vs scattering angle (2θ) form using this ambient pressure pattern. Powder patterns were collected at suitable pressure intervals as the pressure was increased gradually up into the β-tin pressure region. On pressure increase no pure β-tin region was observed. The diffraction patterns showed that the sample contained a three phase mixture of the cubic diamond phase (which is the ambient pressure structure), β-tin and a significant fraction of the higher pressure Imma phase, which is an orthorhombic structure occurring above 13.2 GPa (McMahon *et al*, (1994)). In order to remove the cubic and Imma phase components the pressure was raised further until the sample had completely undergone the transformation to the Imma phase. The pressure was then relaxed slightly and the sample re-transformed to a phase mixture of predominately β-tin plus a small amount of the metastable cubic BC8 phase, which occurs on pressure decrease from the β-tin phase (Wentorf and Kasper, (1963)). A small component of BC8 was considered acceptable as, unlike the Imma phase, the diffraction peaks from the BC8 phase do not overlap with those from the β-tin structure.

A second sample was prepared in a Merrill-Bassett pressure cell in a identical manner to the preparation of the Diacell sample. This sample was taken up to about ~17 GPa and then brought down in pressure to 11.8 GPa. Diffraction spectra collected on the standard mount showed that the sample was pure β-tin phase.

5.1.3 Preferred Orientation studies

The diffraction pattern from the first sample (in the Diacell) collected on the standard mount at 11.7 GPa is shown in figure 5.1.2, along with the calculated pattern from an ideal non-textured sample of the Si β-tin phase. There are obvious differences in relative intensities between observed and calculated spectra, indicating that there is severe preferred orientation in the sample. There is also a marked (hkl) dependence in the peak widths of the observed pattern, an effect which we have observed in all spectra from this phase. There are many possible explanations for such a strong microstructural effect. The crystallite shape could vary significantly in different lattice directions, e.g. the crystallite dimension could be very small in the a-b plane, which would produce a very broad (200) reflection (as observed), and much longer along the c-axis, which would produce a sharp (101) reflection. However the sharpness of the (220) reflection, which would also be expected to be broad in this model rules out such a simple hypothesis. An other possible cause could be some kind of lattice

faulting, which is known (Langford *et al*, (1992)) to cause marked (hkl) dependence of peak widths.

The pressure cell was then removed from the standard mount and transferred to the rotation stage. The rotation stage is not at a calibrated distance from the image-plate and so it is not possible to convert these spectra directly into an intensity vs scattering angle (2θ) form. However as the pressure remained constant during the subsequent exposures, it is justifiable to assume that the lattice parameters of the structure and consequently the 2θ positions of the diffraction peaks remained constant. Thus the data were converted into intensity vs 2θ form by assuming that the diffraction peaks remained at constant 2θ positions and the sample-to-image-plate distance calculated accordingly.

In order to determine the exact position of the gasket reflections, a diffraction pattern from the steel gasket was collected by deliberately mis-aligning the pressure cell so that the beam struck the gasket just on the edge of the sample area. It is important to take the diffraction pattern from the gasket close to the sample. Because the rest of the gasket was likely to be at a different pressure, the gasket diffraction peak positions would have been inaccurate if a gasket region far away from the sample area had been used. Once the positions of the gasket diffraction peaks had been determined, alignment of the sample on the rotation stage was carefully performed (using the optical method described in chapter 2) such that no gasket contamination of the sample diffraction patterns was observed with the pressure cell axis at any angle to the incident beam.

Data were collected with the Diacell pressure-cell axis at various angles to the incident beam between $\omega=0°$ and $\omega=38°$, which is close to the maximum angle of access to this pressure cell. The data collected with the pressure-cell axis at an angle to the incident beam were contaminated heavily with the diffraction pattern from the Be backing plates (see figure 5.1.3), through which the incident beam must enter the pressure cell. Although Be contains less electrons than Si and would thus be expected to produce a weaker powder pattern, the sample volume of Be illuminated by the x-ray beam was far higher than the diffracting volume of the Si sample. Thus the intensity of the Si reflections was much lower than those from the Be backing plate and extracting the intensity of the Si reflections from data recorded with $\omega\neq0°$ required longer exposures than when the pressure cell axis was parallel to the beam ($\omega=0°$). The Be diffraction peaks were close to those from the sample and so, in order to

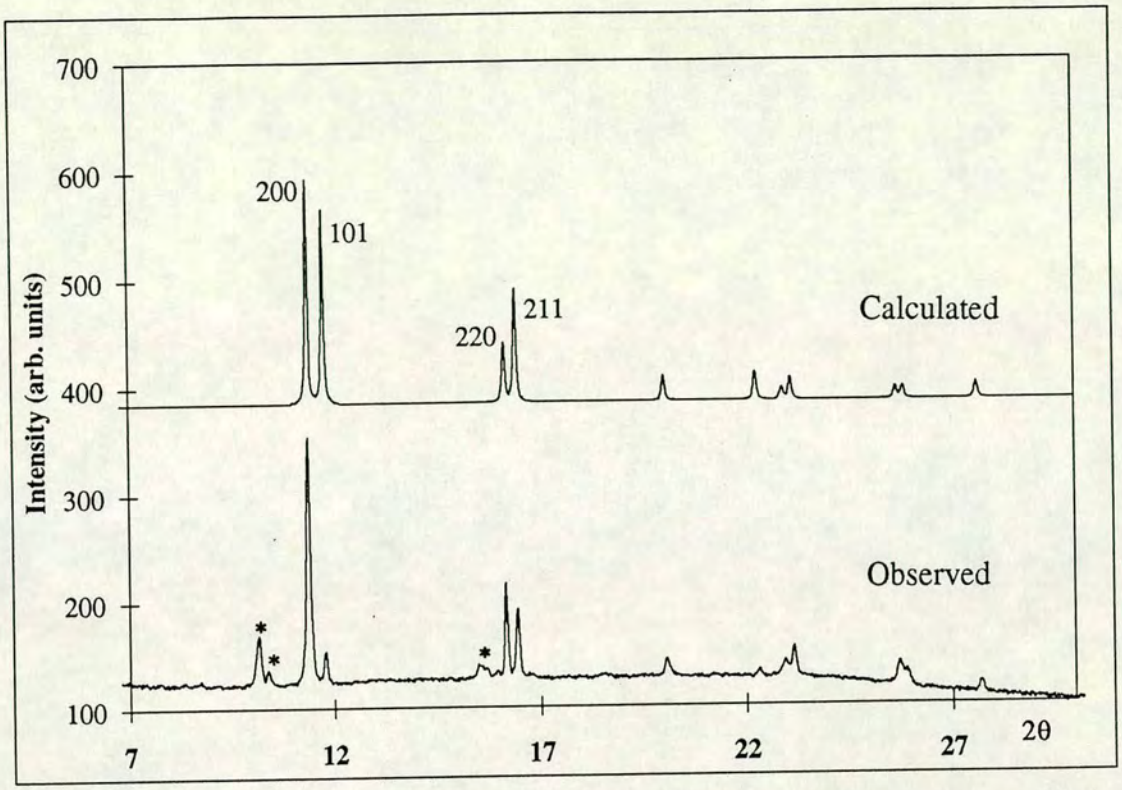

Figure 5.1.2 The calculated average 1-D diffraction profile from an ideal non-textured sample of silicon in the β-tin phase and the observed diffraction pattern from the first sample at 11.7 GPa. The reflections marked * in the observed profile are from the small component of BC8 phase present in the sample.

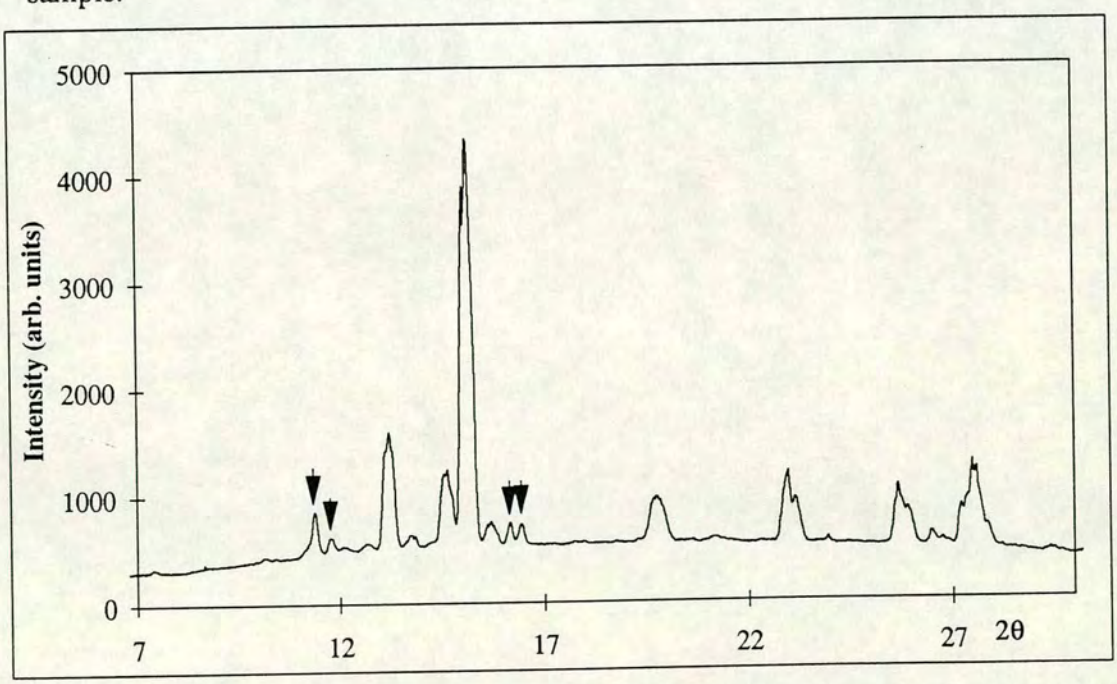

Figure 5.1.3 The observed average 1-D diffraction profile from the first sample with an angle 38° between the pressure-cell axis and the incident beam. The sample lines are marked with an arrow. All other reflections are from the Be backing disc; there are no contaminant peaks from the gasket material.

determine the exact position of the Be reflections, a diffraction pattern from just the Be plate was collected. This established that the Be reflections do not overlap exactly with the sample reflections and that consequently the intensities of the sample peaks could be extracted by fitting pseudo-voigt peak-shapes.

Figure 5.1.4a shows the variation in reflection intensity around the (200) and (101) powder rings with the pressure-cell axis parallel to the incident beam (ω=0°). In both the (200) and (101) reflections there is little variation around the ring, although the noise on the data is considerable. This is caused by two factors: the intensity from the sample is very weak and local sample inhomogeniety. The diffracted intensity from the sample is approximately a factor of 20 lower than that from the alumina sample in chapter 4, which results in considerably worse statistics. In addition it is difficult to obtain a finely powdered sample of this phase, perhaps due to some re-crystallisation process, and so the sample contains small clumps of powder. The non-uniformity of the powder is the larger cause of error and is probably responsible for the outlying points at $\gamma \approx 150°$ in figure 5.1.4a. As in chapter four, outlying data points are discarded from further analysis. The error bars drawn on the data of figure 5.1.4a are calculated from the standard deviation around the powder rings at ω=0° .

As the cell was rotated, significant intensity variation around the powder rings was observed (see figure 5.1.4b). The variation in intensity around the powder rings was sufficiently great that it can be observed visually in the 2-D image. Figure 5.1.5 shows the 2-D images from the data at ω=0° (with the pressure-cell axis parallel to the incident beam) and at ω=38°. In the magnified section of the image at ω=38°, the variation in the (101) powder ring can be clearly seen. The absence of significant intensity variation around the powder rings at ω=0° and its subsequent growth as the cell was rotated indicated that there was strong preferred orientation in the sample and that the crystallite distribution was close to axially symmetric around the pressure-cell axis; i.e. the POA was coincident with the pressure-cell axis. Thus the angle of rotation of the pressure cell was exactly the angle of rotation of the POA with respect to the incident beam. Consequently, the orientation of the POA during each data collection was taken to be $\beta=\omega$ (from the angle of rotation of the pressure cell) and φ=-90°.

Figure 5.1.6 shows the average integrated intensities around the powder rings of the (101), (220) and (211) reflections relative to the (200) reflection with the POA inclined at various angles to the incident beam. This diagram shows that the observed

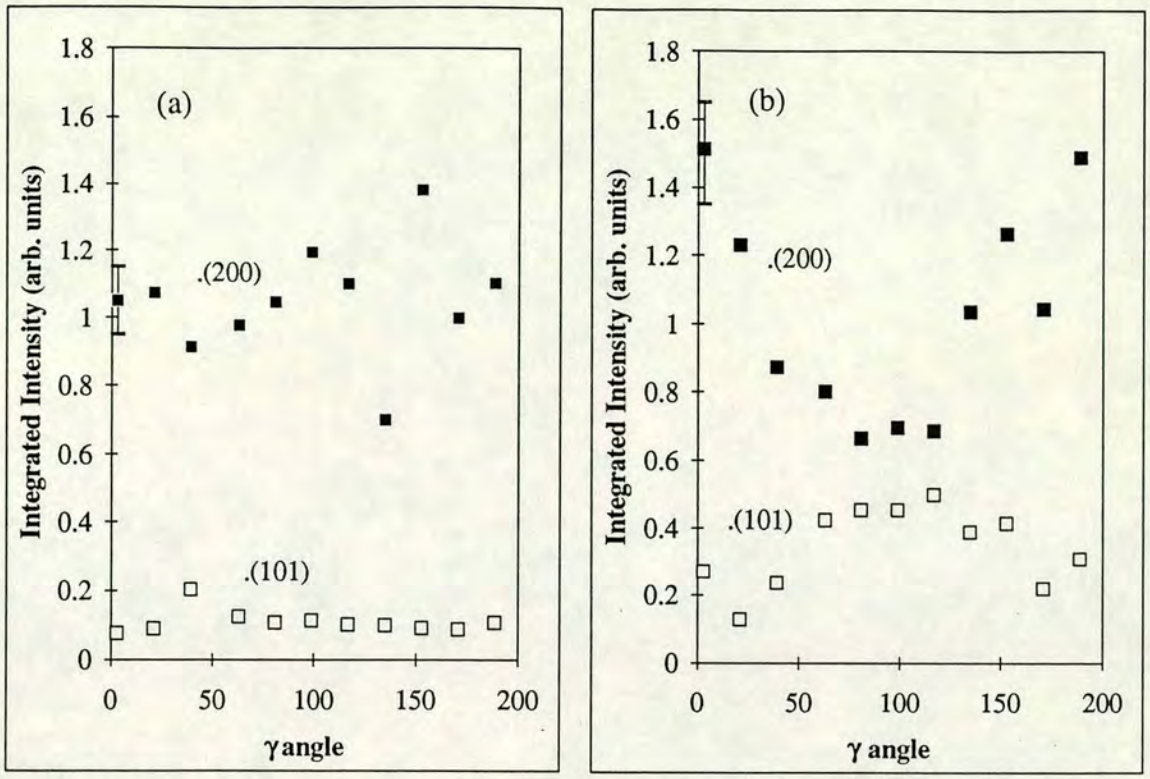

Figure 5.1.4 The observed intensity around the (200) and (101) reflections of the Silicon β-tin phase from the first sample at 11.7 GPa with: (a) the pressure-cell axis parallel with the incident beam and (b) an angle of 38° between the pressure-cell axis and the incident beam.

relative average intensities of the first doublet ((200) and (101) reflections) became closer to those of the ideal calculated pattern (I_{200}/I_{101}=1.118 in a ideal powder sample) as the pressure cell angle is increased. This suggests that the c-axis of this phase forms predominantly parallel to the cell axis and so, in this transmission geometry, those reflections close to the c-axis are measured as too weak. Hence reflections such as the (200) have far more intensity at β=0° than that expected from an ideal sample of this phase.

A possible model of the crystallite distribution in the first sample would be that the (001) scattering vector was the POD. This simple model was fitted to the average integrated intensities around the powder rings using the computer program Texture-Fit (as described in chapter 4), which produced a refined orientation parameter of R=0.323 and a refined ratio of the intensities of the (200) and (101) reflections of I_{200}/I_{101}=0.849. The calculated true ratio of the intensities of the (200) and (101) reflections of 0.849 is much closer to the value (=1.118, calculated from the

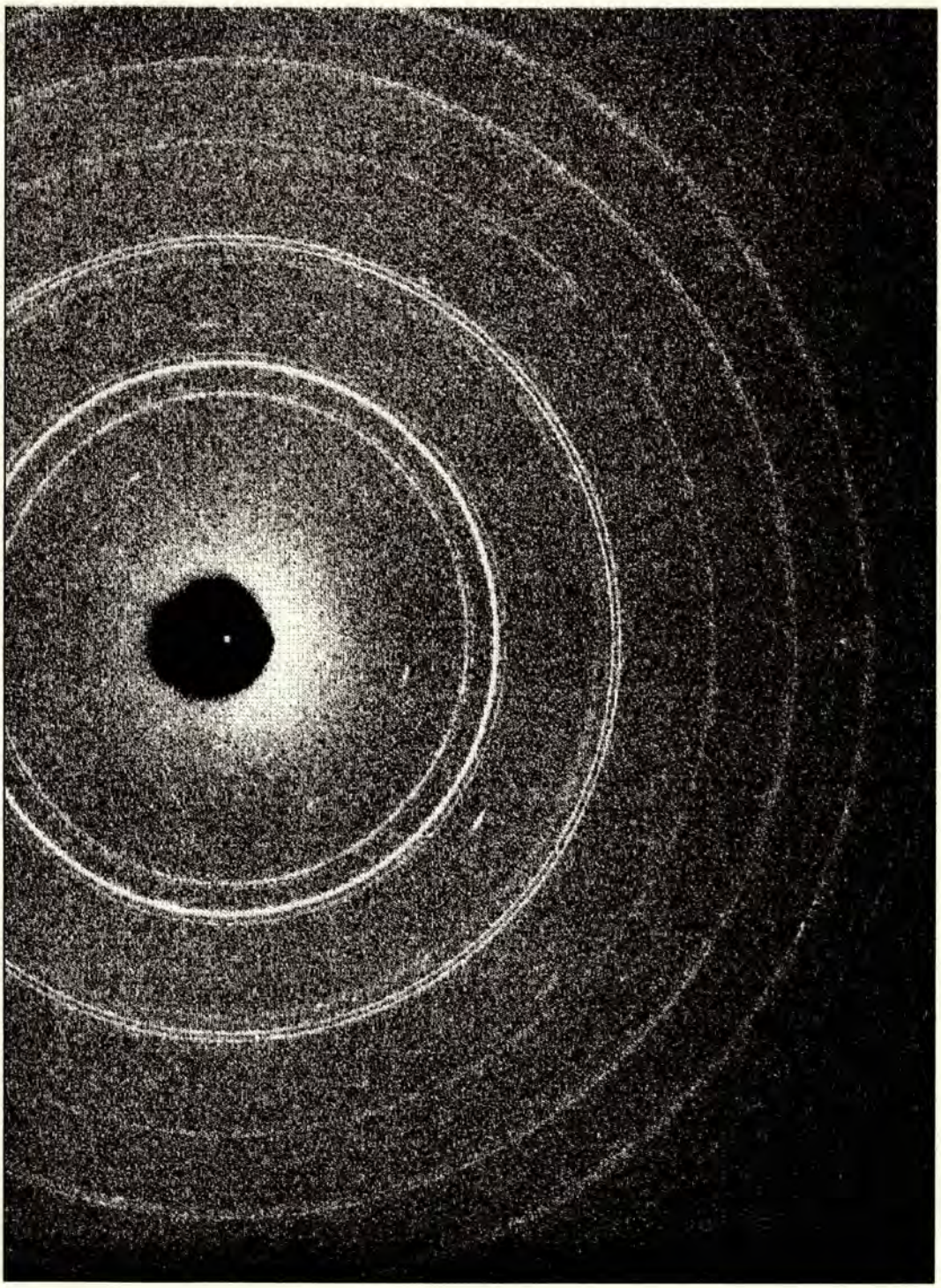

Figure 5.1.5 (a) 2-D image of the Silicon β-tin phase from the first sample at 11.7 GPa with the pressure-cell axis parallel with the incident beam. The low 2θ powder lines are from the BC8 component.

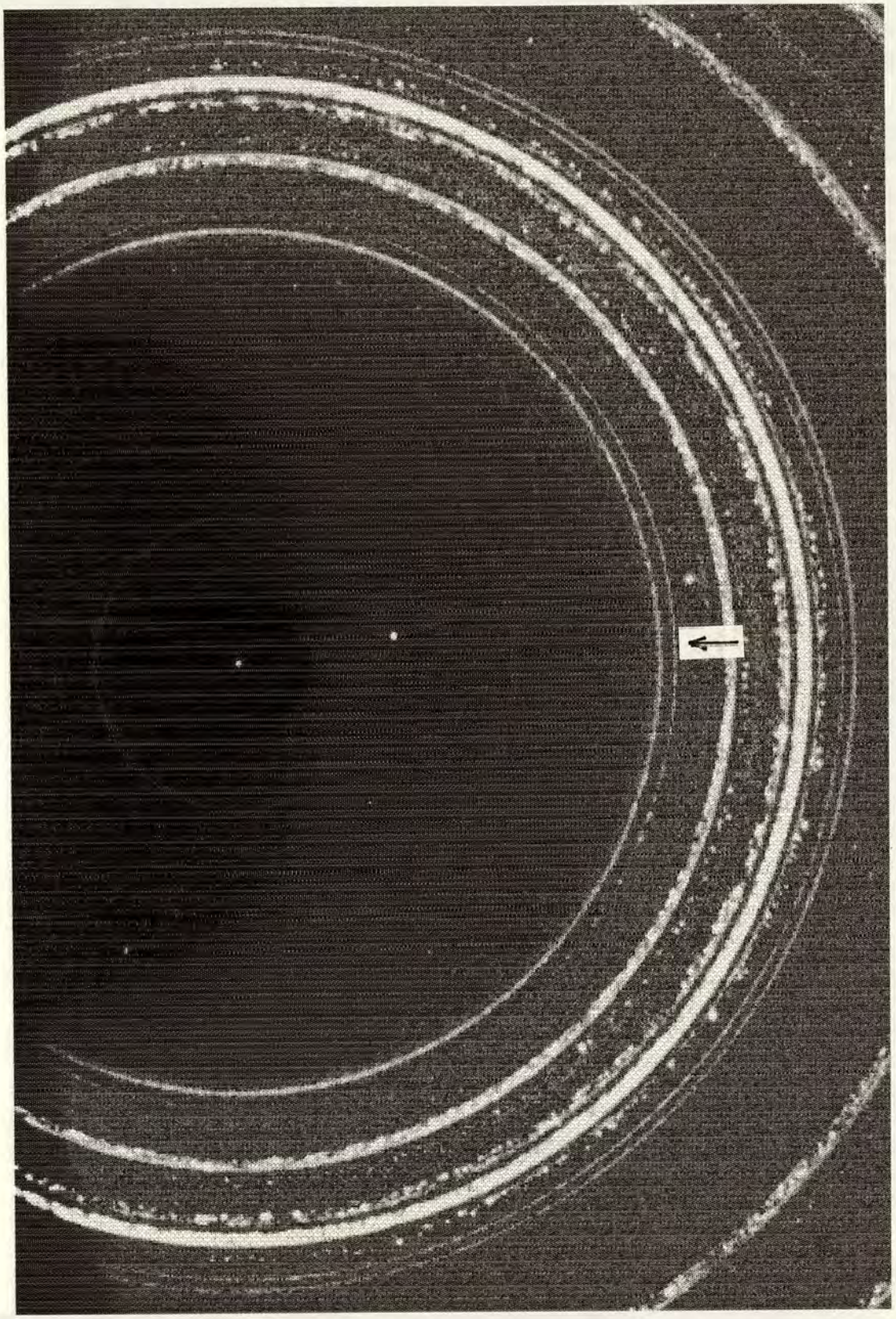

Figure 5.1.5 (b) a highly magnified low 2θ section of a 2-D image of the Silicon β-tin phase from the first sample at 11.7 GPa with an angle of 38° between the pressure-cell axis and the incident beam. Note the strong intensity variation around the (101) powder ring (marked by an arror). The diffracted intensity from the BC8 component is too weak to be seen.

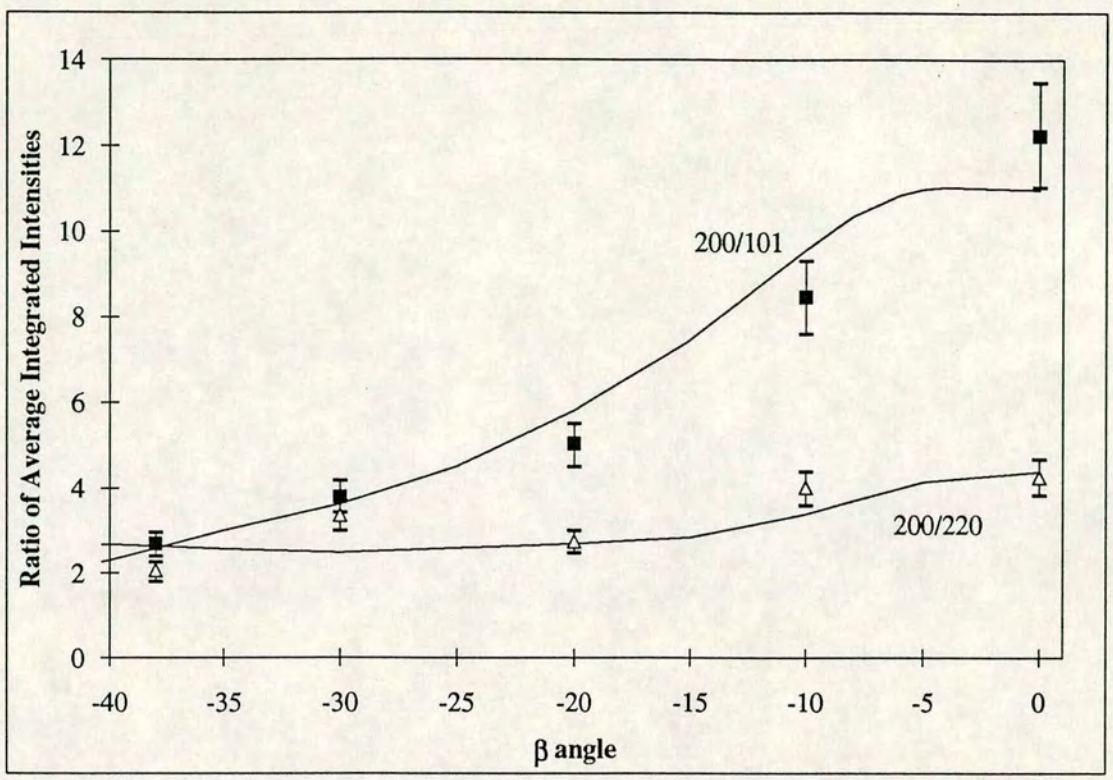

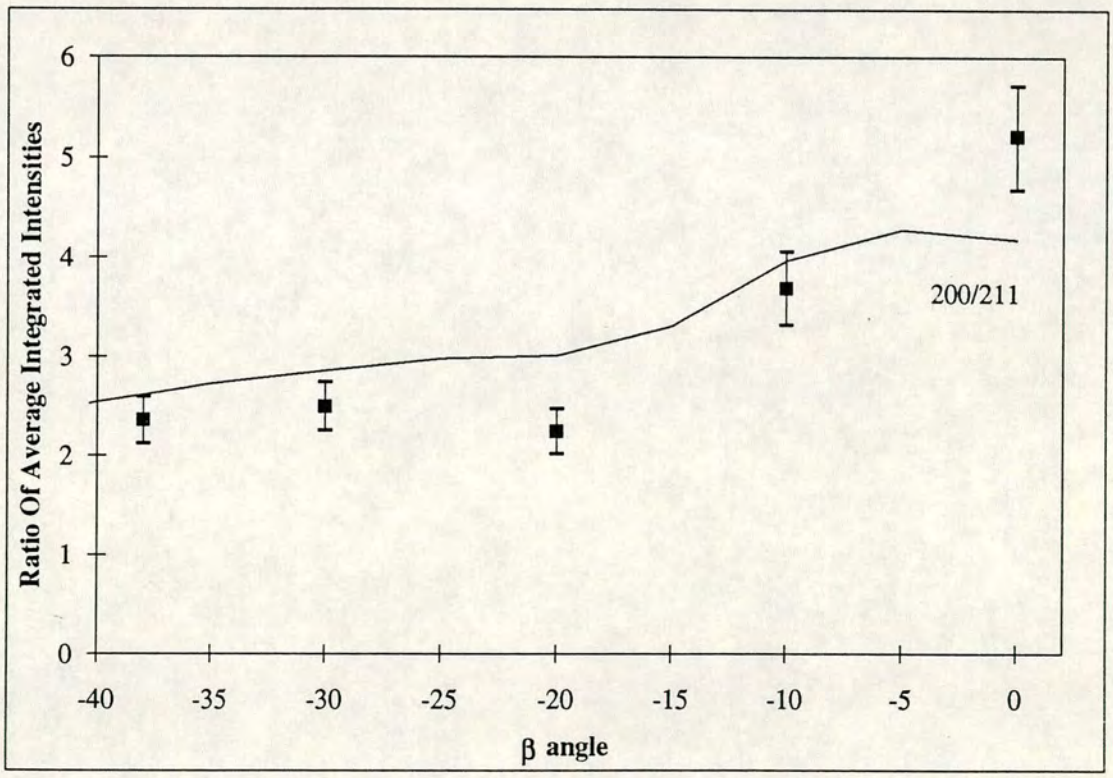

Figure 5.1.6 The average integrated intensities of the (101), (220) and (211) reflections relative to the (200) reflection vs the angle (β) between the POA (assumed to be the pressure-cell axis) and the incident beam. The observed data is shown as points and the solid line is the calculated ratio obtained from refinement of the preferred orientation model discussed in the text.

known structural parameters) from an ideal non-textured sample than any of the observed points, which vary between ~12.3 and ~2.69. However, modelling of the intensity variation around the powder rings at β=38° produced a refined texture parameter of R=0.64 and a refined ratio I_{200}/I_{101}=2.1. This is clearly inconsistent with the modelling of the average intensities vs β angle. Similar inconsistencies occurred in the modelling of the intensities of the (220) and (211) reflections.

Since this simple model did not explain the observed variation in intensity with sufficient accuracy, other possible choices of POD were explored. The best fit to the data was obtained with the (011) reciprocal lattice vector as the POD. Figure 5.1.6 shows the refined fit with this model to the average intensities of the four strongest reflections at different orientations of the sample. The other reflections were too weak to model or obscured by Be diffraction peaks. The data was refined in a ratio form with the (200) reflection chosen as the 'standard' reflection, as discussed in section 4.7. The preferred orientation parameter (R) refined to a value of: R=0.30, consistent with a strong degree of preferred orientation in the sample. The relative reflection intensities obtained from this model are presented in table 5.1.

Figure 5.1.7 shows the fit to the intensity variation around the (200), (101), (220), and (211) powder rings at β=38°, assuming that the (011) reciprocal lattice vector is the POD. The corrected relative intensities for these reflections given by this model are also shown in table 5.1 along with the true intensities for this structure (calculated from the known structural parameters). The refined texture parameter of R=0.45 is still not in exact agreement with the value obtained from modelling the average intensities, although the values for the corrected intensities are in closer agreement with the true values than the raw measured values.

The second sample of Si β-tin phase was aligned on the rotation axis and data collected with various angles between the pressure-cell axis and the incident beam. The degree of preferred orientation in this sample was much less than in the Diacell sample, as can be seen in figure 5.1.8 (c.f. figure 5.1.2). As the sample was rotated the changes in the reflection intensities were very similar in kind, although smaller, to those observed in the first sample. Figure 5.1.9 shows the ratio of the average intensities of the (200) and (101) powder rings as the pressure cell was rotated. As with the first sample, the relative intensity of the (200) and (101) reflections decreases with angle, i.e. the ratio becomes closer to that expected from an ideal sample. It is clear that this sample has a lower degree of preferred orientation than the first sample

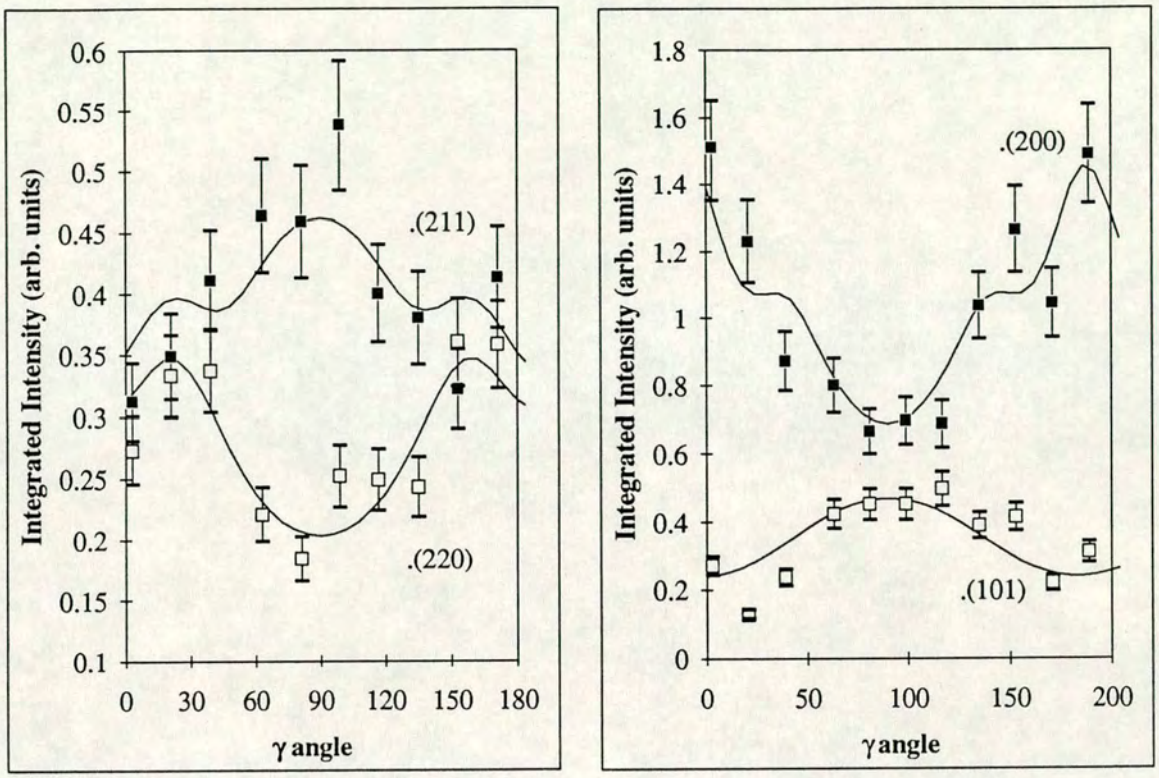

Figure 5.1.7 The observed intensity around the (200) (101), (220) and (211) reflections of the Silicon β-tin phase from the first sample at 11.7 GPa with an angle of 38° between the pressure-cell axis and the incident beam. The solid line is the calculated variation obtained from refinement of the preferred orientation model discussed in the text.

	True Intensities	Observed Intensities at $\beta=0°$	Intensities from modelling the average intensities vs β angle	Intensities from modelling the variation around powder rings at $\beta=38°$
200	100	100	100	100
101	89	8	69	22
220	30	23	37	30
211	57	19	53	46
R Factor	-	45.6%	11.2%	25.7%

Table 5.1 The calculated 'true' intensities predicted by this model from a fit to the average intensities vs β angle and the intensity variation around the powder rings at $\beta=38°$ (i.e. 38° between the POA and the incident beam). Also shown for comparison are the intensities from an ideal sample of the silicon β-tin phase and the observed intensities at $\beta=0°$ (i.e. the POA coincident with the incident beam). A residual R factor ($R=\Sigma| I_{ideal}-I_{calc}| /\Sigma I_{ideal}$) has been given in order to quantify the improvement offered by texture modelling.

but that the crystallite distribution has a similar form. Also shown on figure 5.1.9 is the calculated intensity vs β angle obtained by fitting the same texture model as used with the first sample; i.e. it was assumed that the (011) reciprocal lattice vector was the POD and the POA was coincident with the pressure-cell axis. The texture parameter refined to a value of R=0.43, indicating a lower degree of texture in this sample. The refined intensities from this fit and the intensities of the (220) and (211) reflections, obtained from similar modelling of the average intensities of the (220) and (211) reflections vs β angle, all lie within ~8% of the intensities obtained from the first sample (and thus within the probable error margin).

In both samples, the results from modelling the change in average intensities with β angle are clearly more accurate than those obtained from modelling the intensity variation around the powder rings. The data on intensity variations around the rings were obtained from averaging over a much smaller section of the powder ring than the average intensities and so suffer from poorer statistics as well any effects of local

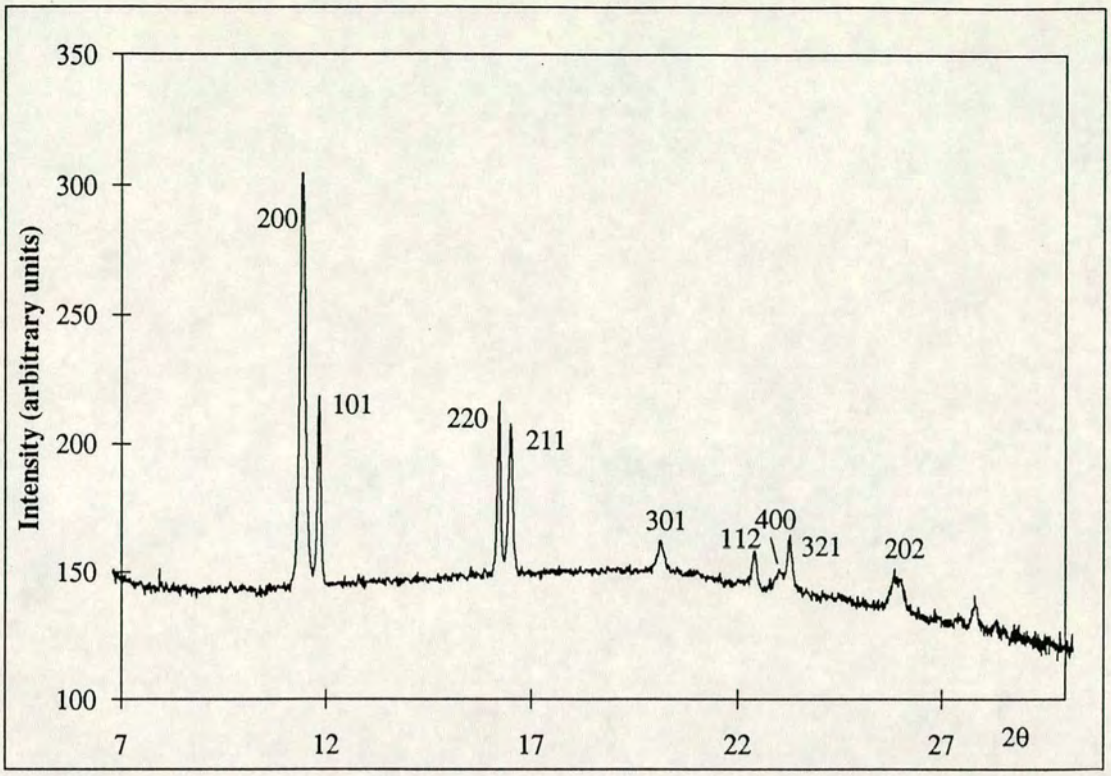

Figure 5.1.8 The observed diffraction profile from the second sample of the Silicon β-tin phase at 12 GPa. The degree of preferred orientation is much lower than in the first sample (c.f. figure 5.1.2).

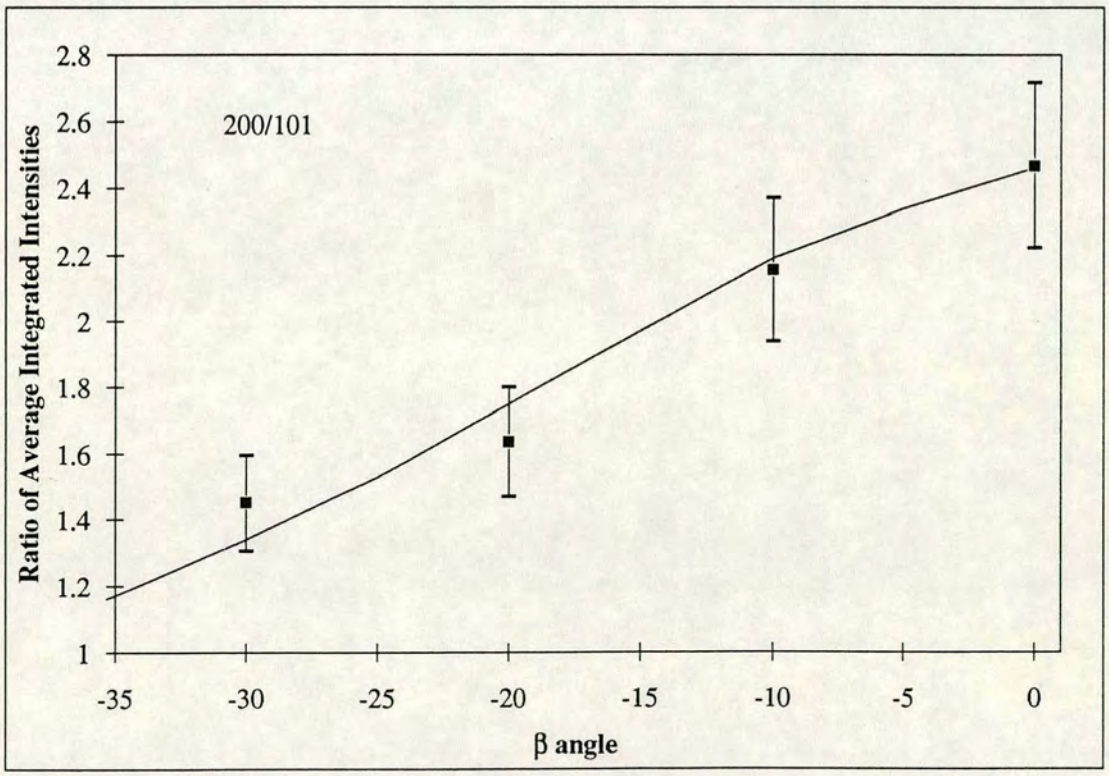

Figure 5.1.9 The ratio of the average integrated intensities of the (200) and (101) reflections vs the angle (β) between the **POA** (assumed to be the pressure-cell axis) and the incident beam. The observed data is shown as ■ and the solid line is the calculated ratio obtained from refinement of the preferred orientation model discussed in the text.

sample inhomogeniety. In such a case the average intensities appear to be a much better measure of the preferred orientation than the variation in intensity around the powder rings. The data presented were obtained in exposure times of approximately 45 minutes, which was the maximum possible within the allotted synchrotron time (considering that exposures had to be made for sample preparation and data collected in many sample orientations). In addition silicon is a relatively weak scatterer of x-rays and so the sample peaks are weak compared to those from the Be backing discs, which makes it difficult to extract intensities reliably by peak fitting. With the current synchrotron source at Daresbury, modelling of the preferred orientation of a sample under pressure that is as weak a scatterer as silicon is only just practical, although the future generation of synchrotrons should remove the problem of low counting statistics.

The intensity predicted for the (101) reflection is still a little low compared to the calculated intensity of this reflection from an ideal sample, which could be due to a variety of factors. The degree of preferred orientation is much more severe than commonly encountered in ambient pressure studies (c.f R=0.642 for the alumina sample of chapter four with R=0.30 for the first silicon sample). The crystallite distributions encountered in samples held under pressure may be different both in degree and form to those observed in ambient pressure studies and it may be that the March-Dollase function cannot model such extreme texture accurately. However the results obtained are a considerable improvement over the raw measured values at $\beta = 0°$ and confirm that the preferred orientation modelling techniques developed in this thesis can be successfully used for *in-situ* studies of samples held under pressure.

Section 2: A Study of the Texture in HgTe phase IV

5.2.1 Introduction

The II-VI materials HgTe, CdTe and ZnTe show a similar pattern of behaviour under pressure: from the ambient pressure zincblende structure they transform to the hexagonal cinnabar structure. HgTe and CdTe then transform to the NaCl structure before transforming to unknown structures above ~ 12 GPa. ZnTe transforms directly from cinnabar to an phase of unsolved structure at ~11 GPa. All three of the unknown high-pressure phases give similar diffraction spectra, although published spectra from EDX work identify only a few lines from these phases. Previous work by other authors (Werner *et al*, (1983), Huang and Ruoff, (1984)) had tentatively indexed (on the basis of four observed reflections) the unsolved HgTe phase IV as tetragonal or possibly orthorhombic. As part of a systematic study by the University of Edinburgh group of the high-pressure behaviour of the II-VI semiconductors, a detailed crystallographic study of the structure of these unsolved phases was performed. Diffraction spectra from all three compounds collected using the standard image-plate set-up on station 9.1 were indexed on similar orthorhombic unit cells. Examination of the absences of the reflections had identified a possible space-group and a trial structure had been obtained (see chapter 6). Initial Rietveld refinement of this trial structure indicated that either the sample was highly oriented or that the trial structure was incorrect. Figure 5.2.1 shows the fit obtained from Rietveld refinement of the trial structure to the data from HgTe at 13.1 GPa. Despite a large preferred orientation correction being applied in the refinement, there are still large misfits to the observed data, especially to the (002) reflection. Similar misfits were found for CdTe and ZnTe.

In order to determine whether the mismatch between the calculated pattern predicted by the trial structure and observed data was due to preferred orientation or an error in the structure, a study of the texture of this phase was made. Because synchrotron time was limited and exposures for texture studies must be quite long if intensities are to be accurate, particular emphasis was placed on HgTe phase IV. This had shown the most extreme misfits and thus was likely to be the most oriented. The intensity changes between different orientations of the sample were expected to be larger and thus easier to measure in HgTe then the other two compounds. This section presents a

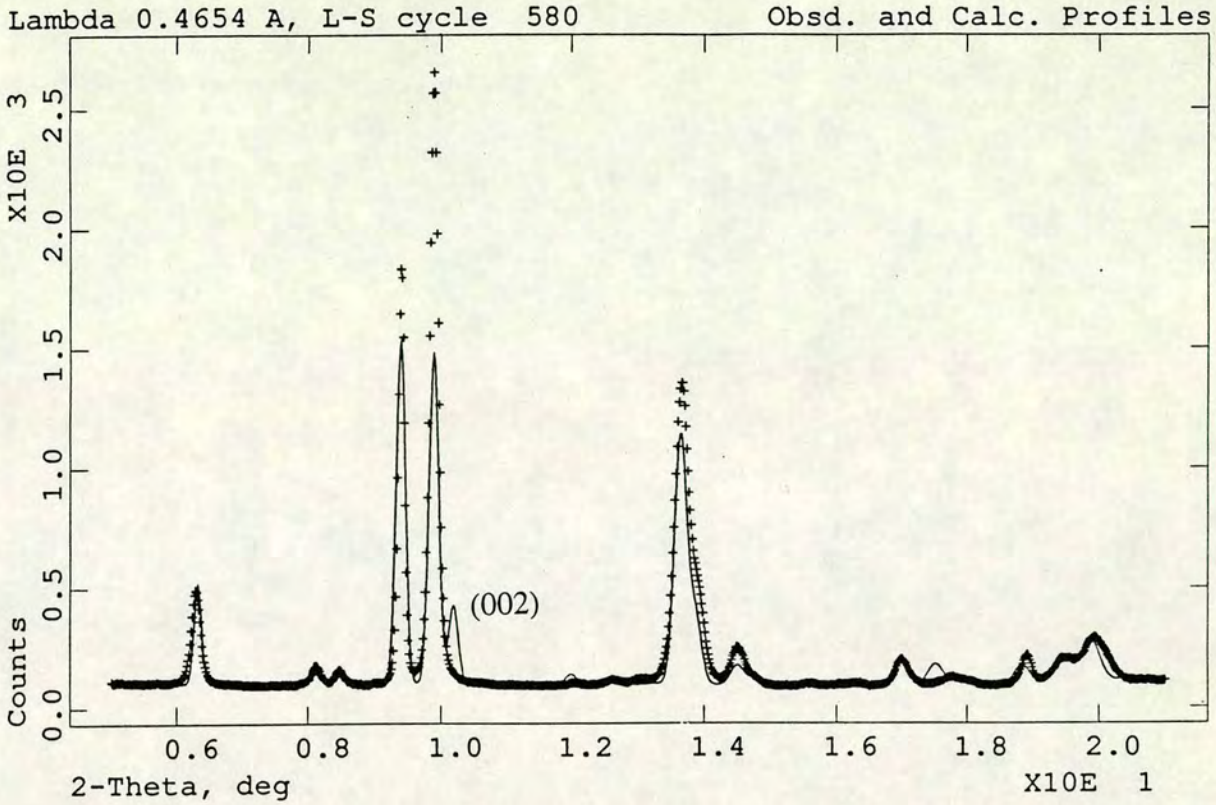

Figure 5.2.1 The calculated profile (shown as a solid line) from full Rietveld refinement of the trial structure to the observed average 1-D profile (shown as +) from HgTe at 13.1 GPa. Note the large misfit to the labelled (002) reflection.

detailed study of the texture observed in HgTe phase IV performed using the techniques and models developed above. A comparison with the texture observed in briefer studies of the isomorphic phases of ZnTe and CdTe is also made.

5.2.2 Sample preparation and basic experimental technique

The sample material was obtained from R. Triboulet, in the form of a specially prepared fine-grained powder (Triboulet, (1986)). The experiments were performed during several different periods of synchrotron time, separated by several weeks. At the beginning of each session new samples were prepared, by grinding the sample material to ensure as fine a powder as possible. Each sample was then loaded into a tungsten gasket hole of size ~150 μm in a diamond-anvil cell, with a full conical aperture of half-angle 40-50°. The pressure-transmitting medium was a 4:1 mixture of methanol:ethanol and the pressure was measured using the ruby fluorescence

technique. The incident x-ray wavelength varied slightly between runs (according to the criteria of other experiments performed simultaneously) but was in the region of ~0.45Å. At the beginning of each experiment the wavelength was calibrated by the station scientist Dr. Bushnell-Wye, using a standard silicon sample. Each sample was then prepared for texture studies in an identical manner. A diffraction pattern from the sample was collected in the ambient pressure zincblende phase on the standard sample mount (as described in chapter 2). This spectra acted as the calibration data for the sample to image-plate distance. The pressure on the sample was raised until the sample was observed (from diffraction spectra) to contain a single-phase, HgTe phase IV, and the sample then transferred onto the rotation stage for texture analysis.

In order to explore fully the texture present in the sample, data were collected with the pressure cell axis at various angles to the incident beam. Obtaining spectra with minimal contamination from gasket material required that the sample was optically aligned (in the straight-on position) to an accuracy of 10μm onto the precision rotation stage. Once aligned, by the procedure discussed in chapter 2, data was recorded by simply rotating the cell up to a maximum of 40° (determined by the steel aperture of the cell). Data collection with the cell inclined to the beam necessarily results in the spectrum being contaminated with the diffraction pattern from the Be backing plates, through which the beam now enters the cell. However, the first Be reflection occurred at a high enough diffraction angle that reliable intensities could be extracted from the first six sample reflections, plus higher order reflections not obscured by the Be. Since this included ample information on all three principal lattice directions, accurate texture modelling was feasible.

5.2.3 Preferred Orientation studies

The diffraction pattern, collected on the standard mount, from the first sample prepared for preferred orientation studies was very similar to that shown in figure 5.2.1. Despite a severe preferred orientation correction being applied during Rietveld refinement, the calculated pattern showed a large misfit to the (002), (200) and (021) reflections, the latter two being observed as far too strong compared to the calculated pattern. The 2-D diffraction pattern showed strong texture around the powder rings, even though the pressure cell axis was along the incident beam. The variation in intensity around the powder rings at $\omega=0^{\circ}$ was much more severe than that observed in either the alumina or silicon experiments, even when those samples were aligned such that the POA was at an angle to the incident beam. The degree of texture around

the powder rings in this image can be seen in figure 3.2, which is a computer enhanced image of data from the first sample of HgTe phase IV. In this scattering geometry, variation in intensity around the powder rings is indicative of either a crystallite distribution which has no axis about which it is radially symmetric, or that there is radial symmetry about some axis (the preferred orientation axis or POA) but that the incident beam is striking the distribution at an angle to POA; i.e. the POA was not coincident with the pressure-cell axis. The latter case could plausibly occur if the alignment of the diamonds was not quite perfect. This would produce on the crystallites a resultant force, which was not along the cell axis. The existing GSAS texture correction, which has been modified by the author in collaboration with R. von Dreele for DAC transmission geometry but with the POA assumed to lie along the incident beam, can not fit such a pattern.

To model the texture in a sample requires the collection of data with different positions of the POA relative to the incident beam. Unfortunately if the POA is not coincident with the pressure-cell axis then any angle that the pressure-cell axis is rotated, which is the experimentally measurable angle, is not identical to the angle of rotation of the POA. Thus in texture studies performed on such a sample by rotating the pressure cell, the location of the POA is unknown and it is difficult to interpret the results. However if an orientation of the pressure cell could be found such that there is no variation in intensity around the powder rings, then the POA must lie coincident with the direct beam. Since the orientation of the POA is then known, texture modelling using the model developed in chapter 2 is more feasible. An other possible explanation of variation in intensity around the powder rings at $\omega=0°$ is that the crystallite distribution is not radially symmetric about the POA. In such a case the corrections calculated by the model are less accurate and contain systematic errors.

Data were collected with the cell inclined at various angles to the incident beam. Figure 5.2.2 shows the average profile in the region of the these reflections as the cell was rotated. It is clear that there was severe preferred orientation of the sample and that in the straight-on position the (002) reflection was being measured as too weak. There was also a substantial increase in the intensity of the (200) reflection relative to the (021). Other reflections such as the (111) were affected by the rotation of the sample but not to the same degree as the (200), (021) and (002). Although data were taken with the pressure cell in many orientations, no position was found such that there was no intensity variation around the powder rings. It is possible that the position of the POA lay beyond the angular access of the pressure cell (~40°)

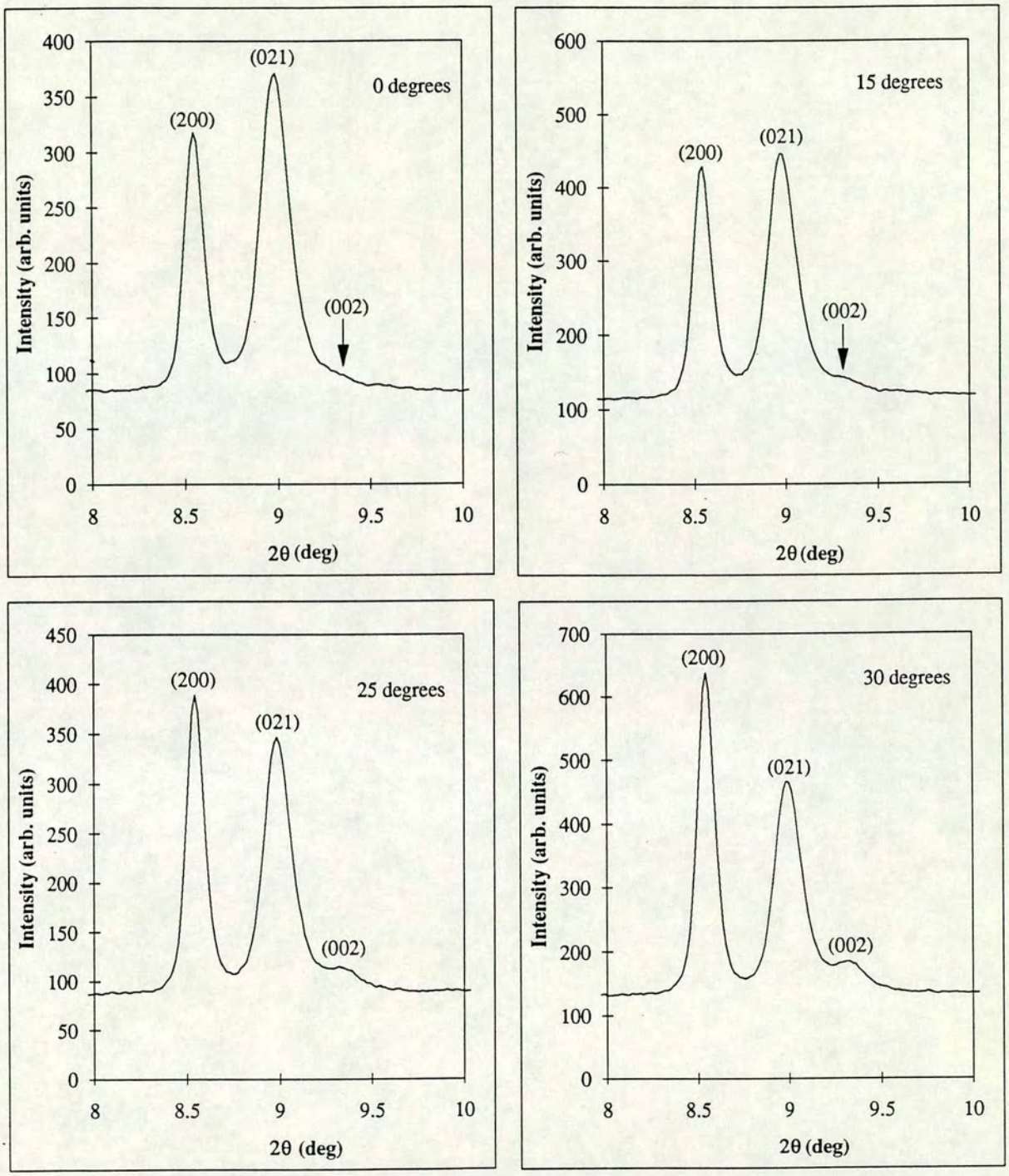

Figure 5.2.2 The low angle region of the observed average 1-D profile from HgTe phase IV with an angle between the pressure-cell axis and the incident beam of: (a) $\omega=0°$, (b) $\omega=15°$, (c) $\omega=25°$ and (d) $\omega=30°$.

although it seems unlikely that it could have been so far from the direction of applied force to the pressure cell. An alternative explanation is that the crystallite distribution was more complex than the simple uniaxial distribution discussed in chapters 3 and 4. A more complex distribution, perhaps one having more than one axis along which the crystallites align (a multi-pole distribution), could be expected to show a considerably different influence on the reflections intensities as the pressure cell was rotated to a simple uniaxial case. However, the preferred orientation studies on the first sample had shown that the sample was indeed highly textured and that the relative intensities of the (200), (021) and (002) reflections were particularly affected by the preferred orientation. Quantitative estimates of the 'true' intensities were not possible with this sample due to the difficulty in modelling what was perhaps a more complex crystallite distribution.

In order to prepare a sample, whose preferred orientation axis (POA) would be coincident with the pressure-cell axis (and hence allow the texture to be more easily modelled), a Diacell DAC with accurately aligned diamonds was used. The 2-D diffraction pattern from a sample in this cell showed less variation around the powder ring indicating that either the POA was close (but not exactly parallel) to the pressure cell axis or that the crystallite distribution was not quite radially symmetric about the pressure cell axis. Ideally the sample should show no variation in intensity around the powder rings with the pressure cell axis along the incident beam. However, due to the difficulty in obtaining such a sample of this phase and the limited synchrotron time available, it was decided to proceed with this sample for preferred orientation studies. The 1-D powder profile of the average intensities around the powder ring (obtained from the Platypus package) from this sample with the pressure cell axis along the incident beam is shown in figure 5.2.3 along with the provisional indexing of the reflections.

Figure 5.2.4 shows the average integrated intensities of the reflections relative to the intensity of the (002) reflection as the pressure cell was rotated. The data are plotted as ratios in order to avoid the use of a scale factor for each data point, which would otherwise be needed to correct for changes in exposure time and synchrotron current. From the figure it is clear that the intensity of the (002) reflection relative to all the other reflections increased with rotation of the pressure cell. In transmission geometry the reflection whose reciprocal lattice vector lies closest to the POD will be diminished the most when the POA lies parallel to the incident beam. Therefore in this sample the angle (ψ) between the POD and the (002) reciprocal lattice vector must

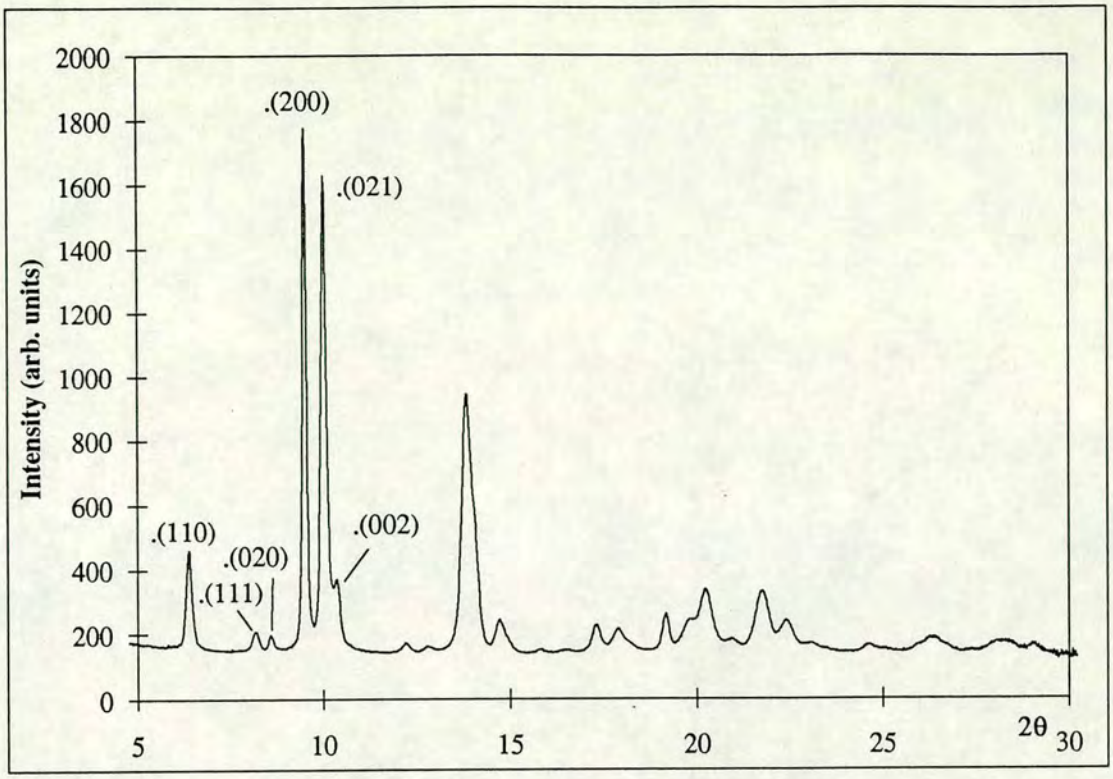

Figure 5.2.3 The observed average 1-D profile from HgTe phase IV in the very carefully aligned Diacell. Note the presence of the (002) reflection (c.f. figure 5.2.1).

have been quite small. Attempts at fitting to the data a preferred orientation model thus focussed on the POD being at a low ψ angle to the (002) reciprocal lattice vector.

At ω=0° clear intensity variation around the powder rings was observed, which implies that the POA was at an angle to the incident beam; i.e. the POA was not quite parallel to the pressure-cell axis. As shown below the variation in intensity around the powder rings at ω=0° could be modelled by assuming the POA to lie at ~-7° to the pressure-cell axis; i.e. $\beta=\omega-7°$ and φ=-90°. Therefore for modelling of the average intensities vs β angle, a 7° offset was subtracted from the measured ω angles. The best fitting model was obtained with the (012) reciprocal lattice vector as the POD. The fit to the data given by this texture model, which assumes that the (012) scattering vector is the POD and that the POA lies at -7° to the pressure-cell axis, is also shown in figure 5.24. The value of the distribution parameter (R) refined to a value of R=0.48. Only the reflections at lower scattering angles than ~12° could be observed all the

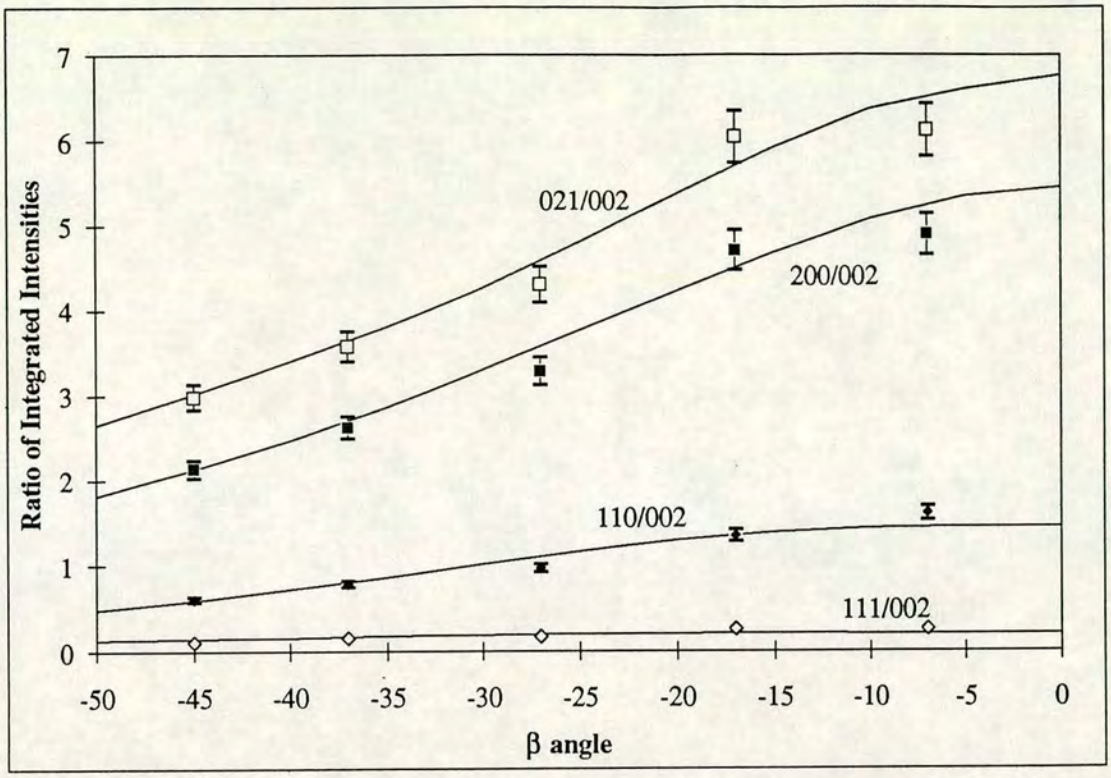

Figure 5.2.4 The ratio of the average integrated intensities of the observed reflections with respect to the intensity of the (002) reflection vs the angle (β) between the POA (assumed to lie at angle of 7° to the pressure-cell axis) and the incident beam for HgTe (Diacell sample). The solid line is the calculated ratio obtained from refinement of the preferred orientation model discussed in the text.

way around the powder rings. Since the intensity around the powder rings is not necessarily uniform, only those reflections whose entire powder rings could be observed were used for the modelling of the changes in average intensities around the powder rings with β angle. The fit to the data can be seen to be good and produced the true intensities of the diffraction peaks given in table 5.2. The true intensities of the (110), (200) and (021) reflections show little relative change compared to the data collected with the pressure cell axis parallel to the incident beam but the true intensity of the (002) reflection exhibits a substantial increase relative to all the other reflections considered.

	Average Intensity at ω=0°	True Intensity from modelling of average intensities.
(110)	160	67
(111)	26	10
(020)	19	26
(200)	489	155
(021)	612	192
(002)	100	100

Table 5.2 The true intensities of the reflections from HgTe phase IV obtained from modelling of the average intensities around the powder rings (from the Diacell sample) using the model discussed in the text. Also given are the observed average intensities with the pressure-cell axis parallel to the incident beam (ω=0°).

The degree of intensity variation around the powder rings with $\omega \neq 0°$ was very severe. Although in the average intensities around the ring the intensity of the (200) reflection was always at least a factor of three larger than that of the (002) reflection, in some sectors of the powder rings the (002) was observed as more intense than the (200). Figure 5.2.5 shows the observed intensities of the group of reflections close to the (002) in the same sector of the powder ring as the angle between the pressure cell axis and the incident beam was increased. By ω=38° (the maximum angle that can be reached by this cell) there was substantially higher intensity in this section of the (002) ring. The difference in the relative intensities of the (200) and (002) reflections between the spectra observed at ω=0° and that at ω=38° is quite striking. It is clear that there was severe preferred orientation of the sample and that the true intensity of the (002) reflection was considerably stronger than the observed value in the straight-on position, which has to be used to collect data for Rietveld refinement (in order to avoid Be contamination).

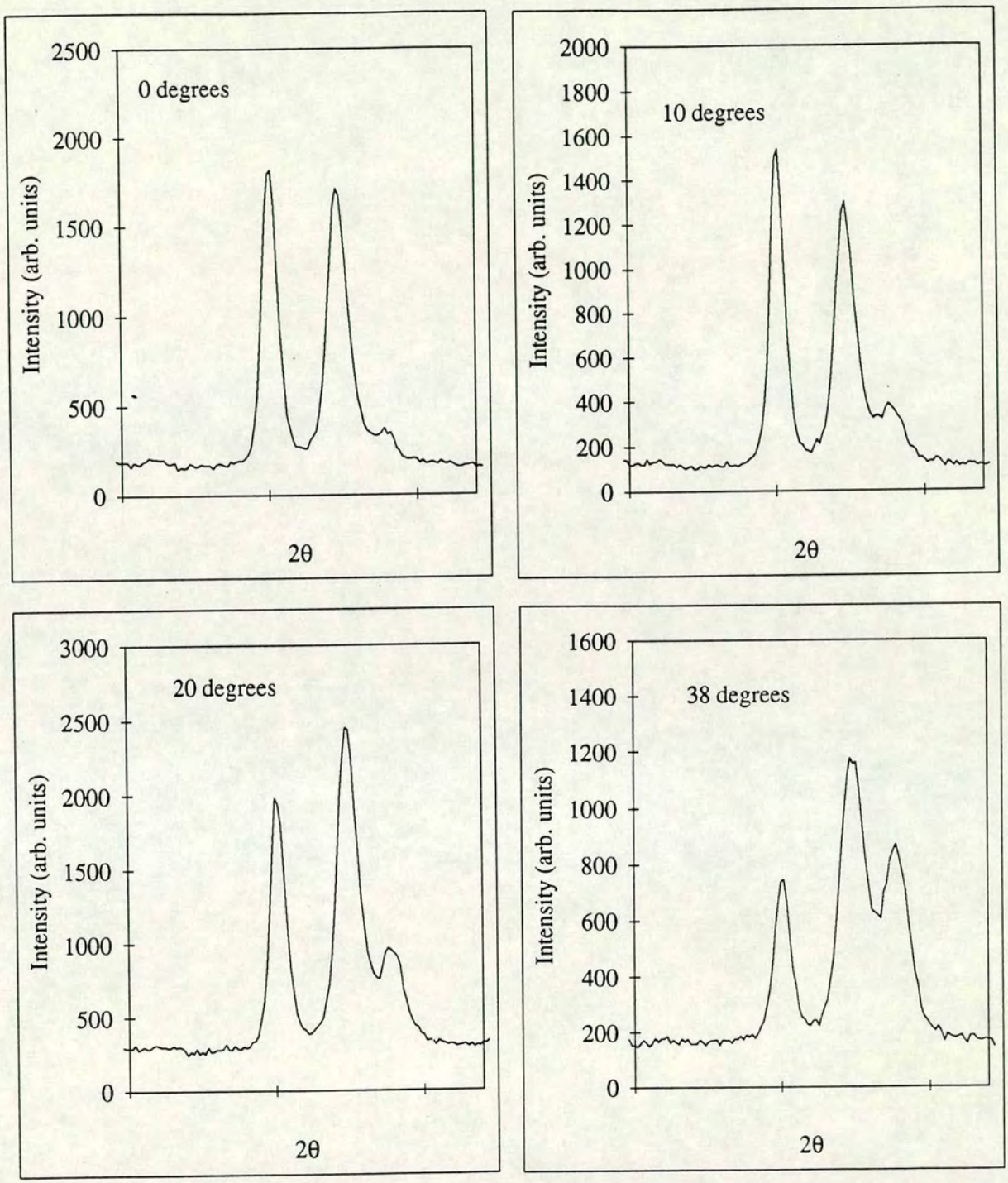

Figure 5.2.5 The low angle region of the observed intensity in one sector of the diffraction pattern from HgTe with an angle between the pressure-cell axis and the incident beam of: (a) ω=0°, (b) ω=10°, (c) ω=20° and (d) ω=38° .

Modelling of the intensity variation around the powder rings was much more difficult than modelling the variation in average intensity with β angle. The position around a powder ring of the maxima and minima of the calculated intensity is influenced strongly by the orientation of the POA. The POA was not quite coincident with the pressure cell axis and so, in this sample, it was impossible to ascertain exactly the orientation of the POA relative to the incident beam. Unfortunately any uncertainty in the orientation of the POA makes modelling of the intensity variation around powder rings very difficult. If the orientation of the POA relative to the incident beam is incorrect, then the positions of the calculated maxima and minima around the powder rings will be shifted and refinement of the model will be unstable. The best fitting model to the data was found using a trial and error approach to be given by introducing a -7° offset for the ω angle; i.e. $\beta=\omega-7°$ and $\varphi=-90°$. Figure 5.2.6 shows the fit to the intensities around the powder rings of the (002), (200) and (021) reflections given by the preferred orientation model used for the average intensities to the data obtained with an angle of 38° between the pressure-cell axis and the incident beam. Despite the large variation in intensity around this powder ring, the match to the data for the (002) reflection is good. The agreement between the calculated and observed intensities of the (200) and (021) reflections is less satisfactory, although the predicted degree of variation around the powder ring is of the correct order. In cases where the orientation of the POA is uncertain then modelling of the intensity variation around the powder rings is less accurate than modelling of the change in average intensity with orientation of the sample. The average intensity is relatively unaffected by small uncertainties in the orientation of the POA and so in such circumstances is much more accurate.

In conclusion, it is clear that the samples studied here of HgTe phase IV formed with very strong preferred orientation, which caused the intensity of the (002) reflection to be observed in the straight-on position as much too weak compared to all the other reflections. The relative intensities of the other reflections were less affected by the preferred orientation although the (200) and (021) were clearly observed as too strong.

5.2.4 A comparison with the texture found in the isomorphic phases of ZnTe and CdTe

Similar studies on the preferred orientation observed in the orthorhombic phases of ZnTe and CdTe were performed, although in less detail due to restricted synchrotron

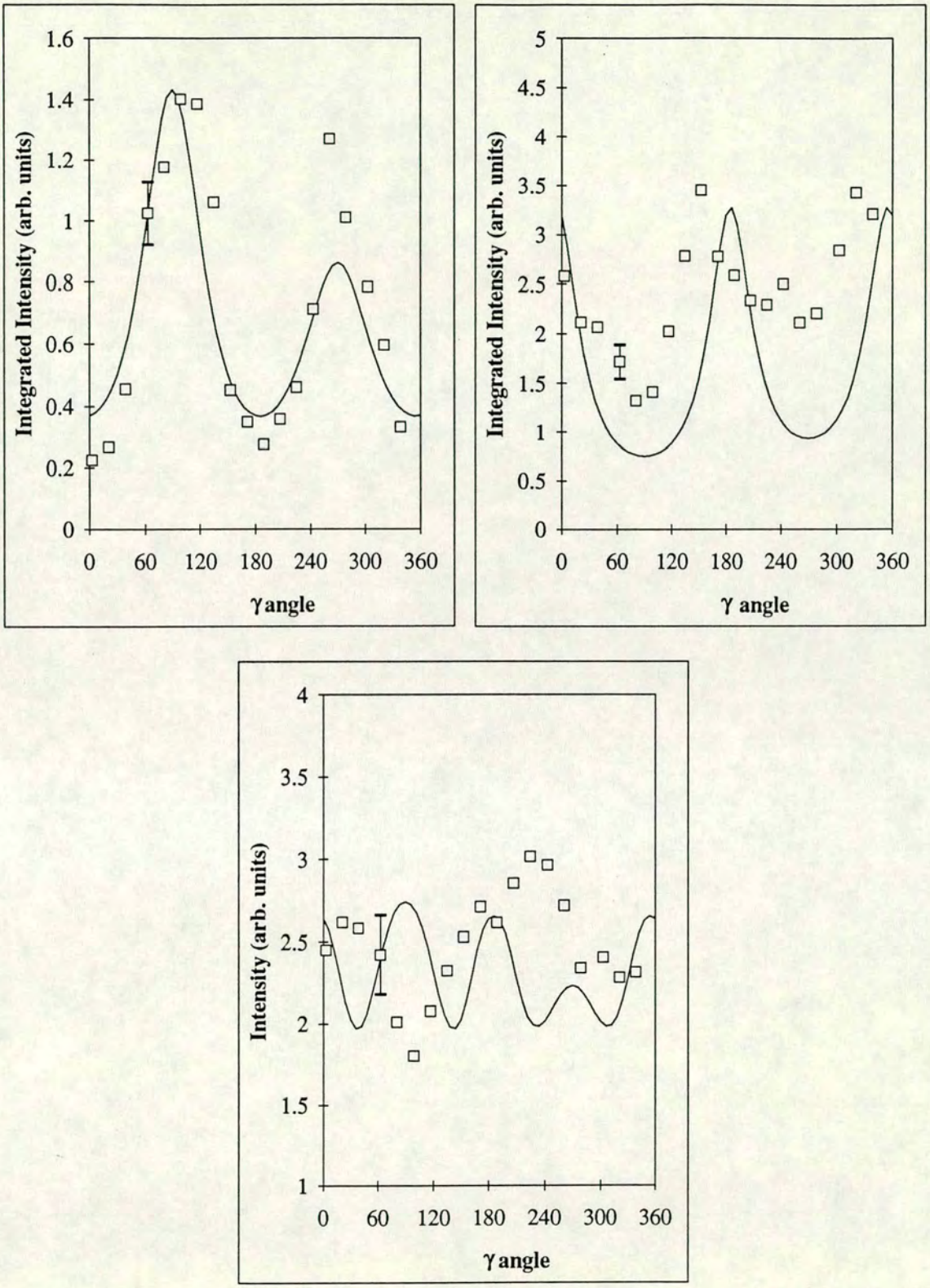

Figure 5.2.6 The observed intensity around the (200) (021) and (002) reflections of HgTe phase IV (Diacell sample) with an angle of 38° between the pressure-cell axis and the incident beam. The solid line is the calculated variation obtained from refinement of the preferred orientation model discussed in the text. For clarity, error bars have been drawn only for the data point at γ=60°.

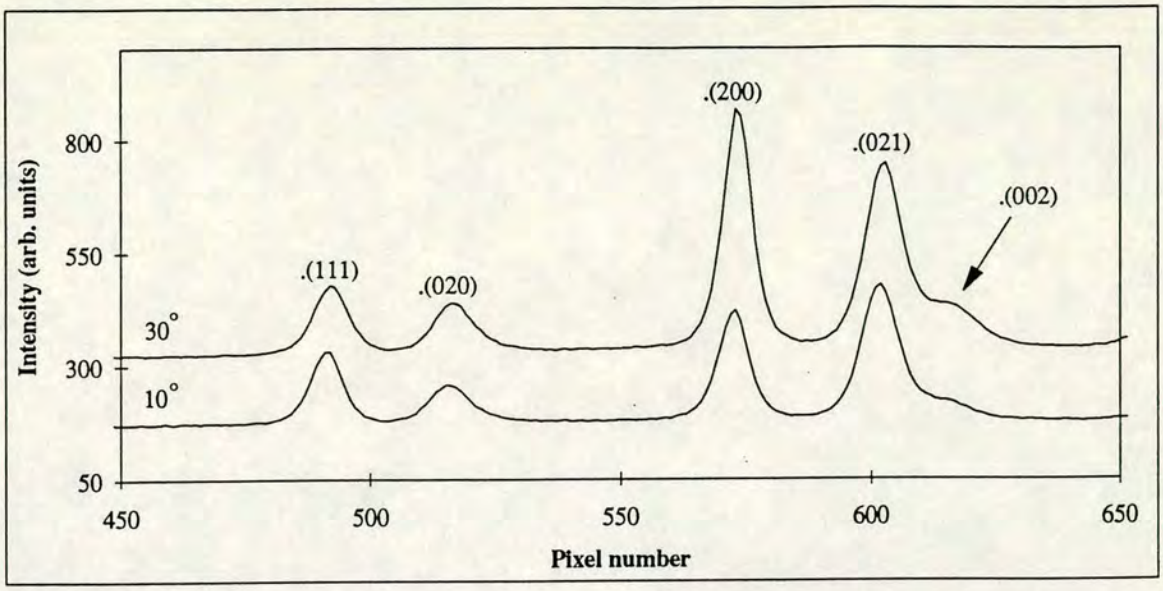

Figure 5.2.7 The low angle region of the observed average 1-D profile from ZnTe with an angle between the pressure-cell axis and the incident beam of ω=10° and ω=30°. Note the increase in intensity of the (002) reflection between the two angles.

time. The samples used in these studies showed intensity variation around the powder rings even with the pressure-cell axis along the incident beam (c.f. with the first HgTe sample). The Rietveld fit to the data collected from both these compounds using the standard image-plate set-up had showed almost identical misfits as those shown in HgTe. Figure 5.2.7 shows the low angle region of the spectra collected from ZnTe with 10° and 30° respectively between the pressure cell axis and the incident beam. As with in HgTe, The relative intensity of the (002) reflection increased in intensity relative to the (021) and (200) reflections as the pressure cell was rotated. As with the HgTe, the (111) and (020) reflections were affected much less.

Similar changes in intensity to both HgTe and ZnTe were observed in CdTe as the pressure cell was rotated (see figure 5.2.8a). The profiles of 5.2.8a show the average intensities around the powder rings with angles of 0° and 30° between the pressure cell axis and the incident beam. As the pressure cell was rotated the (002) reflection could be observed visually in the 2-D image, although in these average profiles the (002) reflection is barely visible. Interestingly the 2θ positions of some of the diffraction lines changed with the orientation of the pressure cell. The (021) reflection

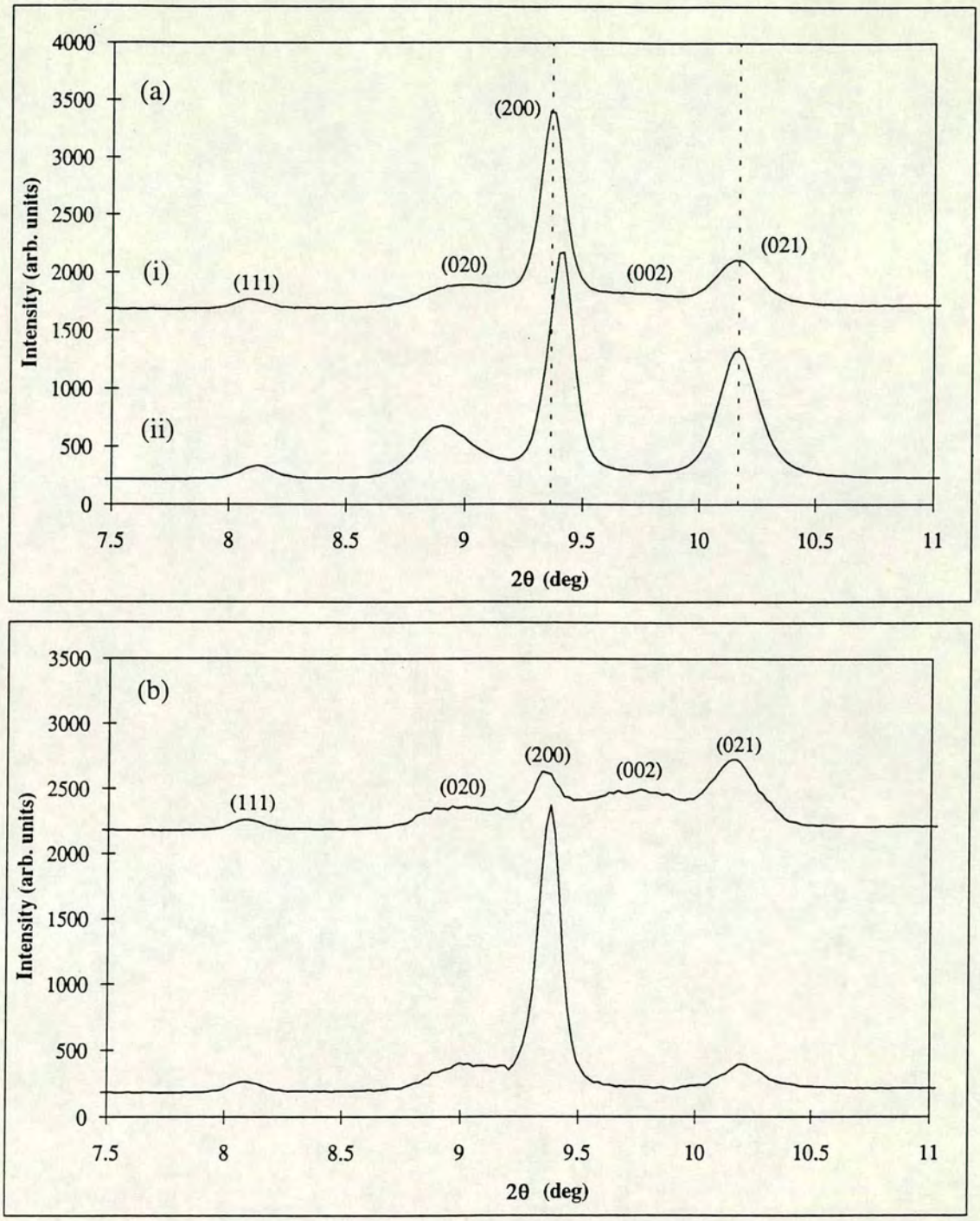

Figure 5.2.8 (a) The low angle region of the observed average 1-D profile from CdTe with an angle between the pressure-cell axis and the incident beam of (i) $\omega=0°$ and (ii) $\omega=30°$ .The dotted vertical lines are guides to the eye to enable comparison of peak positions. (b) The low angle region of the observed intensity in different sectors of the same diffraction pattern from CdTe with an angle between the pressure-cell axis and the incident beam of $\omega=30°$. Note the remarkable difference in intensity of the (200) reflection between the two sectors.

appears unaffected indicating that the shift in the position of reflections such as the (200) could not be due to miscentering of the pressure cell on the rotation axis. A possible explanation of this effect is sample deviatoric stress, which as been shown to cause marked (hkl) dependent shifts in peak position (Singh and Kennedy, (1974)). This sample showed strong variation in intensity around the powder rings, as illustrated by figure 5.2.8b. The profiles in this figure display the observed intensity in different sectors of the same 2-D image at ω=30°. The difference in intensity of the (200) reflection between the two sectors is quite remarkable and the (002) can be clearly observed in the first sector.

As expected both CdTe and ZnTe show similar preferred orientation to that observed in HgTe and it seems clear that these phases of all three compounds have related structures. Such strong preferred orientation may be indicative of a strong anisotropy in the crystallite shape or the result of a similar transition mechanism, although unlike CdTe and HgTe, which transform to this phase from the NaCl structure, ZnTe transforms to this phase directly from the cinnabar structure.

Section 3: A Preferred Orientation study of InSb

An exhaustive study (Nelmes *et al*, (1993)) of the structures of the high-pressure phases of the semiconductor InSb had revealed that the orthorhombic Pmm2 phase (InSb P4), which occurs above ~35 GPa, consisted of a sub-unit cell (~3Å x 3Å x 5Å) and a much larger super-unit cell, which is formed by a complex buckling of the atomic planes within the sub-cell. The existence of the super-cell was revealed by the observation of weak super-cell diffraction peaks (see figure 5.3.1). The exact description of the super-cell depends critically on the intensity of the weak super-cell peaks and so it was vital to identify if any preferred orientation was present in the sample. In addition, this phase forms as a spotty powder, even if the ambient pressure phase is a carefully prepared fine powder. Collecting data in different sample orientations would also act as a check on whether the averaging around the powder rings performed by the Platypus package was successful on such a spotty diffraction pattern.

Samples of InSb P4 were prepared in a Merrill-Bassett DAC on the standard image-plate mount. Once a suitable sample had been obtained it was transferred to the rotation mount and diffraction patterns collected with various angles between the pressure-cell axis and the incident beam. With the cell axis parallel to the beam (ω=0°) there was no intensity variation around the powder rings, although the reflections were quite spotty. As the pressure cell was rotated, the average relative intensities of the diffraction peaks remained constant and no variation around the powder rings was observed (see figure 5.3.1). Thus there was little or no preferred orientation in the sample. This conclusion supported the trial super-cell structure, which depended on the observed intensities being exactly correct (i.e. Rietveld refinement to the observed data required no texture correction).

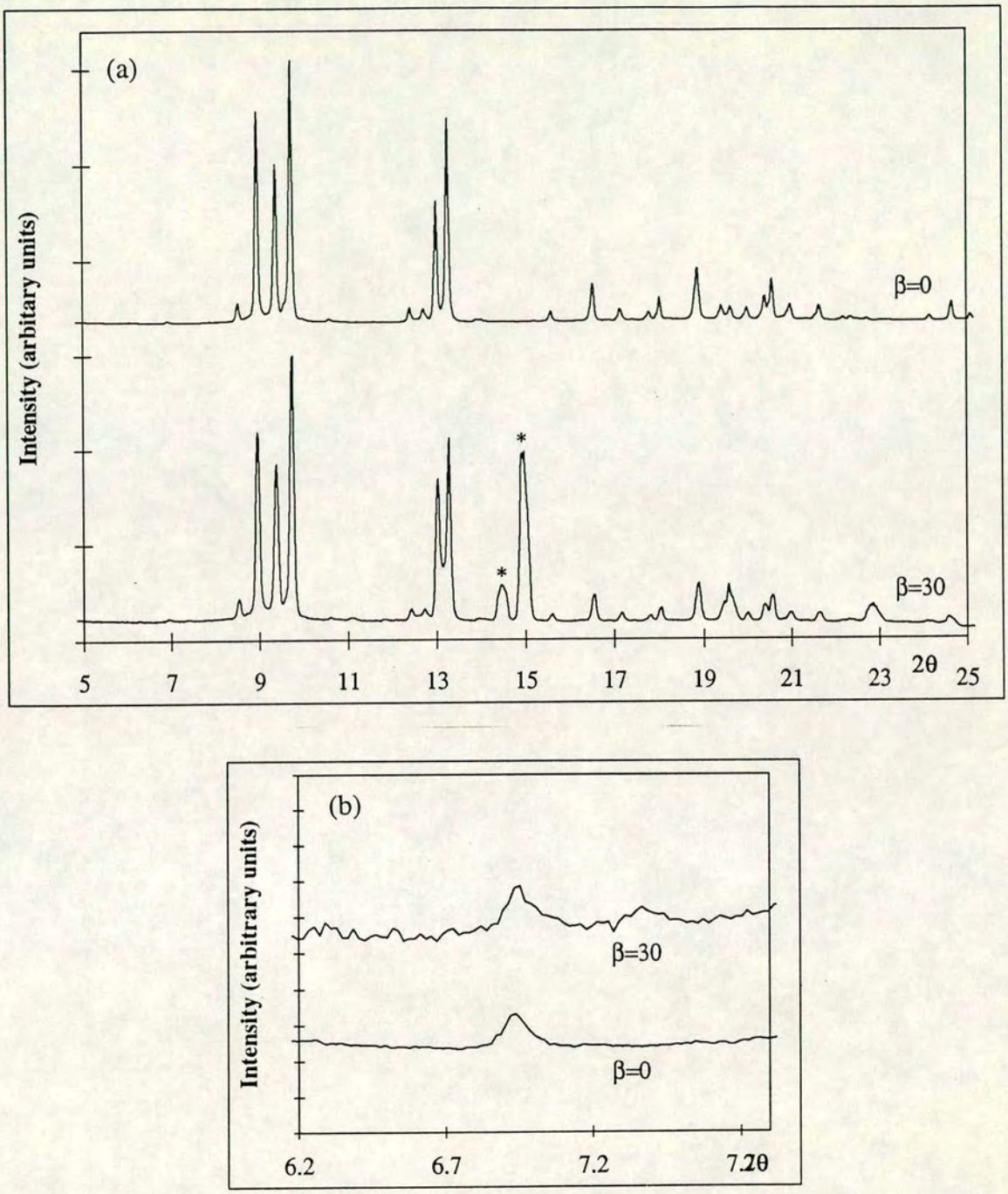

Figure 5.3.1 (a) The observed average 1-D profile from InSb P4 with an angle between the pressure-cell axis and the incident beam of: (i) $\beta=0°$, and (ii) $\beta=30°$. The diffraction peaks marked with * are from the Be backing discs. Note the weak super-cell peak at $2\theta\approx6.8°$. (b) the region around the weak super-cell peak at $2\theta\approx6.8°$ with an angle between the pressure-cell axis and the incident beam of: (i) $\beta=0°$, and (ii) $\beta=30°$. Note that there is no change in intensity with sample orientation.

CHAPTER 6

Applications of Texture Modelling under Pressure

Introduction

This chapter presents the results from high-pressure structural studies of semiconductors, in which the preferred orientation modelling techniques developed in the earlier chapters of this thesis have been used. The focus in this section is on the use of the information gained from preferred orientation modelling as part of high-pressure crystallographic work on semiconductors under pressure. Results from two main studies are presented: a detailed examination of the high-pressure phases of HgTe and a study of possible phase transition mechanisms between high-pressure phases of Si.

Section 1

The high-pressure phases of HgTe

6.1.1 Introduction

This section presents a structural study of three high-pressure phases of HgTe: the hexagonal cinnabar phase (whose crystal structure was known, although detailed atomic coordinates had not been determined) and two previously unsolved phases (although other workers had provisionally identified possible lattices). These studies were performed as part of a systematic examination of the phase diagrams of the II-VI semiconductors by the University of Edinburgh group in collaboration with a group from the Université of Paris VI.

6.1.2 HgTe under pressure

Under pressure, HgTe undergoes several changes in crystal structure and chemical coordination. A phase transition under pressure in HgTe, from the ambient zincblende structure, was first found by Bridgman, who detected a volume discontinuity at ~1.3 GPa in compressibility measurements (Bridgman, (1940)). This transition produces, as the structure moves from being a semimetal to a direct-gap semiconductor, an abrupt change in resistivity (Blair and Smith, (1961)). The semiconducting phase was determined to have the hexagonal cinnabar structure (Mariano and Warekois, (1963)), which was thought until recently to be peculiar to the mercury chalcogenides (Miller *et al*, (1981), Huang and Ruoff, (1984)). The cinnabar structure is well known in the phase diagrams of HgS (Aurivillius, (1950), Huang and Ruoff, (1983)), HgO (Aurivillius and Carlson, (1958)), and HgSe (Mariano and Warekois, (1963), Huang and Ruoff, (1983)), but has now been discovered by the Edinburgh group in CdTe (Nelmes *et al*, (1993)) and by our collaborators from the Université of Paris VI in ZnTe (San Miguel, (1994)). In HgS and HgO, the cinnabar phase occurs at ambient pressure, and full structural studies have been performed for both (Aurivillius, (1950), Aurivillius and Carlson (1958)). Figure 6.1.1 shows the prototype cinnabar structure, that of HgS, where it can be seen that the structure consists of a spiral up the crystallographic c-axis of alternate Hg and S atoms. The spacing along the c-axis between atoms in the chain is fixed by the space-group symmetry ($P3_121$) at c/6. In common with HgSe and CdTe, HgTe transforms to cinnabar under pressure (1.4

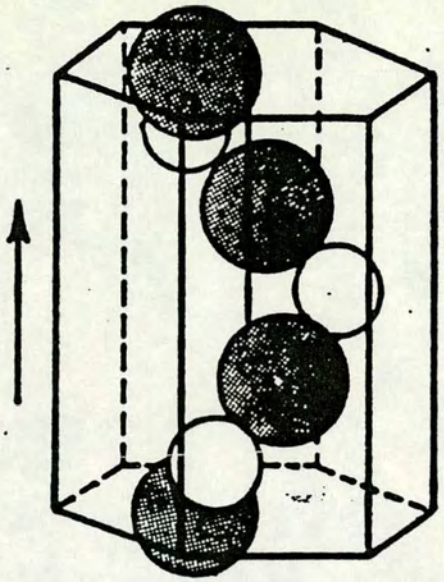

Figure 6.1.1 The crystal structure of HgS cinnabar, showing the spiral of alternate Hg and S atoms up the c-axis. The symbols are: ○ Hg, ● Te (from Huang and Ruoff, (1983))

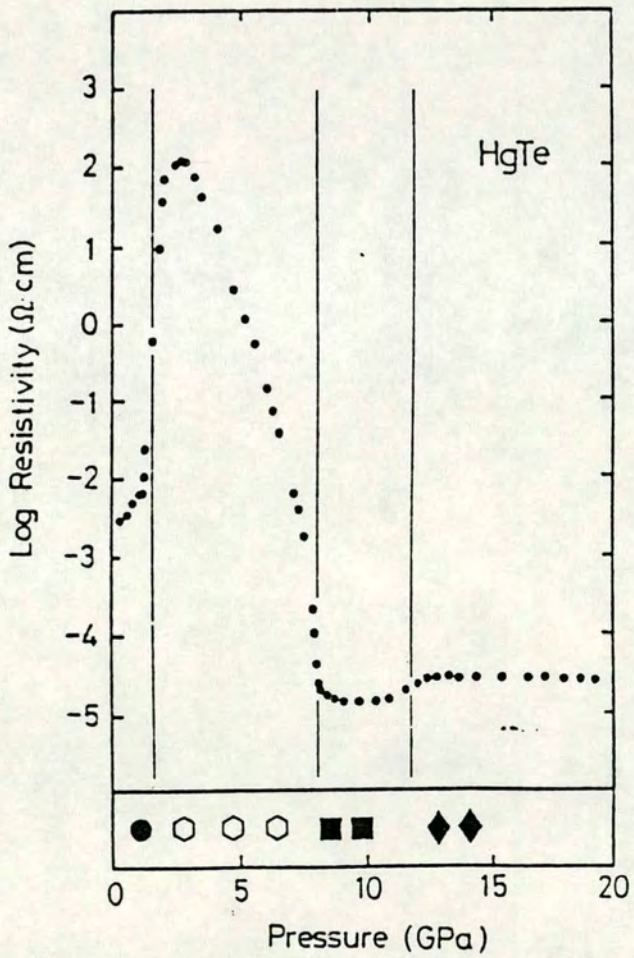

Figure 6.1.2 A graph of Resistivity versus pressure for HgTe. The solid vertical lines mark the boundaries between the various phases, which are shown by the following symbols: ● zincblende, ⬡ cinnabar, ■ NaCl, ◆ unknown (from Onodera *et al*, (1982))

GPa) from an ambient-pressure zincblende phase (Mariano and Warekois, (1963)). As the HgTe cinnabar phase only forms under pressure, the detailed structure of this phase had never been determined.

Further pressure increase in HgTe brings about a transformation to the rocksalt structure at 8 GPa (Onodera *et al*, (1982), Huang and Ruoff, (1983)) and then starting at 11.5 GPa, to another phase (Spain *et al*, (1980), Onodera *et al*, (1982), Ohtani *et al*, (1982), Qadri et al, (1990)), phase IV, first identified as having a β-tin (Werner *et al*, (1983), Huang and Ruoff (1984)) or orthorhombic structure (Huang and Ruoff, (1985)). The latter interpretation was later modified to body-centred tetragonal structure, probably different from β-tin (Huang and Ruoff, (1985). Electrical studies (see figure 6.1.2) have shown the transition at 8 GPa is to a metallic phase and that the 11.5 GPa transition corresponds to a change to a second metallic phase of slightly higher resistivity (Ohtani *et al*, (1982), Onodera *et al*, (1982)). Above 38 GPa there is evidence of a further transformation to an as yet unidentified phase (Huang and Ruoff, (1985)).

6.1.3 A high-pressure structural study of the cinnabar phase of HgTe

There has been particular interest in the cinnabar phase of HgTe and other mercury chalcogenides and efforts have been made to understand the role of this phase as an intermediate stage in the zincblende to NaCl transformation (Miller *et al*, (1981), Huang and Ruoff (1983), Tedenac *et al*, (1993)). However, the atomic coordinates of the Hg and Te atoms within the cinnabar structure have never been determined and discussion has had to be based on the structure of HgS cinnabar. As part of a systematic study by the Edinburgh University group in collaboration with a group from the University of Paris VI of the II-VI semiconductors under pressure, it was decided to perform a detailed diffraction study of HgTe in its cinnabar phase to determine the atomic coordinates, site ordering and structural pressure dependence. In this section the results of this study are presented and discussed in the context of other II-VI materials. The structural results are presented in two parts: the first discusses in detail the structure of HgTe at 3.6 GPa, just inside the pressure region where a pure cinnabar phase was observed, and the second presents results on the structural pressure dependence.

Experimental Techniques

The basic experimental techniques used to perform this study are as described in Chapter 2 of this thesis. The sample material was obtained from R. Triboulet, in the form of a specially prepared fine-grained powder (Triboulet et al, (1986)). Four different samples were prepared, each loaded into a diamond-anvil cell with a full conical aperture of half-angle 40-50°. The pressure-transmitting medium was a 4:1 mixture of methanol:ethanol, and the pressure was measured using the ruby fluorescence technique (Piermarini *et al*, (1975)). The data were collected using the standard image-plate set-up on Station 9.1 at SRS Daresbury. The incident x-ray wavelength was 0.4654Å, calibrated using a standard silicon sample. The structural results presented were all obtained from full Rietveld refinement (Rietveld, (1969)) of the integrated profiles using the program GSAS (Larson and Von Dreele, (1985)).

Results and Discussion

The structure at 3.6 GPa

Figure 6.1.3 shows the 1-D profile obtained after azimuthal integration of the 2-D image obtained at 3.6 GPa from one of the samples. The transition from zincblende to cinnabar results in a reproducible microstructural effect on the peak profiles, which vary significantly in breadth. Reflections with l>>h, k are preferentially sharp which is consistent with the average crystallite being significantly longer along the crystallographic c-axis. This may be important for the actual mechanism of the transformation. Structure refinement was carried out with the Hg atoms on the 3a sites of space group $P3_121$ at (u, 0, 1/3) and the Te atoms on the 3b sites at (v, 0, 5/6), starting from the coordinates of the HgS cinnabar structure at ambient pressure (Aurivillius, (1950)). The variable coordinates u and v refined to 0.641(1) and 0.562(1), respectively, and the lattice parameters refined to a=4.383(1)Å and c=10.022(2)Å. These values, and the refined scale factor, peak-shape parameters (including a model for anisotropic widths, as above) and thermal motion parameters give the fit shown in figure 6.1.3. The results obtained from the other samples agree within the estimated standard deviations.

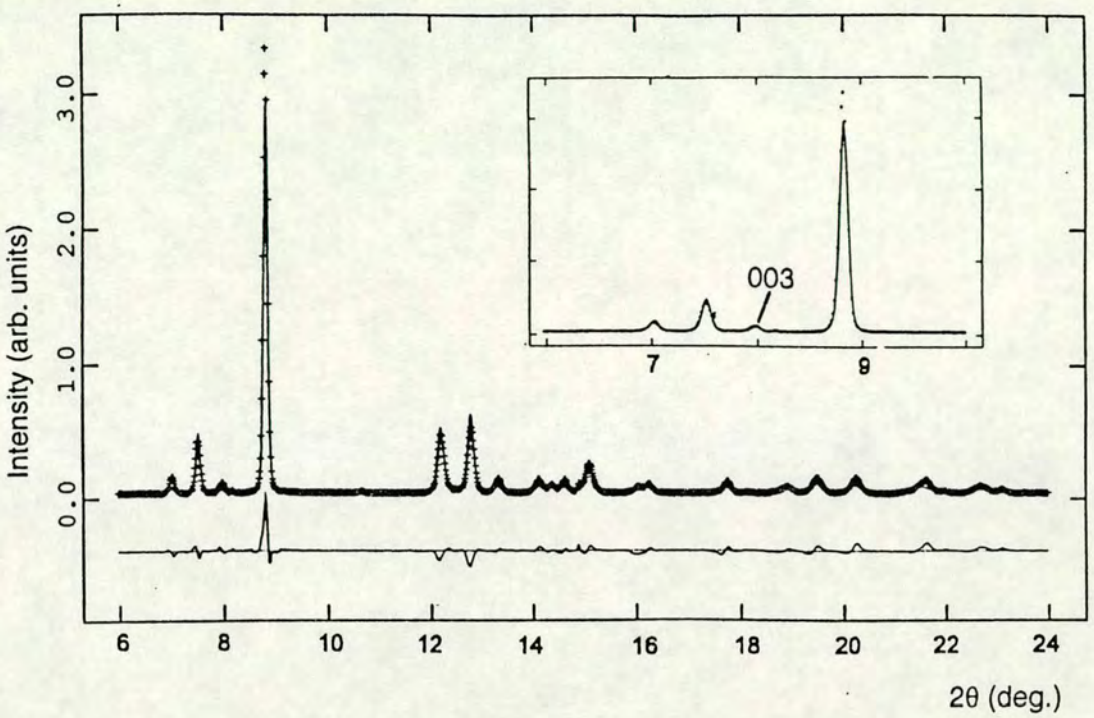

Figure 6.1.3. The integrated profile of a powder pattern collected from HgTe at 3.6 GPa. The solid line shows the fit to the data (crosses) obtained in structure refinement. The difference between the observed and calculated profiles is also displayed. Part of the profile is enlarged in the inset to show the (003) reflection.

The (003) reflection is clearly observed, as shown in the inset in figure 6.1.3. Since this reflection arises from the difference in scattering between the 3a and 3b sites, its presence establishes that the structure is site-ordered. As a further check, the occupancies were allowed to refine freely but showed no movement away from full site-order. The assignment of Hg to the 3a site and Te to 3b was checked by interchanging the Hg and Te atoms and refining first with the occupancies free and then fixed. In the former case the occupancies refined to values consistent with interchanging the atoms back to the original positions, and in the latter case the calculated pattern showed some significant discrepancies with the data. Thus the site assignment can be stated with confidence.

At 3.6 GPa the c/a ratio was observed to be 2.287, close to the value of 2.27 obtained by Qadri *et al* (1990). However, Werner *et al* (1983) reported a significantly different value of 2.222 at 2.6 GPa. The observed change in c/a with pressure is small (Qadri *et al* (1990)) so this discrepancy could not result simply from the difference in sample conditions. The authors observed only 4 reflections which they index as (101), (102), (110), and (201); but a better fit to the relative d-spacings is obtained with the last of these reflections indexed as (200). If the data presented here is re-refined with the same mis-indexing, a c/a ratio of c/a=2.23 (at 3.6 GPa) is obtained, close to the value found by Werner *et al*. Qadri *et al* (1990) also report a study of a $Hg_{0.8}Cd_{0.2}Te$ alloy and obtain a c/a ratio of 2.297 at 3.6GPa. This is ~0.025 larger than they found for HgTe, and in a study of CdTe by the Edinburgh University group (Nelmes *et al*, (1993)) the c/a ratio for CdTe was found to be 0.098(1) larger than that of HgTe (at 3.6GPa). Hence, the c/a ratio appears to vary approximately in proportion to the Cd content.

The refined values of the atomic coordinates and lattice parameters of HgTe are presented in table 6.1, and compared with results for HgS, HgO, HgSe and CdTe. The structure of HgTe is shown in xy projection in figure 6.1.4b. The atoms form infinite -Hg-Te-Hg-Te- spirals along the c-axis, with the two nearest-neighbour distances in the spirals, the a-bonds (2.732(4)Å), being shorter than the b- and c-bonds linking atoms in adjacent spirals (2.995(4)Å and 3.460(5)Å, respectively). The two different bond angles in the spirals, Hg-Te-Hg and Te-Hg-Te, are 104.2(2)° and 165.6(2)° respectively. These distances and angles are also included in table 6.1.

Both HgTe and CdTe have similar fractional coordinates, which are significantly different from those of either HgS or HgO. This difference in fractional coordinates may be related to the fact that HgS and HgO, in contrast to HgTe and CdTe, both form the cinnabar structure at ambient pressure. Figure 6.1.4a shows the cinnabar structure of HgS for comparison with HgTe in figure 6.1.4b. In HgS, the spirals along the c-axis have a smaller radius: the a-bonds, between nearest neighbours in the spirals, are much shorter than the b- and c-bonds. Thus the HgS structure is regarded as 2-coordinated. It has been assumed that the same is true of HgTe (Huang and Ruoff, (1984)), but our results reveal substantial structural differences. The greater radius of the spirals in HgTe (figure 6.1.4) means that atoms in adjacent spirals are closer together than in HgS. The a- and b-bondlengths of HgTe are then similar (table 6.1), and the coordination is close to 4-fold. The same is found in CdTe

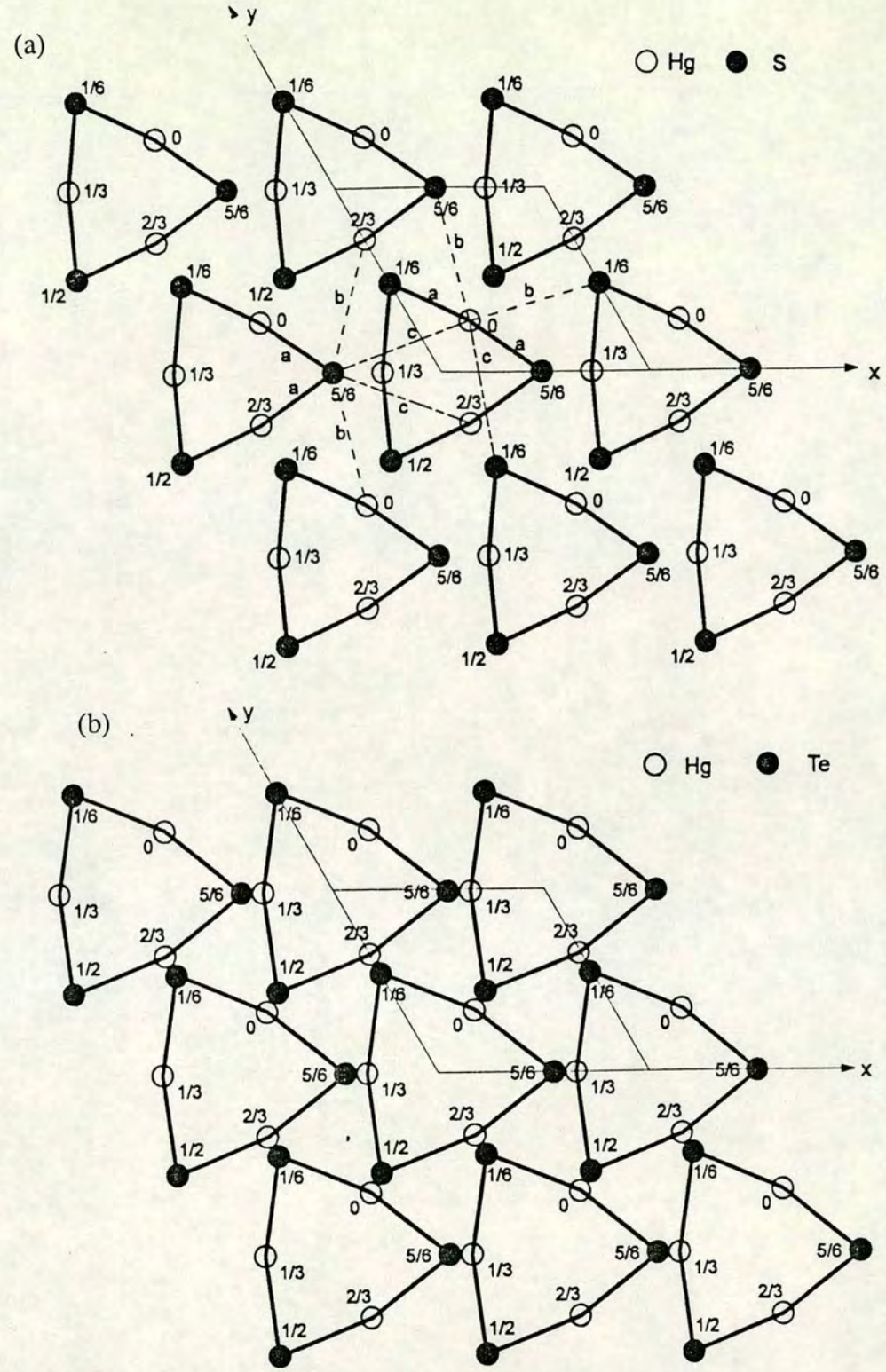

Figure 6.1.4. (a) The cinnabar structure of HgS at ambient pressure shown in projection onto the xy plane. The z-coordinate is given for each atom, and the nearest-neighbour contacts (two a-bonds, two b-bonds, two c-bonds) are shown for one of the Hg atoms (○) and one of the S atoms (●). (b) The cinnabar structure of HgTe at 3.6 GPa shown in the same way. The nearest-neighbour contacts can be identified by comparison with (a).

MX	HgS at ambient pressure[16]	HgO at ambient pressure[18]	HgSe at 1.5 GPa[4]	HgTe at 3.6 GPa This work	CdTe at 3.6 GPa[20]	NaCl structure
a (Å)	4.14	3.577	4.32	4.383(1)	4.292(2)	
c (Å)	9.49	8.681	9.68	10.022(1)	10.235(3)	
c/a	2.292	2.427	2.24	2.287(2)	2.385(2)	2.449
u	0.720(3)	0.745	unknown	0.641(1)	0.641(2)	0.667
v	0.480(10)	0.460		0.562(1)	0.564(2)	0.667
nearest-neighbour distances, (Å)						
a-bonds	2.36(5)	2.03(2)		2.732(4)	2.724(4)	⎫
b-bonds	3.10(5)	2.79(2)		2.995(4)	2.971(5)	⎬ all equal
c-bonds	3.30(5)	2.90(3)		3.460(5)	3.414(5)	⎭
bond angles :						
M-X-M (°)	105.2(2.0)	108(2)		104.2(2)	104.6(3)	90
X-M-X(°)	172.4(1.7)	176(3)		165.6(2)	166.1(4)	180

Table 6.1. Comparison of the lattice parameters (a and c), and refined atomic coordinates (u and v) for the cinnabar phases of HgS, HgO, HgSe, HgTe, and CdTe. (Only lattice parameters are known for HgSe.) Also given are the nearest-neighbour distances and the angles between a-bonds at the X atom (O, S, Se, or Te) and the M atoms (Hg or Cd). The final column shows cubic NaCl referred to the cinnabar unit cell. Estimated standard deviations are quoted in parentheses if they are known.

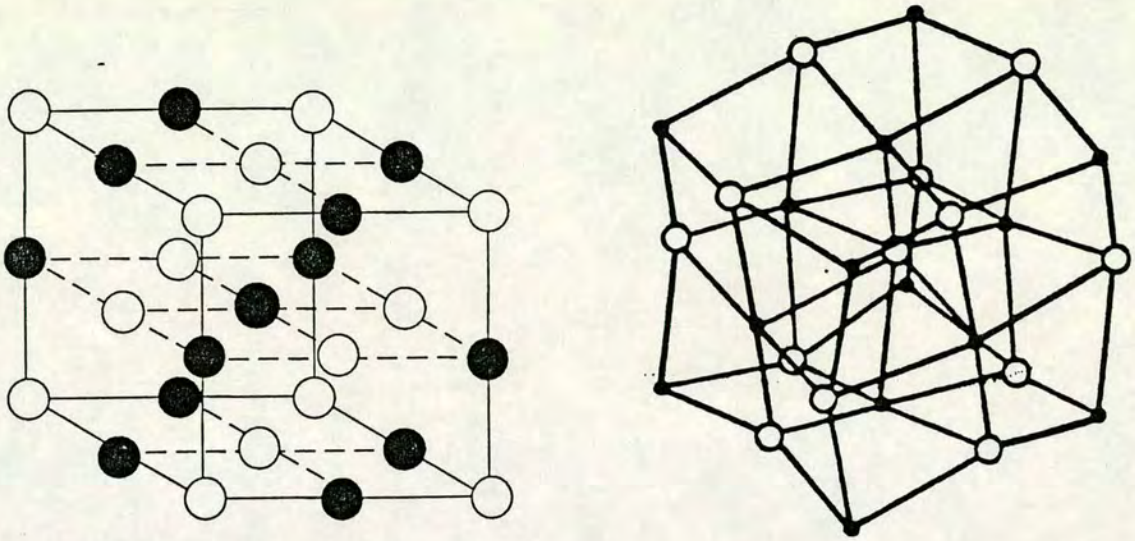

Figure 6.1.5 The NaCl structure and the cinnabar structure of HgTe shown as a form of distorted NaCl. The symbols are: ○ Hg, ● Te

(Nelmes *et al*, (1993)). Taking all six nearest-neighbour contacts into account, HgS and HgO can thus be described as 2+4 coordinated, and HgTe and CdTe as 4+2. The latter is closer to the 6-fold coordination of NaCl. This may partly reflect the fact that HgTe and CdTe at 3.6 GPa are approaching the transition to the NaCl phase (at 8 GPa and ~4 GPa, respectively), while HgS at ambient pressure is far from its transition at 13 GPa (Huang and Ruoff, (1983)).

The cinnabar structure can be viewed as a distorted form of the NaCl structure (Huang and Ruoff, (1985)). This is illustrated in figure 6.1.5, which shows the cinnabar structure for HgS in a form suitable for comparison with the NaCl structure (also shown). On further pressure increase, HgTe transforms to the NaCl structure and it is worth while to examine in detail the relationship between the two structures. The final column of table 6.1 gives values for the NaCl structure referred to the hexagonal unit cell of cinnabar. The cinnabar structure becomes equivalent to that of

NaCl when c/a=√6=2.449 and u=v=2/3. In terms of the c/a ratio, HgTe is further from NaCl than CdTe, although the bond angles in HgTe are marginally closer to those of the NaCl structure than in CdTe. It is clear that a transition from the cinnabar phase to the NaCl structure could occur by a continuous distortion of both the lattice parameters and the atomic positions. Since no bonds between atoms need be broken in the transition, it is possible that the transition could be second-order.

All five of the known cinnabar structures (table 6.1) have c/a less than the value of 2.449 corresponding to a cubic unit cell. This distortion alone has the effect of reducing the bond angle at the anion, M-X-M, below 90°. However, in a 2-coordinated environment this angle is expected to be closer to tetrahedral, while the X-M-X angle remains close to 180° (Aurivllius (1950)). This requires the v coordinate to differ from 2/3 by more than the u coordinate, as observed : the values of u and v in table 6.1 all have u > v, with a mean of ~0.6 rather than 2/3. If the M-X-M and X-M-X angles are indicative of the coordination, it has to be remarked that their values in HgTe are almost the same as in HgS, in contrast to the differences seen in nearest-neighbour distances. Also in terms of the bond angles, HgTe (and CdTe) is as distorted from NaCl as HgS.

The Pressure Dependence of the Structure of HgTe Phase III

In order to determine the pressure dependence of the lattice parameters and atomic coordinates, data were collected at suitable pressure intervals in the cinnabar phase and after the transition to the NaCl structure. Figures 6.1.6a and 6.1.6b show the a and c lattice parameters of the cinnabar phase versus pressure and figure 6.1.6c shows the pressure dependence of the unit cell volume of the cinnabar phase. The volume change at the transition from the cinnabar phase to the NaCl structure (at 8 GPa) was found to be 6.6 %, which is in good agreement with the value of ~8% for the transition to the NaCl phase given by Werner *et al* (1983). Thus the transitions from zincblende to cinnabar (Jayaraman *et al*, (1963)) and then to the NaCl structure are both definitely first-order. The pressure dependence of the c/a ratio is shown in figure 6.1.6d. Also marked on figure 6.1.6d is the value of c/a, which is equivalent to the NaCl structure. Although the c/a ratio can be seen to trend towards the NaCl value (c/a=2.449), the transition to the NaCl phase occurs significantly before c/a reaches 2.449.

The values for the lattice parameters, unit cell volume and volume changes at the transitions are in good agreement with published values. The principal sources of

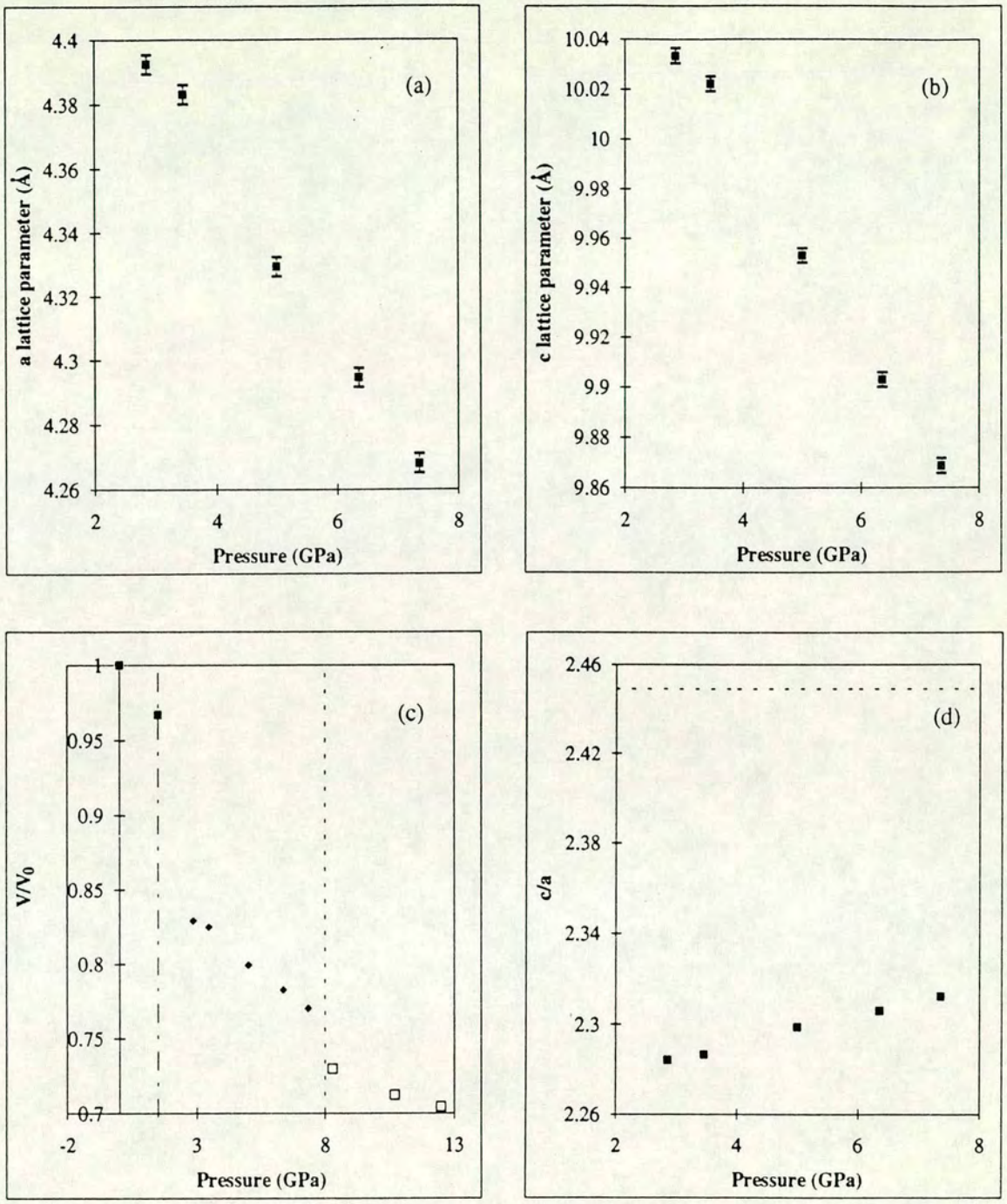

Figure 6.1.6 (a) The a lattice parameter vs pressure. (b) The c lattice parameter vs pressure. (c) a graph showing V/V_0 of the zincblende phase (■ points), the cinnabar phase (◆ points) and the NaCl phase (□ points). V_0 is the volume of the cubic phase at ambient pressure. (d) the c/a ratio vs pressure. The value for the NaCl structure is shown as a dotted line.

error in the lattice parameter results given here are likely to be uncertainty in the sample to image-plate distance and errors in pressure measurement. Calibration of the sample to image-plate was, as described in chapter 2, by the standard method, which has been shown to be accurate in many image-plate studies by the Edinburgh group. Although considerable care was taken to ensure that the pressure cells used had equilibrated after the pressure had been changed, variations in the pressure, while the diffraction pattern was collected, were often greater than the precision of the ruby measurement system. The pressures given here are averages of the measured pressure before and after the diffraction pattern was obtained and the errors on the pressure values are probably of the order of 0.2 GPa. Assessment of the errors on the atom coordinates is more difficult, as there are no similar studies on materials at high-pressure against which this study can be compared. An EXAFS study (San Miguel, (1993)) by our collaborators at the University of Paris VI have produced results in good agreement with those presented here. The error bars on the graphs of lattice parameters and fractional coordinates have been drawn at twice the quoted error given by the refinement package. From the scatter in the data this would seem to be a reasonable estimate of the precision.

The pressure dependence of the atomic coordinates is shown in figure 6.1.7. The transition to the NaCl phase occurs before the Hg u parameter or the Te v parameter reach 2/3, as required in the NaCl structure. The atomic coordinates from the figure above produce the interatomic distances shown in figure 6.1.8 Also marked on this figure are the values of the nearest-neighbour distances in the zincblende and NaCl phases. At the transition from the zincblende structure to the cinnabar phase it is striking that the nearest-neighbour distance is maintained (to a first approximation) across the transition. This has been explained (Miller *et al*, (1981), Tedenac *et al*, (1993)) in terms of a possible transition mechanism between the zincblende and cinnabar structures. They suggest that the transition occurs by a shearing motion on the (110) planes of the zincblende phase, a process which conserves the nearest-neighbour distance between the two phases.

As might be expected, the c-bonds and b-bonds (which are the bonds between spirals) decrease strongly with pressure but the a-bond, which is the bond within the Hg-Te spiral, is much less compressible. In the transition from cinnabar to the NaCl structure, all three nearest-neighbour distances shown in figure 6.1.8 must become equal. There is a general trend towards all three bond lengths becoming equal in the cinnabar phase but the transition occurs well before this point. Interestingly, the

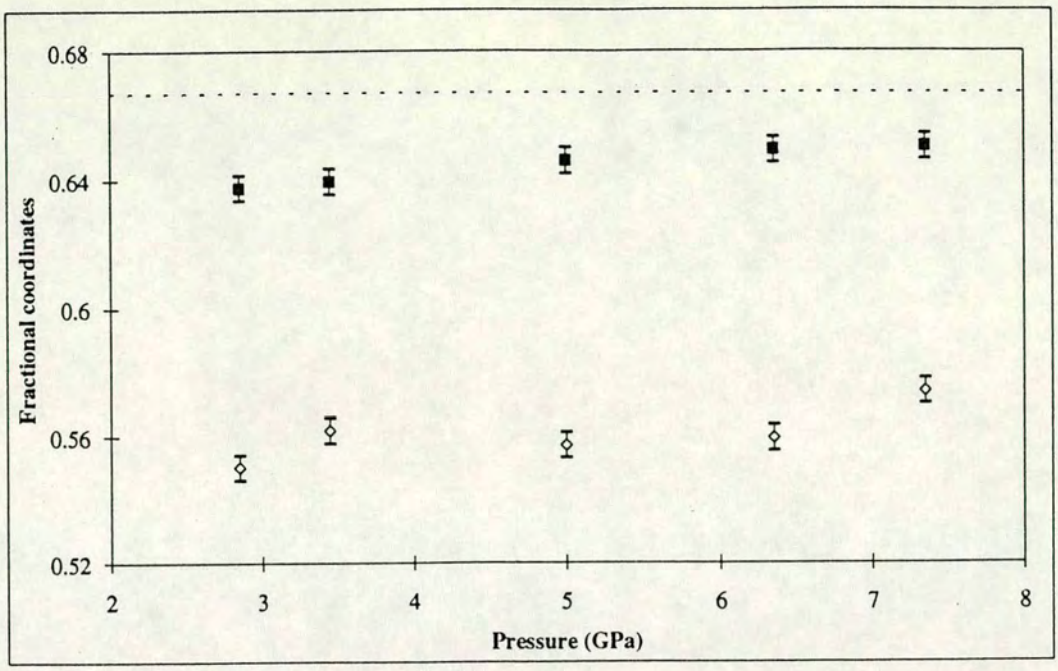

Figure 6.1.7 The pressure dependence of the u and v fractional coordinates of the HgTe cinnabar structure. The value of the NaCl structure is drawn as a dotted line.

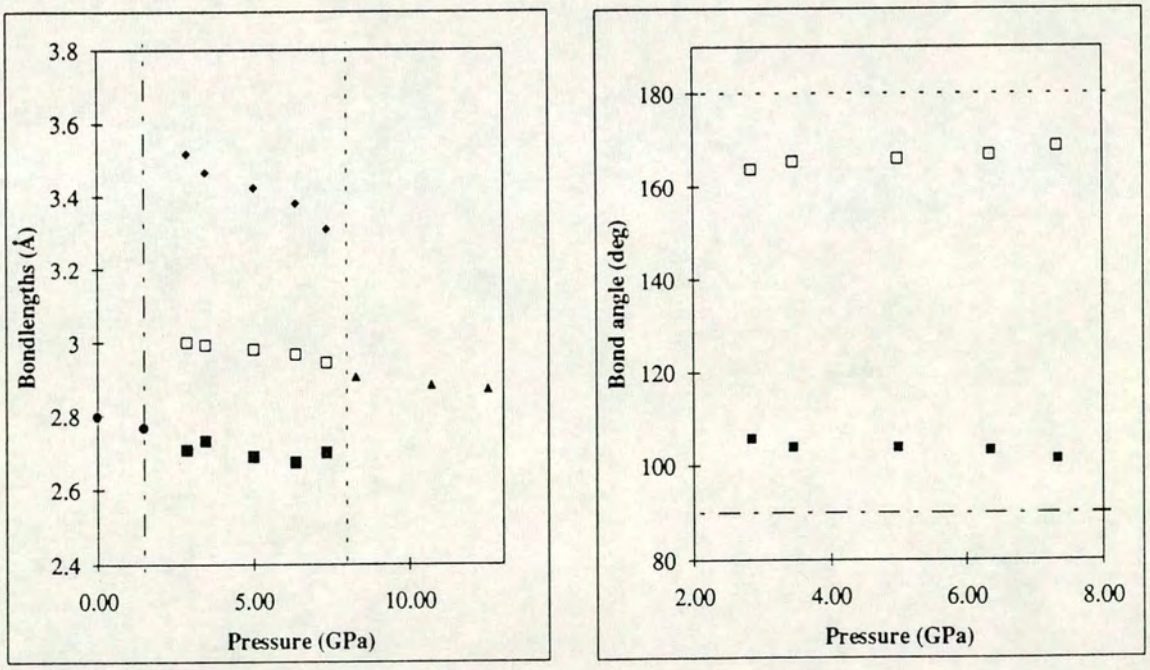

Figure 6.1.8 (a) The pressure dependence of the bondlengths for the zincblende phase (● points), the cinnabar phase (■ = a-bonds, □= b-bonds, ◆= c-bonds) and the NaCl phase (▲ points). (b) The pressure dependence of the bond-angles of the cinnabar phase of HgTe.

b-bond length at ~3 Å would seem to be preserved across the transition to the NaCl structure, in which it represents a/2 of the cubic phase. Similarly, the bond angles (shown in figure 6.1.8b) move towards the values of the NaCl structure but do not reach the cubic values before the transition takes place.

Conclusions

The principal aim of the high-pressure structural study of the cinnabar phase of HgTe was to determine the crystal structure and pressure dependence of the structure of this phase. The use of angle-dispersive diffraction techniques with an image-plate area detector have allowed data of unprecedented accuracy to be collected from HgTe under pressure. This has enabled the structure of the cinnabar phase of HgTe to be determined and valuable information on the transition to the NaCl phase to be extracted.

The results presented in this section have shown that the structure of HgTe in its cinnabar phase is quite different from that of HgS. In terms of nearest-neighbour distances the HgTe structure is closer to 4-coordinated than 2-coordinated. Such results are of considerable importance for *ab initio* calculations of HgTe and other II-VI materials. At present, calculations on materials containing elements with as many electrons as Hg are less accurate than studies on materials, such as Si. It is clear, that the future development of calculations on these technologically important materials depends crucially on accurate experimental data, against which numerical studies can be tested. The unexpected differences between the cinnabar phases of HgS and HgTe, the consequent differences in coordination and the evolution of the structure of the cinnabar phase of HgTe with pressure invite a revised theoretical treatment of this phase and its role in the zincblende-to-NaCl transition.

6.1.4 A high-pressure structural study of HgTe phase IV.

This section presents a structural study of a previously unsolved high-pressure phase of HgTe, phase IV. This structure had eluded solution because of extreme sample preferred orientation, which occurs reproducibly in this phase. Results from a preferred orientation study of data from HgTe phase IV were presented in chapter 5. Drawing on the information gained from that study, this section reports the structure

of HgTe phase IV and discusses the structure in relation to the NaCl phase, from which phase IV transforms.

Experimental techniques

Diffraction data were collected on station 9.1 at the Synchrotron Radiation Source, Daresbury, using the image-plate set-up as discussed in chapter two. The careful preparation of the samples and data collection methods have already been described in chapter five. For the main preferred orientation studies and collection of data for structural refinement the incident x-ray wavelength was 0.4652(1)Å, calibrated using a standard silicon sample.

In order to determine the site-ordering of the structure and to try and distinguish between different possible structures, additional studies of the effect of the change in x-ray scattering factors due to anomalous dispersion at the Hg L-edges and at the Te K-edge were performed. Collecting data at absorption edges is a powerful probe of any scattering due to differences in scattering factor between different sites in the lattice. Any changes in relative intensities of the reflections between data collected at wavelengths close to and far from an absorption edge must be due to variations in the relative scattering factors. Far from an absorption edge of either atom the difference in scattering factor between Hg and Te is proportional to the difference in the number of electrons of each atom. Since Hg has 80 electrons and Te 52, any scattering due to differences in scattering factor between different sites in the lattice will be quite strong. Close to an edge of a particular atom the scattering factor of that atom will be modified by the anomalous dispersion component and these changes in x-ray scattering factor can be very large. Figure 6.1.9 shows the calculated variation in the real part of the anomalous component (FP) of the Hg scattering factor with wavelength of incident radiation. Close to the L-III edge FP≈-20 and the effective difference in the number of electrons is reduced to ~28. Thus if the structure is site-ordered, any reflections that contain a component of difference scattering will be reduced close to the edge. If the structure of a binary compound is 100 % disordered each site in the structure is occupied by a 50% component from each atom and the scattering factor from all sites is equal. Thus in a disordered compound no change in relative intensities will be observed.

For the anomalous dispersion studies, a new sample was prepared in a similar manner to that described in chapter two. Data were collected at the Hg L-II and L-III edges

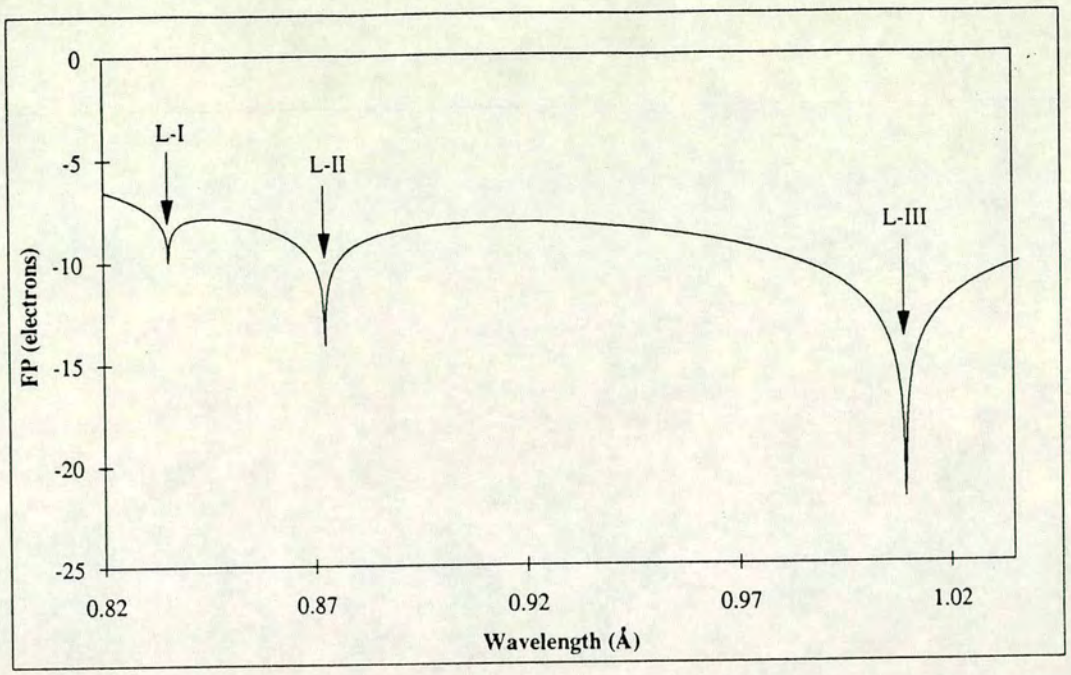

Figure 6.1.9 The calculated real part of the Hg anomalous scattering factor versus wavelength of radiation (close to the Hg L-edges).

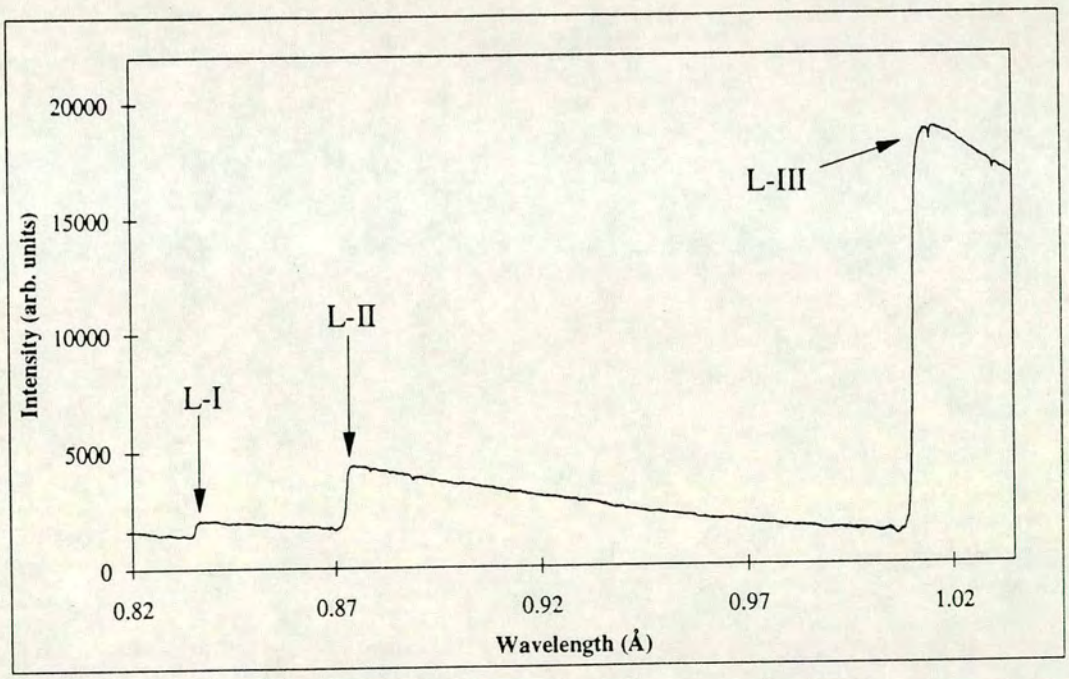

Figure 6.1.10 The observed transmittance (as measured by ion chamber) through a HgTe capillary sample versus incident wavelength. Note the strong variations in transmittance at the Hg L absorption edges.

and at the Te K-edge. The wavelength at these edges was set by measuring with an ion-chamber the transmittance of the x-ray beam through a HgTe capillary sample. Figure 6.1.10 shows the observed intensity in the wavelength region close to the Hg L-edges as the wavelength was varied by scanning the monochromator angle. The three Hg L-edges can be clearly identified. To reduce sample absorption and fluorescence the diffraction data were collected at wavelengths just above the L-II and L-III edges (at the points marked on figure 6.1.10). The wavelength at these points was calculated by the following method: the measured wavelength of the edge in question and the assumed wavelength of the Hg L-edges (from literature) enabled any offset in the monochromator angle to be determined. The monochromator angle was then changed to the desired position relative to the absorption edge (from the data drawn in figure 6.1.10). From this monochromator angle and the known offset, the wavelength at this point was calculated. The wavelengths at the marked positions in figure 6.1.10 were 0.8793(2)Å and 1.0126(2)Å at the L-II and L-III edges respectively. For anomalous dispersion work at the Te K-edge, the wavelength was set by a similar method to be 0.3905(2)Å.

The data presented in this section were collected from the second sample of chapter five (in the carefully aligned Diacell) and the new sample prepared for anomalous dispersion work. The results from all other samples are consistent with the structural parameters given. The structural results presented here were all obtained from full Rietveld refinement of the integrated profiles using the program GSAS, which includes a model to calculated the changes in x-ray scattering factor at the absorption edges.

Results and Discussion

As the pressure is increased in the NaCl phase, phase IV begins to appear at 11.5 GPa. Figure 6.1.11 shows a sequence of the low angle regions of diffraction spectra as the pressure is increased: from a pure NaCl phase (a), through a mixed phase region (b c and d), to a pure phase IV (e). By 13 GPa (as shown by the disappearance of the NaCl (200) reflection) the rock salt phase had completely transformed. The phase IV pattern indexes on an orthorhombic unit cell with lattice parameters a=5.6076, b=6.2115, and c=5.1514 at 17.5 GPa. Earlier attempts at studying this phase have indexed the structure as tetragonal (Werner *et al* (1983) or orthorhombic (Huang and Ruoff, (1983)). Werner *et al* suggested, on the basis of 4 observed reflections, that this phase has the β-tin structure, which has a body-centred tetragonal

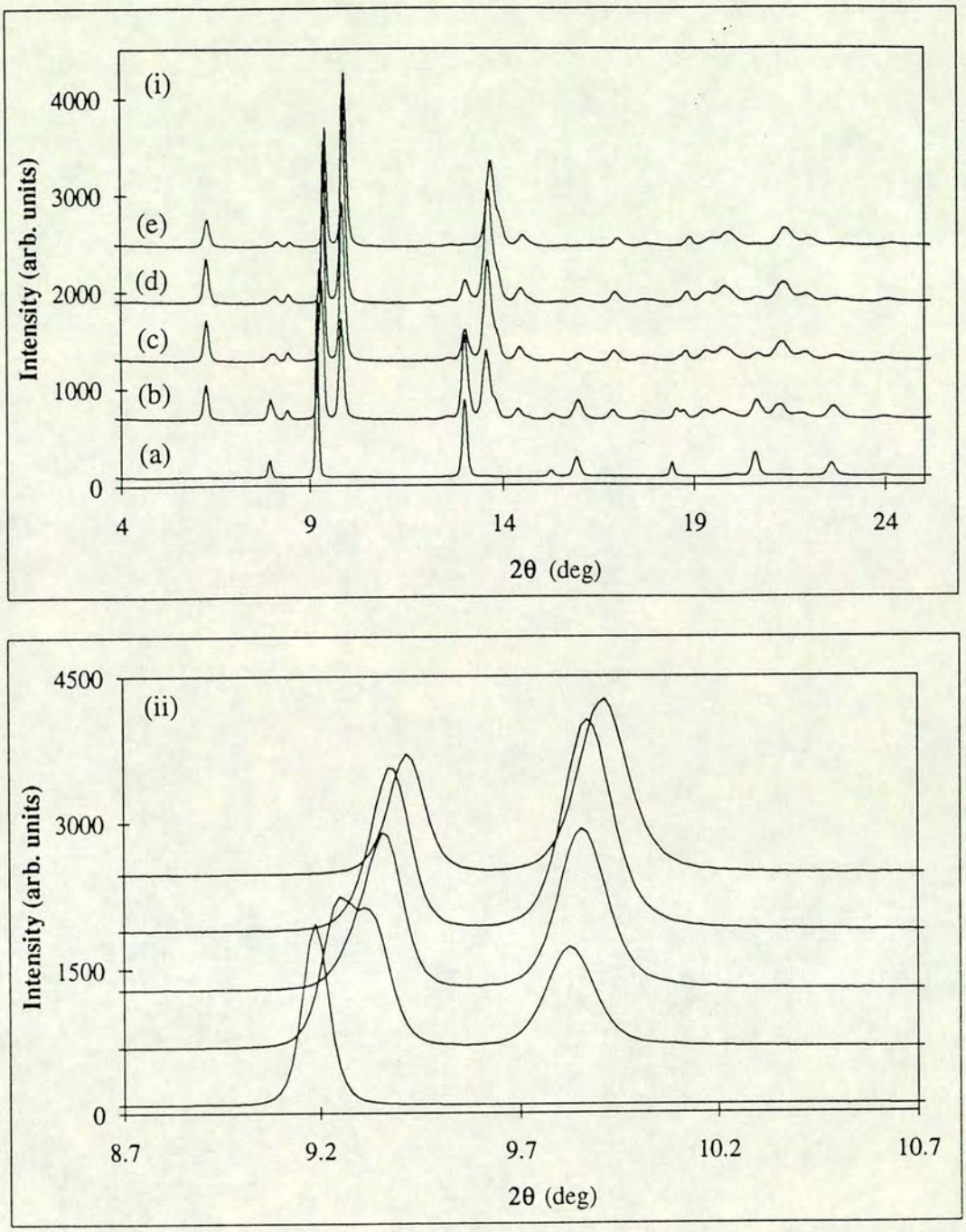

Figure 6.1.11 (i) The low angle region of the observed 1-D powder patterns from HgTe as the pressure was increased from (a) a pure NaCl phase (b), (c) and (d) a mixed NaCl and phase IV region to (e) a pure phase IV pattern. (ii) a highly magnified figure of the region of figure 6.1.11 close to the two strongest diffraction peaks. Note the disappearance of the NaCl peak at 9.2° with pressure. Note that an arbitrary constant intensity has been added to each data set in order to separate the graphs and improve clarity.

structure. Later work by Huang and Ruoff (1985) indexed the structure as body-centred tetragonal with a=5.524Å and c=2.973Å at 17 GPa, although the fit of their published d-spacings to this lattice is very poor.

From the lattice parameters given above, the 2θ positions of all the diffraction peaks from a primitive orthorhombic lattice were calculated. The observed diffraction spectra were then examined to identify which of the reflections from the primitive lattice were observed. Table 6.2 shows the possible reflections from a primitive orthorhombic lattice with the lattice parameters given above. The possible reflections are grouped into classes according to whether a given reflection, can be identified as definitely present, definitely absent or 'unconfirmed absence' from all spectra collected from this phase. The last class is for reflections whose absence cannot be confirmed due to peak overlap with observed reflections. The absence of reflections with h+k odd indicates a C-faced centred lattice. The definite observation of the (021) and (023) reflections rules out many of the C-face centred space-groups and restricts the possible space-group to one of $C222_1$, $Cmc2_1$, Cmcm, C2cm, C2cb and Cmca.

At 10.7 GPa, just below the transition from the NaCl phase to phase IV, the NaCl lattice parameter was determined to be 5.7689(9)Å. With 8 atoms/unit cell in the NaCl structure, the density at 10.7 GPa is 11.35 gcm^{-3}. The density of the orthorhombic phase at 17.5 GPa is 9.11 gcm^{-3} ,12.15 gcm^{-3} or 15.19 gcm^{-3} for 6, 8 or 10 atoms/unit cell respectively. Since the density of phase IV must presumably lie reasonably close to but above that of the NaCl phase, it is likely that there are 8 atoms per unit cell. The multiplicity of a general site in any of the 6 possible space-groups is 8 or 16, which implies that the Hg and Te atoms must, assuming an ordered structure, lie on 4-fold special positions in the unit cell (in order to preserve stoichiometry). The site ordering was verified from the diffraction spectra collected at the Hg LIII- and LII-edges and the Te K-edge. As shown below, significant changes in the relative intensities of the diffraction peaks were observed at all the absorption edges and thus the structure is definitely site ordered. The extra absences, which are implied by the atom sites being on 4-fold positions, limits the likely space groups to either $C222_1$, C2cm, Cmcm or $Cmc2_1$. Table 6.3 shows the 4-fold special positions and the absence conditions (including those from the C-face centred space groups), which are implied by the atoms being on 4-fold positions in these four space-groups.

	Observed	Absent	'unconfirmed absence'.
hkl	111, 112, 221, 131, 311, 222, 132	121, 211, 231	122, 212, 113, 321
h00	200	100	300,
0k0	020	010	030, 040
00l		001, 003	
h0l	202,	101, 102	301, 103, 302
0kl	021, 023	011, 012, 013	022, 031, 032
hk0	110, 220, 310	120, 230, 320	130

Table 6.2 The possible reflections from a primitive orthorhombic space-group grouped into classes according to whether the reflections is definitely observed, definitely absent or 'unconfirmed absence'.

The 4b and 4a positions of Cmcm, the 4a position of C2cm and the 4a position of $C222_1$ can be ruled out by the clear observation of reflections such as the (111). Thus there are only four possible options: the 4c position of Cmcm, the 4b position of $C222_1$, the $Cmc2_1$ 4a position and the 4b position of C2cm. The 4b position of $C222_1$ is not distinguishable from the 4c position of Cmcm and since by convention the higher symmetry group is adopted in such circumstances, $C222_1$ need not be considered further. As the 4c position of Cmcm is a special case of both the $Cmc2_1$ 4a position (with z=1/4) and the 4b position of C2cm (with x=0), initial attempts at obtaining a trial structure concentrated on the Cmcm space group.

Examination of the reflection intensities suggested a trial structure for Rietveld refinement. The (200) reflection was observed strongly which suggests that the atoms lie on or close to (200) lattice planes. The relative strength of the (021) reflection to the weak (020) peak indicates that the atoms lie close to (002) planes and are separated by ~1/4 in y. A trial structure meeting these criteria can be constructed by placing both atoms on the 4c position of Cmcm with one atom at y≈1/8 and the other at y≈5/8. The 6-fold coordinated NaCl structure, from which HgTe IV transforms, is a special case (with y=1/4 and the origin moved to (0, 1/4, 1/4)) of the Cmcm structure here proposed for HgTe IV. The trial structure and the NaCl structure are drawn together in figure 6.1.12 for comparison. The trial structure is a distortion of

		4-fold special positions		Absences implied by space group	Extra Absences from special positions
		(0, 0, 0)+	(1/2, 1/2, 0)+		
Cmcm	**4c**	**(0, y, 1/4)**	**(0, -y, 3/4)**	**hkl: h+k=2n, 0kl: k=2n, h0l: h,l=2n, hk0: h+k=2n, h00: h=2n, 0k0: k=2n, 00l: l=2n**	**none**
	4b	(0, 1/2, 0)	(0, 1/2, 1/2)		hkl:l=2n
	4a	(0, 0, 0)	(0, 0 ,1/2)		hkl:l=2n
C2cm	**4b**	**(x, y, 1/4)**	**(x, -y, 3/4)**	**hkl: h+k=2n, 0kl: k=2n, h0l: h,l=2n, hk0: h+k=2n, h00: h=2n, 0k0: k=2n, 00l: l=2n**	**none**
	4a	(x, 0, 0)	(x, 0, 1/2)		hkl:l=2n
$C222_1$	**4b**	**(0, y, 1/4)**	**(0, -y, 3/4)**	**hkl: h+k=2n, 0kl: k=2n, hk0: h+k=2n, h00: h=2n, 0k0: k=2n, 00l: l=2n**	**h0l:l=2n**
	4a	(x, 0, 0)	(-x, 0, 1/2)		0kl:l=2n
$Cmc2_1$	**4a**	**(0, y, z)**	**(0, -y, z+1/2)**	**hkl: h+k=2n, 0kl: k=2n, h0l: h,l=2n, hk0: h+k=2n, h00: h=2n, 0k0: k=2n, 00l: l=2n**	**none**

Table 6.3 The 4-fold special positions of the possible space-groups and the corresponding absence conditions (including those implied by the C-face centred lattice). The four possible options for the HgTe phase IV structure (as determined from the absences associated with the 4-fold positions) are shown in bold text.

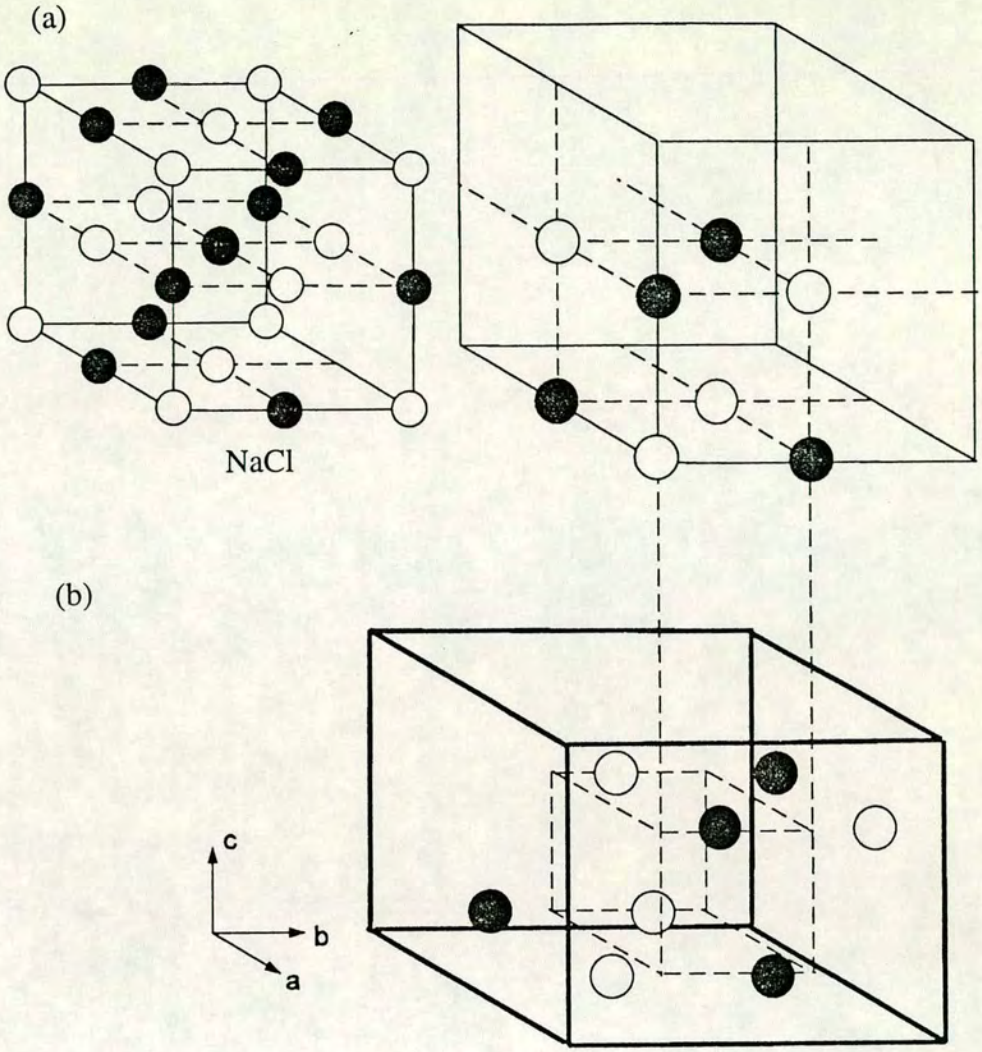

Figure 6.1.12 (a) The NaCl structure and a magnified view of the eight atoms which make up the NaCl unit cell. (b) the eight atoms of the unit cell of the trial structure for HgTe phase IV. By comparing the two figures, the trial structure can be seen to be obtained from the NaCl structure by sliding the horizontal (in this figure) NaCl planes relative to each other and by a small distortion within the planes. The dotted lines are guides to the eye.

the NaCl structure with the x-y planes of atoms at z=0 and z=1/2 moved in opposite directions. Lowering the symmetry from Cmcm to $Cmc2_1$ buckles the NaCl planes by moving the atoms off the x-y planes. The space group C2cm has an additional degree of freedom in x compared to Cmcm, which would buckle the NaCl planes by moving the atoms off the y-z planes.

For refinement, the initial positions of the atoms were selected arbitrarily to be at (0, 1/8, 1/4) and (0, 5/8, 1/4)) for the Hg and Te atoms respectively. Figure 6.1.13 shows the fit, in the Cmcm spacegroup, of the calculated spectrum to the data. Full Rietveld refinement of the structural parameters, thermal and peak shape parameters, and a model for preferred orientation, produced fractional co-ordinates of y=0.130(2) for the Hg atom and y=0.656(2) for the Te atom (both on a 4c position, (0, y, 1/4)). Refinements in the lower symmetry $Cmc2_1$ and C2cm groups produced no significant movement of either atom from z=1/4 or x=0 respectively, indicating that the likely spacegroup is Cmcm.

It is clear that there is still a significant degree of misfit of the (002) reflection (marked by an arrow in figure 6.1.13), which is observed with lower intensity than that predicted by the calculated spectra. The author believes that the residual misfitting in the Rietveld fit of figure 6.1.13 is due both to the degree of texture and to the preferred orientation axis (POA) being not quite along parallel to the cell axis. The GSAS texture correction, which has been modified for this geometry but with the POA assumed to lie along the incident beam, can not fit such a pattern. However, the structure is consistent with the results from the preferred orientation study of chapter 5. Because of this severe preferred orientation, which seems always to occur with this phase and may result from the actual transition mechanism, it is hard to assess the errors on the refined structural parameters. The errors quoted are twice the error given by the refinement package.

Figure 6.1.14a shows the structure projected down the x-axis, with the atoms at x=0 overlapping those at x=1/2. The dashed lines mark nearest-neighbour contacts around the Hg atom at (0, 0.130, 1/4) and the Te atom at (0, 0.656, 1/4). Figure 6.14b shows the single xy plane at z=1/4. The letters label the six different nearest- and next nearest-neighbour distances. The distances are 2.808(2)Å, 2.899(2)Å, 2.946(2)Å, 3.041(2)Å, 3.222(2)Å and 3.265(2)Å in the sequence 'a' to 'f'. The close coordination of the Hg atom is 5-fold, with five unlike neighbours. The next nearest neighbours are the two Hg atoms at 3.041Å and a single Te atom at 3.265Å. The coordination

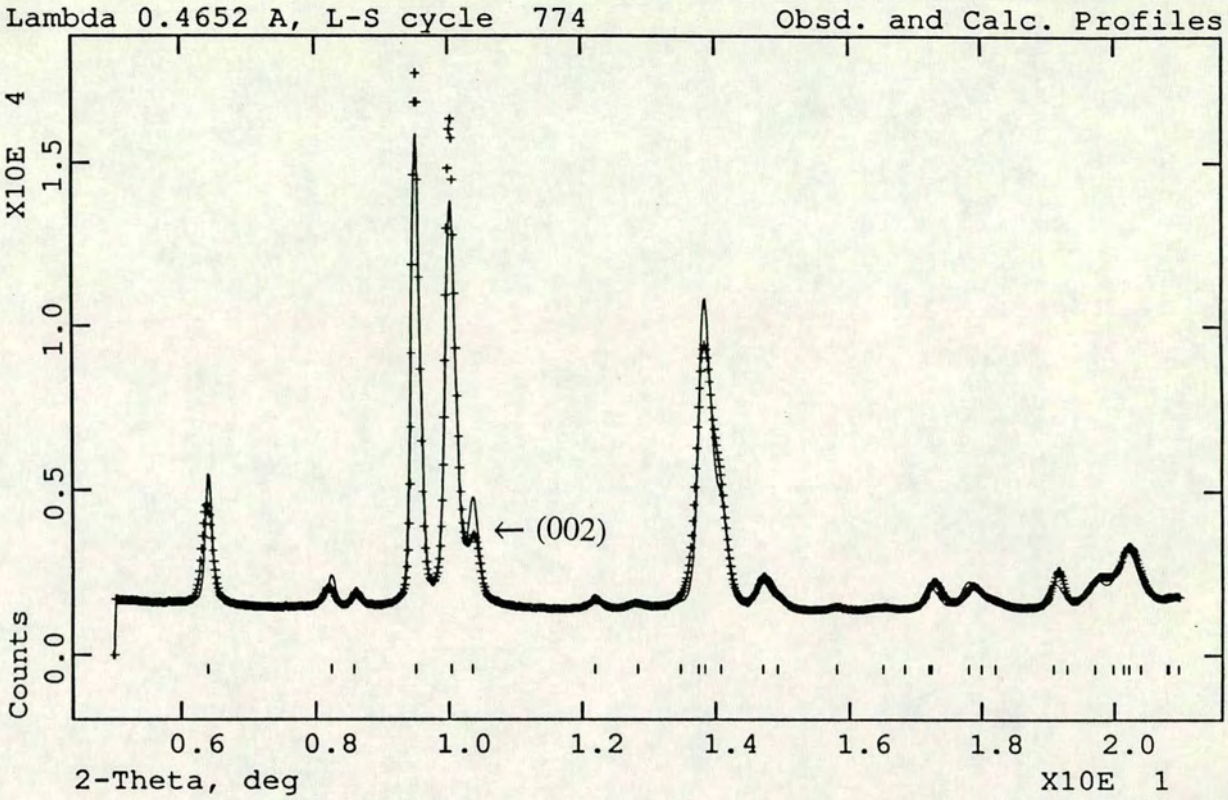

Figure 6.1.13 The integrated profile of a powder pattern collected from HgTe at 17.5 GPa. The solid line shows the fit to the data (crosses) obtained in structure refinement using the structural model discussed in the text.

environment of the Te is different. It shares the same 5-fold close coordination shell as the Hg but the unlike Te atom is at 3.222Å, which is much closer to the unlike neighbour at 3.265Å than in the Hg case. However the coordination shell of both atoms can be described as a distorted octahedron with a close coordination of five unlike atoms.

In this space group there is also another arrangement of the atoms, which gives a distinct structure to that of figure 6.1.14. This structure also gave a stable refinement with fractional coordinates of y=0.105(2) and y=0.619(2) for the Hg and Te atom respectively. The fit to the data from Rietveld refinement was virtually indistinguishable from that given by the first structure. Although the fractional coordinates of this second structure would appear similar to the first, the coordination environment of the atoms is markedly different. In the second structure both atoms have the same two nearest unlike neighbours at 2.805(2)Å but the next nearest atoms are two like atoms at 2.886(2)Å for the Hg atom and 2.969(2)Å for the Te atom respectively. The octahedral coordination shell is then completed by unlike atoms at 3.096(2)Å (two of), 3.018(2)Å and 3.193(2)Å.

The distinction between the two structures is illustrated by figure 6.1.15, which shows the starting trial structure and an average of the two refined structures (the two options are difficult to separate visually). In all the structures the nearest neighbours at ~2.81Å are the unlike atoms at (1/2, 1/2-y, 1/4). In the trial structure all the atoms joined by dashed lines are at the same distance. The first structure results from the y fractional coordinate of each atom refining to larger values than the starting values of y=1/8 and y=5/8. In this case the b-distances and the c-distance become shorter than the d-distances and the close coordination is of five unlike atoms. The second structure arises when the fractional coordinates refine to values smaller than those of the trial structure, which results in the d-distances becoming shorter than the b-distances and c-distance. In this case the close coordination is of the two nearest unlike neighbours at (1/2, 1/2-y, 1/4) and the two like atoms at (0, -y, 3/4).

In order to distinguish between these two possible structures, data were collected at the Hg LII- and LIII-edges and at the Te K-edge. There are no reflections in this structure which result purely from the difference in scattering between the atom sites. However the (111) reflection, which is pure difference reflection in the NaCl structure, contains a strong difference scattering component. Thus, the principal change in the diffraction pattern at the absorption edges is variation in intensity of the

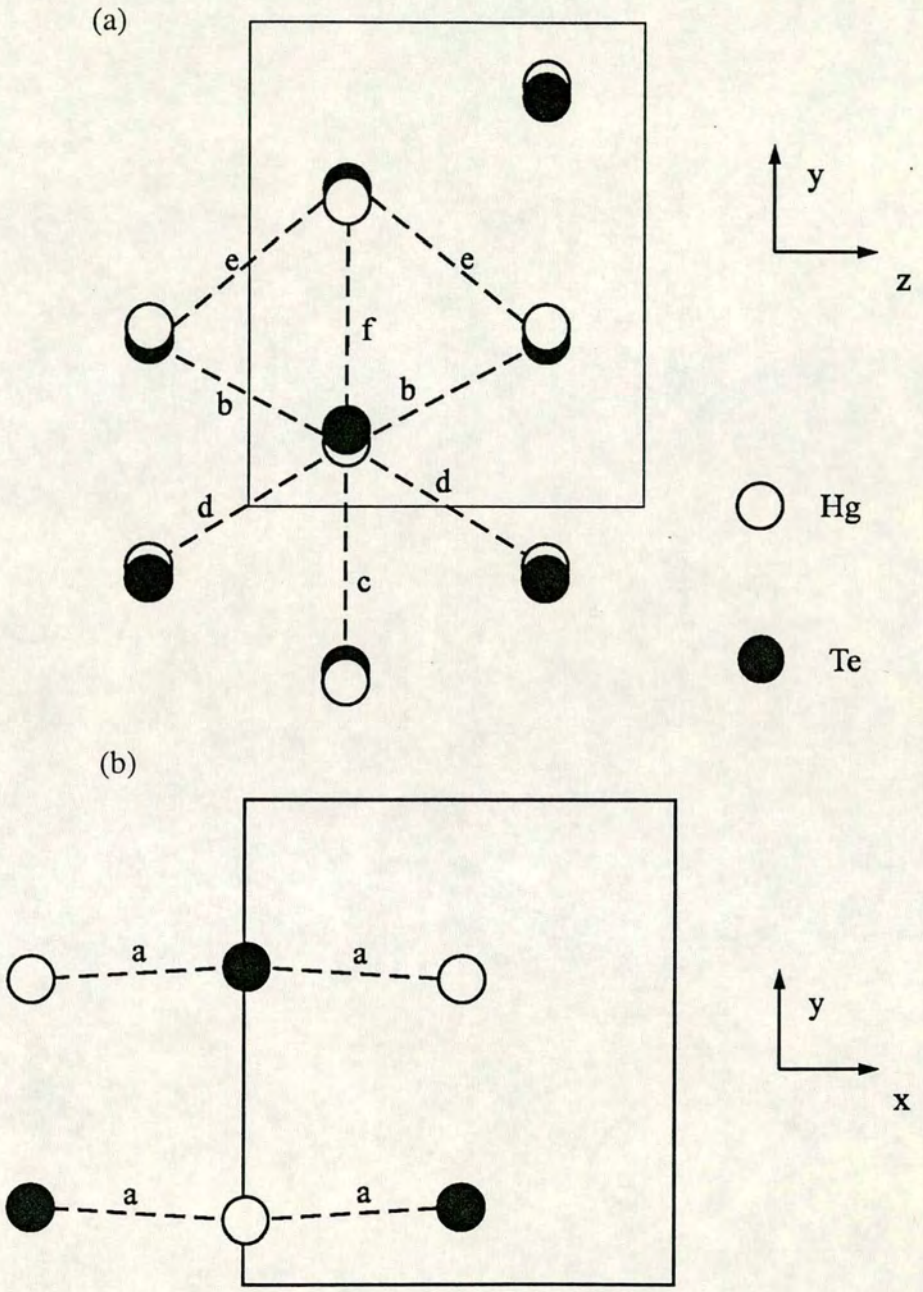

Figure 6.1.14 (a) The Cmcm structure of HgTe phase IV viewed along the x-axis. (b) The Cmcm structure of HgTe phase IV viewed along the z-axis (only the single plane at z=1/4 is shown). The dashed lines mark the nearest-neighbour contacts around the Hg atom at (0, 0.130, 1/4) and the Te atom at (0, 0.656, 1/4). The letters label the six different nearest- and next-nearest-neighbour distances.

(111) peak, which is shown compared to the (020) reflection in figure 6.1.16 at: the 0.4652Å (far from any absorption edges), the Te K-edge, and the Hg LIII-edge. The clear changes in relative intensity indicate that the structure is definitely site ordered. At the Te K-edge the difference in scattering factors between the two atoms increases and thus the intensity of the (111) reflection relative to the (020) increases. At the Hg L-edges the reverse occurs. Figure 6.1.17 shows the fit to the data at the Te K-edge and at the Hg L-III edges from refinements of both structures. At both edges the second structure is able to model the intensity of the (111) reflection more accurately than the first structure, although the difference between the two structures is very marginal and could arise from misfits to the structured background.

It might be possible to distinguish between the two structures by using an EXAFs technique, which measures the local environment of the atoms and should thus be sensitive to the differences in coordination. Unfortunately there are no available x-ray absorption measurements on this phase of HgTe. However a recent study of ZnTe (San Miguel, (1994), which undergoes a similar transition sequence to HgTe, has reported an 8-fold, coordinated structure above ~12 GPa.

In conclusion, it has been shown that the structure of HgTe above ~13 GPa is an orthorhombic distortion of the NaCl structure. The space-group of this orthorhombic phase is Cmcm with both atom types on the 4e special positions (at (0, y, 1/4)). There are two possible structures consistent with the experimental evidence: the first produces refined fractional coordinates at 13.2 GPa of y=0.130(2) and y=656(2) for Hg and Te respectively and has an eightfold coordination shell with close coordination of five unlike atoms. The second possible structure gave fractional coordinates of y=0.105(2) and y=619(2) for Hg and Te respectively and has an eightfold coordination shell with close coordination of two unlike and two like atoms.

6.1.5 A high-pressure structural study of HgTe phase V

Introduction

Previous work on this unsolved phase (Huang and Ruoff, (1985)) had observed phase V using EDX techniques above ~38 GPa from three weak diffraction peaks in a heavily contaminated powder pattern. The three observed reflections could not be indexed on a cubic crystal lattice, although the authors suggested that the structure

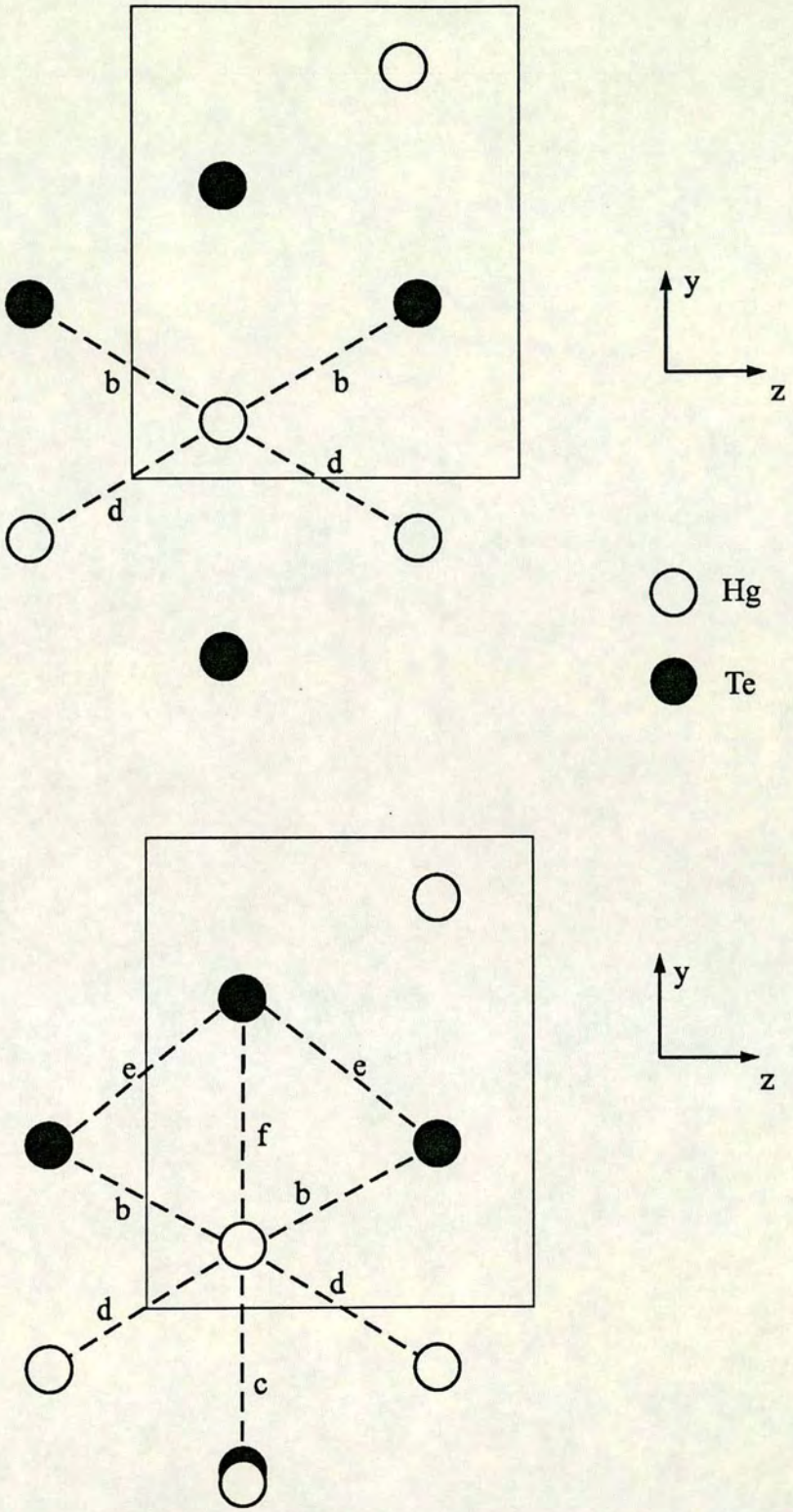

Figure 6.1.15 (a) The starting trial structure for Rietveld refinement shown in projection down the x-axis. For clarity, only the layer of atoms at x=0 are shown. In this structure all the bonds shown with dashed lines are of equal length. (b) An average of the two refined structures. For clarity, only the layer of atoms at x=0 are shown. The dashed lines mark the nearest-neighbour contacts around the Hg atom at (0, 0.130, 1/4) and the Te atom at (0, 0.656, 1/4). The letters label the six different nearest- and next-nearest-neighbour distances.

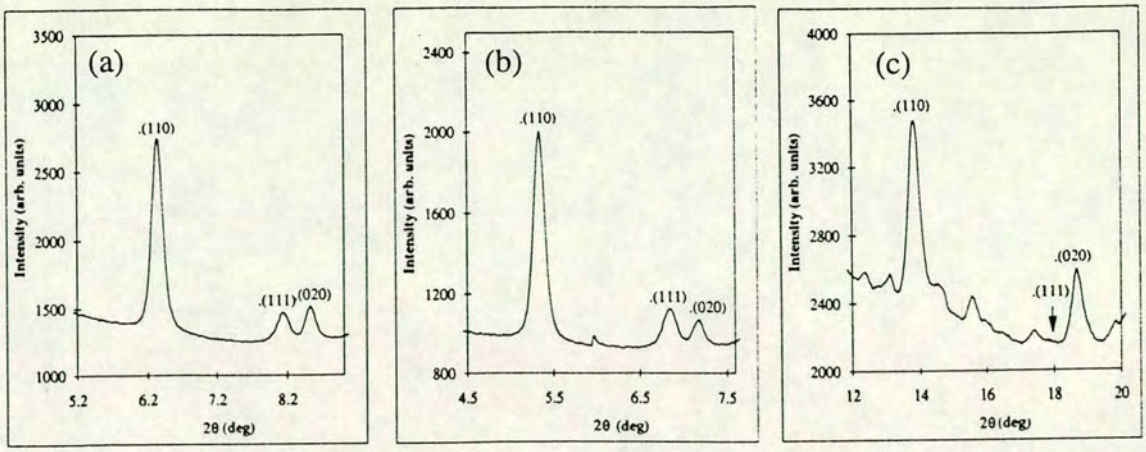

Figure 6.1.16 The low angle region of the 1-D integrated powder profiles from: (a) HgTe at 0.4652Å (far from any absorption edge), (b) at the Te K-edge and (c) the Hg L-III edge. The clear changes in relative intensity of the reflections indicate that the structure is definitly site-ordered. The additional diffraction peaks observed at the Hg L-III edge are from contamination from the λ/3 component in the beam (at this wavelength the filtering ability of the Pt pinhole is negliable).

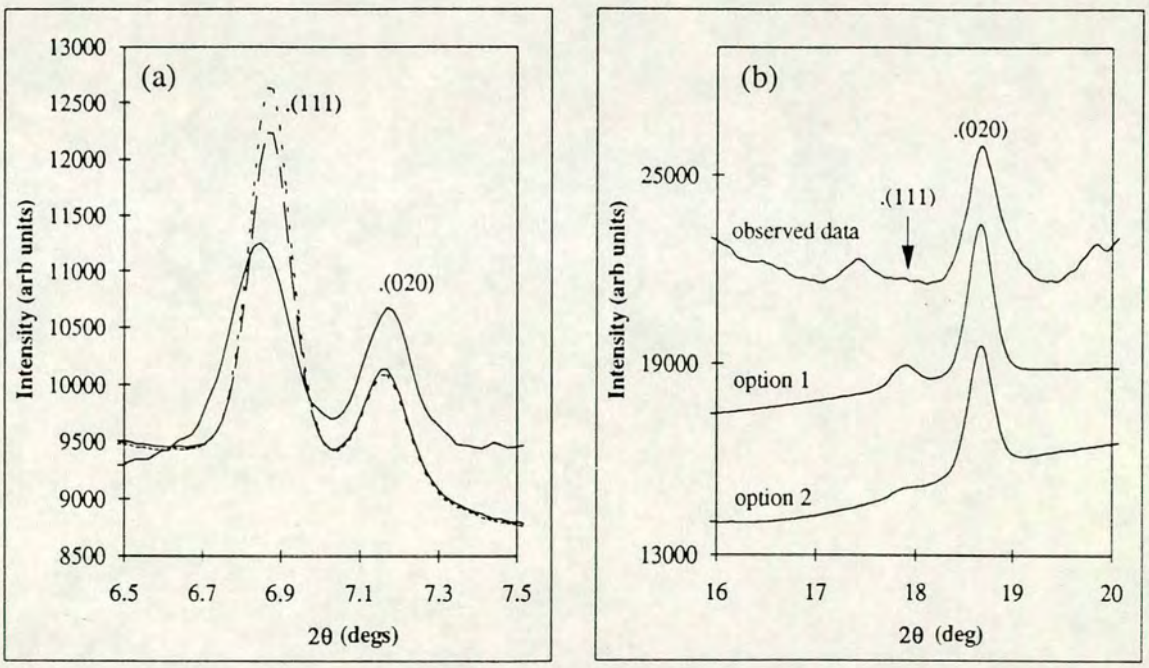

Figure 6.1.17 (a) The observed (solid line) and calculated intensities (dashed lines) to the (111) and (020) reflections from the two possible structures of HgTe phase IV at the Te K-edge. The short dashed line is from option 1 and the long dashed line from option 2. (b) The observed and calculated intensities for the (111) and (020) reflections of HgTe phase IV at the Hg L-III edge.

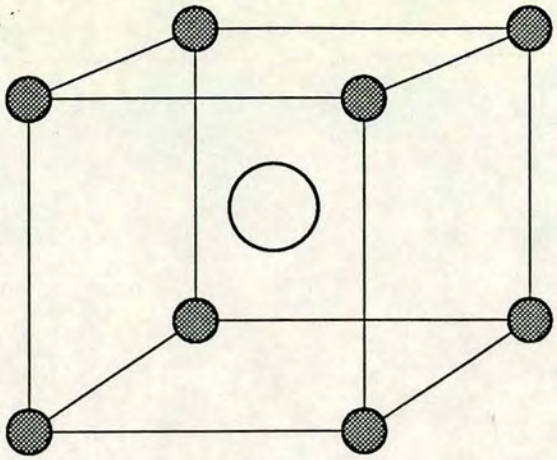

Figure 6.1.18 The CsCl structure. If both atom types are identical (here shown as filled and unfilled spheres), then the structure becomes equivalent to the b.c.c structure.

might be a distorted form of the CsCl structure, which is a diatomic form of the b.c.c. structure (see figure 6.1.18). This section presents results from a short study performed to identify the structure of HgTe V and the exact transition pressure and volume changes at the transition from phase IV.

Experimental techniques

Because HgTe phase V occurs at a much higher pressure than phase IV, it was not possible to obtain this phase by simply increasing the pressure on the samples used in the previous section. Two new samples were prepared in DXR-5 Diacell pressure cells with 300 μm culet diamonds. As before, diffraction data were collected on station 9.1 at the Synchrotron Radiation Source, Daresbury, using the standard image-plate set-up as discussed in chapter 2. The sample material, pressure-transmitting medium and pressure measurement were all as in the two sections above. The incident x-ray wavelength was 0.4652Å, calibrated as before using a standard silicon sample. The structural results presented were all obtained

from full Rietveld refinement (Rietveld, (1969)) of the integrated profiles using the program GSAS (Larson and Von Dreele, (1985)).

Results and discussion

As the pressure was increased in the phase IV region, the first signs of phase V were observed in the first sample at 28.1 GPa as shoulders on the (021) reflection of phase IV. Upon further pressure increase the sample transformed completely to phase V. Unfortunately the fluorescence signal from the ruby became too weak to record above 45 GPa and the transition pressure to pure phase V could not be measured. The ruby signal weakens at high pressures due to the shift with pressure of the fluorescence line away from the laser excitation wavelength. This makes it difficult to measure the pressure above 40 GPa unless a large ruby chip is used. The transition pressure was estimated from the force on the pressure cell as above 50 GPa. The second sample, which had been prepared with a larger ruby chip, showed similar signs of the growth of phase V at 28.9 GPa. A large coexistence region of the two phases was observed and until 50.5 GPa, the maximum pressure that could be reached with this loading, the transformation was not complete. However the phase IV reflections could only just be observed and the proportion of phase IV at 50 GPa was therefore very small. The transition pressure from phase IV to phase V is thus only very slightly in excess of 50 GPa.

The 5 observed reflections of phase V indexed well using the program TREOR90 (Werner *et al*, (1985)) on a cubic lattice with a=3.3074(3)Å at 50.5 GPa. With this lattice the specific volume change ($\delta V/V_0$) at the transition from phase IV to phase V was observed to be 1.45 % at 50.5 GPa (with V_0=269.66Å, from the cubic phase lattice parameter at ambient pressure). Following the suggestion of Huang and Ruoff, Rietveld refinement of the pure phase V data from the first sample was performed in the Pm3m space group starting from the CsCl structure with the Te atoms on the 1a sites at (0, 0, 0) and the Hg atoms on the 1b sites at (1/2, 1/2, 1/2). The fit to the data at ~50 GPa obtained from Rietveld refinement of this structure with profile and scale parameters is shown in figure 6.1.19. At this unknown pressure the lattice parameter refined to 3.2981(3)Å. There are clearly significant misfits to the (100), (111) and (210) reflections, which all appear absent in the observed profile. In this structure these reflections result purely from the difference in scattering between the 1a and 1b sites, which suggests that the structure is disordered over the length scale of the

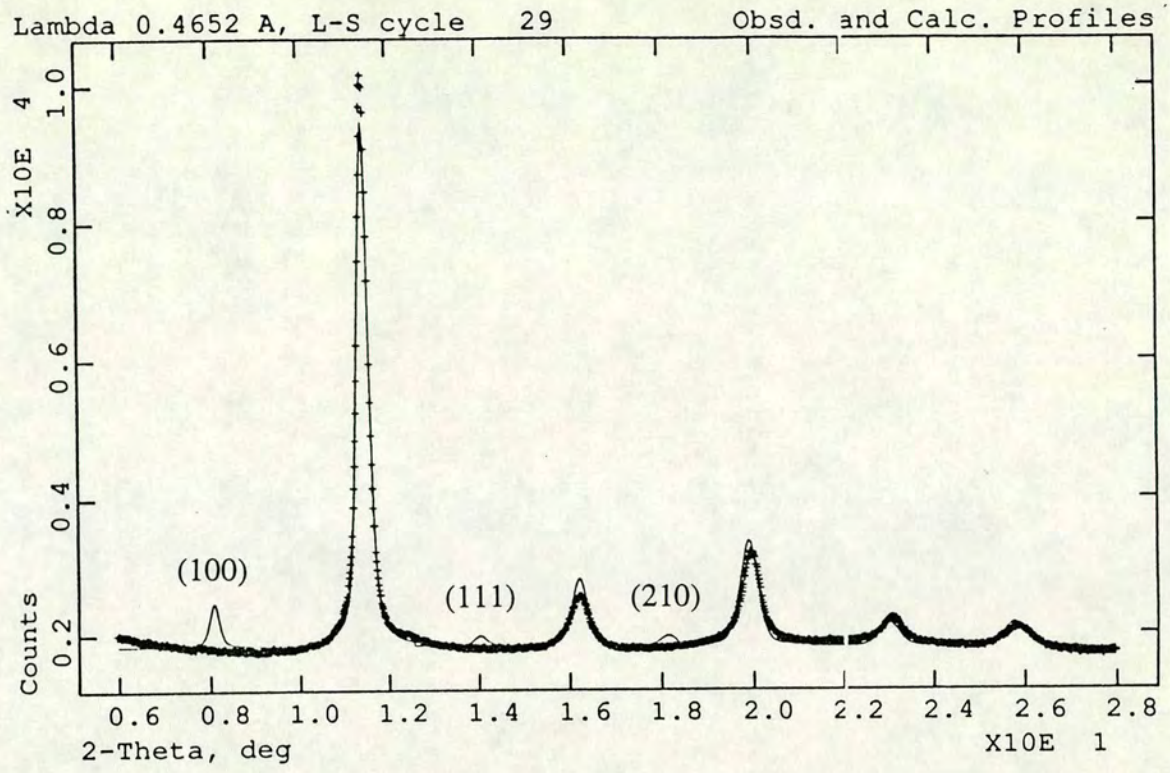

Figure 6.1.19 The integrated profile of a powder pattern collected from HgTe phase V at ≈50 GPa. The solid line shows the fit to the data (crosses) obtained in structure refinement using a site-ordered CsCl structure.

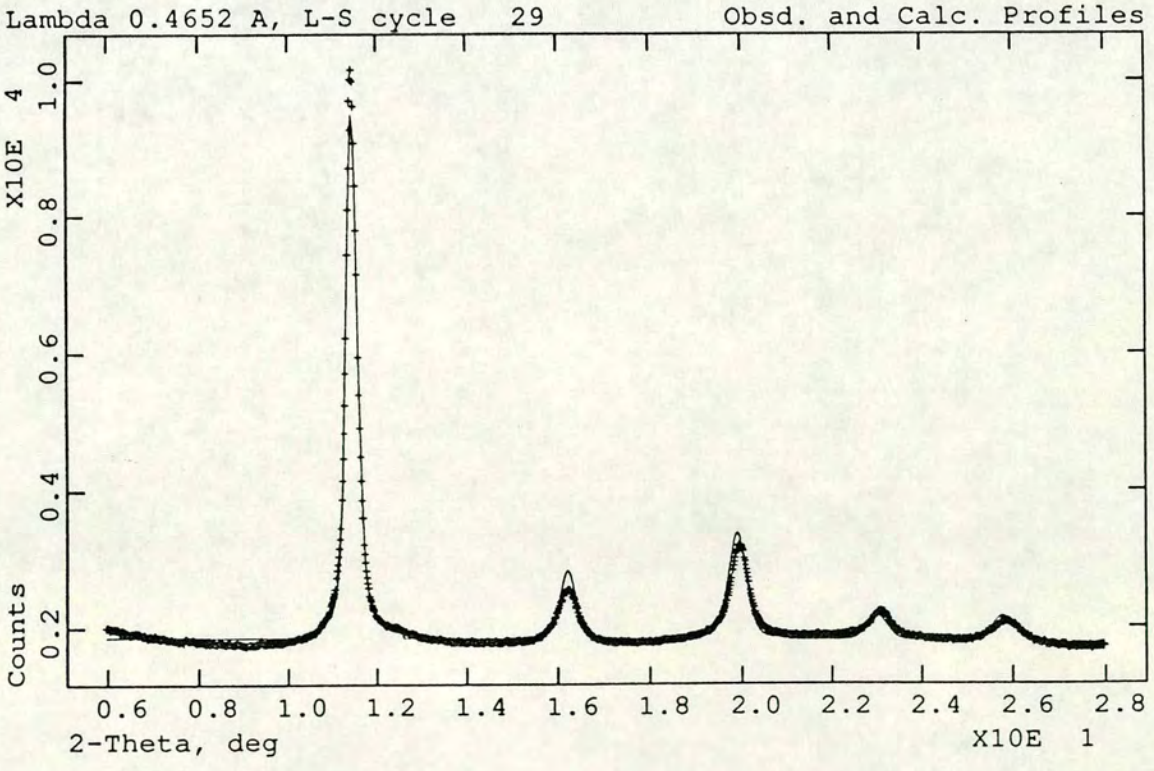

Figure 6.1.20 The integrated profile of a powder pattern collected from HgTe phase V at ≈50 GPa. The solid line shows the fit to the data (crosses) obtained in structure refinement using a disordered CsCl structure.

diffraction measurement. The fit to a disordered CsCl structure, which is then equivalent to the b.c.c. structure, is shown in figure 6.1.20. The match between the observed and calculated profiles using a disordered structure is good, although there appears to be a very small misfit to the reflection at $2\theta \approx 20°$. This is likely to be due to the pressure cell not being placed quite reproducibly on the sample mount or residual problems with the spatial calibration, although other possible causes such as deviatoric stress effects cannot be ruled out. However it is clear that the structure of HgTe phase V is b.c.c. and not, as previously reported, distorted CsCl.

It is interesting that the crystal becomes disordered after the transition from phase IV, although it is possible that the local structure remains ordered, which should be observable using a high-pressure EXAFS technique (Itié *et al* (1992)). The HgTe phase IV structure can be distorted continuously to the hexagonal close-packed structure (h.c.p.). Since h.c.p. is the most efficient packing of atoms and has a high coordination, it might be expected that the structure of phase V of HgTe would be h.c.p. not the b.c.c. structure. However, the b.c.c. structure has been identified as the (possibly) final high-pressure phase in other semiconductors; e.g. above 28 GPa the structure of InSb is either CsCl or b.c.c. (Vanderborgh *et al*, (1989)). There is no evidence of InSb being ordered above 28 GPa although the difference in x-ray scattering factors between In and Sb is very low. A further transformation to the h.c.p. structure (or the other close-packed structure, f.c.c.) may occur upon further pressure increase, although this was not observed in InSb up to 66 GPa (Vanderborgh *et al*, (1989)). It is possible that the b.c.c. structure is the lowest energy structure for many semiconductors at high-pressures and it seems likely that the final high-pressure phases of ZnTe and CdTe will have either the b.c.c. or CsCl structures.

Section 2

A study on the transition mechanisms between three high-pressure phases of Si.

6.2.1 Introduction

Under pressure many simple systems undergo structural phase transitions involving a change of coordination accompanied by large changes in the unit cell volume (~20%). Elemental semiconductors such as Si and Ge transform from the cubic diamond structure to the tetragonal β-tin structure whilst the more ionic III-V and II-VI semiconducting compounds tend to go from the cubic zincblende structure to NaCl, orthorhombic or hexagonal phases. Despite a great deal of interest, and the accumulation of much partial information, the precise mechanisms by which such transitions occur remain unknown; and this is one of the most significant unsolved problems in condensed matter science. The principal experimental difficulty is that a single-crystal cannot be taken through this type of transition without being reduced to a powder by the abruptness of the structural change. Hence it has been very difficult to establish the orientational relationship and atomic displacements between the two phases involved. Much valuable information could be extracted from the microstructure exhibited by the sample (e.g. preferred orientation or texture of the sample yields the orientation relationship and peak widths the relative particle size of the two phases). But unfortunately powder-diffraction studies have not, until the development of area detector techniques such as image-plates, had sufficient resolution and statistics for this task.

Perhaps because of the experimental difficulties, international work in this area is still scarce. A detailed microstructural study on the III-V compound GaAs has been performed (Besson *et al* (1991)). They report significant microstructure (a lamellar structure of alternate (111) sheets of the low and high pressure phases) from their electron microscopy studies on samples recovered to ambient pressure. One of the principal limitations of work of this type has been that is not conducted *in situ*, but after recovery to ambient pressure. This means that the sample is not in the true high-pressure phase and is no longer subjected to the relevant stress. Hence there is always an element of indirectness about the conclusions drawn. Work on the effect of uniaxial stress on the transition pressure in several semiconductors and the orientation

of an InSb powder sample recovered to ambient pressure has been reported (Okai and Yoshimoto, (1978)). By observing the relative effect of different uniaxial stress directions on the transition pressure and the partial orientation information they extract from the InSb they are able to rule out the most obvious structural path from the cubic to high-pressure phase, but they did not have sufficient information to determine the true path.

The image-plate system developed on station 9.1 at SRS Daresbury by the University of Edinburgh group has sufficient resolution and sensitivity to enable *in situ* studies of sample microstructure under pressure to be performed. This opens up the possibility of using the sample microstructure to extract vital information on transition mechanisms between phases. This section presents a study (that makes use of the techniques of preferred orientation modelling developed in this thesis) of the microstructure in Si through the transition sequence: cubic diamond to β-tin to Imma. The purpose of these experiments was to establish the orientational relationships between the different phases, i.e. to identify the exact relationship between the lattice planes before and after the transitions. These results are discussed in the light of a possible transition mechanism between these phases.

6.2.2 The physics of Si under pressure

Because of its well-known semiconducting properties, Si, which at ambient pressure has the cubic diamond structure, is one of the most studied of all materials. The first work on Si under pressure was a study of resistivity vs pressure (Minomura and Drickamer, (1962)), which reported a drop in resisitivity of about five orders of magnitude at ~13 GPa. The pressure at which this transition to a metallic state occurred varied between 9 and 13 GPa, according to experimental conditions. In experiments using pressure transmitting discs made of pyrophyllite, which supports high shear stress, the transition occurred as early as 9 GPa. When little shear stress was present in the cell (by using the low shear strength material AgCl as a replacement for pyrophyllite), the transition took place at ~13 GPa. Minomura and Drickamer also noted that this transition to a metallic state occurred well below the pressure suggested by extrapolations (from the semiconducting phase) of the change in band gap with increasing pressure. They observed no further discontinuities in resisitivity up to ~40 GPa and noted that on pressure decrease the sample resisitivity returned to close to its original value, although quantitative measurements were not possible with their apparatus.

This high-pressure metallic phase of Si was determined by x-ray diffraction studies (Jamieson, (1963)) to have the β-tin structure. Jamieson, using a carbide pressure cell with boron as a pressure transmitting medium, reported significant microstructure in the β-tin phase. Initial studies with flat pistons (up to ~6 GPa) saw only the (200), (220), (400) and (420) β-tin reflections. By using tapered pistons, pressures upto ~13 GPa were obtained. Over a period of 3 days at 13 GPa additional β-tin lines appeared, including many with l≠0. Refinement of the unit cell produced the lattice parameters a=4.686Å and c=2.585Å at ~13 GPa. Jamieson also noted that the intensity of the (101) reflection was abnormally weak, indicating strong preferred orientation in the high-pressure phase. He suggested that this texture occurred as a result of the shearing action of the transition, which left the c-axis of the β-tin phase oriented along the normal to the piston faces. In addition to the reflections from the β-tin phase, two extra lines were observed (at d-spacings of 2.613Å and 1.713Å). These two extra reflections observed by Jamieson were attributed in 1963 (Wentorf and Kasper, (1963)) to a metastable phase of Si, which occurs on downloading from the β-tin phase. This metastable phase (space-group Ia3) was determined to be a distorted tetrahedral structure.

The advent of the diamond anvil pressure cell and the energy-dispersive diffraction technique using synchrotron radiation allowed higher pressure studies of Si to be performed. Transitions from: the β-tin structure to a simple hexagonal phase (s.h.) (at ~16 GPa), to an unsolved structure (at ~35 GPa) and then to the hexagonal close packed phase (h.c.p.) (at ~40 GPa) were observed by several groups (Olijnyk *et al*, (1984) and Zhu Hu *et al*, (1986)). The 'intermediate' structure between the s.h. and h.c.p was assumed to be a simple restacking of hexagonal layers, although this was later disputed (Duclos *et al*, (1990)). A transition at ~79 GPa from h.c.p. to a f.c.c. structure has been reported by a group at the CHESS synchrotron (Duclos *et al*, (1990), who found no further transitions up to 248 GPa.

The lower pressure region of the Si phase diagram was re-examined by the University of Edinburgh group, in which the author is a PhD student, using an image-plate area detector and angle-dispersive techniques. A new phase of Si, an orthorhombic structure with space-group Imma, was discovered in the pressure region between the β-tin and s.h. phases (McMahon and Nelmes, (1993)). The superior data quality obtained by using an image-plate allowed full Rietveld refinement of the structure, which is shown in figure 6.2.1. A further more detailed study (McMahon *et al*,

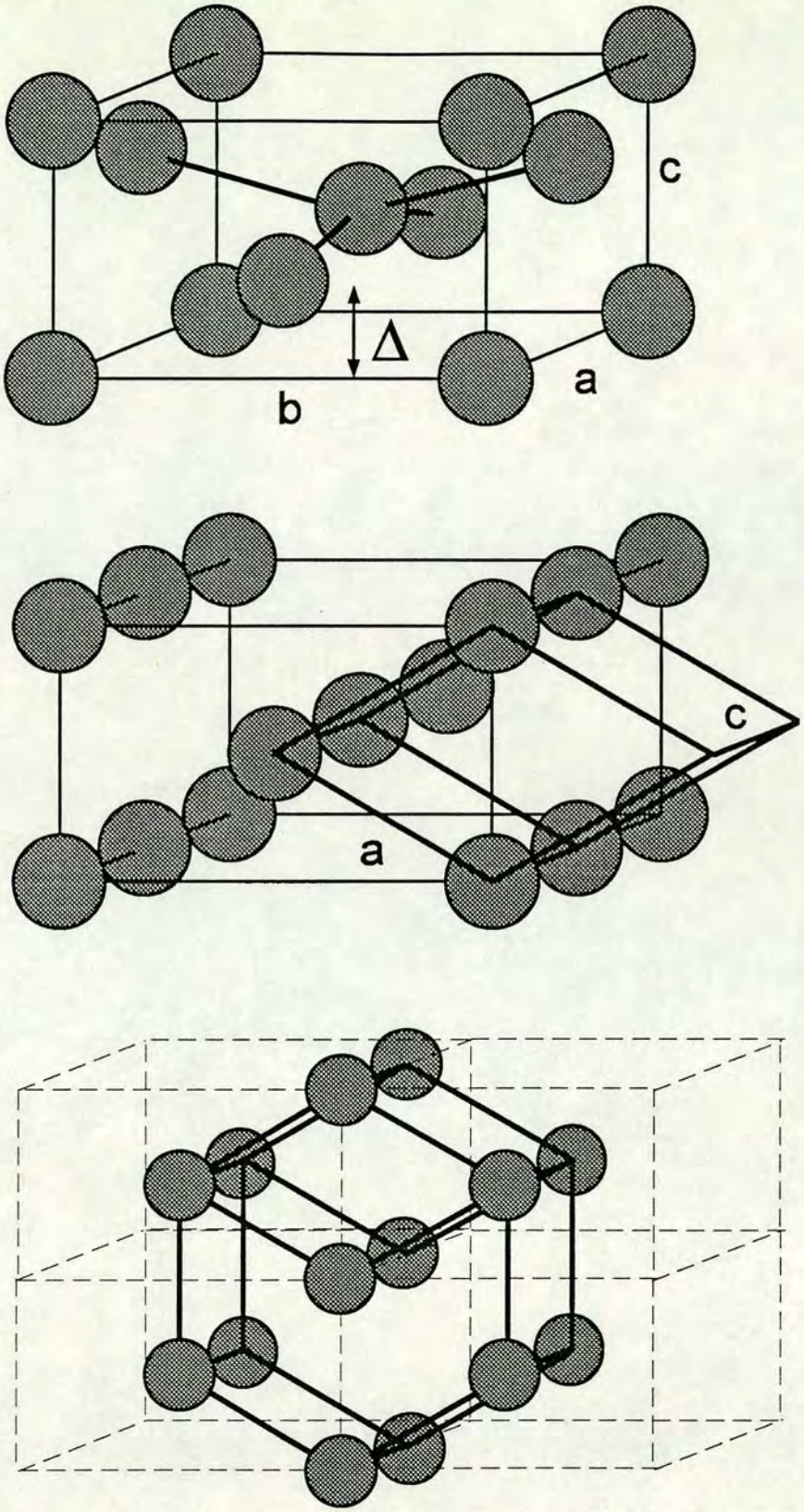

Figure 6.2.1 (a) The crystal structure of Si in the Imma phase. If Δ=0.25 and a=b, then the structure becomes equivalent to the β-tin structure. (b) The crystal structure of the simple hexagonal phase of Si, viewed in an orthorhombic setting. When Δ=0.5 and b/c=√3, the Imma structure becomes equivalent to the simple hexagonal structure. (c) The simple hexagonal structure of Si viewed in the conventional hexagonal setting. The relationship between the orthorhombic and hexagonal setting of the simple hexagonal structure can be seen by comparing 6.2.1b and 6.2.1c.

(1994)), in which the author was involved, revealed that the Imma phase acts as a path between the β-tin and s.h. structures. All three structures can be considered in terms of the orthorhombic Imma structure, which has one free structural parameter (Δ, see figure 6.2.1). The β-tin structure is a special case of the Imma structure when Δ=0.25 and a=b. After the transition to the Imma phase Δ>0.25 and a>b and as the pressure is increased Δ→0.5 and b/c→√3. When Δ=0.5 and b/c=√3, the structure becomes equivalent to the s.h. structure. The relationship between the conventional hexagonal description of the s.h. structure and the orthorhombic setting used here is shown in figure 6.21b and 6.2.1c. Figure 6.2.2 shows a graph of Δ vs pressure and it can be seen that, although the transitions themselves are first-order, an evolution with pressure appears to take place between the special cases of Δ=0.25 (the β-tin structure) and Δ=0.5 (the s.h. phase).

The evolution of the Imma structure parameter (Δ) from the value equivalent to the β-tin structure, through the Imma phase proper to the s.h. phase suggests that the transition mechanism is one of a semi-continuous movement of atoms. The transitions could occur through a continuous distortion of the lattice parameters and the required motion of the atoms in the face of the tetragonal/orthorhombic unit cell. However both the transitions β-tin→Imma and Imma→s.h. are definitely discontinuous (McMahon *et al*, (1994)) and so there was no direct proof that the transitions take place by such a simple mechanism.

6.2.2. Preferred orientation studies of Silicon.

It had been noted during previous studies of the Imma phase of Si (McMahon and Nelmes (1993), McMahon *et al* (1994)) that significant texture occurs reproducibly in this phase. In light of this preferred orientation in the Imma phase and the known strong texture in the β-tin phase (see chapter 5), it was decided to investigate the preferred orientation in Si as the pressure was increased (and decreased) throughout the whole pressure range between the ambient pressure cubic structure and the simple hexagonal phase with the aim of extracting information on the transition mechanisms. A sample was prepared in a Diacell diamond anvil pressure cell and diffraction spectra collected at ambient pressure and at 8.1 GPa, just before the transition to the β-tin phase. At this stage, there was no significant variation in intensity around the powder rings and the intensities, azimuthally integrated using the PLATYPUS package, showed little difference with the expected values from the known structure of this phase.

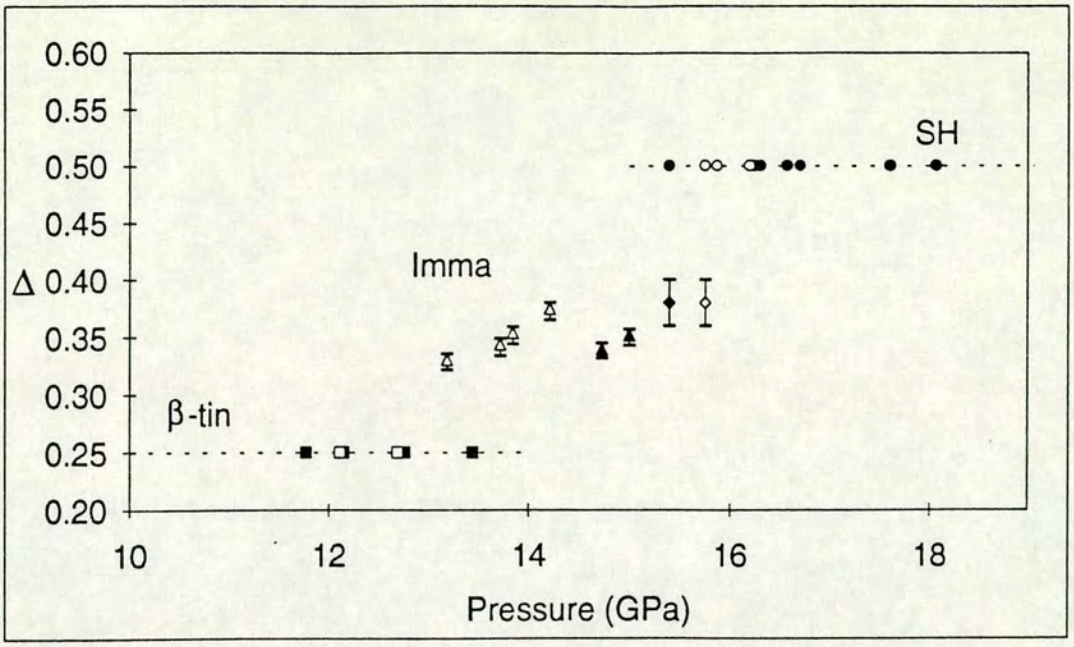

Figure 6.2.2 The Imma structural parameter Δ versus pressure.

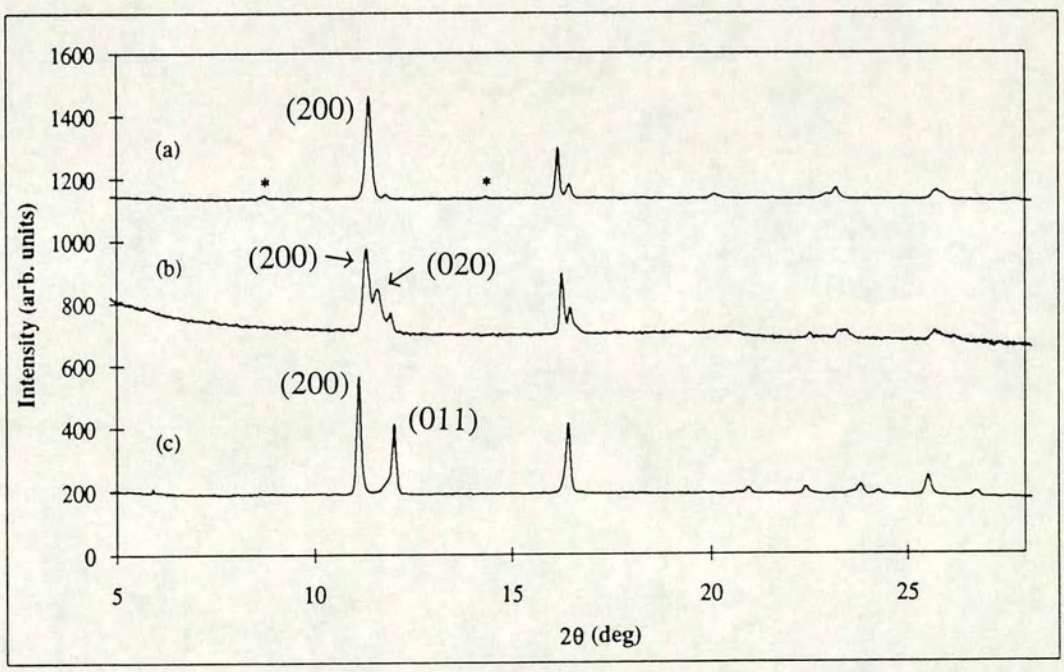

Figure 6.2.3 (a) The integrated 1-D powder profile from the first silicon sample at: (a) 13.2 GPa in the β-tin phase, (b) at 14.9 GPa in the Imma phase, and (c) at 16.3 GPa just beforethe transition to the simple hexagonal phase was complete. Note the splitting of the (200) β-tin reflection into the (200) and (020) reflections of the orthorhombic Imma phase.

Figure 6.2.3.a shows the spectrum recorded at 13.2 GPa, at which pressure the transition to the β-tin phase was almost complete. Comparison with the calculated spectra from an ideal sample (see section 5.4) shows that this sample is highly textured, in a similar manner to that observed in section 5.4; i.e. the (011) scattering vector is the POD and the POA is coincident with the pressure cell axis.

The pressure was then increased and data recorded in the straight-on position at different pressures during the transition from the β-tin structure to the Imma phase and up in pressure towards the simple hexagonal structure. Unfortunately this sample could not be taken to high enough pressure to obtain a single phase of the s.h. structure (because of the condition of the gasket hole). Figure 6.2.3 shows three diffraction spectra collected in: (a) the β-tin phase (at 13.2 GPa), (b) in the Imma phase on pressure decrease (at 14.9 GPa) and (c) just before the transition to the simple hexagonal phase was complete (at 16.3 GPa). The most obvious distinction between the diffraction patterns from the β-tin structure and the Imma structure is the splitting of the strong indistinguishable β-tin (200) and (020) reflections into the (200) and (020) reflections of the orthorhombic Imma structure (c.f. 6.2.4.a with 6.2.4.b). Because of preferred orientation the β-tin (101) and (011) reflections are often very weak and consequently the splitting of these lines is difficult to observe. The Imma (020) reflection moves with increasing pressure to a higher 2θ position until it lies, after the transition to the s.h. structure, under the (011) reflection of the s.h. phase. On pressure decrease the reverse sequence is seen.

Figure 6.2.4 shows the intensity variation around the powder rings observed in the s.h. (200) and (011)/(200) reflections, the orthorhombic (200) and (020) peaks (on pressure decrease) and the (200) reflection of the β-tin phase at 10.5 GPa (also on pressure decrease). Because of the extreme preferred orientation in this sample, the intensity of the β-tin (101) reflection and the Imma (011) and (101) reflections were too weak to measure in the sectored data.

Because the first sample did not reach a high enough pressure such that the sample was purely in the s.h. phase and the statistics on the first set of data were not that good, a second sample was prepared in the Diacell diamond anvil cell. A diffraction pattern was collected at 10.5 GPa just before the transition to the β-tin phase. At this stage there was no variation in intensity around the powder rings and the average intensities were close to those expected from an ideal sample. Data were collected on the standard mount (in the straight-on position) at similar points in the transition

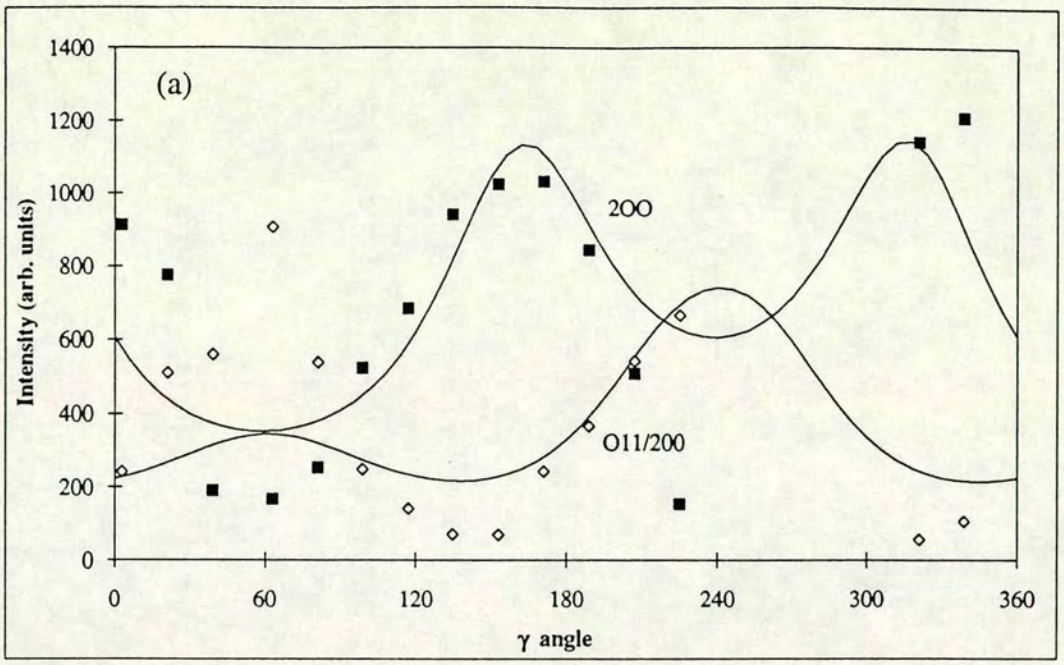

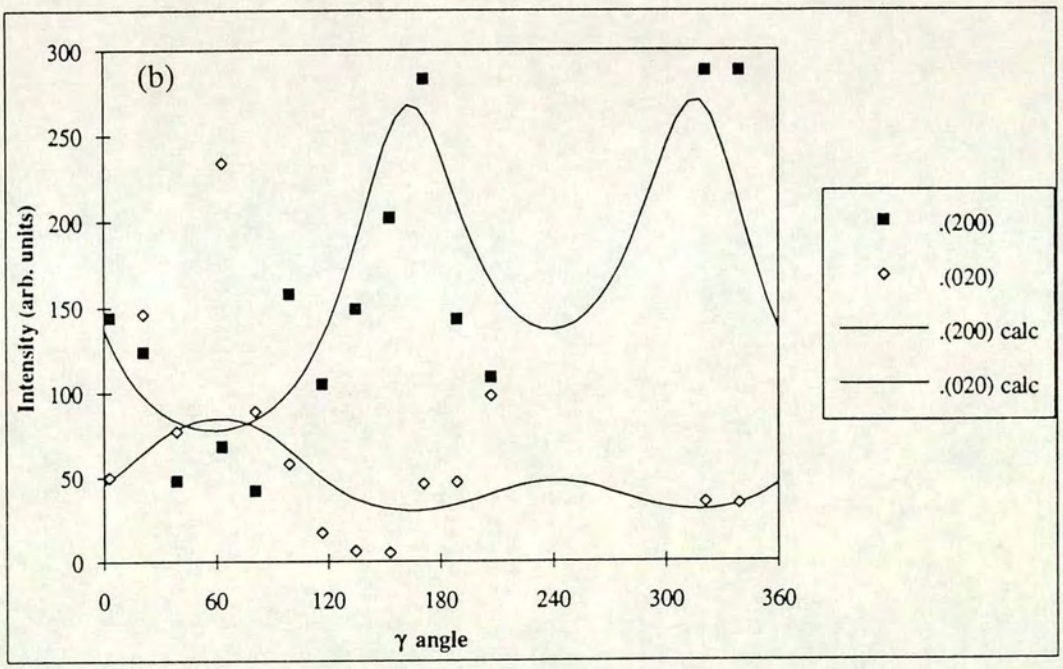

Figure 6.2.4 The observed (points) and calculated (solid lines) intensities versus angle, γ, around the powder ring of the first silicon sample for: (a) the (200) and (011/020) s.h. reflections, (b) the (200) and (020) Imma reflections, and (c) the β-tin (200) reflection. In the first two figures the calculated intensity is obtained from the preferred orientation model discussed in the text.

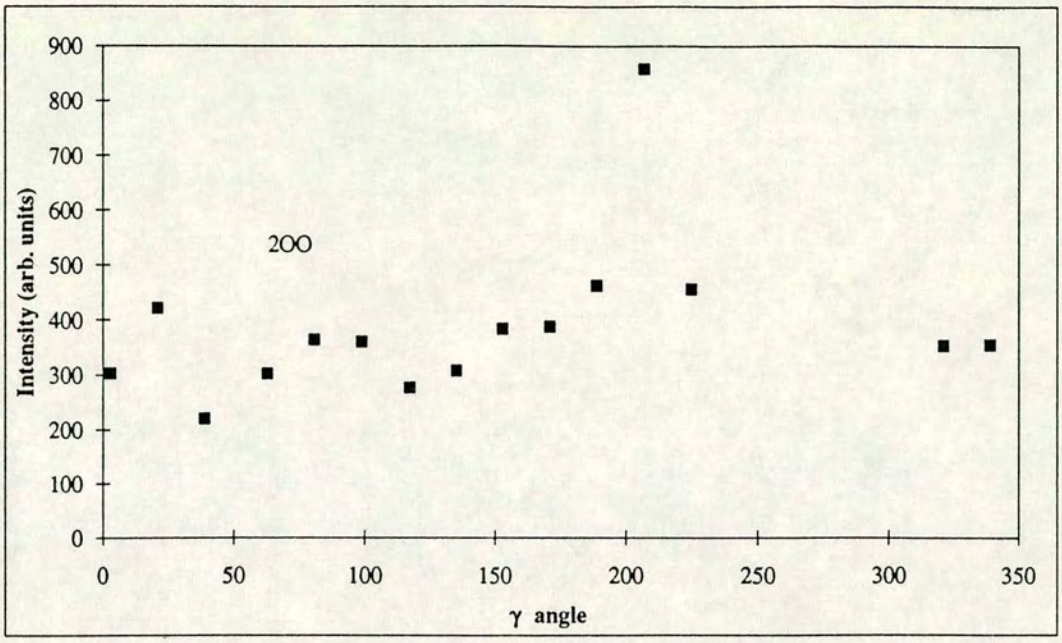
900
800
700
600
500
400
300
200
100
0
Intensity (arb. units)
200
0
50
100
150
200
250
300
350
γ angle

Figure 6.2.4c

sequence β-tin→Imma→s.h. as with the first sample. Figure 6.2.5 shows the intensity around the powder rings (as in figure 6.2.4) from the second sample in: the s.h. phase at 18.4 GPa, the Imma phase at 13.0 GPa (on pressure decrease) and the β-tin phase at 10.3 GPa (also on pressure decrease). In this sample the degree of preferred orientation was lower and the intensities of the Imma (011) and (101) reflections and the β-tin (101) reflection were measurable above the noise in the background intensity. The intensities of these reflections are also plotted in figure 6.2.5. Figure 6.2.6 shows the 2-D images of the data in figure 6.2.5. It can be seen that, despite the β-tin phase exhibiting little variation in intensity around the powder rings, the Imma phase showed marked differences in intensity at different points around the powder rings. Interestingly, the positions of the maxima of intensity of the (200) and (020) peaks were separated by 90° (in γ, the angle which describes the angle around the powder ring). The 2-D image of the data at 16.3 GPa indicates that the s.h. phase also had strong orientation around the powder ring.

In both samples there was little intensity variation around the powder rings in the β-tin phase, although the relative intensities of the reflections indicates that the sample was highly oriented. In the Imma and s.h. phases the intensity around the powder rings was clearly not constant. Since the pressure-cell axis was parallel to the incident beam, this would imply one of two possible causes: the preferred orientation axis (POA) was not coincident with the axis of the pressure cell (although it appears to be during the β-tin phase) or the distribution of crystallites was not axially symmetric around the pressure-cell axis. A possible explanation is that the POA was not coincident with the pressure cell axis (and hence not parallel to the incident beam) in all three phases and that the high symmetry of the lattice in the β-tin phase gave a false impression. A constant intensity powder ring is obtained if the **sum** of the intensities around the powder rings of **all** reflections (in the multiplicity set) is constant. If the (011) scattering vector is the POD (as observed in the study of chapter 5) and the POA lies at a small angle (~20°) to the pressure cell axis, then the maxima of the (200) and (020) reflections would be expected to have positions separated by a γ angle of 90° (as observed in the Imma phase). In such a model the (011) reflection would have its maxima/minima at similar positions as the maxima/minima of the (020) reflection (see figure 6.2.5). Figure 6.2.7 shows the intensity around the (200) β-tin powder ring and the sum of the (200) and (020) reflections of the Imma phase. In the β-tin phase, the (200) and (020) reflections occur at the same 2θ angle and so the (200) β-tin powder ring exhibited little variation in intensity around the ring. Thus, if the lattice has high symmetry, it is possible to

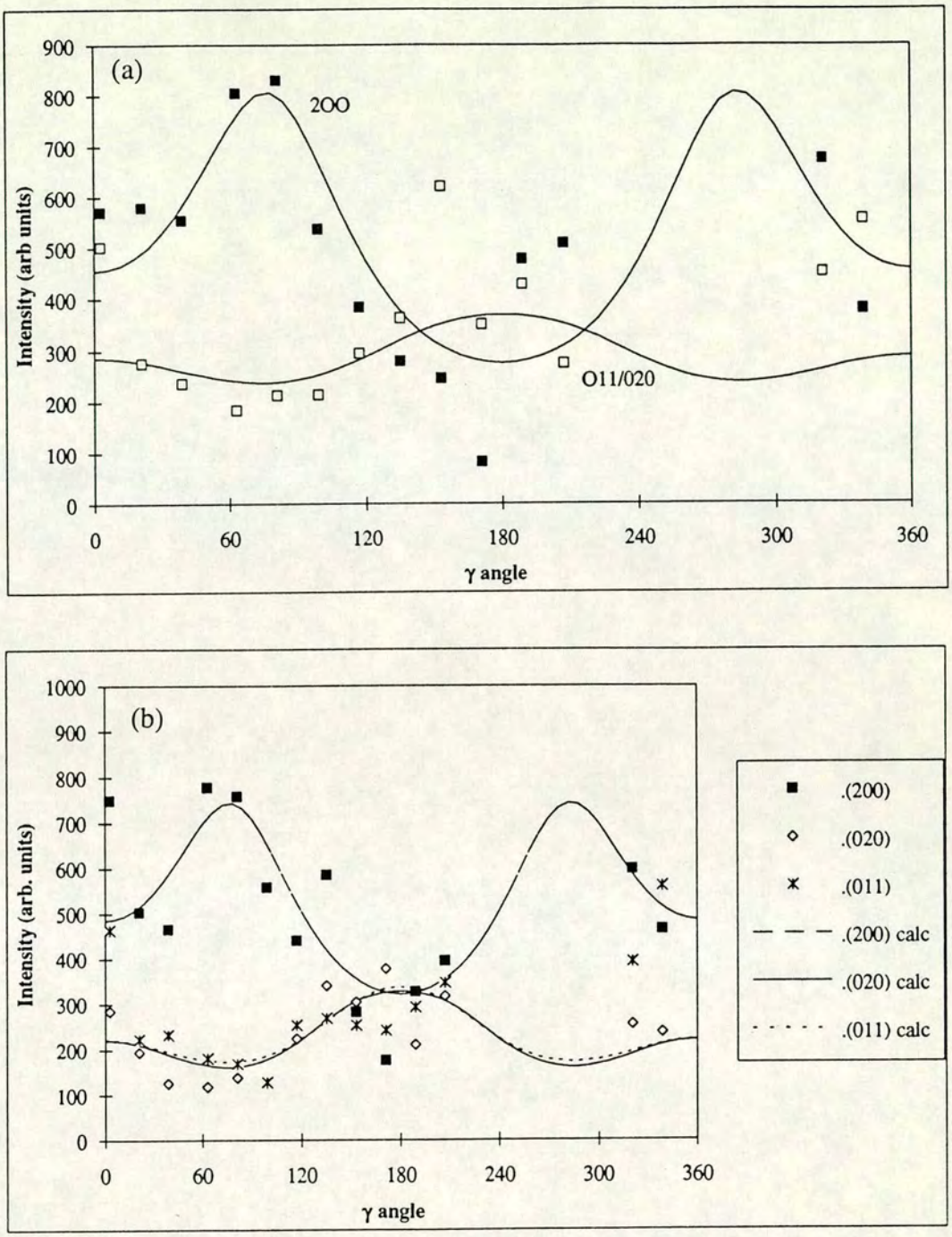

Figure 6.2.5 The observed (points) and calculated (solid lines) intensities versus angle, γ, around the powder ring of the second silicon sample for: (a) the (200) and (011/020) s.h. reflections, (b) the (200) and (020) Imma reflections, and (c) the β-tin (200) reflection. In the first two figures the calculated intensity is obtained from the preferred orientation model discussed in the text.

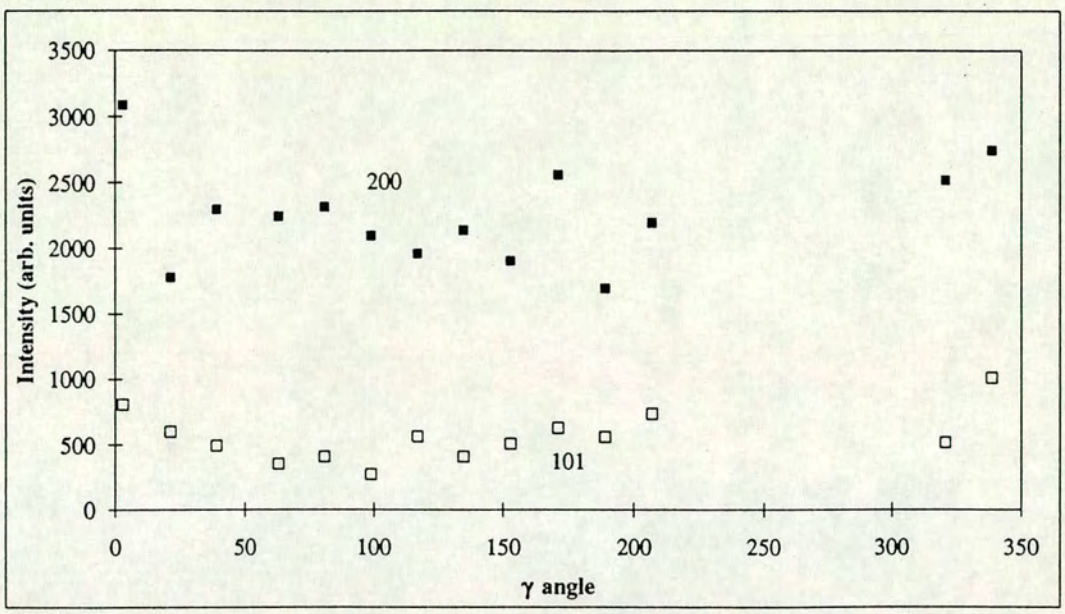
3500
3000
2500
2000
1500
1000
500
0
Intensity (arb. units)
200
101
0
50
100
150
200
250
300
350
γ angle

Figure 6.2.5c

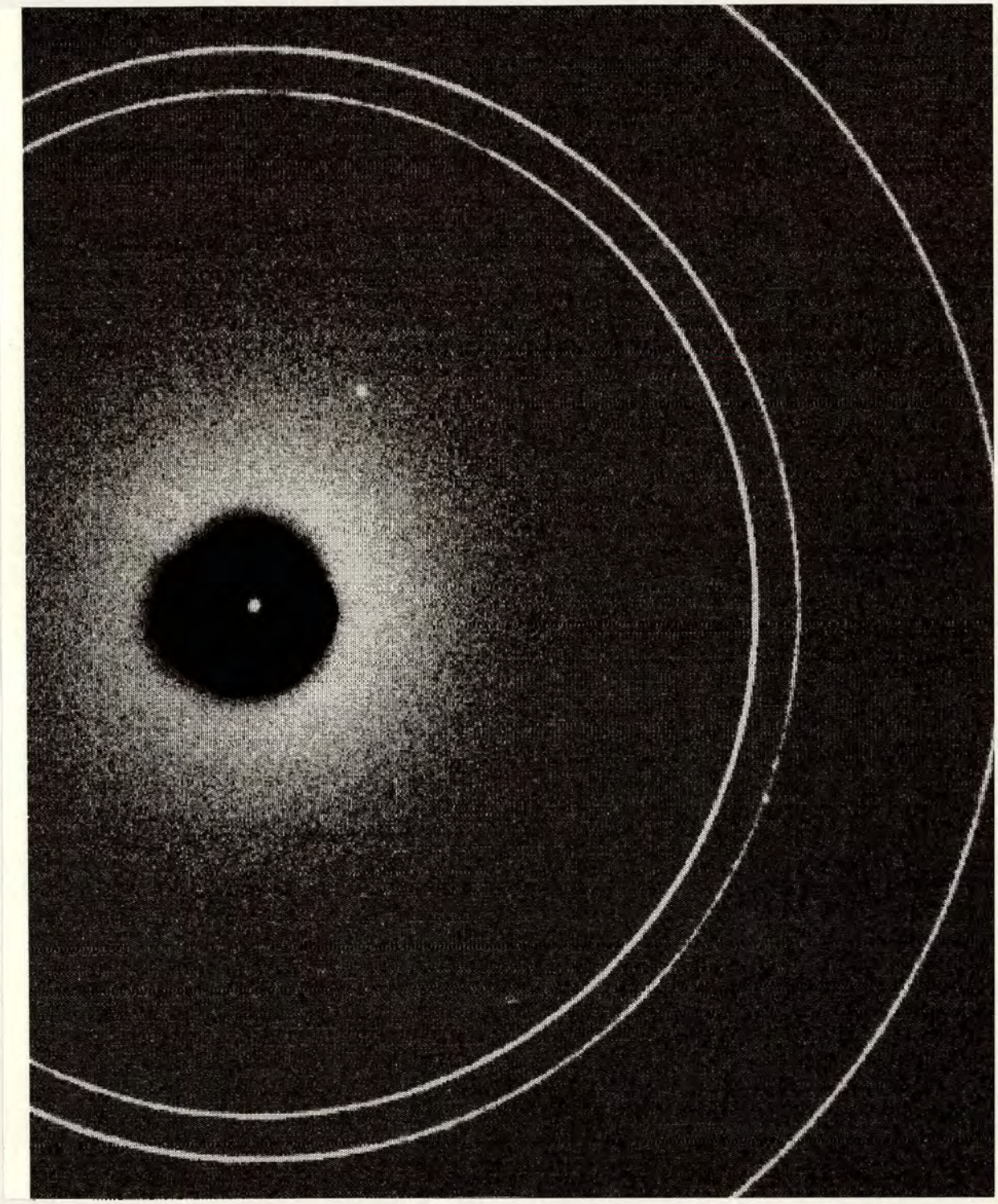

Figure 6.2.6 (a), (b) and (c) show the 2-D images obtained from the second silicon sample at the points shown in figure 6.2.5 (a), (b), and (c) respectively.

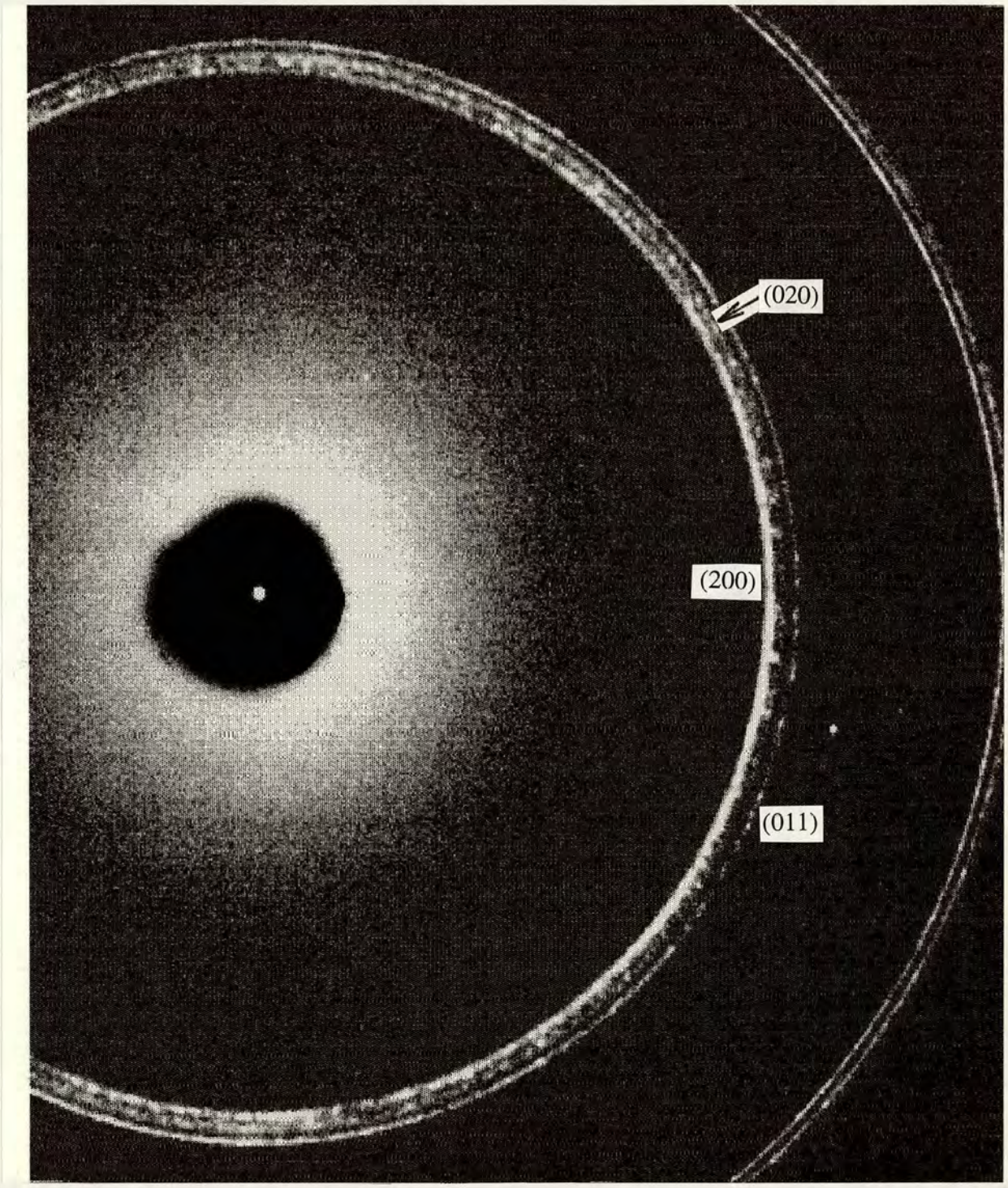

Figure 6.2.6b

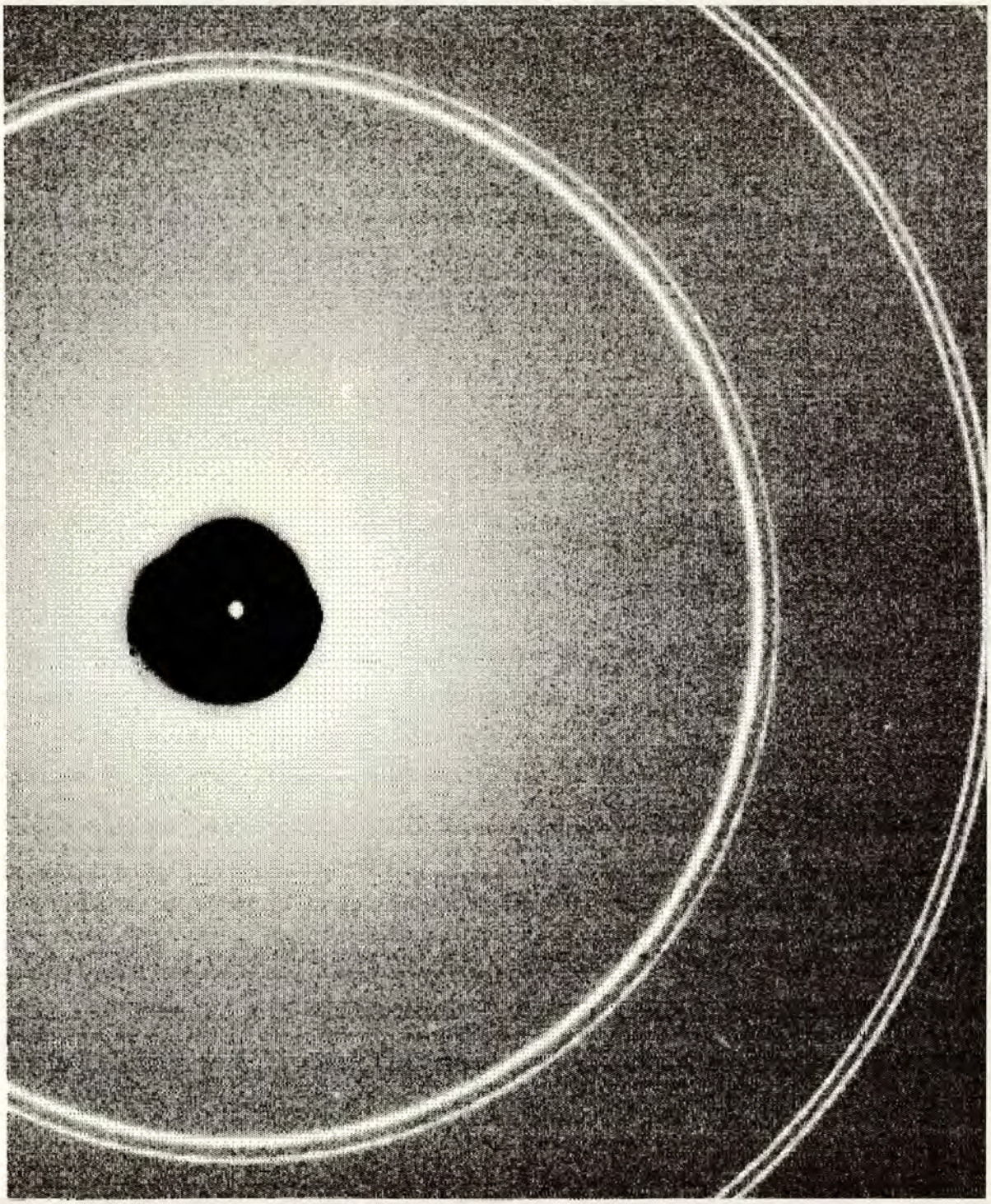

Figure 6.2.6c

misinterpret constant intensity powder rings as proving that the POA is coincident with the incident beam. In the Imma phase, the (200) and (020) reflections occur at different 2θ angles and so clear intensity variation around both the (200) and (020) reflections was observed.

This kind of preferred orientation model was fitted to the observed data from the two samples. Since the angle between the POA and the incident beam was not known it was difficult to model the preferred orientation in these samples. By a trial and error approach, the best fit was found to the Imma phase data from samples 1 and 2 by assuming the POD to be the (011) reflection (as expected from the study in chapter 5) and the orientation of the POD relative to the incident beam to be given by $\omega=20°$, $\varphi=-120°$ and $\omega=20°$, $\varphi=0°$ for the first and second samples respectively. With this model the value of the preferred orientation parameter refined to R=0.36 for the first sample and R=0.48 for the second, which is in agreement with the observed intensities. This model for the Imma phase and the corresponding model for the observed intensities of the s.h. phase is plotted on figures 6.2.4 and 6.2.5. The successful modelling of the data from both phases with the same preferred orientation model indicates that the positions with respect to the beam of the lattice planes of each phase were the same, i.e. the (200) lattice plane of the Imma phase transformed to the (200) plane of the s.h. phase and that (011) plane of the Imma phase transformed to the (011) plane of the s.h. phase. This is in complete agreement with the suggested transition mechanism above and strongly suggests that this simple transition mechanism for the transformation from the Imma phase to the s.h. structure does occur.

The identification of the Imma phase lattice planes with those of the β-tin structure was less clear (in the sense that definite maxima/minima could not be observed in the β-tin reflections). Figure 6.2.7 also shows the calculated fit to the Imma phase and the β-tin phase data using the same preferred orientation model as used above. If the data point at $\gamma\approx180°$ is discarded (perhaps as resulting from a clump in the powder) then the degree of intensity variation in the β-tin (200) reflection and that in the sum of the (200) and (020) Imma reflections was very similar. Since the calculated intensity variations lie within the noise on the data, the experimental evidence is completely consistent with the β-tin (200) lattice planes transforming to the Imma (200) and (020) planes, as expected from the proposed transition mechanism between the two phases.

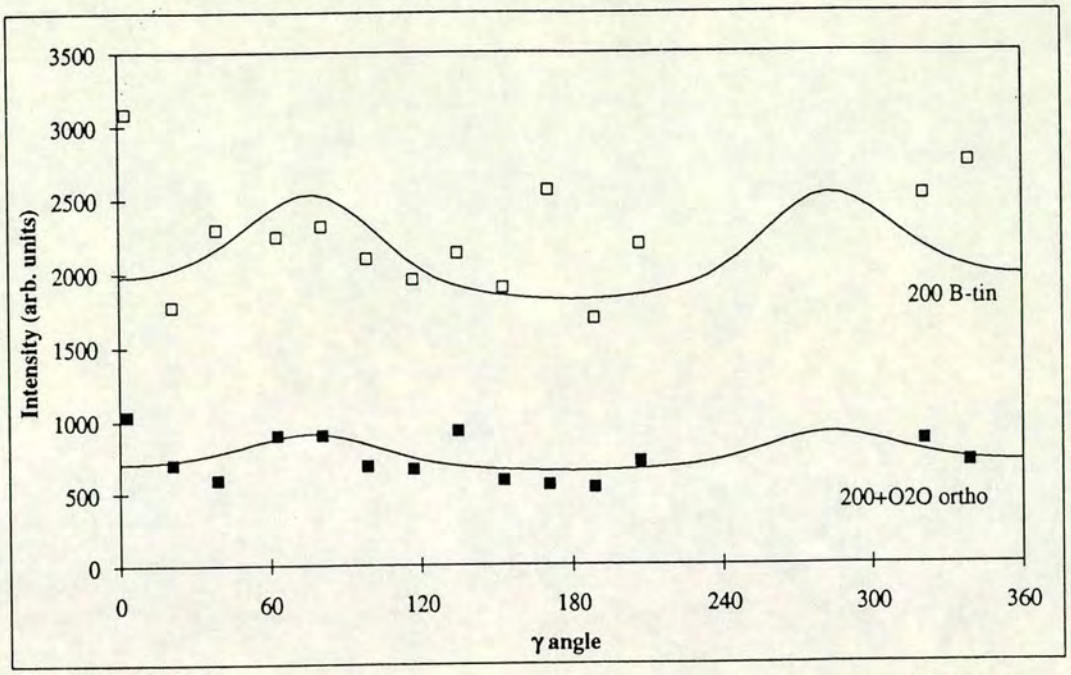

Figure 6.2.7 The observed (points) and calculated intensities (solid lines) of the Imma (200)+(020) reflection (the intensity of the reflections has been added together) and the β-tin (200) reflection for the second silicon sample. The calculated intensities have been obtained by fitting a consistent preferred orientation model to the data from both phases.

The crucial distinction that should be made here is that the orientation of the lattice planes before and after the transitions is constant with respect to an external reference (the incident beam). Provided that the sample in both phases suffers from preferred orientation, this technique offers a way to conclusively relate lattice planes before and after a first-order transition. In the case of Si presented here preferred orientation modelling confirms the expected simple model of the transition mechanism in Si from the β-tin phase through the Imma structure to the s.h. phase. In more complex cases where there may be no obvious relationship between the lattice planes, modelling of the preferred orientation of samples before and after first-order transitions could be a powerful technique for extracting vital information on how these transitions proceed.

Chapter 7

Conclusions

Preferred orientation is one of the main problems encountered in structure refinement from samples held under high pressure and any correlation between the effects of structure and preferred orientation on the reflection intensities may result in serious errors in refined structural parameters from Rietveld refinement. Therefore in high-pressure studies, it is particularly crucial to determine any sample texture independently from the crystal structure. The aim of this thesis was to improve the understanding of preferred orientation as it affects high-pressure powder diffraction and to develop techniques to measure and model sample preferred orientation under pressure.

Experimental techniques have been developed that allow the diffraction pattern to be collected with minimal contamination from gasket scatter from a sample under pressure with the pressure cell axis inclined to the incident beam. A new technique has been presented which makes use of the ability of area detectors, such as image-plates, to record simultaneously data from crystallites in many different orientations to model texture from samples under pressure. This enables data on the crystallite distribution to be collected. A new texture model suitable for the transmission geometry used in high-pressure angle-dispersive diffraction is presented and techniques developed which exploit the 2-D character of the effect of preferred orientation on the powder pattern to de-correlate the effects of texture and structure on the powder pattern. The model has been successfully tested against diffraction data collected in a wide range of sample orientations from a sample of known texture and from a sample of known structure held under pressure in a diamond-anvil pressure cell.

The experimental and preferred orientation modelling techniques have been applied as part of a structural study of three high-pressure phases of HgTe. The results presented

in this section have shown that the structure of HgTe in its cinnabar phase is quite different from that of HgS, the prototype cinnabar structure. The unexpected differences between the cinnabar phases of HgS and HgTe, the consequent differences in coordination and the evolution of the structure of the cinnabar phase of HgTe with pressure invite a revised theoretical treatment of this phase and its role in the zincblende-to-NaCl transition. Preferred orientation modelling has been shown to play a crucial part in the structure solution of HgTe phase IV. The structure of this phase is found to be an orthorhombic distortion of the NaCl structure with an eight-fold coordination shell. The structure of HgTe phase V is shown to be the b.c.c. structure and not a distorted form of the CsCl structure.

The preferred orientation techniques developed in this thesis can also be used to extract information on the phase transition mechanisms between crystal structures. This was illustrated by results on the texture in the transition sequence between the Si β-tin→Imma→simple hexagonal structures. The data and results from preferred orientation modelling confirm the expected simple transition mechanism between these phases.

At present modelling of microstructural effects (such as preferred orientation) observed in samples held under pressure is limited by the quality of data that can be obtained. In general, to extract information from the sample microstructure requires reliable intensities in all sectors of the diffraction pattern and not just in the average intensities around the powder rings. One of the main factors affecting data quality in microstructural studies at high pressure is contamination of the diffraction pattern by scattering from the Be backing discs. At present, the maximum angle between the pressure-cell axis and the incident beam that allows the direct beam to enter and leave the pressure cell without striking the Be backing disc, is ~10°. Because of improved diamond cuts and pressure cell designs, pressure cells should be available in the near future with wider apertures in the Be discs. This will significantly improve the quality of data that can be obtained, with considerable improvement in the accuracy of modelling techniques. The maximum angle of access to a pressure cell is limited by the opaque steel cell body. At present the maximum angle between the pressure-cell axis and the incident beam that still allows a significant fraction of the diffraction pattern to leave the cell through the Be discs is in the range 30°-40°. Future designs of pressure cell should allow the angular access to be extended to over 50°, which should allow vital information on the variation in reflection intensity with angle between the POA and incident beam to be improved.

The high brilliance of third generation synchrotron sources is well suited to high-pressure diffraction, which requires intense beams of low cross-sectional area. The extra diffracted intensity will allow data to be collected to excellent statistics in all sectors of the diffraction pattern. This will make preferred orientation modelling more feasible on weaker scattering materials.

At present the processing of the data for microstructural modelling is too time consuming to be done during an experiment but is done after the data collection has been completed. Because of this, it is hard to ensure that the relevant data is collected to suitable statistics, which is very inefficient. Future increases in computing power and special interactive software complete with graphics will allow microstructural modelling to be performed during the experiment. Improvements in computer visualisation of effects such as intensity variation around the powder ring should facilitate improved analysis of sample texture and allow possible models to be explored more easily. These developments will also allow more complex crystallite distributions to be explored and modelled.

One of the great unsolved problems of condensed matter science is the transition mechanisms between different high-pressure phases. The image-plate system developed on station 9.1 at SRS Daresbury by the University of Edinburgh group has sufficient resolution and sensitivity to enable *in situ* studies of sample microstructure under pressure to be performed. This technique is potentially a powerful new development in the study of the mechanisms of first-order phase transitions under pressure. It has been shown in this study and by other authors that a great deal of valuable information can be extracted from the microstructure exhibited by the sample, which with the development of area detector techniques is now experimentally feasible. In the near future it will be possible to perform *in situ* experiments on powder samples of high-pressure phases produced from aligned single crystals. If (as suggested in other preliminary studies, e.g. Besson *et al*, (1991)) these types of transitions nucleate on specific lattice planes, the resulting diffraction pattern will show a complex multi-pole distribution. By collecting data with the pressure cell axis inclined at various angles to the beam, the resulting crystallite distribution can be modelled. From this work it might be possible to determine valuable information on the orientational relationships between the phases, the shape of the nucleating grains (from any hkl dependent peak widths) and the orientation of the high-pressure phase

axes relative to this shape. Such information could play a vital role in understanding the many first-order phase transitions under pressure.

It seems clear that modelling of many microstructural effects such as preferred orientation, deviatoric stress, lattice faulting etc., will become increasingly important in the future for high-pressure powder-diffraction studies. The recent development of angle-dispersive diffraction techniques using area detectors has enabled some long-standing problems in the structural systematics of semiconductors under pressure to be solved. The extra sensitivity of these techniques has allowed data of unparalleled quality to be collected, which is raising many interesting questions on the behaviour of materials under pressure. Answering many of these questions will require accurate understanding of the microstructure of the sample.

REFERENCES

Adams D.M., Private communication (1992).

Ahsbahs H., Rev Sci Instrum **55**, 99 (1984).

Ahtee M., Nurmela M., Suortti P., and Järvinen M., J. Appl. Cryst. **22**, 261 (1989)

Allan D.R., PhD thesis University of Edinburgh (1994)

Arndt U.W. and Stubbings S.J., J. Appl. Cryst. **21**, 577 (1988).

Aurivillius K. L., Acta Chemica Scan. **4**, 1423 (1950).

Aurivillius K. L. and Carlson I., Acta Chemica Scan. **12**, 1297 (1958).

Barrett C., and Massalski T.B., in 'Structure of Metals', International Series on Materials Science and Technology, Vol 35, Pergamon Press (1992).

Besson J. M., Hamel G., Grima T., Nelmes R. J., Loveday J. S., Hull S., Häusermann D., High Pressure Research **8**, 639 (1992).

Besson J.M., Itié J.P., Polian A., Weill G., Phys Rev B **44**, 4214 (1991)

Blair J. and Smith A. C. , Phys. Rev. Lett. **7**, 124 (1961).

Bourgeois D., Moy J.P., Svensson S.O., and Kvick Å, J. Appl. Cryst. (in press) (1994)

Bridgman P. W., Proc. Am. Acad. Arts. Sci. **74**, 24 (1940).

Bridgman P. W., 'The Physics of High Pressure', Dover Publications, New York (1971).

Bunge H.J., Dahms M., and Brokmeier H.G., Cryst. Rev. **2**, 67 (1989).

Bushnell-Wye G., Private Communication (1993).

Capkova P. and Valvoda V., Czech. J. Phys. **B24**, 891 (1974)

Cernik R.J., Private Communication (1994)

Dahms M. and Bunge H.J., J. Appl. Cryst. **22**, 439 (1989)

Decker D.L., Bassett W. A., Merrill L., Hall H. T. and Barnett J.D., J. Phys. Chem. Ref. Data **1**, 773 (1972).

Dollase W.A., J. Appl. Cryst. **19**, 267 (1986)

Duclos S.J., Vohra Y.K., and Ruoff A.L. Phys Rev B **41**, 12021 (1990).

Fujii Y., Shimomura O., Takemura K., Hoshino S., and Minomura S., J. Appl. Cryst. **13**, 284 (1980).

Fujii Y., Hose K., Ohishi Y., Fujihisa H., Hamaya N., Takemura K., Shimomura O., Kikegawa T., Amemiya Y., and Matsushita T., Phys. Rev. Lett. **63**, 536 (1989).

Hall H.T., Merrill L., and Barnett J.D., Science **146**, 1297 (1964).

Hamilton W.C., 'Statistics in Physical Science', Ronald Press (1964).

Hammersley A., Private Communication (1993).

Huang T. and Ruoff A. L., Phys. Stat. Sol.(a) **77**, K193 (1983).

Huang T. and Ruoff A. L., Proceedings of 9th AIRAPT Conference, in 'High Pressure Science and Technology', Pt 3, **22**, 37 (1984) (North Holland, NY).

Huang T. and Ruoff A. L., Phys. Rev. B **31**, 5976 (1985).

Huang T. and Ruoff A. L., J. Appl. Phys. **54**, 5459 (1983).

Huang T. and Ruoff A. L., Phys. Rev. **27**, 7811 (1983)

Itié J.P., Baudelet F., Dartgye E., Fontaine A., Tolentino H., and San-Miguel A., High Pressure Research **8**, 697 (1992).

Jamieson J.C., Science **139**, 764 (1964).

Järvinen M., Merisalo M., Pesonen A., and Inkinen O., J. Appl. Cryst. **3**, 313 (1970)

Järvinen M., J. Appl. Cryst. **26**, 525 (1993)

Jayaraman A., Klement W. Jr., and Kennedy G. C. , Phys. Rev. **130**, 2277 (1963).

Kahn R., Fourme R., Gadet A., Janin J., Dumas C., and André D., J. Appl Cryst **15**, 330 (1982)

Kikegawa T., High Pressure Research **8**, 639 (1992).

Langford J. I., in 'Accuracy in Powder Diffraction II', NIST Spec. Pub. no. **86**, pg 110 (1992) (Gaithersburg MD: U.S. Dept. of Commerce).

Larson A. C. and Von Dreele R. B. (unpublished) (1985).

Lewis J., Schwarzenbach D. and Flack H. D., Acta Cryst **A38**, 733 (1982)

Malinowski M., J. Appl. Cryst. **20**, 379 (1987).

Mao H. K., Bell P. M., Shaner J. W. and Steinberg D. J., J. Appl. Phys **49**, 3276 (1978).

March A., Z. Kristallogr. **81**, 285 (1932).

Mariano A. N. and Warekois E. P., Science **142**, 672 (1963).

Mathies S., Wenk H.R., and Vinel G.W., J. Appl. Cryst. **21**, 285 (1988).

McKeever S. W. S., 'Thermoluminescence of Solids', pg 210 Cambridge University Press (1985).

McMahon M.I. and Nelmes R.J., Phys Rev B **47**, 8337 (1993).

Merrill L. and Bassett W. A. Rev. Sci. Instrum. **45**, 290 (1974).

Miller A. J., Saunders G. A., Yogurtçu Y. K., and Abey A. E., Phil. Mag. **43**, 1447 (1981).

Minomura S. and Drickamer H.G., J. Phys. Chem. Solids **23**, 451 (1962).

Moy J.P., Koch A., and Nielsen M.B., Nuclear Instruments and Methods **A326**, 581 (1993).

Naday I., Strauss M.G., Sherman I.S., Kraimer M.R., and Westbrook E.M., Opt. Eng. **8**, no 26, 788 (1987).

Nelmes R. J., McMahon M. I., Wright N. G. and Allan D. R, Phys. Rev. B Rapid Communications, in press.

Nelmes R.J., Hatton P.D., McMahon M.I., Piltz R.O., Crain J., Cernik R.J. and Bushnell-Wye G., Rev. Sci. Instrum. **63**, 1039 (1992).

Nelmes R.J., McMahon M.I., Hatton P.D., Piltz R.O., Crain J., Cernik R.J. and Bushnell-Wye G., High Pressure Research **8**, 677 (1992).

Nelmes R.J., McMahon M.I., Hatton P.D., Crain J., and Piltz R.O., Phys. Rev. B **47**, 35 (1993)

Newsam J.M., Deem M.W., and Freeman C.M., in 'Accuracy in Powder Diffraction II', NIST Spec. Pub. no. **86**, pg 80 (1992) (Gaithersburg MD: U.S. Dept. of Commerce).

Ohtani A. H., Seike T., Motobayashi M., and Onodera A. , J. Phys. Chem. Solids **43**, 627 (1982).

Okai B. and Yoshimoto J., J. Phys. Soc. Japan **45**, 1880 (1978).

Olijnyk H., Sikka S.K., and Holzapfel W.B., Physics Letters **103A**, 137 (1984).

Onodera A., Ohtani A., Motobayashi M., Seike T., Shimomura O., and Fukunaga O., Proceedings of the 8th AIRAPT conference, Uppsala, Sweden 1981, **1**, 321 (1982) (Arkitektopis Uppsala)

Parrish W. and Huang T.C., Adv. X-ray Anal **26**, 35 (1983).

Papiz M.Z. and Helliwell J.R., Daresbury Lab. Tech. Memorandum DL/SCI/TM42E (1985)

Pawley G. S., J. Appl. Cryst. **13**, 630 (1980)

Peisser H.S., Rooksby H.P., and Wilson A.J.C., in 'X-ray Diffraction by polycrystaline Materials', Institute of Physics (1955).

Pesonen A. J. Appl. Cryst. **12**, 460 (1979)

Piermarini G. F., Block S., Barnett J. D., and Forman R. A., J. Appl. Phys **46**, 2774 (1975)

Piltz R.O. , McMahon M.I., Crain J., Hatton P.D., Nelmes R.J., Cernik R.J. and Bushnell-Wye G, Rev. Sci. Instrum. **63**, 700 (1992).

Qadri S. B., Skelton E. F., and Webb A. W., J. Vac. Sci. Technol. A **4**, 1975 (1986).

Qadri S. B., Webb A. W., Skelton E. F., Moulton N., Furdyna J., and Colombo L., High Pressure Res. **4**, 303 (1990)

Rietveld H. M., J. Appl. Cryst. **2**, 65 (1969).

Ruoff A. L., High Pressure Research **8**, 639 (1992).

Shaw C.C., Herron J.M., and Gur D., Medical Imaging VI: Instrumentation SPIE Vol. 1651, 156 (1992)

Shimomura O., Takemura K., Fujihisa H., Fujii Y., Ohishi Y., Kikegawa T., Amemiya Y. and Matsushita T., Rev. Sci. Instrum **63**, 967 (1992)

Singh A.K. and Kennedy G.C., J. Appl. Phys. **45**, 4686 (1974).

Spain I. L., Skelton E. F., and Rachford F., in 'High Pressure Science and Technology' eds B. Vodar and Ph. Markeau, **1**, 150 (Pergamon Press, Oxford, 1980)

Stanton M., Phillips W.C., Li Y., and Kalata K., J. Appl. Cryst. **25**, 549 (1992)

Takemura K., Minomura S., and Shimomura O., Phys Rev Lett **49**, no 24, 1772 (1982)

Tedenac J. C., Record M. C., Ayral-Marin R. M., Brun G., Jun J., Grzegory I., Krukowski S., and Bockowski M., Jpn. J. Appl. Phys. **32**, Suppl. 32-1, 26 (1993)

Takemura K., Shimomura O., Tsuji K., and Minomura S., High Temperatures-High Pressures **11**, 311 (1979)

Triboulet R., Lasbley A., Toulouse B., and Granger R., J. Cryst. Growth **79**, 695 (1986)

Ude M., Z. Anorg. Allg. Chem. **350**, 105 (1967).

Valvoda V., in 'Accuracy in Powder Diffraction II', NIST Spec. Pub. no. **86**, pg 127 (1992) (Gaithersburg MD: U.S. Dept. of Commerce).

Vanderborgh C.A., Vohra Y.K., and Ruoff A.L., Phys Rev B **40**, 12450 (1989)

Warren B.E., 'X-ray Diffraction', Dover Publications (1969)

Weir C. E., Block S. and Piermarini G, J. Res. Nat. Bur. Stand. **C69**, 275 (1965).

Wentorf R.H. and Kasper J.S., Science **139**, 339 (1963).

Werner A., Hochheimer H. D., and Strössner K., Phys. Rev. B **28**, 3330 (1983).

Werner P. E., Eriksson L., Westdahl M., J. Appl. Cryst **18**, 367 (1985).

Zhu Hu, J. Solid State Com. **63**, 471 (1987)

Wright N. G., McMahon M. I., Nelmes R. J., and San-Miguel A., Phys. Rev B, **48**, 13111 (1993).

Wright N. G., McMahon M. I., and Nelmes R. J. in Proceedings of the Joint AIRAPT/APS Topical Conference on High Pressure Science and Technology, Colorado Springs (American Institute of Physics), pg 449, 1993

PUBLISHED WORK

Brief Reports

ief Reports are accounts of completed research which, while meeting the usual **Physical Review** *standards of scientific quality, do warrant regular articles. A Brief Report may be no longer than four printed pages and must be accompanied by an abstract. The e publication schedule as for regular articles is followed, and page proofs are sent to authors.*

Crystal structure of the cinnabar phase of HgTe

N. G. Wright, M. I. McMahon, and R. J. Nelmes
Department of Physics, The University of Edinburgh, Mayfield Road, Edinburgh, EH9 3JZ, United Kingdom

A. San-Miguel
Physique des Milieux Condensés, Université Pierre et Marie Curie, B77, 4 Place Jussieu, F-75252 Paris CEDEX 05, France

(Received 7 June 1993)

Angle-dispersive powder-diffraction techniques with an image-plate area detector and synchrotron radiation have been used to perform a structural refinement of mercury telluride in its cinnabar phase. We find that the structure is site-ordered with fractional coordinates of $(u=0.641(1),0,\frac{1}{3})$ and $(v=0.562(1),0,\frac{5}{6})$ for Hg and Te, respectively, at 3.6 GPa. The structure is substantially different from that of HgS cinnabar, with coordination much closer to fourfold.

I. INTRODUCTION

phase transition in HgTe under pressure was found Bridgman, who detected a volume discontinuity at 3 GPa in compressibility measurements.[1] The overy that the transition is accompanied by an abrupt ge in resistivity[2] has led to extensive further k.[3–15] HgTe is one of the II-VI compounds that ex- a cinnabar phase,[3,4,7] thought until recently to be liar to the mercury chalcogenides.[6,11] This phase is known in the phase diagrams of HgS,[16,17] HgO,[18] HgSe,[4,19] but has now been discovered in CdTe[20] In HgS and HgO, the cinnabar phase occurs at am- pressure, and full structural studies have been per- ed for both.[16,18] In common with HgSe and CdTe, e transforms to cinnabar under pressure (1.4 GPa) an ambient-pressure zincblende phase.[4,7] Further sure increase brings about a transformation to the salt structure at 8 GPa (Refs. 7 and 10) and then, ing at 11.5 GPa, to another phase,[5,7,8,14] phase IV, identified as having a β-tin[9] or orthorhombic[10,11] ture. The latter interpretation was later modified to dy-centered tetragonal structure, probably different β-tin,[12] and evidence of another phase above 38 was also reported.[12]

ere has been particular interest in the cinnabar e of HgTe and other mercury chalcogenides, and s have been made to understand the role of this e as an intermediate stage in the zincblende to NaCl formation.[6,10,12,15,17,19] However, the atomic coordi- of Hg and Te have never been determined and dis- on has had to be based on the structure of HgS cin- r. We have now embarked on a detailed diffraction of HgTe in its cinnabar phase to determine the site ing and structural pressure dependence. In this paper we report the crystal structure and show that it is significantly different from that of HgS.

II. EXPERIMENTAL TECHNIQUES

Diffraction data were collected on station 9.1 at the Synchrotron Radiation Source, Daresbury, using angle-dispersive techniques and an image-plate area detector. The two-dimensional powder patterns collected on the image plates were read on a Molecular Dynamics 400A PhosphorImager and then integrated to give conventional one-dimensional diffraction profiles. Details of our experimental setup and pattern integration program have been reported previously.[21–23] The sample material was obtained from R. Triboulet, in the form of a fine-grained powder prepared as described in Ref. 24. Four different samples were prepared, each loaded into a diamond-anvil cell with a full conical aperture of half-angle 40–50°. The pressure-transmitting medium was a 4:1 mixture of methanol:ethanol, and the pressure was measured using the ruby fluorescence technique.[25] The incident x-ray wavelength was 0.4654 Å, calibrated using a standard silicon sample. The structural results presented were all obtained from full Rietveld refinement[26] of the integrated profiles using the program GSAS.[27]

III. RESULTS AND DISCUSSION

Figure 1 shows the one-dimensional (1D) profile obtained after azimuthal integration of the 2D image obtained at 3.6 GPa from one of the samples. The transition from zincblende to cinnabar results in a reproducible microstructural effect on the peak profiles, which vary significantly in breadth. Reflections with $l \gg h,k$ are preferentially sharp, which is consistent with the average crystallite being significantly longer along the crystallo-

1829/93/48(17)/13111(4)/$06.00

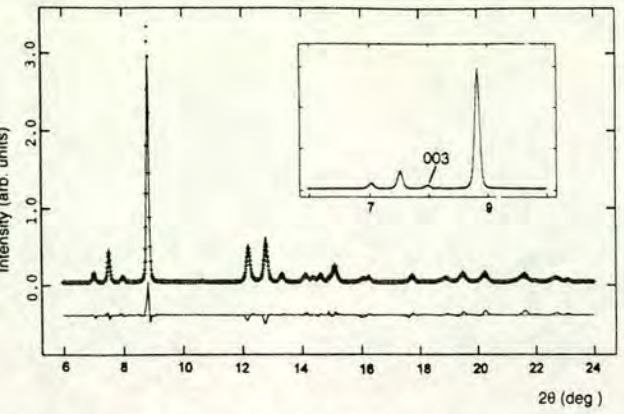

FIG. 1. The integrated profile of a powder pattern collected om HgTe at 3.6 GPa. The solid lines shows the fit to the data rosses) obtained in structure refinement. The difference be- ween the observed and calculated profiles is also displayed. art of the profile is enlarged in the inset to show the 003 flection.

aphic c axis. This may be important for the actual echanism of the transformation. Structure refinement as carried out with the Hg atoms on the $3a$ sites of ace group $P3_121$ at $(u,0,\frac{1}{3})$ and the Te atoms on the $3b$ es at $(v,0,\frac{5}{6})$, starting from the coordinates of the HgS nnabar structure at ambient pressure.[16] The variable ordinates u and v refined to 0.641(1) and 0.562(1), re- ectively, and the lattice parameters refined to $=4.383(1)$ Å and $c=10.022(2)$ Å. These values, and e refined scale factor, peak-shape parameters (including model for anisotropic widths, as above), and thermal otion parameters give the fit shown in Fig. 1. The re- lts obtained from the other samples agree within the es- mated standard deviations (e.s.d.'s).

The 003 reflection is clearly observed, as shown in the set in Fig. 1. Since this reflection arises from the fference in scattering between the $3a$ and $3b$ sites, its resence establishes that the structure is site ordered. As a further check, the occupancies were allowed to refine freely but showed no movement away from full site order. The assignment of Hg to the $3a$ site and Te to $3b$ was checked by interchanging the Hg and Te atoms and refining first with the occupancies free and then fixed. In the former case the occupancies refined to values consistent with interchanging back to the original positions, and in the latter case the calculated pattern showed some significant discrepancies with the data. Thus the site assignment can be stated with confidence.

We observe the c/a ratio to be 2.287, close to the value of 2.27 obtained by Qadri, Skelton, and Webb.[13] However, Werner, Hochheimer, and Strössner[9] reported a significantly different value of 2.222 at 2.6 GPa. The observed change in c/a with pressure is small[13] so this discrepancy could not result simply from the difference in sample conditions. The authors observed only four reflections which they index as 101, 102, 110, and 201; but a better fit to the relative d spacings is obtained with the last of these reflections indexed as 200. If we re-refine our data with the same misindexing, we obtain $c/a=2.23$ (at 3.6 GPa), close to the value found by Werner, Hochheimer, and Strössner.[9] Qadri, Skelton, and Webb[13] also report a study of a $Hg_{0.8}Cd_{0.2}Te$ alloy and obtain a c/a ratio of 2.297 at 3.6 GPa. This is ~ 0.025 larger than they found for HgTe, and we find the c/a ratio for CdTe to be 0.098(1) larger than that of HgTe (at 3.6 GPa). Hence, the c/a ratio appears to vary approximately in proportion to the Cd content.

The refined values of the atomic coordinates and lattice parameters of HgTe are presented in Table I, and compared with results for HgS, HgO, HgSe, and CdTe. The structure of HgTe is shown in xy projection in Fig. 2(b). The atoms form infinite -Hg-Te-Hg-Te- spirals along the c axis, with the two nearest-neighbor distances in the spirals, the a bonds [2.732(4) Å], being shorter than the b and c bonds linking atoms in adjacent spirals [2.995(4) Å and 3.460(5) Å, respectively]. The two different bond an-

TABLE I. Comparison of the lattice parameters (a and c), and refined atomic coordinates (u and v) for the cinnabar phases of HgS, gO, HgSe, HgTe, and CdTe. (Only lattice parameters are known for HgSe.) Also given are the nearest-neighbor distances and the ngles between a bonds at the X atom (O, S, Se, or Te) and the M atoms (Hg or Cd). The final column shows cubic NaCl referred to e cinnabar unit cell. Estimated standard deviations are quoted in parentheses if they are known.

MX	HgS at ambient pressure (Ref. 16)	HgO at ambient pressure (Ref. 18)	HgSe at 1.5 GPa (Ref. 4)	HgTe at 3.6 GPa (this work)	CdTe at 3.6 GPa (Ref. 20)	NaCl structure
(Å)	4.14	3.577	4.32	4.383(1)	4.292(2)	
(Å)	9.49	8.681	9.68	10.022(1)	10.235(3)	
/a	2.292	2.427	2.24	2.287(2)	2.385(2)	2.449
	0.720(3)	0.745	not yet determined	0.641(1)	0.641(2)	0.667
	0.480(10)	0.460		0.562(1)	0.564(2)	0.667
earest-neighbor stances, (Å)						
bonds	2.36(5)	2.03(2)		2.732(4)	2.724(4)	
bonds	3.10(5)	2.79(2)		2.995(4)	2.971(5)	all equal
bonds	3.30(5)	2.90(3)		3.460(5)	3.414(5)	
ond angles						
-*X*-*M*(°)	105.2(2.0)	108(2)		104.2(2)	104.6(3)	90
-*M*-*X*(°)	172.4(1.7)	176(3)		165.6(2)	166.1(4)	180

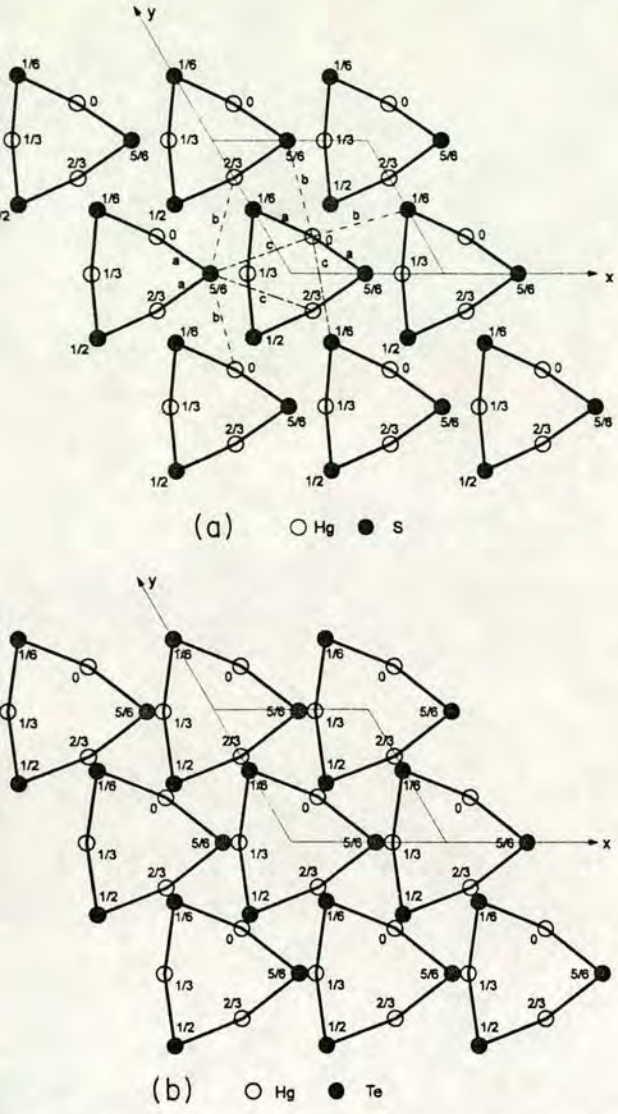

FIG. 2. (a) The cinnabar structure of HgS at ambient pressure shown in projection onto the xy plane. The z coordinate is given by each atom, and the nearest-neighbor contacts (two a bonds, two b bonds, two c bonds) are shown for one of the Hg atoms (○) and one of the S atoms (●). (b) The cinnabar structure of HgTe at 3.6 GPa shown in the same way. The nearest-neighbor contacts can be identified by comparison with (a).

es in the spirals, Hg-Te-Hg and Te-Hg-Te, are 104.2(2)° nd 165.6(2)°, respectively. These distances and angles e also included in Table I.

The final column of Table I gives values for the NaCl ructure referred to the hexagonal unit cell of cinnabar. he cinnabar structure becomes equivalent to that of aCl when $c/a=\sqrt{6}=2.449$ and $u=v=\frac{2}{3}$. In terms of ie c/a ratio, HgTe is further from NaCl than is CdTe ut both have similar fractional coordinates. These are gnificantly different from those of either HgS or HgO, hich both form the cinnabar structure at ambient pres-ire. Figure 2(a) shows the cinnabar structure of HgS for omparison with HgTe in Fig. 2(b). In HgS, the spirals along the c axis have a smaller radius: the a bonds, between nearest neighbors in the spirals, are much shorter than the b and c bonds. Thus the HgS structure is regarded as 2-coordinated. It has been assumed that the same is true of HgTe,[11,12] but our results reveal substantial structural differences. The greater radius of the spirals in HgTe (Fig. 2) means that atoms in adjacent spirals are closer together than in HgS. The a and b bond lengths of HgTe are then similar (Table I), and the coordination is close to fourfold. The same is found in CdTe.[20] Taking all six nearest-neighbor contacts into account, HgS and HgO can thus be described as 2+4 coordinated, and HgTe and CdTe as 4+2. The latter is closer to the sixfold coordination of NaCl. This may partly reflect the fact that HgTe and CdTe at 3.6 GPa are approaching the transition to the NaCl phase (at 8 GPa and ~4 GPa, respectively), while HgS at ambient pressure is far from its transition at 13 GPa.[17]

All five of the known cinnabar structures (Table I) have c/a *less* than the value of 2.449 corresponding to a cubic unit cell. This distortion alone has the effect of reducing the bond angle at the anion, M-X-M, below 90°. However, in a 2-coordinated environment this angle is expected to be closer to tetrahedral, while the X-M-X angle remains close to 180° (Ref. 16). This requires the v coordinate to differ from $\frac{2}{3}$ by more than the u coordinate, as observed: the values of u and v in Table I all have $u>v$, with a mean of ~0.6 rather than $\frac{2}{3}$. If the M-X-M and X-M-X angles *are* indicative of the coordination, it has to be remarked that their values in HgTe are similar to those of HgS, in contrast to the differences seen in nearest-neighbor distances. And HgTe (and CdTe) is as distorted from NaCl as HgS in terms of the bond angles.

In conclusion, we have shown that the structure of HgTe in its cinnabar phase is quite different from that of HgS. In terms of nearest-neighbor distances the HgTe structure is closer to 4-coordinated than 2-coordinated. This, the bond angles, and the recent discovery of a cinnabar phase in CdTe invite a revised theoretical treatment of this phase and its role in the zincblende-to-NaCl transition.

ACKNOWLEDGMENTS

We gratefully acknowledge the assistance of our colleagues D. R. Allan and J. S. Loveday in many aspects of the experimental work. We would also like to thank A. A. Nield and G. Bushnell-Wye of the Daresbury Laboratory for help in preparing the beam-line equipment and R. Triboulet for providing the sample material. This work is supported by a grant from the U. K. Science and Engineering Research Council and from the Spanish Science and Education Council (A.S-M.), and also by facilities made available by Daresbury Laboratory. We acknowledge the use of the SERC-funded Chemical Database Service at Daresbury Laboratory. Physique des Milieux Condensés is Unité Associé URA782 au Centre National de la Recherche Scientifique.

P. W. Bridgman, Proc. Am. Acad. Arts Sci. **74**, 24 (1940).
J. Blair and A. C. Smith, Phys. Rev. Lett. **7**, 124 (1961).
A. Jayaraman, W. Klement, Jr., and G. C. Kennedy, Phys. Rev. **130**, 2277 (1963).
A. N. Mariano and E. P. Warekois, Science **142**, 672 (1963).
I. L. Spain, E. F. Skelton, and F. Rachford, in *High Pressure Science and Technology,* edited by B. Vodar and Ph. Markeau (Pergamon, Oxford, 1980), Vol. 1, p. 150.
A. J. Miller, G. A. Saunders, Y. K. Yogurtçu, and A. E. Abey, Philos. Mag. **43**, 1447 (1981).
A. Onodera, A. Ohtani, M. Motobayashi, T. Seike, O. Shimomura, and O. Fukunaga, *Proceedings of the 8th AIRAPT Conference, Uppsala, Sweden 1981* (Arkitektopis, Uppsala, 1982), Vol. 1, p. 321.
A. H. Ohtani, T. Seike, M. Motobayasi, and A. Onodera, J. Phys. Chem. Solids **43**, 627 (1982).
A. Werner, H. D. Hochheimer, and K. Strössner, Phys. Rev. B **28**, 3330 (1983).
[0]T. Huang and A. L. Ruoff, Phys. Status Solidi A **77**, K193 (1983).
[1]T. Huang and A. L. Ruoff, *Proceedings of 9th AIRAPT Conference,* in *High Pressure Science and Technology* (North Holland, New York, 1984), Pt. 3, Vol. 22, p. 37.
[2]T. Huang and A. L. Ruoff, Phys. Rev. B **31**, 5976 (1985).
[3]S. B. Qadri, E. F. Skelton, and A. W. Webb, J. Vac. Sci. Technol. A **4**, 1975 (1986).
[4]S. B. Qadri, A. W. Webb, E. F. Skelton, N. Moulton, J. Furdyna, and L. Colombo, High Pressure Res. **4**, 303 (1990).
[15]J. C. Tedenac, M. C. Record, R. M. Ayral-Marin, G. Brun, J. Jun, I. Grzegory, S. Krukowski, and M. Bockowski, Jpn. J. Appl. Phys. **32**, Suppl. 32-1, 26 (1993).
[16]K. L. Aurivillius, Acta Chem. Scand. **4**, 1423 (1950).
[17]T. Huang and A. L. Ruoff, J. Appl. Phys. **54**, 5459 (1983).
[18]K. L. Aurivillius and I. Carlson, Acta Chem. Scand. **12**, 1297 (1958).
[19]T. Huang and A. L. Ruoff, Phys. Rev. **27**, 7811 (1983).
[20]R. J. Nelmes, M. I. McMahon, N. G. Wright, and D. R. Allan, Phys. Rev. B **48**, 1314 (1993).
[21]R. J. Nelmes, P. D. Hatton, M. I. McMahon, R. O. Piltz, J. Crain, R. J. Cernik, and G. Bushnell-Wye, Rev. Sci. Instrum. **63**, 1039 (1992).
[22]R. O. Piltz, M. I. McMahon, J. Crain, P. D. Hatton, R. J. Nelmes, R. J. Cernik, and G. Bushnell-Wye, Rev. Sci. Instrum. **63**, 700 (1992).
[23]R. J. Nelmes, M. I. McMahon, P. D. Hatton, R. O. Piltz, J. Crain, R. J. Cernik, and G. Bushnell-Wye, High Pressure Res. **8**, 677 (1992).
[24]R. Triboulet, A. Lasbley, B. Toulouse, and R. Granger, J. Cryst. Growth **79**, 695 (1986).
[25]G. F. Piermarini, S. Block, J. D. Barnett, and R. A. Forman, J. Appl. Phys. **46**, 2774 (1975).
[26]H. M. Rietveld, J. Appl. Cryst. **2**, 65 (1969).
[27]A. C. Larson and R. B. Von Dreele (unpublished).

PHYSICAL REVIEW B VOLUME 48, NUMBER 2 1 JULY 1993-II

Rapid Communications

Rapid Communications are intended for the accelerated publication of important new results and are therefore given priority treatment both in the editorial office and in production. A Rapid Communication in **Physical Review B** *should be no longer than four printed pages and must be accompanied by an abstract. Page proofs are sent to authors.*

Observation of a high-pressure cinnabar phase in CdTe

R. J. Nelmes, M. I. McMahon, N. G. Wright, and D. R. Allan
Department of Physics, The University of Edinburgh, Mayfield Road, Edinburgh EH9 3JZ, United Kingdom
(Received 15 March 1993)

Angle-dispersive powder-diffraction techniques with an image-plate area detector and synchrotron radiation have been used to reexamine the high-pressure behavior of cadmium telluride. We find that the well-known structural phase transition at ~3.5 GPa from the zinc-blende to NaCl structure actually involves two closely spaced transitions—zinc blende to cinnabar, and cinnabar to NaCl. This is the example of the cinnabar structure outside the mercury chalcogenides. The Cd and Te atoms are site ordered, and the coordination of the structure is closer to fourfold than is found in HgS cinnabar.

I. INTRODUCTION

The high-pressure behavior of CdTe has been a subject of interest for over 30 years following observations of a discontinuity in its optical[1] and electrical[2] behavior, and its density,[3] just above 3 GPa. Subsequent diffraction measurements[4–6] showed that this effect coincides with a phase transition from the ambient-pressure zinc-blende structure to the NaCl structure, with a volume decrease of ~16%.[6,7] A further transition to a β-tin structure was observed at a pressure of ~10 GPa.[2,5,6] More recent diffraction studies have confirmed these results, and revealed yet another transition from the β-tin structure to an orthorhombic structure (space group $Pmm2$) above 12 GPa.[8] Because of the very similar scattering power of Cd ($Z=48$) and Te ($Z=52$), it has not yet proved possible to determine the site ordering of any of these high-pressure structures.

In order to investigate the site ordering and compare the pressure dependence of CdTe with the complex behavior we have recently reported in the III–V analogue InSb,[9] we have commenced a study of CdTe using angle-dispersive diffraction techniques and synchrotron radiation. In this paper we report the observation of a new phase existing over a narrow pressure range between the zinc-blende and NaCl phases. This phase has the cinnabar structure, which has not previously been found outside the mercury chalcogenides. Its discovery in CdTe opens up the possibility that it is a more general feature of the transition between the zinc-blende and NaCl structures than has been supposed.

II. EXPERIMENTAL TECHNIQUES

Diffraction data were collected on station 9.1 at the Synchrotron Radiation Source, Daresbury, using angle-dispersive diffraction techniques and an image-plate area detector. In order to enhance the difference in scattering

FIG. 1. The integrated profiles of the patterns recorded from CdTe on pressure increase. (a) The ambient zinc-blende phase at 3.4 GPa, (b) the new (cinnabar) phase mixed with zinc blende at 3.6 GPa, and (c) the NaCl phase at 3.9 GPa with some very weak residual features from (b). The arrow in (b) indicates the (003) reflection of the cinnabar phase. Region A of profile (b) is enlarged in Fig. 2. In all three profiles, $\lambda=0.4654$ Å, and the sample-plate distance is ~365 mm. The exposure times were (a) 28 min, (b) 5 h, and (c) 18 min.

0163-1829/93/48(2)/1314(4)/$06.00

ower of the Cd and Te atoms, we used an incident wavelength of 0.4654 (1) Å, which is only 59 eV from the measured position of the Cd K-absorption edge. The two-dimensional powder patterns collected on the image plates were read on a Molecular Dynamics 400A PhosphorImager and then integrated to give conventional one-dimensional diffraction profiles. Details of our experimental setup and pattern integration program have been reported previously.[10–12]

The CdTe was a finely ground powder prepared from a starting material of 99.99+% purity supplied by the Aldrich Chemical Company. Three different samples were prepared, each loaded into a diamond-anvil cell with a full conical aperture of half-angle 40°–50°. The pressure-transmitting medium was a 4:1 mixture of methanol:ethanol, and the pressure was measured using the ruby fluorescence technique.[13] The structural results described were all obtained from full Rietveld[14] refinement of the integrated profiles using the program GSAS PROF.[15]

III. RESULTS AND DISCUSSION

On increasing pressure from ambient, no change was seen in the diffraction profile until 3.4 GPa, when extra reflections began to appear, as shown by the asterisks in Fig. 1(a). These extra peaks grew in intensity as the pressure was slowly increased, giving an approximately 50:50 mixture with the zinc-blende phase at a pressure of 3.6 GPa [Fig. 1(b)]. A further small increase in pressure to 3.9 GPa resulted in an almost complete transformation to a pure NaCl-like pattern [Fig. 1(c)], with just a very weak residue remaining of the mixture seen at 3.6 GPa.

It is evident that the pattern of Fig. 1(b) is not a two-phase mixture of zinc-blende and NaCl structures: there are many peaks that are not accounted for by either structure. Instead, these peaks were recognized as belonging to a pattern very similar to that obtained in a parallel study of HgTe in its cinnabar phase. So we attempted to fit the pattern with a three-phase mixture of zinc blende, cinnabar, and NaCl, and this resulted in a much-improved fit that accounted for all the observed diffraction peaks. However, the refined scale factor for the NaCl component became very small or negative, indicating that no NaCl phase was in fact required to fit the data: the observed pattern resulted from a mixture of zinc-blende and cinnabar structures alone. Analysis of the patterns collected from all three samples showed that the zinc-blende-to-cinnabar transition was seen in every case.

As yet, we have been unable to obtain a pattern of the cinnabar phase without a zinc-blende component. The crystal structure of the cinnabar phase has thus been obtained from a two-phase Rietveld refinement. An ordered structure was adopted since the weak (003) reflection of the cinnabar phase is clearly discernible, as shown in Fig. 2. [This reflection is indicated by an arrow in the complete profile of Fig. 1(b).] The intensity of the (003) reflection results from the difference in scattering between the Cd and Te atoms, and it would be absent if the structure were site disordered. In fact the intensity can be seen to be very similar to that of the adjacent (200) difference reflection of the (ordered) zinc-blende phase.

The refinement was carried out with the Cd atoms on the 3a sites of space group $P3_121$ and the Te atoms on the 3b sites, starting from the coordinates of the HgS cinnabar structure at ambient pressure.[16] The refined positions obtained were $(u=0.641(2),0,\frac{1}{3})$ for Cd and $(v=0.564(2),0,\frac{5}{6})$ for Te. These values, along with the refined scale factors, peak-width parameters, and atomic thermal parameters, gave the fit shown in Fig. 3.

Because the difference in scattering between Cd and Te is so small, it requires some care to be certain that the Cd atom, rather than Te, is at $(u>v,0,\frac{1}{3})$—and conversely for the other site. A test of this was made by interchanging the atoms and refining the site occupation while keeping the scale factor constant. Within error, the occupancies refined to values equivalent to the atoms interchanging back again. We also carried out refinements with the Cd and Te atoms interchanged and the occupancies fixed at 100%. This led to a poorer fit to the data, with some small but significant residual discrepancies between the observed and calculated profiles. We thus have a reasonably high level of confidence in the original site assignment.

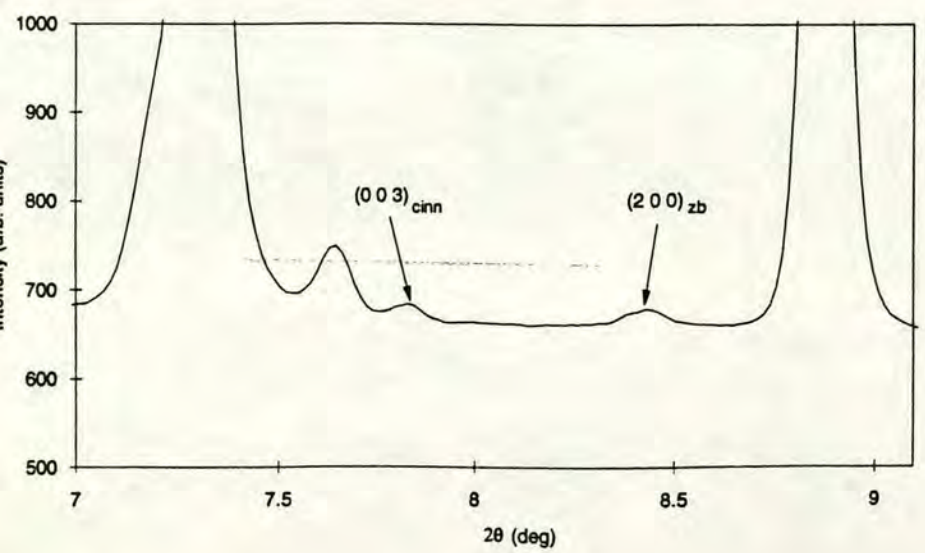

FIG. 2. Enlargement of region A in Fig. 1(b), showing the weak (003) Cd-Te difference reflection of the cinnabar phase and the corresponding (200) reflection of the zinc-blende phase.

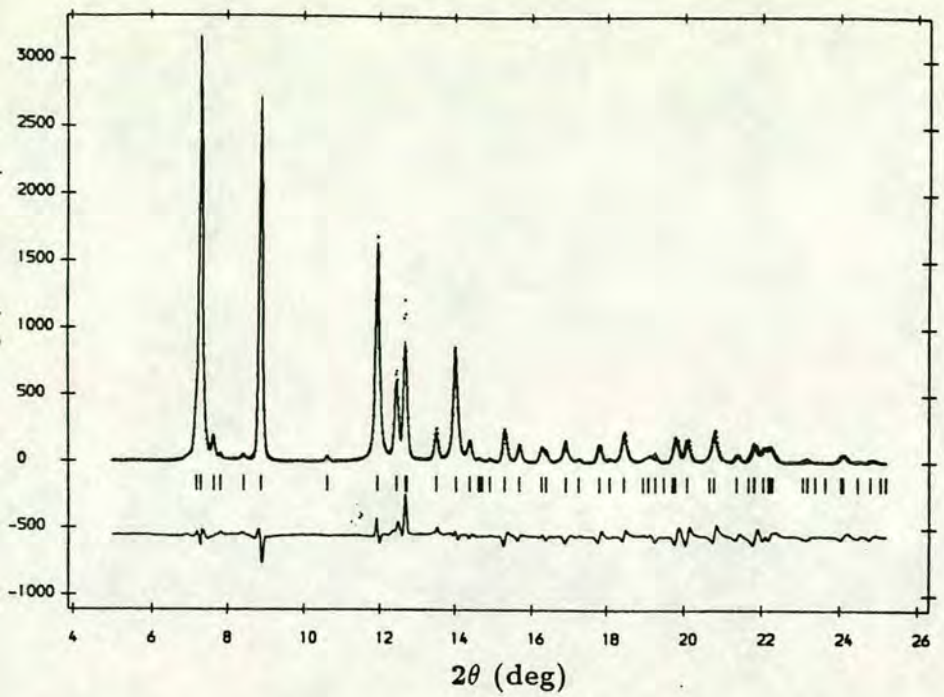

FIG. 3. A multiphase Rietveld refinement of the mixed cinnabar and zinc-blende profile in Fig. 1(b). The tick marks show the positions of all the allowed reflections of both phases. The difference between the observed and calculated profiles is shown below the tick marks.

The refined unit-cell dimensions at 3.6 GPa are =4.292(2) Å and $c=10.235(3)$ Å for the cinnabar ase [which thus has six atoms in a volume =163.3(1) Å^3], and $a=6.326(1)$ Å for the zinc-blende ase [eight atoms in $V=253.2(1)$ Å^3]. The volume decease ($\Delta V/V_0$) at the zinc-blende–cinnabar transition is en 13.3%. The unit-cell dimension of the NaCl phase mediately after the cinnabar-NaCl transition is =5.930(1) Å, implying a further volume decrease of 2.8%, and hence a total volume change for the two nsitions of 16.1%. This is within the range of values m 16% to 17.5% reported previously.[6,7,17,18]

The cinnabar structure can be interpreted as a distort- NaCl structure. The two become equivalent when $a=2.449$ ($\sqrt{6}$) and $u=v=\frac{2}{3}$. In CdTe, $c/a=2.385$, =0.641(2), and $v=0.564(2)$. The Cd atoms [at ,0,$\frac{1}{3}$)] are thus close to their NaCl positions, but the atoms are significantly displaced. The shortest Cd-Te tances around each atom are two of 2.724(4) Å, with o of 2.971(5) Å and two more of 3.414(5) Å. This is nificantly different from HgS in which there are two ort and four much longer nearest-neighbor Hg-S disces, and the structure is regarded as twofold coordited.[16] CdTe is much closer to a 4+2 coordination, inrmediate between the fourfold coordination of the c-blende structure (which has four Cd-Te distances of 2.74 Å) and the sixfold coordination of NaCl (which s six Cd-Te distances of ~2.97 Å).

Until now, the cinnabar structure has been believed to unique to the mercury chalcogenides.[19] It has been rted only in HgO and HgS at ambient pressure, and in Se and HgTe under high pressure.[20] In fact, an interediate cinnabar phase has probably been encountered eviously in CdTe, not on pressure increase but in the verse cycles of compressibility measurements by Cline d Stephens.[7] However, the phase was not identified d the possibility of its being cinnabar was subsequently ruled out explicitly.[6] In later studies of HgTe and $Hg_{0.8}Cd_{0.2}Te$ it was estimated that the cinnabar structure should become unstable above about 73% Cd.[21]

The supposed difference between Cd and Hg compounds has been attributed to a possible effect of the $4f$ electrons of Hg (Ref. 22) (Cd does not have them); and the cinnabar phase in the Hg compounds has been interpreted as an intermediate stage in which the sp^3 bonding of the zinc-blende structure first changes to NaCl.[23] The discovery of a cinnabar phase in CdTe, and the fact that the structure is approximately fourfold coordinated, invite a revised understanding of the bonding changes and the role of the cinnabar structure in the zinc-blende-to-NaCl transformation.

In conclusion, we have observed a cinnabar phase between the previously known zinc-blende and NaCl phases of CdTe, and this is the first known example of the cinnabar structure outside the Hg chalcogenides. The CdTe structure is site ordered, and its coordination is much closer to fourfold than is found in HgS cinnabar.

ACKNOWLEDGMENTS

We gratefully acknowledge the assistance of our colleagues J. S. Loveday and U. Schwarz in various aspects of the experimental work, and some helpful discussions with A. San Miguel and J. M. Besson. We would also like to thank A. A. Neild and G. Bushnell-Wye of the Daresbury Laboratory for their help in preparing the beam-line equipment, and Professor E. Sinn of Hull University for the loan of one of the pressure cells. This work was supported by a grant from the Science and Engineering Research Council and by facilities made available by Daresbury Laboratory. We also acknowledge the use of the SERC-funded Chemical Database Service at Daresbury Laboratory.

. L. Edwards and H. G. Drickamer, Phys. Rev. **122**, 1149 (1961).
. A. Samara and H. G. Drickamer, J. Phys. Chem. Solids **23**, 457 (1964).
. Jayaraman, W. Klement, Jr., and G. C. Kennedy, Phys. Rev. **130**, 2277 (1963).
. N. Mariano and E. P. Warekois, Science **142**, 672 (1963).
. B. Owen, P. L. Smith, J. E. Martin, and A. J. Wright, J. Phys. Chem. Solids **24**, 1519 (1963).
Y. Borg and D. K. Smith, Jr., J. Phys. Chem. Solids **28**, 49 (1967).
. F. Cline and D. R. Stephens, J. Appl. Phys. **36**, 2869 (1965).
Z. Hu, Solid State Commun. **63**, 471 (1987).
. J. Nelmes, M. I. McMahon, P. D. Hatton, J. Crain, and R. O. Piltz, Phys. Rev. B **47**, 35 (1993).
R. J. Nelmes, P. D. Hatton, M. I. McMahon, R. O. Piltz, J. Crain, R. J. Cernik, and G. Bushnell-Wye, Rev. Sci. Instrum. 63, 1039 (1992).
R. O. Piltz, M. I. McMahon, J. Crain, P. D. Hatton, R. J. Nelmes, R. J. Cernik, and G. Bushnell-Wye, Rev. Sci. Instrum. **63**, 700 (1992).
[12]R. J. Nelmes, M. I. McMahon, P. D. Hatton, R. O. Piltz, J. Crain, R. J. Cernik, and G. Bushnell-Wye, High Pressure Res. **8**, 677 (1992).
[13]G. F. Piermarini, S. Block, J. D. Barnett, and R. A. Forman, J. Appl. Phys. **46**, 2774 (1975).
[14]H. M. Rietveld, J. Appl. Crystallogr. **2**, 65 (1969).
[15]A. N. Fitch and A. D. Murray (unpublished).
[16]K. L. Aurivillius, Acta Chem. Scand. **4**, 1413 (1950).
[17]K. Strössner, S. Ves, W. Dieterich, W. Gebhardt, and M. Cardona, Solid State Commun. **56**, 563 (1985).
[18]S. B. Qadri, E. F. Skelton, A. W. Webb, E. R. Carpenter, M. W. Schaefer, and J. Furdyna, Phys. Rev. B **35**, 6868 (1987).
[19]T. Huang and A. L. Ruoff, in *Proceedings of 9th AIRAPT Conference*, edited by C. Homan, R. K. Maccrone, and E. Whalley, High Pressure Science and Technology, Vol. 22 (North-Holland, New York, 1984), Pt. 3, p. 37.
[20]Metals Crystallographic Data File, CISTI, Canada.
[21]S. B. Qadri, E. F. Skelton, A. W. Webb, and J. Dinan, J. Vac. Sci. Technol. A **4**, 1974 (1986).
[22]T. Huang and A. L. Ruoff, Phys. Rev. B **31**, 5976 (1985).
[23]T. Huang and A. L. Ruoff, J. Appl. Phys. **54**, 5459 (1983).

Phase transitions in CdTe to 5 GPa

M. I. McMahon, R. J. Nelmes, N. G. Wright, and D. R. Allan
Department of Physics, The University of Edinburgh, Mayfield Road, Edinburgh EH9 3JZ, United Kingdom
(Received 7 June 1993; revised manuscript received 16 August 1993)

Angle-dispersive powder-diffraction techniques using an image-plate area detector have been used to study the high-pressure phases of CdTe to 5 GPa. The recently discovered cinnabar phase between the zinc-blende and NaCl phases is found to be stable on both pressure increase and decrease. No pressure range of single-phase cinnabar has been found on pressure increase, but a single phase is obtained on pressure decrease, between 3.6 and 2.7 GPa. The cinnabar phase has an average bulk modulus of 32(1) GPa and is significantly more compressible than the zinc-blende and NaCl phases. All three phases are site ordered. Each atom in the cinnabar structure has two nearest-neighbor distances of ~2.74 Å (*a* bonds) and two of ~2.94 Å (*b* bonds), and the structure is thus close to fourfold coordinated. The next-nearest-neighbor distances are two of ~3.5 Å (*c* bonds). The *a* bonds are very similar in length to the nearest-neighbor distance in the zinc-blende phase, and the *b* bonds increase with pressure towards the nearest-neighbor distance in the NaCl phase. The *c*-bond distance and the interbond angles also become closer to the geometry of the NaCl structure with increasing pressure, but there are still large discontinuities in bond lengths and angles at the cinnabar-to-NaCl transition.

I. INTRODUCTION

The high-pressure behavior of CdTe has attracted continuing interest for over 30 years. A phase transition at bout 3.5 GPa was first found in optical studies,[1] and en confirmed in electrical measurements which realed a further transition at ~10 GPa.[2] Density measrements[3] showed the transition at 3.5 GPa was to a lid phase, with a volume decrease ($\Delta V/V_0$) of about %; the authors speculated that the high-pressure phase d the NaCl structure. Subsequent diffraction studies nfirmed this,[4–6] giving a more accurate estimate of % for the volume decrease at the zinc-blende-NaCl nsition,[6,7] and the transition at ~10 GPa was found to to the β-tin structure.[5,6] More recent diffraction work s reproduced these results and revealed yet another nsition, to an orthorhombic structure with space oup *Pmm*2, above 12 GPa.[8]

We have embarked on a diffraction study of CdTe, to mpare its structural pressure dependence and site orring with the behavior found recently in the isoelectnic compound InSb.[9] Using angle-dispersive techques and synchrotron radiation, we have shown[10] that Te has *two* transitions over a narrow pressure range at 3.5 GPa—first zinc-blende-to-cinnabar and then nabar-to-NaCl. The cinnabar structure has not, to our owledge, previously been reported outside the mercury alcogenides. In fact, Cline and Stephens[7] found evince of an intermediate phase in their direct-mpression measurements, but only on pressure dease, between 3.5 and 2.7 GPa. They speculated that phase was cinnabar, but neither they nor, later, Borg l Smith[6] could find any evidence for it in diffraction dies. Recent studies of HgTe and $Hg_{0.8}Cd_{0.2}Te$ (Ref. suggested that the cinnabar structure would be unstaabove ~73% Cd.

n our refinements of the cinnabar phase,[10] we obtained a crystal structure significantly different from HgS cinnabar.[12] In particular, the CdTe structure is close to fourfold coordinated, whereas the coordination of HgS is twofold. We were able to detect the weak (003) reflection, which arises from the difference in scattering between the Cd and Te atoms, and thus show the structure to be site ordered. These previous refinements were carried out on a powder pattern from a mixture of the zinc-blende and cinnabar phases, because we were unable to obtain single-phase cinnabar on pressure increase. The results of Cline and Stephens[7] suggest that this can be achieved on pressure decrease and we have now carried out a detailed study on pressure increase and decrease over the range up to 5 GPa. In this paper we report the results, including the compressibility and structural pressure dependence of the cinnabar phase.

II. EXPERIMENTAL DETAILS

Diffraction data were collected on station 9.1 at the Synchrotron Radiation Source, Daresbury, using angle-dispersive diffraction techniques and an image-plate area detector. To enhance the difference in scattering power of the Cd and Te atoms, the incident wavelength was set at 0.4650(1) Å, 59 eV from the measured position of the Cd *K* edge. The incident monochromatic beam was collimated by a platinum pinhole to a diameter of 75 μm. The two-dimensional powder patterns collected on the image plates were read on a Molecular Dynamics 400A PhosphorImager and then integrated to give conventional one-dimensional diffraction profiles. Details of our experimental setup and pattern integration program have been reported previously.[13–15]

The CdTe sample was a finely ground powder prepared from starting material of 99.99+% purity supplied by the Aldrich Chemical Company. Merill-Bassett diamond-anvil cells, having full conical apertures of 40° half angle, were used, with diamond-anvil cutlets of di-

3-1829/93/48(22)/16246(6)/$06.00

ameter 600 or 800 μm. Samples were loaded into 175-μm holes in tungsten gaskets with a 4:1 mixture of methanol:ethanol as the pressure-transmitting medium. The pressure was measured before and after each exposure using the ruby-fluorescence technique,[16] which gives a precision of 0.05 GPa. Taking into account small pressure drifts which sometimes occurred during exposures, we estimate the standard deviation on our pressure measurements to be 0.1 GPa. The structural results described were obtained from Rietveld refinement[17] of the integrated profiles using the program MPROF.[18]

III. RESULTS AND DISCUSSION

On pressure increase, the cinnabar phase was first detected at 3.53 GPa, slightly higher in pressure than in our first study (3.4 GPa).[10] At 3.74 GPa, the proportion of the cinnabar phase was sufficiently increased to carry out a two-phase refinement of the crystal structure; the integrated powder profile and the fit are shown in Fig. 1. The refined lattice parameters are $a = 6.324(2)$ Å for the zinc-blende phase, and $a = 4.282(2)$ Å, $c = 10.219(3)$ Å for the cinnabar phase. The volume decrease ($\Delta V/V_0$) at the transition is then 13.4(1)%, where V_0 is the volume per formula unit in the zinc-blende phase at ambient pressure (17.01 Å^3).

A further increase in pressure to 3.80 GPa resulted in an almost complete transition to the NaCl phase, as shown by the integrated profile in Fig. 2. Although the cinnabar and NaCl phases are closely related, and very little cinnabar remains, it was possible to obtain lattice parameters for both phases from this profile. The refined values are $a = 4.279(1)$ Å, $c = 10.205(18)$ Å for the cinnabar phase, and $a = 5.932(1)$ Å for the NaCl phase. The volume decrease at this second transition is thus 12.6(2)%.

The profile in Fig. 2 also contains very weak peaks from a residual zinc-blende component, as marked. In a second sample, this residual component was detectable at 3.95 GPa—beyond the full completion of the cinnabar-to-NaCl transformation. The V/V_0 values obtained from this pattern give the highest pressure point plotted for zinc blende in Fig. 3, and the corresponding point for NaCl. The open symbols in Fig. 3 show all the V/V_0 values obtained from both samples on pressure increase up to 5 GPa in the zinc-blende, cinnabar, and NaCl phases, and the region of coexistence of zinc blende and cinnabar is bounded by the two dashed vertical lines.

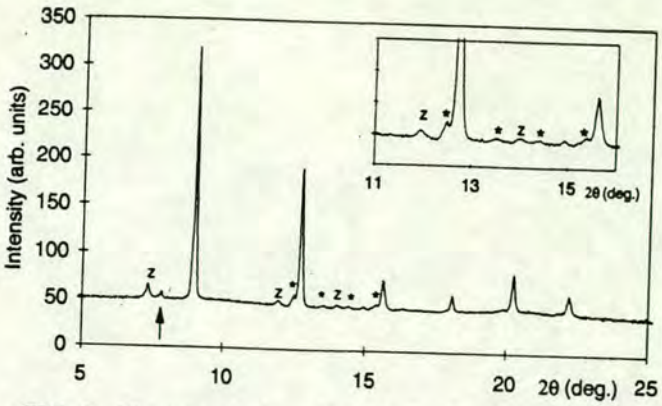

FIG. 2. The integrated profile of a pattern recorded from a mixture of zinc-blende, cinnabar, and NaCl phases at 3.80 GPa. The peaks marked z correspond to the same zinc-blende reflections marked in Fig. 1. Asterisks mark the positions of the cinnabar reflections, which are enlarged in the inset, while the arrow indicates the position of the (111) difference reflection in the NaCl phase.

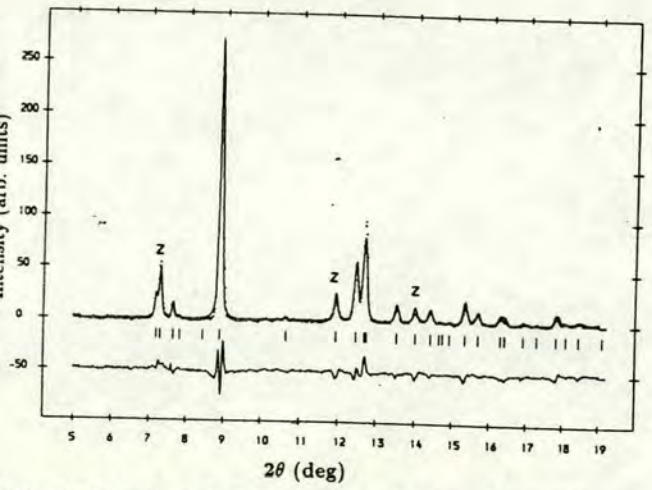

FIG. 1. The fit to the mixed zinc-blende-cinnabar profile collected at 3.74 GPa. The tick marks show the positions of all the reflections allowed by symmetry. The difference between the observed and calculated profiles is displayed below the tick marks. The (111), (220), and (311) reflections from the zinc-blende phase are marked z.

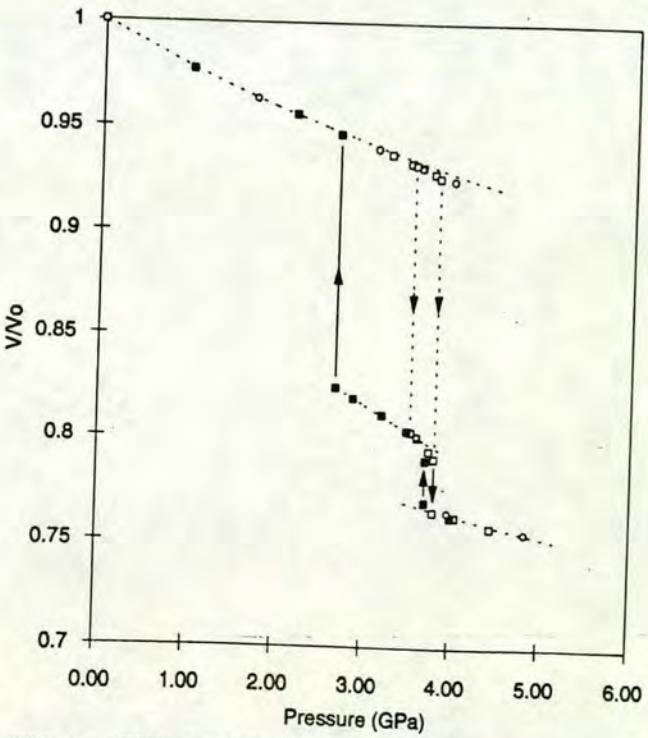

FIG. 3. V/V_0 as a function of pressure for two samples of CdTe on pressure increase (○ and □) and one of them on pressure decrease (■). The dotted curves are first-order Murnaghan equations of state as discussed in the text; those for the zinc-blende and NaCl phases are reproduced from Ref. 19.

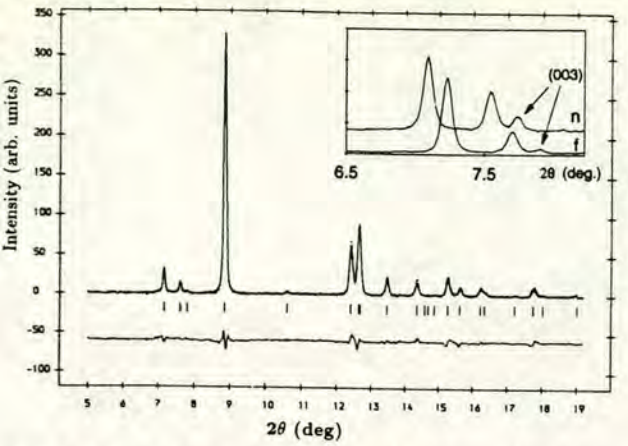

FIG. 4. The fit to the single-phase cinnabar profile collected 3.48 GPa. The tick marks show the positions of all the flections allowed by symmetry. The difference between the ob-rved and calculated profiles is displayed below the tick marks. ie inset shows the weak (003) difference reflection recorded at .175 keV, far (f) from the Cd K edge, and at 26.656 keV, near) the Cd K edge (at 26.715 keV), as in the main profile.

After reaching 5 GPa, the pressure was slowly reduced both samples. The reverse transition from NaCl to nnabar was found at 3.70 GPa, possibly indicating a all hysteresis as shown in Fig. 3. A further reduction pressure to 3.48 GPa for one sample, and 3.60 GPa for e other, resulted in patterns that contained peaks from *ly* the cinnabar phase, as shown for the first sample in g. 4. Further patterns were collected from this sample 3.20 and 2.87 GPa, and then the reverse cinnabar-to-ic-blende transition was observed at 2.67 GPa. There thus a difference of ~0.8 GPa between this pressure d the first appearance of the cinnabar phase on pres-re increase. The volume increase ($\Delta V/V_0$) between aCl extrapolated to 3.50 GPa and the fully transformed nnabar phase at that pressure is 3.4(2)%, followed by an rease of 2.0(2)% as the pressure falls through the cin-bar phase (to 2.67 GPa), and then a 12.2(1)% increase the transition to the zinc-blende phase.

Cline and Stephens[7] obtained remarkably similar re-ts in their direct volume measurements on pressure de-ase. They found a relatively abrupt volume increase of % from the NaCl phase, starting at 3.6 GPa; then a dual increase of 1.2% through the intermediate phase; l finally another abrupt increase of 12.9%, which is npleted at 2.65 GPa in the zinc-blende phase. It seems ond reasonable doubt that this is the same sequence of nges as we have now seen, and that their intermediate se was cinnabar.

Values of V/V_0 obtained on pressure increase and de-ase lie on common curves in all three phases, as shown Fig. 3. The dashed curves through the zinc-blende and Cl data are first-order Murnaghan equations of state culated from an initial bulk modulus B_0 of 42(2) GPa first derivative B' of 6.4(6) for the zinc-blende phase, $B_0=69(5)$ GPa, $B'=5.1(6)$ for the NaCl phase, as ermined by Strössner *et al.*[19] The agreement can be n to be good, except that our zinc-blende data require a smaller value of B': A best fit to our data gives $B_0=43.7(1.0)$ GPa and $B'=3.8(6)$. There are insufficient data to obtain new values of B_0 and B' in the NaCl phase. Our data for the cinnabar phase give an average bulk modulus of 32(1) GPa, corresponding to the straight line shown in Fig. 3. The highest pressure points for this phase lie below the line; this may be an artifact of the refinements of the mixed cinnabar-NaCl patterns, in which cinnabar is the minority phase and has many reflections overlapped with those from the NaCl component. This feature and the small pressure range prevent the refinement of a reliable value for B'. But the average compressibility is well determined, and is clearly much larger than for either the zinc-blende or NaCl phases. (Consequently, the volume changes between the cinnabar and other two phases are significantly pressure dependent.) The cinnabar phases of HgTe and HgS are also known to have anomalously small bulk moduli.[20] This probably reflects the fact that the cinnabar structure can respond to pressure by changes in interbond angles and reduction of the distance between the -Cd-Te-Cd-spirals (see below), as well as by direct compression of nearest-neighbor distances. By contrast, only the last of these is possible in the zinc-blende and NaCl structures.

The results shown in Fig. 3 were all obtained from refinements in which the atomic coordinates and thermal parameters, an overall scale factor for each phase, and peak-width parameters were all varied, as well as the lattice parameters used to derive V/V_0 values. Before carrying out these refinements, a careful check was made that the observed reflections conform to the cinnabar space group $P3_121$. As required, the only systematic absences found were $(00l)$ reflections with $l\neq 3n$. But these absences are also consistent with the lower symmetry $P3_1$ (or, equivalently, $P3_2$). Test refinements in $P3_1$ showed a very small change of ~0.01 in the difference in z coordinate between the Cd and Te atoms, while their y coordinates both remained zero within error. We concluded that any departure from $P3_121$ is too small to determine with confidence, and all further refinements were carried out in $P3_121$. As before, the Cd atoms were placed on the 3(a) at $(u,0,1/3)$, and the Te atoms on the 3(b) sites at $(v,0,5/6)$.

Refinement of the mixed zinc-blende-cinnabar pattern shown in Fig. 1, recorded on pressure increase at 3.75 GPa, gave $u=0.643(2)$ and $v=0.566(2)$, close to the values obtained at 3.6 GPa in our first study.[10] A typical fit to a *single*-phase pattern obtained on pressure decrease is presented in Fig. 4, using the data recorded at 3.48 GPa. The refined values for the u and v coordinates, and the c/a ratio, from the single-phase patterns are shown in Fig. 5, together with the results from the mixed-phase pattern at 3.75 GPa. There is no evidence of strong preferred orientation effects; but a preferred orientation parameter has been included in all the refinements, and this shifts the values of u and v by about one estimated standard deviation. There are some small but significant and systematic variations of peakwidth, such that reflections with $l>h,k$ are sharper than those with $l\leq h,k$. This indicates that the average crystallite is longer along the crystallographic c axis than perpendicular to it, as we

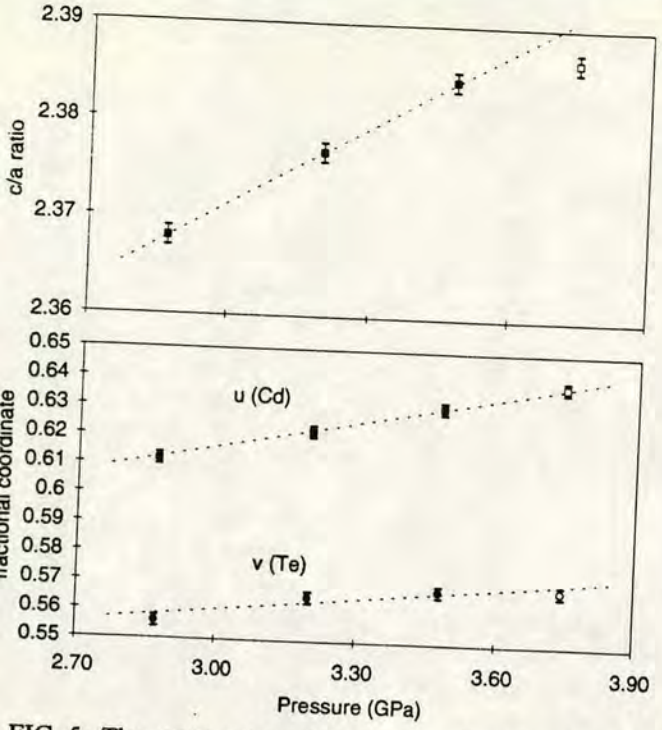

FIG. 5. The pressure dependence of the c/a ratio, and the u nd v atomic coordinates for the cinnabar phase of CdTe. The oints shown as ○ and □ were obtained from the mixed-phase rofile observed on pressure increase (see Fig. 1), while points own as ● and ■ were obtained from the single-phase cinnabar ofiles observed on pressure decrease. The dotted lines are ides for the eye.

ve also found in HgTe.[21]

The c/a ratio at 3.75 GPa on pressure increase can be en to deviate from the trend of the values obtained on essure decrease (Fig. 5). In case this could be an ar- act of the two-phase refinement, we fitted to the cinna- r reflections alone, but the same c/a values was ob- ned. Further work is needed to establish whether this reproducible feature of CdTe. However, we note that we have found other evidence of unit-cell distortion in mixed-phase environments—in InSb for example.[22]

The (003) reflection is enlarged in the inset of Fig. 4, which also includes the corresponding part of a profile recorded with an x-ray energy much further (540 eV) from the Cd K edge. The evident change in the relative intensity of (003) shows directly that it arises from the difference in scattering between Cd and Te, and hence that the structure is site ordered. [The arrow in Fig. 2 marks the (111) reflection of the NaCl phase. This reflection also arises from Cd-Te difference scattering, and hence the NaCl phase is shown to be site ordered too.] The site assignment was also examined further with the present single-phase refinements. As before,[10] if the Cd and Te atoms are interchanged and then the site occupancies are refined (keeping the scale factor constant), the values obtained are equivalent to the atoms interchanging back again. And refinements carried out with the atoms interchanged and the occupancies fixed at 100% give a significantly poorer fit to the data, as illustrated in Fig. 6. We thus conclude that the original site assignment is correct.

Table I compares the structural results obtained from the single-phase refinements of CdTe with the corresponding values for HgTe in its cinnabar phase at 3.6 GPa (Ref. 21) and for HgS cinnabar at ambient pressure.[12] The cinnabar structure can be interpreted as a distorted NaCl structure, and the final column gives values for ideal (cubic) NaCl referred to the hexagonal unit cell of cinnabar. As shown, the cinnabar structure becomes identical with NaCl when $c/a=2.449$ $(\sqrt{6})$ and $u=v=\frac{2}{3}$. The six equal nearest-neighbor distances in NaCl become two short distances (a bonds), two longer ones (b bonds) and two yet longer ones (c bonds) in cinnabar. These distances are given for CdTe, HgTe, and HgS in Table I. In the prototype cinnabar structure of HgS, the b and c bonds are similar in length, and much longer than the a bonds. Hence the structure is regarded as twofold coordinated. The a bonds link the Hg and S

TABLE I. The refined lattice parameters, c/a ratio, and u and v atomic coordinates of CdTe obtained from refinements of the three single-phase cinnabar patterns collected on pressure decrease. The calculated values for the nearest-neighbor (a bond and b bond), and next-nearest-neighbor (c bond) distances, and the intrachain bond angles are also given. The corresponding structural results for the cinnabar phase of HgTe at 3.6 GPa, and for HgS at atmospheric pressure (AP), are given for comparison. The final column gives the structural parameters of the NaCl phase expressed in terms of the cinnabar structure.

MX	CdTe			HgTe (Ref. 21)	HgS (Ref. 12)	
Pressure	2.87 GPa	3.20 GPa	3.48 GPa	3.6 GPa	AP	NaCl
a (Å)	4.338(1)	4.319(1)	4.301(1)	4.383(1)	4.146	
c (Å)	10.273(1)	10.265(2)	10.255(2)	10.022(1)	9.497	
c/a	2.368(2)	2.378(2)	2.384(2)	2.287(2)	2.292	2.449
u	0.612(2)	0.622(2)	0.631(2)	0.641(1)	0.720(3)	0.667
v	0.556(2)	0.565(2)	0.568(2)	0.562(1)	0.480(10)	0.667
a bonds (Å)	2.741(4)	2.749(4)	2.745(3)	2.732(4)	2.36(5)	
b bonds (Å)	2.929(5)	2.937(5)	2.948(4)	2.995(4)	3.10(5)	all equal
c bonds (Å)	3.567(5)	3.493(5)	3.441(5)	3.460(5)	3.30(5)	
M-X-M (°)	110.2(2)	107.7(2)	106.1(2)	104.2(2)	105.2(2.0)	90
X-M-X (°)	159.9(3)	162.7(2)	164.7(2)	165.6(2)	172.4(1.7)	180

be unique to the mercury chalcogenides,[23] which were all assumed to have the same twofold-coordinated structure as HgS. The structure has been interpreted as an intermediate step in which the sp^3 bonding of the zinc-blende structure first changes to *sp* bonding (in twofold coordination) before completing the change to NaCl.[24,25] The discovery of a cinnabar phase in CdTe, with a structure closer to fourfold coordinated, indicates that a broader interpretation may be required. Also, the magnitudes of the nearest-neighbor distances, in relation to those in the zinc-blende and NaCl phases, suggest a geometrical aspect to the role of the cinnabar phase in the zinc-blende-to-NaCl transition.

ACKNOWLEDGMENTS

We gratefully acknowledge several helpful discussions with A. San Miguel, and the assistance of J. S. Loveday and U. Schwarz in various aspects of the experimental work. We would also like to thank A. A. Neild and G. Bushnell-Wye of Daresbury Laboratory for their help in preparing the beamline equipment. This work is supported by a grant from the Science and Engineering Research Council and by facilities made available by Daresbury Laboratory. We also acknowledge the use of the SERC-funded Chemical Database Service at Daresbury Laboratory.

[1]A. L. Edwards and H. G. Drickamer, Phys. Rev. **122**, 1149 (1961).

[2]G. A. Samara and H. G. Drickamer, J. Phys. Chem. Solids **23**, 457 (1964).

[3]A. Jayaraman, W. Klement, Jr., and G. C. Kennedy, Phys. Rev. **130**, 2277 (1963).

[4]A. N. Mariano and E. P. Warekois, Science **142**, 672 (1963).

[5]N. B. Owen, P. L. Smith, J. E. Martin, and A. J. Wright, J. Phys. Chem. Solids **24**, 1519 (1963).

[6]I. Y. Borg and D. K. Smith, Jr., J. Phys. Chem. Solids **28**, 49 (1967).

[7]C. F. Cline and D. R. Stephens, J. Appl. Phys. **36**, 2869 (1965).

[8]J. Z. Hu, Solid State Commun. **63**, 471 (1987).

[9]R. J. Nelmes, M. I. McMahon, P. D. Hatton, J. Crain, and R. O. Piltz, Phys. Rev. B **47**, 35 (1993).

[10]R. J. Nelmes, M. I. McMahon, N. G. Wright, and D. R. Allan, Phys. Rev. B **48**, 1314 (1993).

[11]S. B. Qadri, E. F. Skelton, A. W. Webb, and J. Dinan, J. Vac. Sci. Technol. A **4**, 1974 (1986).

[12]K. L. Aurivillius, Acta Chem. Scand. **4**, 1413 (1950).

[13]R. J. Nelmes, P. D. Hatton, M. I. McMahon, R. O. Piltz, J. Crain, R. J. Cernik, and G. Bushnell-Wye, Rev. Sci. Instrum. **63**, 1039 (1992).

[14]R. O. Piltz, M. I. McMahon, J. Crain, P. D. Hatton, R. J. Nelmes, R. J. Cernik, and G. Bushnell-Wye, Rev. Sci. Instrum. **63**, 700 (1992).

[15]R. J. Nelmes, M. I. McMahon, P. D. Hatton, R. O. Piltz, J. Crain, R. J. Cernik, and G. Bushnell-Wye, High Pressure Research **8**, 677 (1992).

[16]G. F. Piermarini, S. Block, J. D. Barnett, and R. A. Forman, J. Appl. Phys. **46**, 2774 (1975).

[17]H. M. Rietveld, J. Appl. Crystallogr. **2**, 65 (1969).

[18]A. N. Fitch and A. D. Murray (unpublished).

[19]K. Strössner, S. Ves, W. Dieterich, W. Gebhardt, and M. Cardona, Solid State Commun. **56**, 563 (1985).

[20]A. Werner, H. D. Hochheimer, K. Strössner, and A. Jayaraman, Phys. Rev. B **28**, 3330 (1983).

[21]N. G. Wright, M. I. McMahon, R. J. Nelmes, and A. San-Miguel, Phys. Rev. B **48**, 13 111 (1993).

[22]See "A third interesting characteristic . . . ," p. 40, Ref. 9.

[23]T. Huang and A. L. Ruoff, *Proceedings of the 9th AIRAPT Conference*, edited by C. Homan, R. K. Maccrone, and E. Whalley, High Pressure Science and Technology, Vol. 22 (North-Holland, New York, 1984), Pt. 3, p. 37.

[24]T. Huang and A. L. Ruoff, J. Appl. Phys. **54**, 5459 (1983).

[25]The words "to *sp* bonding (in twofold coordination) before completing the change" were inadvertently omitted from a similar statement in the penultimate paragraph of Ref. 10.

Submitted to Phys. Rev. B, Dec.1993.

Pressure Dependence of the Imma Phase of Silicon

M.I. McMahon, R.J. Nelmes, N.G. Wright and D.R. Allan

Department of Physics and Astronomy, The University of Edinburgh,
Mayfield Road, Edinburgh, EH9 3JZ, UK.

PACS: 61.50.Ks, 62.50.+p

ABSTRACT

A detailed structural study of the newly-observed orthorhombic phase of silicon (spacegroup Imma) has been made using angle-dispersive powder-diffraction techniques and an image-plate area detector. The Imma phase is found to be stable between 13.2(3)GPa and 15.0(6)GPa, and both the β-tin-to-Imma and Imma-to-simple hexagonal transitions are found to be first order with volume changes ($\Delta V/V_0$) of 0.2(1)% and 0.5(1)% respectively. The volume discontinuities at the transitions are accompanied by pronounced discontinuities in Δ, the atomic coordinate of the Imma phase, which is found to vary from ~0.3 to 0.4 over the stability range of the Imma phase.

I. INTRODUCTION

Of all the semiconductors, the high-pressure behaviour of silicon continues to attract the most attention. Diffraction measurements have been performed at pressures up to 248GPa, and until recently ten high-pressure polymorphs were known to exist. The long-accepted phase transition sequence on compression is: cubic diamond (Si-I) to β -tin (Si-II) at ~11 GPa [1-3], β-tin to simple hexagonal (Si-V) at ~13–16GPa [2,3], simple hexagonal (SH) to an intermediate phase (Si-VI) at 37.6GPa [2], intermediate phase to hcp (Si-IX) at 42GPa [2], and hcp to fcc (Si-X) at 78GPa [4]. The crystal structure of the intermediate phase is uncertain, despite several attempts to solve this long-standing problem [5,6]. On pressure release, the metastable BC8 (Si-III) phase is obtained on slow pressure release from the β-tin phase [7], while two tetragonal phases (Si-VIII and Si-IX) are obtained on very rapid pressure release [8]. Si-IV, which is thought to have the hexagonal-diamond structure, can be obtained by heating BC8-Si at ambient pressure [9].

Stimulated by the extensive experimental studies, the high-pressure behaviour of silicon has also been the subject of a large number of theoretical studies [10]. These have been concerned primarily with understanding the relative stability of the various structures through total-energy calculations, while band-structure calculations predicted correctly that the high-pressure phases of silicon would be superconducting [11]. More recent calculations have predicted the structural pressure dependence of the metastable BC8 phase [12,13], and the phonon spectra of the high-pressure phases [10].

Recently, we have reported a previously-unobserved orthorhombic phase of silicon (spacegroup Imma) existing between the β-tin and SH phases [14]. The possibility of such a phase has been considered previously in theoretical calculations [15,16], and its existence explains the wide range of transition pressures reported for the β-tin to

SH transition [3]. The Imma phase may also account for the previously unexplained behaviour of the superconducting transition temperature, T_c, in the range 10-16GPa [17-20]. Very recently, Lewis and Cohen have performed *ab initio* calculations on the Imma phase [21], and have found the energy of the orthorhombic structure to be lower than, or equal to, the β-tin and SH structures for all unit cell volumes. Predictions were also made as to the pressure dependence of ratios of the unit-cell parameters c/a and b/a, and the (single) variable atomic coordinate, Δ.

In this paper we report a detailed structural study of the Imma phase of silicon using angle-dispersive powder-diffraction techniques and an image-plate area detector. The range of stability of the Imma phase has been determined, and the pressure dependence of the atomic volume, unit-cell parameters, and single variable atomic coordinate have been measured.

II. EXPERIMENTAL DETAILS

Diffraction data were collected on station 9.1 at the Synchrotron Radiation Source, Daresbury, using angle-dispersive diffraction techniques and an image-plate area detector. The incident wavelength was 0.4654(1)Å. The two-dimensional powder patterns collected on the image plates were read on a Molecular Dynamics 400A PhosphorImager and then integrated to give conventional 1-dimensional diffraction profiles. Details of our experimental set-up and pattern integration program have been reported previously [22-24]. The sample was a finely ground powder prepared from starting material of 99.9999% purity supplied by the Aldrich Chemical Company.

A Diacell DXR-4 diamond-anvil pressure cell [25] (DAC), having a full conical aperture of 50° half angle, was used. The diamond anvils had 600μm diameter culets while the preindented tungsten gasket had a spark-eroded hole 150μm in diameter. The incident beam was collimated by a platinum pinhole to a diameter of 75μm. Great care was

taken to reduce background levels and to avoid parasitic scatter from the gasket. Samples were loaded with a 4:1 mixture of methanol:ethanol as the pressure-transmitting medium, and the pressure was measured using the ruby-fluorescence technique [26].

Whenever possible, structural parameters, including lattice parameters, were obtained from Rietveld refinement [27] of the full integrated profiles using the program MPROF [28]. In some cases, however, such as the first appearance of very weak reflections from a new phase, or in the case of diffraction profiles containing more than one phase, the lattice parameters were determined by least-squares refinement of the measured d-spacings of the observed reflections.

III. RESULTS AND DISCUSSION

The measured lattice parameter of silicon at ambient pressure was 5.430(1)Å. On compression, the β-tin phase was first observed at 11.7GPa, in good agreement with transition pressure of 11.3(2)GPa observed previously for a sample under hydrostatic conditions [29]. The lattice parameters of the diamond and β-tin phases obtained at 11.7GPa were a=5.256(1)Å, and a=4.665(1)Å and c=2.565(3)Å, respectively. The c/a ratio for the β-tin phase is thus 0.550, with which the theoretical value of 0.549 agrees well [21], and the measured volume change ($\Delta V/V_0$) at the diamond-to-β-tin transition is 21.0(1)%. A least squares fit of a Murnaghan equation of state to our compressibility data for the diamond phase gives B_0=99.9(2.1)GPa, B'=3.8(4), in excellent agreement with the values of B_0=97.88GPa, B'=4.24 obtained from elastic constant measurements [30].

Comparison of the structural parameters of the β-tin, Imma and SH phases is greatly facilitated if the SH structure is described in terms of a pseudo-orthorhombic cell. The geometrical relationship between the three cells is shown in Figure 1. The Imma

structure becomes the β-tin structure when a=b and Δ=0.25, and the SH structure when b/c=√3 and Δ=0.50.

On pressure increase, diffraction profiles containing a mixture of the diamond and β-tin phases were observed up to 13.4GPa. At 14.4GPa, however, only peaks from the Imma phase were observed. The Imma phase remained stable until 15.4GPa, when lines from the SH phase began to appear. A least-squares fit to the measured d-spacings of the two phases gives lattice parameters of a=2.553(1)Å and c=2.382(1)Å for the simple hexagonal phase (a=4.764(1)Å, b=4.422(1)Å and c=2.553(1)Å in the orthorhombic setting), and a=4.737(1)Å, b=4.479(2)Å and c=2.552(3)Å for the Imma phase. The volume change ($\Delta V/V_0$) at the SH-to-Imma transition is thus 0.5(1)%. Thus only ~50% of the 1.4% change in atomic volume between the β-tin and SH phases occurs through compression of the Imma phase.

A further increase in pressure to 16.2GPa resulted in a pattern predominantly from the SH phase although a small fraction of the Imma phase remained. The SH cell parameters at this pressure are a=2.549(1)Å and c=2.383(1)Å (a=4.766(1)Å, b=4.415(1)Å and c=2.549(1)Å in the orthorhombic setting). The c/a ratio for the SH phase (in the orthorhombic setting) is 0.535, in excellent agreement with the value of 0.533 observed previously [14] and with the theoretical value of 0.534 [21].

After increasing the pressure further to 16.6GPa, the pressure was decreased. The Imma phase first appeared at 15.9GPa, resulting in a mixed-phase Imma–SH pattern. Reducing the pressure to 15.1GPa resulted in single-phase Imma patterns. The Imma-to-β-tin transition on further pressure decrease occurred at a pressure between 13.2GPa and 12.7GPa. No mixed β-tin–Imma patterns were observed in this pressure region. After decreasing the pressure to 12.1GPa to ensure that the sample contained only the β-tin phase, the pressure was again increased, and data collected at a further 6 pressures up to 18.1GPa, the highest pressure reached in this study. Single-phase

Imma patterns were observed between 13.5GPa and 15.2GPa, with single-phase SH patterns being observed above 16.3GPa. We therefore conclude that the Imma phase is stable from 13.2(3)GPa to 15.0(6)GPa, and note that this stability range corresponds very closely to the wide range of pressures previously assigned to the β-tin–SH transition [3].

The measured compressibilities of the β-tin, Imma and SH phases is shown in Figure 2, and the pressure dependences of the a, b and c lattice parameters of the three phases (all in the orthorhombic settings) are shown in Figure 3. Although we observed no mixed-phase β-tin–Imma patterns, and thus a direct determination of their relative densities at the same pressure was not possible, the compressibility data strongly suggest that the β-tin-to-Imma transition is first order with a volume change, $\Delta V/V_0$, at 13.2GPa of 0.2(1)%.

A volume discontinuity of ~0.2% would also seem to occur *within* the Imma phase at ~15GPa (Figure 2), and analysis of Figure 3 reveals that this is a result of discontinuities in all three lattice parameters. However, we note that 15GPa was the upper pressure at which single-phase Imma patterns were observed, and that above this only mixed-phase Imma–SH patterns occurred. We believe that the apparent discontinuity in the unit-cell volume of the Imma structure is an artefact of the mixed-phase nature of the samples, with the Imma unit cell being 'stretched' towards the shape required in the SH phase. We have seen similar unit cell distortions in mixed-phase samples of InSb [31] and CdTe [32]. With this is mind it is probably incorrect to determine the volume change at the Imma-to-SH transition from the mixed phase sample obtained at 15.4GPa. Extrapolation of the SH equation-of-state to 15GPa gives a volume change at the Imma-to-SH transition of 0.5(1)%.

The pressure dependence of the variable atomic coordinate in the Imma structure (denoted Δ) is shown in Figure 4. Six refinements of single-phase Imma patterns were

possible, two on profiles collected on pressure increase and four on profiles collected on pressure decrease. These are indicated in Figure 4 by the symbols ■ and □ respectively. Although the precision of the structural refinements was limited both by the hkl-dependent peakwidths observed in the Imma phase, and by correlations between Δ (the relative displacement of the atoms along the z axis) and strong preferred orientation (PO) along the (001) direction, the six points clearly suggest that Δ does not vary continuously from Δ=1/4 to Δ=1/2 in the Imma phase. Rather, the results suggest that the discontinuities in atomic volume are accompanied by possibly even more pronounced discontinuities in Δ at both the β-tin-to-Imma and Imma-to-SH transitions.

Further evidence of a discontinuity at the Imma-to-SH transition can be obtained from the mixed-phase Imma–SH profiles collected on both pressure increase and decrease at pressures above 15GPa. Although it was not possible to perform full Rietveld analysis on these profiles, a determination of Δ could be made from the relative intensities of the (020), (121) and (031) reflections from the Imma phase. The (121) reflection – which is absent in the SH phase and strong in the β-tin phase, and the intensity of which is therefore strongly dependent on Δ – is clearly visible in the mixed Imma–SH profile collected on pressure decrease at 15.8GPa. From the intensity of (121) relative to (020) and (031), taking into account the PO in the sample as obtained from the full Rietveld refinements, Δ can be estimated as 0.38(1). Thus even at a pressure at which the sample has mostly transformed to the SH phase, the remaining Imma component has a Δ very significantly different from Δ=0.5. Performing a similar analysis on a mixed-phase sample collected at 15.4GPa on pressure increase again yields Δ=0.38(1). These two points are plotted in Figure 4 using ● and ○ for data collected on pressure increase and pressure decrease respectively. Although some uncertainties remain as to precise values due to the effects of strong preferred orientation, our results show that Δ varies only from ~0.3 to 0.4 over the stability range of the Imma phase. (As for the atomic volume, this represents only 50% of the

difference between the β-tin and Imma phases - probably less in this case (see Figure 4).)

The discontinuous nature of the β-tin-to-Imma and Imma-to-SH transitions, and the small range of stability of the Imma phase, from V/V_0 ~0.69 to 0.68, differ from the behaviour predicted by the recent calculations of Lewis and Cohen [21]. Their results indicate continuous transitions, with the Imma phase having an energy lower that or equal to those of the other two phases over a wide range of V/V_0, from ~0.80 to 0.63. Some possible reasons for this are discussed [21], including the effect of finite temperature. It is to be noted that the calculations show Δ varying only from ~0.34 to 0.37 over the actual range of stability of the Imma phase [21] - in approximate agreement with the observed behaviour (see Figure 4).

On the basis of continuous transformations, Lewis and Cohen question our previous suggestion [14] that the β-tin-to-Imma and Imma-to-SH transitions might account for the discontinuities in the superconducting transition temperature, T_c, at similar pressures [17-20]. But the quite strongly discontinuous character of the transition keeps the question open.

In summary, our main conclusions are as follows:

(1) An orthorhombic Imma phase is confirmed to exist between the β-tin and simple hexagonal (SH) phases of silicon. The stability range of the Imma phase is 13.2(3)GPa to 15.0(6)GPa.

(2) Both the β-tin-to-Imma and Imma-to-SH transitions are found to be first-order with volume discontinuities of 0.2(1)% and 0.5(1)% respectively.

(3) The volume discontinuities at the β-tin-to-Imma and Imma-to-SH transitions are accompanied by discontinuities in Δ, the variable atomic coordinate of the Imma phase, which is found to vary from ~0.3 to 0.4 over the stability range of the Imma phase.

ACKNOWLEDGEMENTS

We gratefully acknowledge the assistance of our colleague J.S. Loveday in various aspects of the experimental work, and Dr. S.P. Lewis and Professor M.L. Cohen for making a preprint of reference 21 available. We would also like to thank A.A. Neild and G. Bushnell-Wye of the Daresbury Laboratory for their help in preparing the beam-line equipment. and Professor E. Sinn of Hull University for the loan of one of the pressure cells. This work is supported by a grant from the Science and Engineering Research Council and by facilities made available by Daresbury Laboratory. Valued assistance with the maintenance and development of pressure cells has been given by D.M. Adams of Diacell Products.

REFERENCES

[1] J.C. Jamieson, Science **139**, 762 (1963).

[2] H. Olijnyk, S.K. Sikka and W.B. Holzapfel, Phys. Lett. **103a**, 137 (1984).

[3] J.Z. Hu and I.L. Spain, Solid State Commun. **51**, 263 (1984).

[4] S.J. Duclos, Y.K. Vohra, and A.L. Ruoff, Phys. Rev. Lett. **58** , 775 (1987).

[5] S.J. Duclos, Y.K. Vohra, and A.L. Ruoff, Phys. Rev. B **41** , 12021 (1990).

[6] V. Vijaykumar and S.K. Sikka, High Pressure Research **4**, 306 (1990).

[7] J.S. Kasper and S.M. Richards, Acta Cryst. **17** , 752 (1964).

[8] Y.X. Zhao, F. Buehler, J.R. Sites and I.L. Spain, Solid State Commun. **59** , 679 (1986).

[9] R.M. Wentorf, Jr., and J.S. Kasper, Science **139** , 338 (1963).

[10] S.P. Lewis and M.L. Cohen, Phys. Rev. B **48**, 3646 (1993), and references therein.

[11] K.J. Chang and M.L. Cohen, Phys. Rev. B **30** , 5376 (1984).

[12] J. Crain, G.S. Ackland, S.J. Clark, P.D. Hatton, V. Milman, M.C. Payne and B. Reid, Phys. Rev B. In Press

[13] S.J. Clark, G.S. Ackland and J. Crain, Phys. Rev B. In Press

[14] M.I. McMahon and R.J. Nelmes, Phys. Rev. B **47**, 8337 (1993).

[15] K.J. Chang and M.L. Cohen, Phys. Rev. B **31**, 7819 (1985).

[16] R.J. Needs and R.M. Martin, Phys. Rev. B **30**, 5390 (1984).

[17] M.A. Il'ina and E.S. Itskevich, Fiz. Tverd. Tela (Leningrad) 22 , 3139 (1980) [Sov. Phys. Solid State **22**, 1833 (1980)].

[18] K.J. Chang, M.M. Dacorogna, M.L. Cohen, J.M. Mignot, G. Chouteau and G. Martinez, Phys. Rev. Lett. **54**, 2375 (1985).

[19] T.H. Lin, W.Y. Dong, K.J. Dunn, C.N.J. Wagner and F.P. Bundy, Phys. Rev. B **33**, 7820 (1986).

[20] J.M. Mignot, G. Chouteau and G. Martinez, Phys. Rev. B **34**, 3150 (1986).

[21] S.P Lewis and M.L. Cohen, Phys. Rev. B **48**, 16144 (19930.

[22] R.J. Nelmes, P.D. Hatton, M.I. McMahon, R.O. Piltz, J. Crain, R.J. Cernik and G. Bushnell-Wye, Rev. Sci. Instrum. **63**, 1039 (1992).

[23] R.O. Piltz, M.I. McMahon, J. Crain, P.D. Hatton, R.J. Nelmes, R.J. Cernik and G. Bushnell-Wye, Rev. Sci. Instrum. **63**, 700 (1992).

[24] R.J. Nelmes and M.I.McMahon, Advances in X-Ray Analysis, Vol 43, To be Published

[25] D.M. Adams, Diacell Products, 54 Ash Tree Road, Leicester, UK.

[26] G.F. Piermarini, S. Block, J.D. Barnett, and R.A. Forman, J. Appl. Phys. **46**, 2774 (1975).

[27] H.M. Rietveld, J. Appl. Cryst. **2** , 65 (1969).

[28] A.N. Fitch and A.D. Murray (Unpublished) (1990).

[29] J.Z. Hu, L.D. Merkle, C.S. Menoni and I.L. Spain, Phys. Rev. B **34**, 4679, (1986).

[30] *Crystal and Solid State Physics*, Vol. I of *Landolt-Börnstein Numerical and Functional Relationships in Science and Technology* (Springer-Verlag, Berlin, 1966)

[31] R.J. Nelmes, M.I. McMahon, P.D. Hatton, J. Crain and R.O. Piltz. Phys. Rev. B **47**, 35 (1993).

[32] M.I. McMahon, R.J. Nelmes, N.G. Wright and D.R. Allan In Press, Phys. Rev. B (Dec. 1993).

FIGURE CAPTIONS

Fig. 1. (a) The Imma structure of silicon, illustrating the variable atomic coordinate, Δ, which defines the height of the atoms in the faces of the unit cell. When a=b and Δ =0.25, the Imma structure is equivalent to that of the β-tin structure, while if b/c=$\sqrt{3}$ and Δ=0.50, the Imma structure is equivalent to that of the SH structure. This latter case is illustrated in (b), where the hexagonal unit cell is shown for comparison.

Fig. 2. V/V_0 as a function of pressure for the , Imma, and simple hexagonal (SH) phases of silicon. Points shown as ■ were collected on pressure increase, while points shown as □ were collected on pressure decrease. The dotted lines are guides for the eye.

Fig. 3. The pressure dependence of (a) the a and b lattice parameters, and (b) the c lattice parameter, of the β-tin, Imma, and simple hexagonal (SH) phases of silicon. For the SH phase the lattice parameters are referred to the orthorhombic setting as discussed in the text. The points shown as ■ were obtained on pressure increase, while points shown as □ were obtained on pressure decrease.

Fig. 4. The pressure dependence of the atomic coordinate Δ in the β-tin, Imma, and simple hexagonal (SH) phases of silicon. In the β-tin phase, Δ is fixed by symmetry at 0.25, while in the SH phase it is fixed at 0.5. Points shown as ■ and □ were obtained from single-phase Imma samples observed on pressure increase and decrease respectively, while points labelled ● and ○ were obtained from mixed-phase Imma–SH samples.

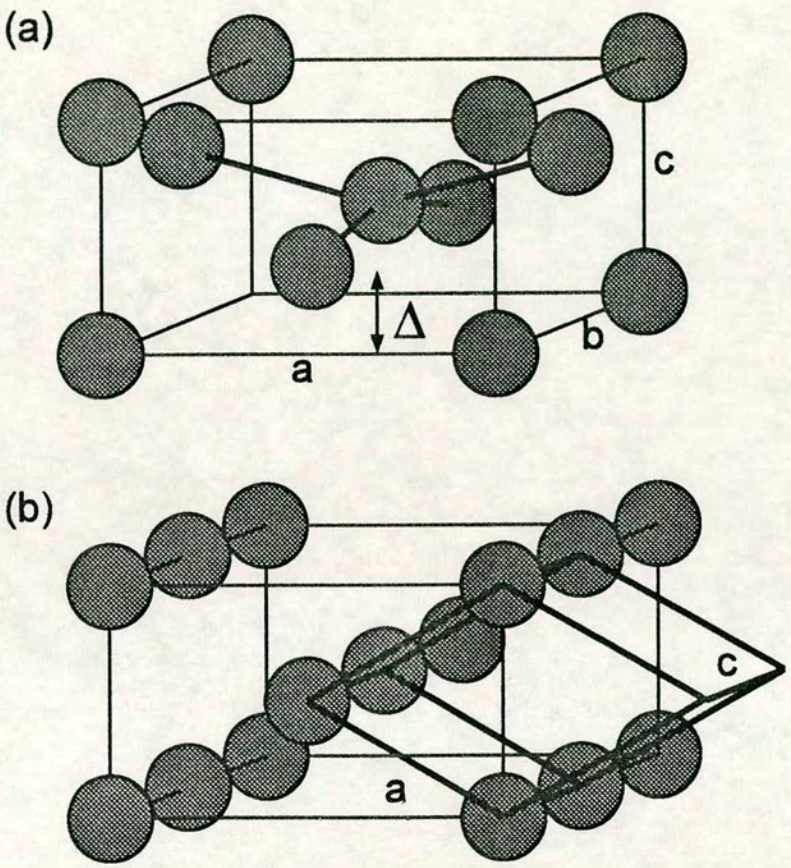
(a)
c
Δ
b
a
(b)
c
a

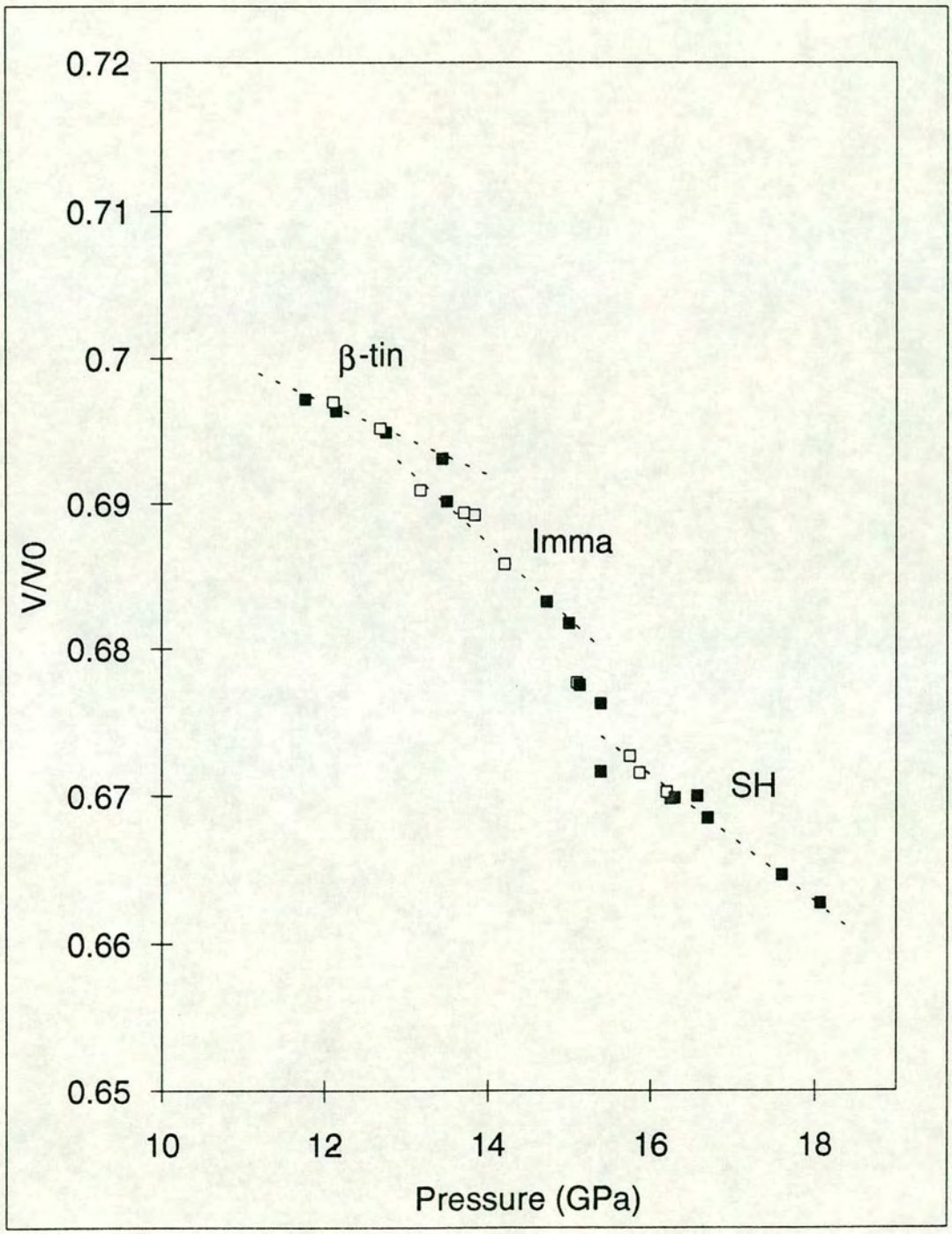
0.72
0.71
0.7
0.69
0.68
0.67
0.66
0.65
V/V0
β-tin
Imma
SH
10
12
14
16
18
Pressure (GPa)

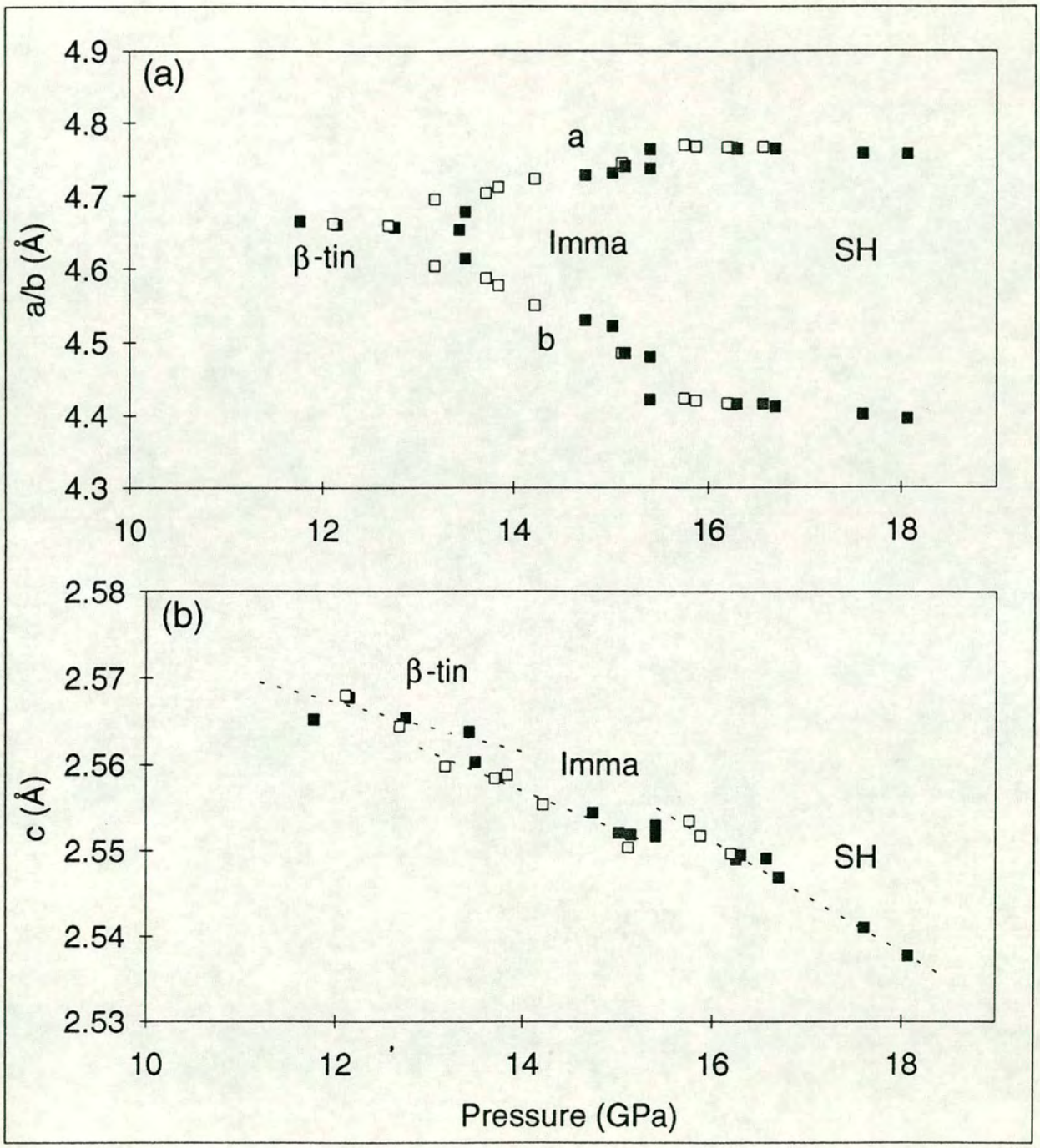
(a)
a/b (Å)
4.9
4.8
4.7
4.6
4.5
4.4
4.3
a
b
β-tin
Imma
SH
10
12
14
16
18
(b)
c (Å)
2.58
2.57
2.56
2.55
2.54
2.53
β-tin
Imma
SH
10
12
14
16
18
Pressure (GPa)

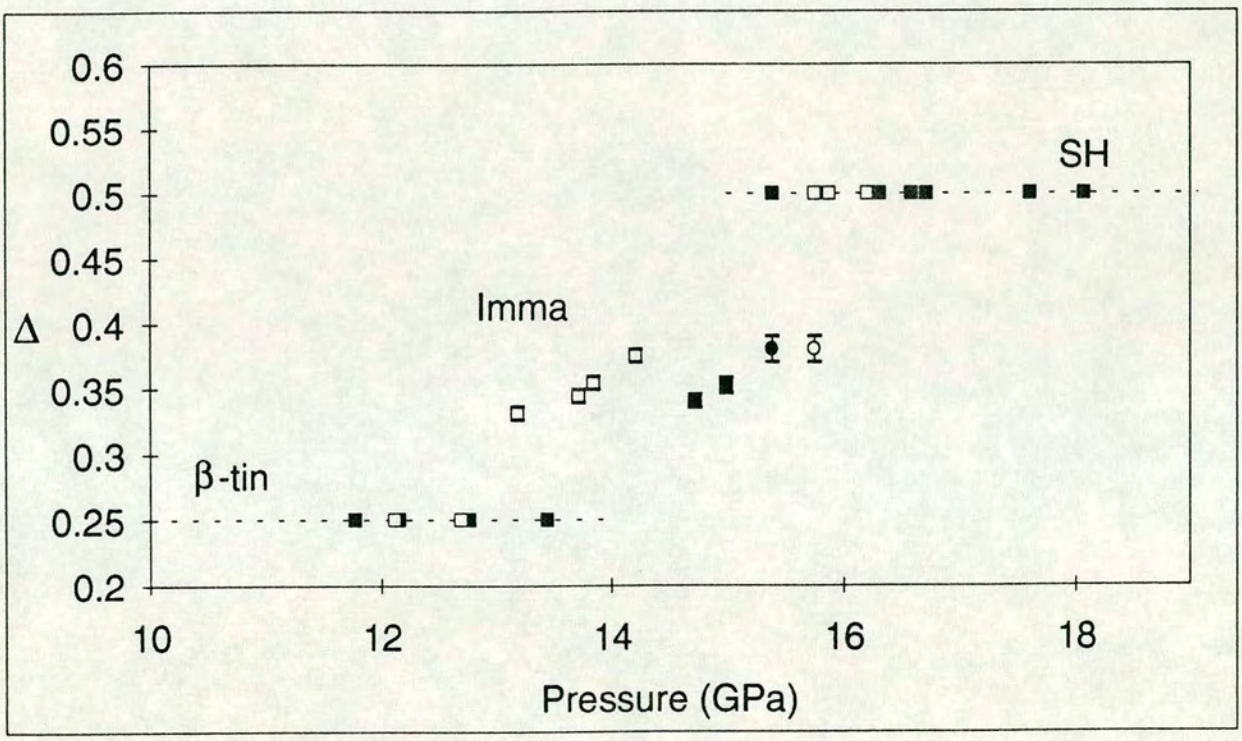
0.6
0.55
0.5
0.45
0.4
0.35
0.3
0.25
0.2
Δ
SH
Imma
β-tin
10
12
14
16
18
Pressure (GPa)